Qualitative and Quantitative analysis of compound semiconductors using Atom Probe Tomography

Arul KUMAR

Examination committee:
Prof. Dr. Ir. Ewald Janssens, chair
Prof. Dr. Ir. Wilfried Vandervorst, supervisor
Prof. Dr. Ir. Marc Heyns
Prof. Dr. Andre Vantomme
Dr. Janusz Bogdanowicz

Prof. Dr. Angela Vella
(Université de Rouen)
Prof. Dr. Christophe Detavernier
(Universiteit Gent)
Prof. Dr. Ir. Frank Renner
(Universiteit Hasselt)

Dissertation presented in partial fulfillment of the requirements for the degree of Doctor in Engineering Science

May 2016

Uitgegeven in eigen beheer, Arul KUMAR, Celestijnenlaan 200D, B-3001 Leuven (Belgium)

Acknowledgments

The work carried out in this thesis as well as my personal and professional growth during the five years at IMEC would not have been possible without a long list of people that I would like to acknowledge here.

Firstly, I would like to express my sincere gratitude to my supervisor Prof. Dr. Wilfried Vandervorst for his continuous support during my Ph.D. study and related research, for his patience, motivation, and immense knowledge. His guidance helped me in all the time of research and writing of this thesis. I could not have imagined having a better advisor and mentor for my Ph.D. study. I would also like to express my special appreciation and thanks to my daily supervisor Dr. Janusz Bogadonwicz, you have been a tremendous guide for me. I would like to thank you for encouraging my research and for allowing me to grow as a research scientist. Your advice on both research as well as on my career have been priceless. I would also like to thank my committee members, Prof. Dr. Andre Vantomme , Prof. Dr. Marc Heyns, Prof. Dr. Ewald Janssens, Dr. Angela Vella, Prof. Dr. Christophe Detavernier and Prof. Dr. Frank Renner for serving as my committee members. I also want to thank you for letting my defense be an enjoyable moment, and for your brilliant comments and suggestions.

I wish to sincerely acknowledge the Atom Probe Tomography team at IMEC - Dr. Matthieu Gilbert, Dr. Jelle Demeulemeester, Dr. Claudia Fleischmann, Davit Melkonyan, Dr. Laurent Arnoldi, Dr. Richard Morris- for the stimulating discussions and for all the fun we have had in the last four years. I would especially like to thank Dr. Matthieu Gilbert for his patience during my initial period of training on the Atom Probe. A special thanks to Dr. Angela Vela and the team at GPM, Université et INSA de Rouen, France for the important role they played during this thesis project.

I want to acknowledge all the colleagues of the material and component analysis (MCA) group for the fruitful discussions and continuous support. In particular, special thanks to Chris Drijbooms and Patricia Van Marcke for their support on the SEM and focused ion beam. I would also like to acknowledge the TEM team for accommodating all the special requests on the APT samples. I am furthermore grateful to Dr. Federica Gencarelli for the samples she provided me during this project.

A special thanks to my family. Words cannot express how grateful I am to my mother, and father for all of the sacrifices that you have made on my behalf. Your prayer for me was what sustained me thus far. I would also like to thank all of my friends who supported me in writing, and encouraged me to strive towards my goal. At the end I would like express appreciation to my beloved wife Phalguni who spent sleepless nights with and was always my support in the moments when there was no one to answer my queries.

Abstract

Current state of the art electronic devices are nanoscaled, three-dimensional and employ compound semiconductors like SiGe, InP, InGaAs etc. as the active components. The metrology requirements for these devices are structural and elemental analysis in three-dimensions with sub-nanometer resolution. Laser assisted Atom Probe Tomography (L-APT) is one metrology tools that fulfills this criteria and is being developed actively for routine analysis of semiconductor devices. In this thesis, we evaluate and develop L-APT for qualitative and quantitative analysis of compound semiconductors. To do this, we identified two main focus areas, firstly improve the understanding of the interaction between the laser and the semiconducting specimen and secondly develop and apply statistical data mining approaches to understand the impact of physical mechanisms like cluster formation on material properties.

It is well known that the pulsed laser generates a thermal pulse in the specimen. We developed a new method to quantify the temperature at the apex of the semiconducting specimen. A major advantage of the proposed method is that the determined temperature value is a function of derivatives, thereby keeping the error low. Subsequently, we used the method to gain insight into the impact of the laser on the apex shape of moderately absorbing materials (e.g. Si under green illumination) and laser absorption by a-priori non-absorbing materials (e.g. absorption of 515 nm laser by GaN). In this work we will show that the apex shape is a function of both the absorption depth and the spatial distribution of the resonantly coupled light. In situations when the light couples in close proximity to the apex of the tip, minimal diffusion of the locally generated heat occurs before field evaporation, leading to an asymmetrical apex shape. The non-hemispherical shape in turns degrades spatial resolution due to magnification variations across the apex. Regarding the

absorption by a-priori transparent samples, we observed that amorphized shell created due to the Ga ion beam damage during sample preparation is highly absorptive and plays a vital role in laser absorption.

In this work we used L-APT to understand the role of Sn clusters formation in layer relaxation of $Ge_{(1-x)}Sn_{(x)}$ layers. To do this, we first verified the absence of field and laser induced artifacts in the reconstructed layers and also developed a new cluster analysis algorithm to extract ultra-fine scaled clusters (few 10's of atoms). We will demonstrate that Sn cluster formation is not the dominant relaxation mechanism in layers relaxing due to its thickness or due to a post growth thermal anneal and defect generation is potentially the main cause of relaxation.

Abstract (nl)

Hedendaagse micro-elektronica chips worden opgebouwd uit 3-dimensionele componenten met afmetingen in de orde van enkele tot tientallen nanometers. Alhoewel Si en Ge de voorbij decennia hun dienst bewezen hebben als halfgeleidermateriaal bij uitstek, worden samengestelde halgeleidermaterialen zoals SiGe, InP, InGaAs, enz. steeds vaker geïmplementeerd in hedendaagse performante microelektronica. Deze evoluties in micro-elektronica vertalen zich op hun beurt in uitdagende noden op het gebied van metrologie, waarbij toegang tot structurele- en kwantitatieve elementele analyse in 3 dimensies en met sub-nanometer resolutie een "must" is. De laser-geassisteerde atoom probe tomograaf (L-APT) is in dit opzicht een techniek die aan deze voorwaarden voldoet. De mogelijkheden om deze techniek routineus in te zetten als analyse techniek in de halfgeleider industrie vormt dan ook een actief onderzoeksgebied binnen de metrologie. Algemeen gezien situeert deze thesis zich in de evaluatie en ontwikkeling van L-APT analyse, specifiek voor samengestelde halfgeleidermaterialen. Binnen dit domein werd gefocust op een fundamenteel begrip van de interacties tussen de laser en een samengestelde halfgeleidercomponent met dimensies in de orde van enkele nanometer. Naast de fundamentele laser-specimen interactie werden statistische "data mining" technieken ontwikkeld voor de studie van fysische mechanismen en hun impact op de materiaaleigenschappen (bv. clustervorming).

Aan de basis van L-APT ligt het genereren van een thermische puls in het te analyseren specimen door middel van een laser puls. In deze thesis werd een methode ontwikkeld om de temperaturen ontwikkeld in de apex van het specimen te kwantificeren. Het grootste voordeel van deze voorgestelde methode is dat de temperatuur beschreven wordt als een functie van afgeleiden, wat de foutmarge laag houdt. Vervolgens werd

deze methode ingezet om een beter inzicht te krijgen in de impact van de laser op de apex-vorm. Dit zowel voor materialen die a priori geen fotonen absorberen (bv. De combinatie van GaN met een laser golflente van 515 nm) en middelmatige absorptie regimes (bv. Si in combinatie met een 515 nm golflengte laser). De bevinding van dit werk is dat de apex-vorm een functie is van zowel de absorptie diepte als de ruimtelijke distributie van het resonant-gekoppelde licht. In situaties waarbij de resonantie dicht bij de apex piekt is de diffusie van de lokaal gegenereerde warmte minimaal vóór de veld-emissie van ionen plaats vindt. Dit leidt op zijn beurt tot een asymmetrische apex vorm. De niet-hemisferische vorm vertaalt zich vervolgens in een lagere ruimtelijke resolutie in de analyse omwille van variaties in lokale vergroting. In het geval van niet-absorberende materiaal-laser combinaties speelt fotonen-absorptie in de amorfe oppervlaktelaag een cruciale rol in het L-APT proces. Deze amorfe laag wordt niet-intentioneel geïnduceerd tijdens de specimen preparatie door Ga-ionen implantatie.

Met betrekking tot materiaalanalyse werd in dit werk L-APT ingezet om de rol van Sn-clustervorming in de relaxatie van $Ge_{(1-x)}Sn_{(x)}$ dunne films te begrijpen. Hiervoor werd eerst geverifieerd in welke mate er veld- of laser geïnduceerde artefacten aanwezig zijn in de gereconstrueerde data, en in welke mate ze een impact hebben op de analyse. Vervolgens werd een nieuw cluster-analyse algoritme ontwikkeld om structurele data ivm ultra fijne clusters (enkele 10-tallen atomen) te extrageren. In deze thesis wordt aangetoond dat Sn-clustervorming niet het belangrijkste relaxatiemechanisme is, zowel voor thermisch geïnduceerde relaxatie als relaxatie die voorkomt in dikkere films. De generatie van defecten werd geïdentificeerd als grootste oorzaak voor relaxatie.

List of Abbreviations

α-GaN Amorphous GaN

C_P Heat capacity

d_{core} Characteristic distance for core atoms in core linkage cluster algorithm

d_{link} Characteristic distance for border atoms in core linkage cluster algorithm

d_{max} Characteristic distance for DBSCAN cluster algorithm

$E_{100-500}$ Energy required to heat the sample from 100 K to 500 K

E_{20-500} Energy required to heat the sample from 20 K to 500 K

F_0 Field required to evaporate at 0 K temperature

F_{ev} Threshold field evaporation

Q_0 Barrier height at zero applied field

Q_b Potential barrier height under applied field

R_K Resonant radius for light coupling

R_T Threshold radius for Delaunay based clustering algorithm

V_0 Voltage required to field evaporate at 0 K temperature

ADLD Advanced delay line detector

APT Atom Probe Tomography

CMOS Complementary-Metal-Oxide-Semiconductor

CSR Charge State Ratio

CVD Chemical vapor deposition

DBSCAN Density-Based Clustering algorithm

EDS Energy-dispersive X-ray spectroscopy

F Electric field at the apex

FDTD Finite-difference time domain

FIB Focused Ion Beam

FTF Fourier Transform Filter

L-APT Laser Assisted Atom Probe Tomography

MBE Molecular beam epitaxy

MOSFET Metal-oxide-semiconductor field effect transistors

NIR Near-infrared

PMOR Photo-modulated optical reflectance

PSD Position sensitive detector

QW Quantum well

RBS Rutherford Backscattering Spectroscopy

RHEED Reflection high-energy electron diffraction

RTA Rapid thermal anneal

SEM Scanning electron microscope

SIMS Secondary Ion Mass spectroscopy

SRD Strain relaxation degree

STEM Scanning Transmission Electron Microscope

TEM Transmission Electron Microscope

TFET Tunneling FET's

TOF Time of Flight

XPS X-Ray Photoelectron Spectroscopy

XRD X-Ray diffraction

Contents

List of Figures

List of Tables

Chapter 1

Introduction

The aim of this doctoral thesis is to evaluate and develop atom probe tomography (APT) for metrology of advanced semiconducting materials like $Ge_{(1-x)}Sn_{(x)}$, SiGe, GaN etc. The interest in these new semiconducting materials stems from the aspiration of achieving higher performance and functionality in micro-electronic devices. Conventional microelectronic devices (namely metal-oxide-semiconductor field effect transistors (MOSFET)) were predominately made up of Si and its compounds like SiO_2, nickel silicides etc. Until about the early 2000s, increased performance was achieved by pure geometrical scaling of these devices. However, when the physical channel lengths of MOSFET's approached $\sim$ 100 nm and the thickness of the gate oxide reached $\sim$ 1 nm, further shrinking their dimensions did not significantly improve performance. This was due to a myriad of new semi-classical and quantum phenomena occurring in the device like short channel effects [4], gate leakage due to electron tunneling [5] etc.. These in-turn lead to multiple effects which degraded device performance like increased power consumption due to leakage current, lower carrier mobility due to increased surface scattering, variation in threshold voltage due to oxide charging, device breakdown due to gate-oxide tunneling etc.

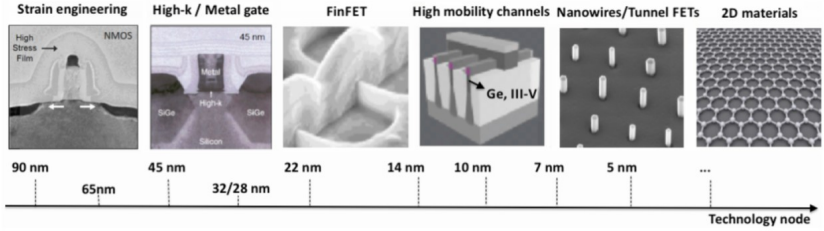

Figure 1.1 – Innovation in CMOS device technology introduced in large scale production from the 90 nm node till 22 nm node and future device structures under consideration for 14 nm node and beyond. Reproduced from [6].

To improve the performance of devices with smaller gate dimensions new concepts both in terms of device structure and materials were introduced (**Fig. 1.1**). Examples include, introduction of SiGe and Si_3N_4 as stressors to improve charge carrier mobilities [7], substitution of SiO_2 gate oxide and ploy-Si gate with higher permittivity materials (high-k dielectrics) and a metal gate, respectively, in order to reduce the leakage currents and maintain acceptable OFF-state performance [7], introduction of FinFET's like device architecture for improved electrostatic control of the gate [8] etc. Next generation microelectronic devices from 14 nm node and beyond are envisioned to include new novel semiconductors like GeSn, III/V compounds, nanowires etc. and device architectures like gate all around FET, tunneling FET's (TFET) etc. [9]. This ever-evolving landscape leads to new interactions at the atomic scale often resulting in unexpected outcomes. For example, to keep the costs down, structures based on materials like Ge and III/V need to be co-integrated onto Si substrates. This can be done among others via heteroepitaxy of these materials in nanoscaled trenches [10]. However, the latter is challenging as integrating these materials onto Si leads to the generation of crystal defects (like vacancies, misfit dislocations, threading dislocations etc.) due to lattice mismatch, which are detrimental for device performance [11]. Furthermore, due to the different thermodynamics and kinetics of growth in confined volumes as compared to bulk, the resulting layers often have increased surface roughness, enhanced relaxation etc. [12]. To understand the physical mechanisms leading to these new phenomena, metrology of these devices is required to determine layer compositions, layer thickness, dopant distributions, interface characteristics etc. Faced with the reduced dimensionality of these devices, there is therefore a need for a metrology concept that would provide this information [13]:

- in confined volumes of a few 100 nm^3,
- with sub-nanometer or ideally atomic resolution in three dimensions, and
- with high (equal) detection efficiency for all elements.

Conventional metrology tools like Secondary Ion Mass spectroscopy (SIMS), Rutherford Backscattering Spectroscopy (RBS), X-Ray Photoelectron Spectroscopy (XPS) and X-Ray diffraction (XRD), are generally not up to these challenges, primary due to their lack in spatial resolution. Techniques like SIMS, RBS rely on the interaction of an ion beam with the sample and are typically used for elemental mapping. In dynamic SIMS the lateral resolution and the detection limit (i.e. the lowest concentration detectable) is a function of the ion beam size. However, while the lateral resolution increases as the beam size decreases, the detection limit decreases with beam size. In most cases with acceptable detection limit ($\sim 1 \times 10^{16}$ atoms/cm^3) the lateral resolution of SIMS is a few $100's$ nm^2 [14]. Two- or three-dimensional information is possible using SIMS [14] but not with required nanometer resolution. RBS can not only provide elemental profiling but can also provide useful insight into (1) the crystal structure via RBS channeling experiments [15], (2) kinetics and thermodynamics of growth via real time RBS measurements [16]. However RBS can only provide one-dimensional information and the minimum feature size it can probe is of the order of a $\sim 50\,\mu m^2$ using commercially available lenses to focus the ion beam. XPS and XRD, as the names suggest, are based on the interaction of X-Rays with the sample. XPS is a surface sensitive technique and gives access to the elemental composition (in parts per thousand), chemical and electronic state of the elements present in the sample. XRD provides information about the crystal structure of the sample. However, both techniques do not provide any spatial information. Currently, Transmission Electron Microscope (TEM) and Scanning Transmission Electron Microscope (STEM) are mostly used for characterizing devices/materials at the atomic scale. Nonetheless, these techniques are inherently two-dimensional and image columns of atoms instead of single atoms. The only techniques available currently for three-dimensional metrology at the nanometer scale are the TEM-based methods like tomography; however, they provide limited chemical information and are insensitive to concentrations below a few atomic

percent. In other words, to meet the metrology challenges presented by today's nanoelectronic devices new techniques are needed.

On the other hand APT is a powerful metrology tool that is inherently three-dimensional and can provide atom distribution in the sample with elemental identification and near atomic resolution (0.5 Å - 3 Å). In fact, analysis of semiconductor materials and devices with sub-nanometer resolution using APT has been demonstrated in the scientific literature [17]. K. Inoue et al. used APT to study dopant distribution in n- and p- type MOSFET from the 65 nm node [18, 19]. APT analysis on Ge and Si nanowires (radius $\sim$ 20 nm) revealed non-uniform dopant distribution in these nanowires [20]. The reason behind these interesting characteristics of APT is the basic working principle of the technique. Instead of relying on the interaction between either the ion (like in SIMS, RBS, ERD) or the electron beam (like in TEM, AES) with the sample, which will fundamentally limit its spatial resolution and sensitivity, it relies on the process of field evaporation. Field evaporation involves the transition of a surface atom from its atomic state to its ionic state and its subsequent removal under the influence of an electric field [21]. The electric field required to evaporate an atom is of the order of a few volts/nm. Such high fields can normally not be obtained in a planar configuration but are obtained in APT by applying a few kilo-volts of positive electric potential to a needle-shaped specimen (with an apex radius of a few tens of nanometers) (**Fig. 1.2(A)**). Once the atom is ionized, it is projected on to a position sensitive detector (PSD) due to the potential gradient between the tip and the PSD (**Fig. 1.2(B)**). The ionized atom follows a diverging trajectory from the tip to the PSD (**Fig. 1.2(A)**) [22] hence, if the ion is collected at a distance of a few centimeter's from the tip, a magnification of $\sim 10^6$ is obtained. Furthermore, APT analysis are done at 10's of Kelvin, thereby suppressing the lateral motion of the atom. This minimizes the variability on the emission point thereby providing a more univocal relation between the point of detection and atom position at the tip apex. This unique relation is the essence of the atomic resolution of the APT.

The probability of field evaporation is very sensitive to the electric field on the surface and the temperature of the surface atoms [23]. Therefore, it is possible to timely control the evaporation of an atom by pulsing the electric field or the temperature. The timed evaporation allows elemental identification of the evaporating ion by employing 'Time Of Flight' (TOF) spectrometry. Pulsing of the electric field is achieved by superimposing a standing DC voltage and a pulsed voltage, such that the atoms acquire

the energy required for field evaporation only during the pulse [23]. The temperature pulsing is obtained by illuminating the sample by a femtosecond pulsed laser instead of a voltage pulse [24, 25]. Furthermore, in APT only the surface atoms field evaporate as only they experience high enough fields required for evaporation. Hence, the sequence of field evaporation and the impact location on the PSD allows to obtain three-dimensional distribution of the evaporated ions by using reconstruction algorithms [26].

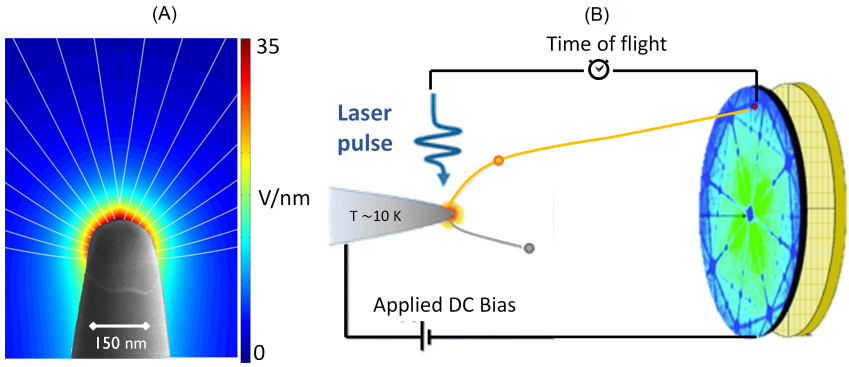

Figure 1.2 – (A) Field enhancement at the tip apex and diverging trajectories (white lines) of evaporated ions in APT. (B) Schematic representation of APT

Therefore, in theory, APT gives us the capability to map elemental composition in three dimensions with atomic resolution for nanoelectronic devices. APT on metallic samples has shown some exceptional results like the identification of ultra-small scale clusters (few 10's of atoms) along crystal defects [27]. However, the use of APT for characterizing semiconducting materials and devices still faces hurdles like reduced spatial resolution and high tip failure etc. The cause of these problems are linked to the specific properties of semiconductors/insulators and are discussed in detail below:

- The main cause of the *reduced spatial resolution* is the inability to use voltage pulsed APT due to the high electrical resistance of these materials. The high electrical resistance leads to distortion of the electric pulse propagating through the material in time and space and therefore adversely affects the TOF measurement leading to a low mass resolution. A solution to this problem is the introduction of

Laser Assisted Atom Probe Tomography (L-APT) where by a laser pulse instead of a voltage pulse is used to stimulate the ion emission by generating a thermal pulse. However, at the same time the increased temperature also creates a transverse kinetic energy, which reduces the accuracy to determine the original position of the atoms and results in a lower achievable spatial resolution. Another factor effecting the spatial resolution is the asymmetrical apex shapes usually observed while analyzing these materials using L-APT [28, 29, 30]. The causes for the asymmetry in the apex shape are (1) the non-uniform temperature distribution at the apex due to non-uniform laser absorption and (2) the difference in the field required to evaporate the various elements/layers present simultaneously at the apex when analyzing heterogeneous structures like FinFET or when analyzing an interface in a multi-layer structure. In both cases, the tip apex reshapes to accommodate the impact of the non-uniform temperature distribution or the differences in required field on the evaporation probability over the tip apex. These local distortions inherently decrease the spatial resolution of the reconstructed data [31, 22] since they are not accounted for in the currently available reconstruction algorithms. To improve the limited spatial resolution due to the non-hemispherical apex shape, it is imperative to gain a deeper understanding of the effect of (1) laser absorption on the tip apex and (2) differences in threshold fields required for evaporation. The main impact of the reduced spatial resolution ($\sim$0.2 - 0.3 nm lateral resolution and $\sim$0.05 - 0.1 nm depth resolution) is the limited ability for structural analysis in small volumes ($\sim$ 10-100 of nm^3) as all crystallographic information is lost. Furthermore, due to the 50 % detection efficiency of the PSD [32], the reduced statistics in these small volumes also limits compositional analysis. To overcome these limitations various statistical analysis tools have been developed [33, 34, 35, 36]. However, better methods are still required especially to extract ultra-fine-scaled clusters (few 10's of atoms).

- The causes of the *high failure rate* of these materials/structures is still a subject of debate in the scientific community. One of the causes for tip failure could be the mechanical stress created due the electric field [37]. The high failure rate observed when analyzing multi-layer stacks could potentially be due to this mechanical stress. Indeed if the adhesion between the different layers is not strong

enough to withstand the mechanical stress, the whole tip above the interface could be ripped-off during analysis. Another cause of tip failure could be the inefficient heating of the tip apex due to the poor laser absorption by high bandgap materials like SiO_2, Si_3N_4, HfO_2 etc. commonly found in current state of the art semiconducting devices. Due to the poor absorption of the commonly used wavelength (∼515 nm, ∼343 nm) by these materials, the electric field needs to be increased to enable field evaporation. Furthermore, the threshold field for evaporation these materials is generally higher compared to other constituent materials like Si, SiGe, III-V compound semiconductors etc. The higher field leads to higher mechanical stress and hence tip failure. To improve the success rate of analysis of these tips an improved understanding of (1) the laser absorption by high band gap materials and (2) the thermal response (i.e. heating and cooling) of the specimen under laser illumination is required.

In this thesis, we will try to improve on some of the above listed shortcomings. We mainly focused on two aspects:

- Improving our understanding of the interaction between the sample and the pulsed laser.
- Statistical analysis of the acquired data. More specifically on cluster analysis of ultra-fine scaled clusters.

The thesis is structured as follows. In Chapter 2, I will first discuss the theoretical aspects of field evaporation and subsequently experimentally verify them for semiconductors. Chapter 3 is related to the interaction of the laser with the nanoscaled tip. More specifically, I will first present a new method to derive the temperature reached at the apex during L-APT analysis of semiconductors (Section 3.1). I will then use the method to study (1) the thermal response of the tip under laser illumination, (2) effect of laser absorption on the apex shape of the tip (Section 3.2) and (3) propose a new absorption mechanism for tips prepared with high band gap materials (Section 3.3). In chapter 4, I will apply L-APT to understand the role of Sn cluster and/or defect formation in relaxation of a strained $Ge_{(1-x)}Sn_{(x)}$ layer. To this end, I will first verify the presence (or absence) of potential artefacts and discuss the optimum parameters for analyzing $Ge_{(1-x)}Sn_{(x)}$ layers (Section 4.1). I will also present a new cluster analysis algorithm to detect ultra-fine-scaled clusters (Section 4.2).

In the final chapter 5, I will give a general conclusion and an outlook of the work. A brief summary on sample preparation and running a L-APT measurement is presented in Appendix A. Furthermore, a summary of the most commonly used reconstruction algorithm is discussed in Appendix B.

Chapter 2

Fundamentals of Atom Probe Tomography

The current chapter aims to introduce the physics of field evaporation. We will first (section 2.1) discuss the models that describe the process of field evaporation. These models aim at predicting the rate of field evaporation and the electric field necessary to evaporate the atom of a specific material. In section 2.2, we will discuss the theory of post-ionization. This theory predicts the formation of higher ionized states of the evaporated atoms as a function of the applied electric field on the surface. The resulting curves from the theory of post-ionization provide an invaluable tool to experimentally quantify the electric field distribution on the surface. In the last section (2.3), we will experimentally verify the theory of field evaporation for semiconductors.

2.1 Theory of field evaporation

Field evaporation is described as a physical phenomenon by which an atom transitions from its neutral state to its ionic state and is subsequently removed under the influence an applied electric field. The underlying mechanism behind field evaporation can be visualized using one-dimensional potential energy diagrams (**Fig. 2.1**). In the absence of an electric field, the surface atoms are bound in a potential well (i.e. neutral state) which can approximated using a Lennard-Jones

potential. Furthermore, when no field is applied, the various ionic levels are metastable, i.e. have a higher potential energy, with respect to the neutral state (**Fig. 2.1(a)**). Upon the application of an electric field, the ionic states become increasingly stable as the atom moves away from the surface of the specimen (**Fig. 2.1(b)**). Thus, in the presence of an electric field, a potential barrier (Q_b) is created between the neutral and the ionic state (**Fig. 2.1(b,c,d)**). The height and the width of the potential barrier can be reduced by increasing the electric field. Therefore, at a high enough field, the desorption of the ion over the reduced potential barrier is possible by electronic transition and thermal activation.

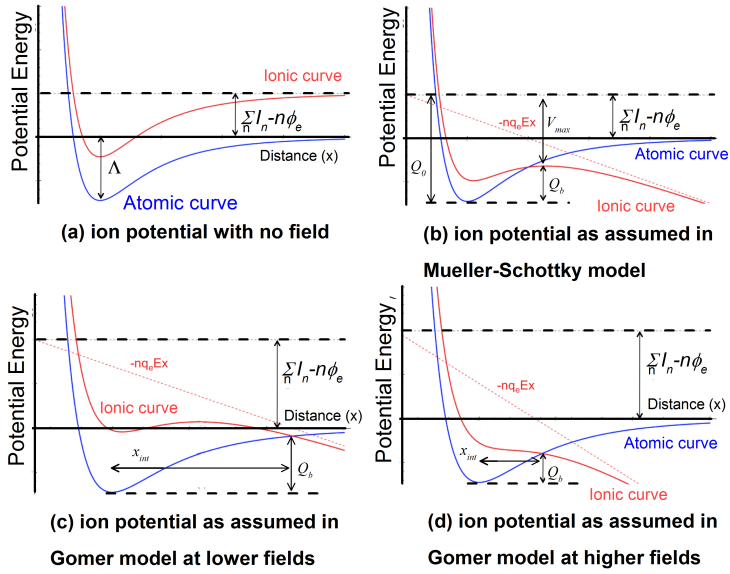

Figure 2.1 – One-dimensional potential energy diagrams. Q_b is the potential barrier height, an atom has to overcome to field evaporate. Reproduced from ref [38]

The probability of field evaporation is typically modeled by a Maxwell-Boltzmann distribution of the velocity of the atoms at the surface and can be mathematically described by an Arrhenius equation [21], i.e.

$$P_{evap} = \nu_{atom} exp\left(\frac{-Q_b}{K_B T}\right) \tag{2.1}$$

where P_{evap} is the probability of evaporation in s^{-1}, ν_{atom} is the vibration frequency of the surface atom in s^{-1}, K_B is the Boltzmann constant and T

is the temperature of the sample. **Eq. 2.1** is also known as the rate law for field evaporation. To evaluate equation 2.1, it is imperative to model the barrier height and its dependence on the applied field. This can be done as follows:

In the absence of an applied field, one can express the energy (Q_0) required to evaporate an n-fold ion as:

$$Q_0 = \Lambda + \sum_n I_n - n\phi_e \tag{2.2}$$

where Λ is the heat of sublimation of a neutral atom, I_n is n^{th} ionization energy of the atom, ϕ_e is the work function of the emitting surface. Two basic theories exist to evaluate the variation of the barrier height with the applied field, namely, (1) Mueller-Schottky model (or image hump, or image force model) [39] and (2) Gomer charge exchange model (or intersection, or Gomer model) [40]. Both models are based on atomic and ionic forces, polarization effects and image potentials and are one-dimensional in nature.

2.1.1 Mueller-Schottky model

This model was presented by Mueller et al. [39]. In this model, field evaporation is described as a thermally activated process where an integrally charged ion overcomes energy hump Q_b (**Fig. 2.1(b)**). The model is based on classical electrostatics and the reduction of the potential barrier is modeled based on the Schottky effect [41]. Furthermore, the model explicitly implies that full ionization of the atom has to occur before it crosses the energy barrier. From **Fig. 2.1(b)** it is clear that the height of Q_b is given by:

$$Q_b = Q_0 - V_{max} \tag{2.3}$$

where V_{max} is the maximum potential energy of an ion in the presence of an electric field. To calculate V_{max} we first need an expression for the ionic potential energy term ($V_n(x)$) of an n-fold ion. Mueller proposed that this is given by the sum of a simple image potential term and the potential generated by the applied field (**Eq. 2.4**), assuming that the contribution form the ion-core repulsion is negligible [39].

$$V_n(x) = \underbrace{\frac{-n^2 q_e^2}{16\pi\varepsilon_0 x}}_{image\,potential} - \underbrace{nq_e F_x}_{field\,term} \tag{2.4}$$

where q_e is the electron charge, ε_o is the permittivity of free space and F is the electric field strength. The position of where $V_n(x)$ is maximum (x_{max}) is given when:

$$\frac{d(V_n(x))}{dx} = 0 \implies x_{max} = \frac{1}{2}\sqrt{\frac{nq_e}{4\pi\varepsilon_0 F}} \tag{2.5}$$

the potential energy (V_{max}) at this position is then given by:

$$V_{max} = -\frac{1}{2}\sqrt{\frac{n^3 q_e^3 F}{4\pi\varepsilon_0}} \tag{2.6}$$

In the Mueller-Schottky model, this maximum is assumed to always lie on the right of the crossing point between the atomic and ionic energy curve. Using equation 2.2, 2.3 and 2.6, the potential barrier for field evaporation is given by:

$$Q_b = \underbrace{\Lambda + \sum_n I_n - n\phi_e}_{Q_0} - \underbrace{\frac{1}{2}\sqrt{\frac{n^3 q_e^3 F}{4\pi\varepsilon_0}}}_{V_{max}} \tag{2.7}$$

Equation 2.7 can be used to calculate the field required to evaporate at 0 K for a particular material by setting Q_b to zero. The calculated field values are in good agreement for a number of metals like Ni, Pt, Cu etc. [21]. However careful theoretical and experimental verification have shown this model to be inconsistent:

- The distance of the Schottky hump (x_{max}) predicted via the model is too small to ignore the contribution from the ion-core repulsive forces. Hence, this model is not self-consistent. Furthermore, on including the repulsive contribution, the calculated ionic potentials at the high electric fields required for evaporation do not show the hump [42].

- The calculated activation energy required for field evaporation after accounting for the repulsive terms is overestimated by 3 % to 20 % as compared to experimentally determined ones [43].

- The model is not able to correctly predict the experimentally determined dependence of the evaporation rate as a function of applied field for materials like Mo, Ru, W, Ir etc. [44].

- In cases when the hump lies to the left of the crossing point between the atomic and ionic potential curves (**Fig. 2.1(c)**), Q_b calculated using this model would be overestimated.

Forbes et al. [45] argued that the reason for good agreement between experimental and predicted barrier height for certain materials could be due the fact that, in certain cases, Mueller's formula corresponds closely to the energetics of the more accurate charge exchange mechanism (discussed below) than to the image hump mechanism.

2.1.2 Charge Exchange model

The Gomer charge exchange model overcomes the limitations of the Mueller- Schottky model. While the Mueller-Schottky model stipulated that complete ionization has to occur before the atom crosses the potential barrier, Gomer et al. [40] postulated a physically different mechanism for field evaporation. They explained field evaporation using charge-exchange type model, i.e. ionization and escape occur together, at or near the potential energy barrier. Theoretical and experimental verification of the model has shown it to be a more correct description of field evaporation. For example:

- Physically the process of charge exchange is argued to be more realistic than the one proposed in the image hump [46].
- The activation energies and the distance of the potential barrier predicted using this model is in good agreement with experiments [46, 47].
- The relationships predicted between (1) barrier height and field $\left(\sqrt{Q_b} \sim \frac{1}{F}\right)$ and (2) barrier height and the distance (x_{int}) from the surface to the energy barrier $\left(\sqrt{Q_b} \sim x_{int}\right)$($x_{int}$ represented in **Fig. 2.1(c,d)**) are compatible with experiments [48, 46]
- The predicted dependence of the evaporation rate on applied field is compatible with experiments [44].

The height of the potential barrier as modeled using the Gomer charge exchange model is given by:

$$Q_b^{'} = \Lambda + \sum_n I_n - n\phi_e - \frac{n^2 q_e^2}{16\pi\varepsilon_0 x_{int}} - neFx_{int} - \frac{B_a}{2} - \triangle E_a + \mu_a F + \frac{\frac{1}{2}\left(\alpha_a - \alpha_i\right)F^2}{4\pi\varepsilon_0} \tag{2.8}$$

where x_{int} is the distance between the metal surface and the point where the potential curves intersect, B_a and $\triangle E_a$ are the broadening and shift of the energy level of the adsorbate species due to the interaction with the substrate, μ_a is the zero-field dipole of the adsorbate species and α_a and α_i are the adsorbate polarizabilities in the neutrally bound and ionic states. Although this model is more accurate compared to the Mueller-Schottky model, several parameters used to calculate the barrier height are difficult to obtain experimentally thereby, making it difficult to use this model. However, some general conclusions can be made about the potential barrier required for field evaporation. It is clear from equation 2.8 that the sublimation energy, which is a material property, impacts the barrier height. Hence materials with higher sublimation energies (e.g. refractory materials) will have larger barrier height and hence will require a higher field to evaporate. Furthermore, the work function also important. Since the work function of a material is crystallographic orientation dependent (higher for low index planes and vice-versa for high index planes), the field required for evaporation will vary depending on the crystallographic orientation. Work functions typically vary by 1-2 eV, leading to a predicted regional variation in field of ~10-20 % [49]. During this project the presence of these high fields at low index crystallographic orientations were regularly observed in experimental data (**Fig.** 3.16, 3.20, 4.5).

The success of the charge exchange model has triggered debate about the nature of the exchange mechanism. Essentially two mechanisms have been proposed: (1) charge hopping and (2) charge draining [50, 51]. The former describes the process as a sharp transition from the atomic to the ionic state. The latter describes it as a quantum mechanical process in which the charge is gradually drained from the evaporating atom to the surface of the specimen. This mechanism is believed to be the most accurate description of field evaporation [46]. Based on the charge draining mechanism, Kreuzer and Nath [52] derived a generalized scaling law for the barrier height using density functional theory:

$$\frac{Q_b}{Q_0} = \sqrt{1 - \frac{F}{F_0}} + \frac{1}{2} \times \frac{F}{F_0} ln \left(\frac{1 - \sqrt{1 - \frac{F}{F_0}}}{1 + \sqrt{1 - \frac{F}{F_0}}} \right) \tag{2.9}$$

where Q_0 is the barrier height at zero field, F is the applied field and F_0 is the field required to evaporate at 0 K. This scaling law has been found to be in good agreement with a number of metals [53]. Experimental verification of this scaling law for Si is discussed in section 2.3.1. We used

this law extensively during this doctoral project to obtain the variation of barrier height as a function of applied field.

2.2 Postionization

As it is quite evident from the discussion above, determining the field values at the apex is essential for calculating the height of the potential barrier at the time of field evaporation. However, calculating the field values from the applied voltage is not trivial as the field is a complex interplay between the applied voltage, tip geometry, material conductivity and surface properties. One way of quantifying the field at the apex is via the theory of postionization. Haydock and Kingham [55] showed that the experimentally observed multiple charge states of the field evaporated ions are linked to the strength of the field at the apex (**Fig. 2.2**). They postulated that an ion may ionize to higher charge states while it passes through the high field region adjacent to the apex of the specimen post field evaporation. They modeled the probability of postionization based on the probability of tunneling of the electrons of the evaporated ion back into the specimen [54]. The tunneling probability was calculated by first approximating the potential distribution for a given field near the apex. Subsequently, the tunneling probability was derived as a function of the distance of the ion from the surface by using the Schrödinger Equation of the model system. Finally, by integrating the tunneling probability over the surface ion path, the postionization probability for a given field was calculated. This process is repeated for different electric fields at the apex and the corresponding charge states ratios (CSR) are calculated. CSR for an element A is defined as $A^{i+}/(\sum_i A^{i+})$, where A^{i+} (i=1, 2...) is the measured number of counts of A^{i+} ions. The thus calculated curves between the field and the charge state ratios are known as Kingham curves (**Fig. 2.2**). Comparisons

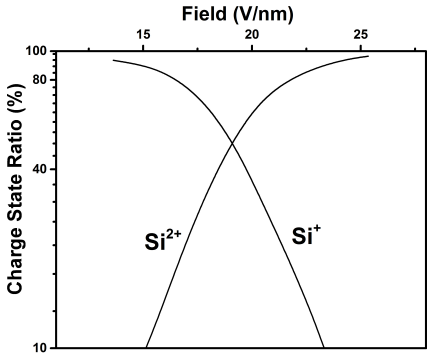

Figure 2.2 – Kingham curve for Si. The charge state ratio is defined as $(Si^{n+}/(Si^{1+} + Si^{2+})) \times 100$,where n=1,2. reproduced from [54]

of theory and experiment, of the dependence of observed charge state ratios on the field at the apex show good qualitative agreement for many metals [54, 56]. However, Lam et al. [57] argued that the expression derived by Kingham et al. for the potential distribution and the tunneling probability as a function of distance from the apex surface had certain deficiencies. For example, the tunneling potential determined by Kingham et al. was not an equipotential over the surface which, according to Lam et al., should effect the tunneling probability and hence the probability of postionization. These deficiencies may explain the poor quantitative agreement between the theoretically calculated and the experimentally determined curves [56]. In section 2.3.2 we will compare the theoretical and experimental Kingham curves for Si.

One of the most interesting features of post-ionization is that it is independent of the temperature, making it an extremely useful tool to determine the electric field at the apex in L-APT analysis. In this thesis, we will use the experimentally determined Kingham curves extensively to determine the global and the local electric field distributions over the apex surface.

2.3 Experimental verification of the theory of field evaporation for semiconductors

The theory of field evaporation discussed above was originally only developed for metals. In this section, we will verify it experimentally for semiconductors using Si. We will first look at the dependence of evaporation probability, i.e. flux, as a function of applied voltage (barrier height) and laser power (temperature). Subsequently, we will describe a procedure to calculate the Kingham curves experimentally and compare them to the theoretical curves. In the end we will discuss the validity of **Equation 2.9** for calculating the barrier height in semiconductors.

2.3.1 Evaporation probability versus the applied field and temperature

According to **Equation 2.1,** the evaporation portability increases exponentially with any decrease in barrier height or increase in temperature. The evaporation probability, barrier height and temperature are proportional to the experimentally observed flux (atoms/pulse),

$\frac{1}{applied\,voltage}$ and laser power respectively. Hence, the rate law can be verified experimentally by observing the dependence of the flux with respect to (a) applied electric field (@ constant laser power) and (b) temperature (@ constant applied voltage). Taking the natural log of equation 2.1 and replacing P_{evap}, Q_b and T with their experimental counterparts we get:

$$ln(\phi) = -\frac{Q(V)}{K_B T(LP)} + ln(A) \tag{2.10}$$

where ϕ is the flux in atoms/pulse, Q(V) is the barrier height as a function of the applied voltage V, T(LP) is the temperature at the apex as a function of laser power (LP) and A is the pre-exponential constant.

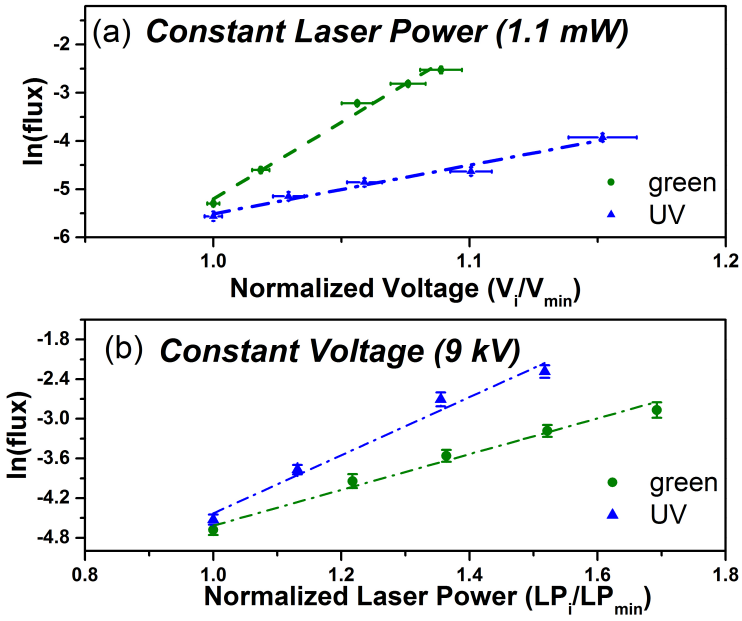

Figure 2.3 – Experimental verification of the rate law. (a) Evaporation flux as a function of applied voltage at constant laser power (green (λ = 515 nm) and UV (λ = 343 nm)) (b) Evaporation flux as a function of laser power (green and UV) at constant voltage.

Assuming that in Si illuminated by green or UV laser temperature varies linearly with laser power, the behavior predicted **Eq. 2.10** was experimentally verified by running an L-APT analysis at constant voltage

and measuring the impact of a changing laser power on the observed flux (**Fig. 2.3(a)**). Alternatively, the impact of the field was experimentally verified by running an L-APT analysis at constant laser power and changing the applied voltage (**Fig. 2.3(b)**). Please note, the interval of the applied DC bias shown in **Fig. 2.3(b)** was such that the barrier height can be approximated to vary linearly with voltage. As theoretically predicted, we observed a linear behavior between the $\ln(\phi)$ and (a) voltage (@ constant LP), (b) LP (@ constant voltage) (**Fig. 2.3**). Interestingly, if we can calculate the barrier height from the applied voltage, the temperature at the apex can be calculated from the slope of the curve in **Fig. 2.3(a)**. This forms the basis of the new temperature determination method we developed and is discussed comprehensively in chapter 3**.**

2.3.2 Kingham curves for postionization

In this section, we will first discuss the procedure to experimentally obtain the Kingham curves for postionization and then compare them to the theoretical curves.

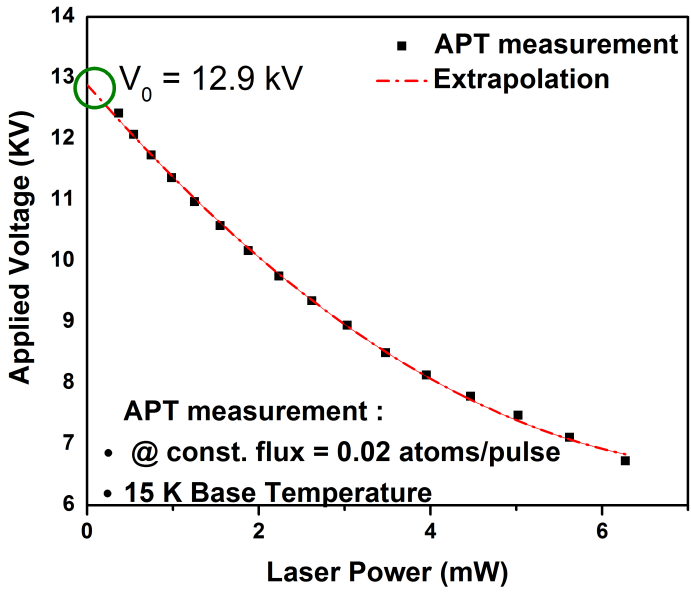

Figure 2.4 – Laser power versus Voltage curve to calculate V_0. APT measurements done on Si samples illuminated by a green laser ($\lambda = 515$ nm) at constant flux (0.02 atoms/pulse) and a base temperature of 15 K.

For the experimental verification of the curves, a two-step approach was used. As the first step, we calculated the voltage V_0 required to field evaporate the Si specimen at 0 K. In the second step, we will calculate the field values at each measurement point using the previously determined V_0 value.

Step 1: To calculate the V_0 value APT measurements were done on Si samples illuminated by the green laser (λ = 515 nm) at constant flux (0.02 atoms/pulse) and a base temperature of 15 K [58]. The laser power was then changed and the corresponding change in applied voltage required to maintain the constant flux was noted. The resulting curve was then extrapolated to calculate the ordinate at zero laser power. This ordinate value represents the V_0 value of that specific tip (**Fig. 2.4**).

Step 2. The field values at every measurement point in **Fig. 2.4** were calculated as follows. As discussed in Appendix A.1, the field (F) at the apex is proportional to the applied voltage (V). Hence, at constant radius

$$\frac{F_i}{F_0} = \frac{V_i}{V_0} \tag{2.11}$$

where F_i is field at the i^{th} data point, V_i is voltage at the i^{th} data point and F_0 is the field required for evaporation at 0 K temperature. $\frac{F_i}{F_0}$ is known as the field fraction and is the measure of the fraction of energy provided by the field for evaporation. Similarly, $\frac{V_i}{V_0}$ is known as the voltage fraction. Using **Equation 2.11** we can now plot field fraction versus the observed CSR at each data point (**Fig. 2.5(A)**). In this thesis we will refer to these curves as calibration curves.

In order to compare the experimental calibration curve to theoretically predicted Kingham curves, we need to assume a value of F_0. In scientific literature F_0 values for Si range from 27 V/nm to 33 V/nm have been reported [21, 59, 60]. In this thesis we calibrated the F_0 value (= 27.5 V/nm) such that experimental field value at CSR = 50% matches with the theoretically predicted value (**Fig. 2.5(B)**). As can be seen in **Fig. 2.5(B)** the experimental results were repeatable for different specimen shape, flux used to calculate V_0 etc., i.e. the observed CSR as a function of field is only material dependent. Although the experimental Kingham curves have a similar shape as the theoretically predicted ones, their dependency on field is less pronounced. The potential sources of error on the experimental curve are V_0 and the *excess* increase in the voltage required at each point due the increase in the radius of the tip apex. Regarding the error due to V_0, it is calculated using the assumption that at zero laser power, the temperature of the tip

is 0 K. However, at zero laser power the temperature at the apex is equal to the base temperature set during the measurement, i.e. 15 K hence, underestimating V_0. This underestimation would result in a less pronounced dependence of CSR on field. However, to obtain the same dependence as predicted by theory implies that V_0 is underestimated by ~4 times. Such a large underestimation of V_0 is not expected considering the V_0 value of calculated using a base temperature of 15 K is higher by only 1.06 times as compared to the value calculated at 80 K. The second source of error, i.e. the excess voltage required due to the increase in radius also leads to a broadening of the experimental curve. The impact of this was minimized by reducing the number of collected atoms per data point (~10 000 atoms/data point) such that only a few mono-layers are evaporated during the whole measurement. Indeed, the repeatability of the experimental curves for tips with different shank angles proves that the increasing radius has negligible impact (**Fig. 2.5**).

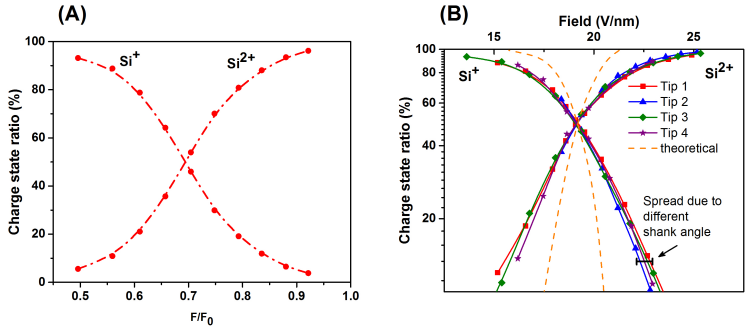

Figure 2.5 – (A) Experimentally determined dependence of CSR on the field fraction for Si samples illuminated by a green laser (λ = 515 nm). In this thesis we will refer to this curve as the calibration curve. (B) Experimental Kingham curves derived from the calibration curve by using an F_0 = 27.5 V/nm. The experimental curve is compared to the theoretical Kingham curve for Si [54]. To check the independence of the experimental Kingham curves to experimental parameters like tip shape, flux etc., the curves were calculated on multiple tips, i.e. each tip had a different shape and the flux used to calculate V_0 of the different specimens ranged between 0.01 - 0.04 atoms/pulse.

Hence the disagreement between theory and experimental data is potentially a result of the deficiencies in the theoretical treatment of postionization as discussed section 2.2. In this thesis, all mentioned field fraction values were calculated using experimental calibration curves, unless stated otherwise.

2.3.3 Barrier Height as a function of applied field: Mueller-Schottky model versus Gomer's model

The models for field evaporation discussed in Section 2.1 were developed for metals. Hence, it is necessary to test the accuracy of these models for semiconductors before we can use them. Mazumder et al. [58] reported that the Mueller-Schottky model accurately predicts the change in barrier height as a function of field in Si. However, as discussed by Forbes et al. [45], the accurate predictions of the Mueller-Schottky model could be due to the fact that in certain field ranges the model corresponds more closely to the energetic of the charge exchange mechanism and thereby accurately predicts Q(F). In this section we will experimentally test the validity of the two models for a broad range of applied fields.

One method to experimentally gauge the applicability of each model is by observing the behavior of the locus of constant flux in the (F,LP) plane. Rewriting **Equation 2.10**

$$Q_b = ln\left(\frac{A}{\phi}\right) K_B \times T \tag{2.12}$$

Equation 2.12 states that the shape of the locus of constant flux in the (Q_b, T) plane is a straight line. Assuming linear absorption of green laser by Si, the locus of constant flux in the (Q_b, LP) plane is also a straight line. Hence **Equation 2.12** becomes**,**

$$Q_b = B \times LP \tag{2.13}$$

where B is a function of ϕ, absorption coefficient of Si, the pre-exponential constant A and K_B. Since the theoretical models predict the dependence of Q_b as a function of applied field (F), the theoretical model can be validated by comparing the experimental and theoretical shapes of the locus of constant flux in the (F,LP) space (**Fig. 2.6**). As can be seen in **Fig. 2.6**, for Si the scaling law presented by Kreuzer and Nath (**Eq. 2.9**) can predict the change in the barrier height as a function of applied field. While the Mueller-Schottky model (**Eq. 2.7**) can predict this dependence only for a small range of field values (16 V/nm - 20 V/nm). As expected from the discussion in section 2.1, Gomer's charge exchange model is a more reliable way to estimate the barrier height in semiconductors.

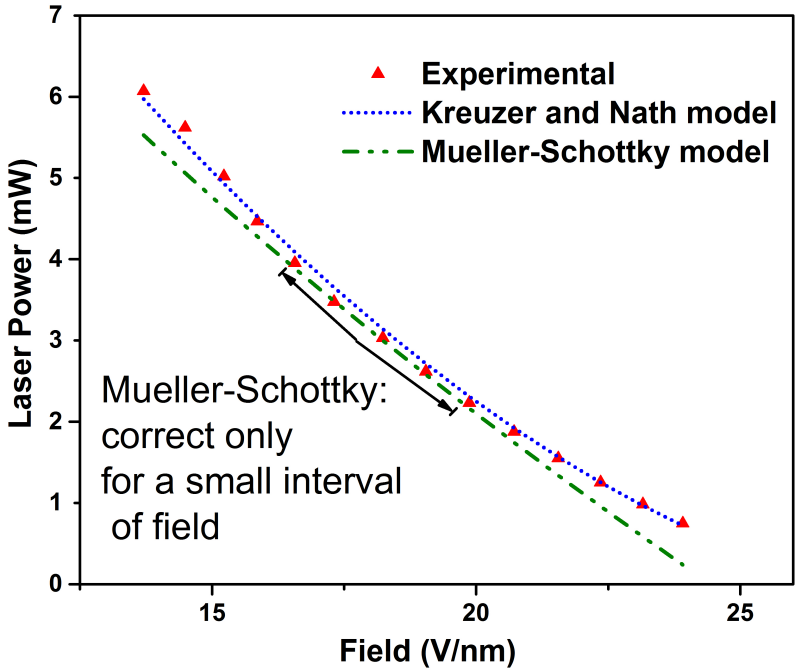

Figure 2.6 – Experimental verification of the models predicting the dependence of barrier height (Q_b) on applied field. L-APT analysis was done on a Si tip using green laser. The Kreuzer and Nath's scaling law based on Gomer's charge exchange model can predict this dependence over a wide range of applied field values. While, the Mueller-Schottky model correctly predicts this dependence over a very short range on applied field values.

2.4 Conclusions

In this chapter, we described the theoretical framework that describes the process of field evaporation. We discussed the dependence of the evaporation probability/flux of a given element on the field and temperature at the surface of the specimen. Furthermore, we presented the available models that describe the dependence of (1) the observed charge state ratios and (2) the potential barrier height for field evaporation as a function of the applied field. In general the theoretical models discussed here and those present in scientific literature were developed for metals. We tested the models experimentally for semiconductors (using Si as an example) and observed that:

- The rate law (**Eq. 2.1**), which states that the evaporation probability increases exponentially with any increase in field or temperature, is also valid for semiconductors. However, at the start of this thesis project, it could only be used for qualitative assessment since, the relations between the input parameters (Q_b, T and A) and experimental parameters (voltage and laser power) were not well defined. With the progression of the thesis project, a better understanding of these relations (especially in regards to semiconductors) was realized and the law was used extensively. In chapter 3, we will describe an experimental procedure to derive the temperature at the apex of the specimen using this law.

- The Kingham curves for postionization describe the observed CSR as a function of applied field. On comparing the theoretically predicted and experimental curves, we observed that the theoretical curves describe the dependence qualitatively. However, the theoretical curves overestimate the sensitivity of postionization to the electric field for a number of semiconductors (Si, Ge, GaN). This discrepancy can be explained on the basis of the use of an inaccurate potential distribution over the surface to calculate the tunneling probabilities. In this thesis, we used the experimental Kingham curves to calculate the field distributions over the apex at the time of field evaporation.

- There are mainly two models, the Mueller-Schottky model and the Gomer's charge exchange model, available in scientific literature to describe the dependence of Q_b as a function of applied field. While the input parameters for the Mueller-Schottky model are easily accessible, it can correctly predict the dependence for a very limited number of metals. On the other hand the Gomer's model is more accurate but the input parameters required are not known for most materials. Kreuzer and Nath presented a scaling law for the dependence based on the Gomer's model. We experimentally tested the two models for Si and observed that the scaling law can predict the change in the barrier height as a function applied field. We will use this scaling law in chapter 3 to derive the temperature reached by the specimen under laser pulsing.

Chapter 3

Laser-tip interaction

In this chapter, we will present the current understanding of the interaction between a pulsed laser and a semiconducting nanometric tip and our contribution to this understanding. To this end, we will first describe the current state of the art. Our contribution to the subject is briefly discussed in Section 3.1, 3.2 and 3.3. The results of the work done on laser-tip interaction are discussed in more detail in the articles (Article I, II and III) attached at the end of the chapter.

The introduction of laser pulsing to APT helped broaden the scope of its application to lowly conductive materials [61]. However, the actual mechanism by which the laser helps in field evaporation is still a topic of discussion. It is well known that absorption of laser light could lead to a temperature increase. However, the laser being an electromagnetic wave also has an inherent electric field which could potentially lead to field enhancement at the tip surface [62]. Hence, in theory the laser could stimulate field evaporation both by decreasing the potential barrier height and as well as increasing the temperature at the apex.

In semiconductors, heating under laser illumination includes carrier excitation; carrier redistribution through drift/diffusion, scattering and carrier relaxation. **Fig. 3.1** outlines some of the processes (and their respective timescales) that take place in a semiconductor [63]. The typical timescale for field evaporation is of the order of a few picoseconds [64] hence, ~complete thermalization of the charge carriers is expected to occur before field evaporation.

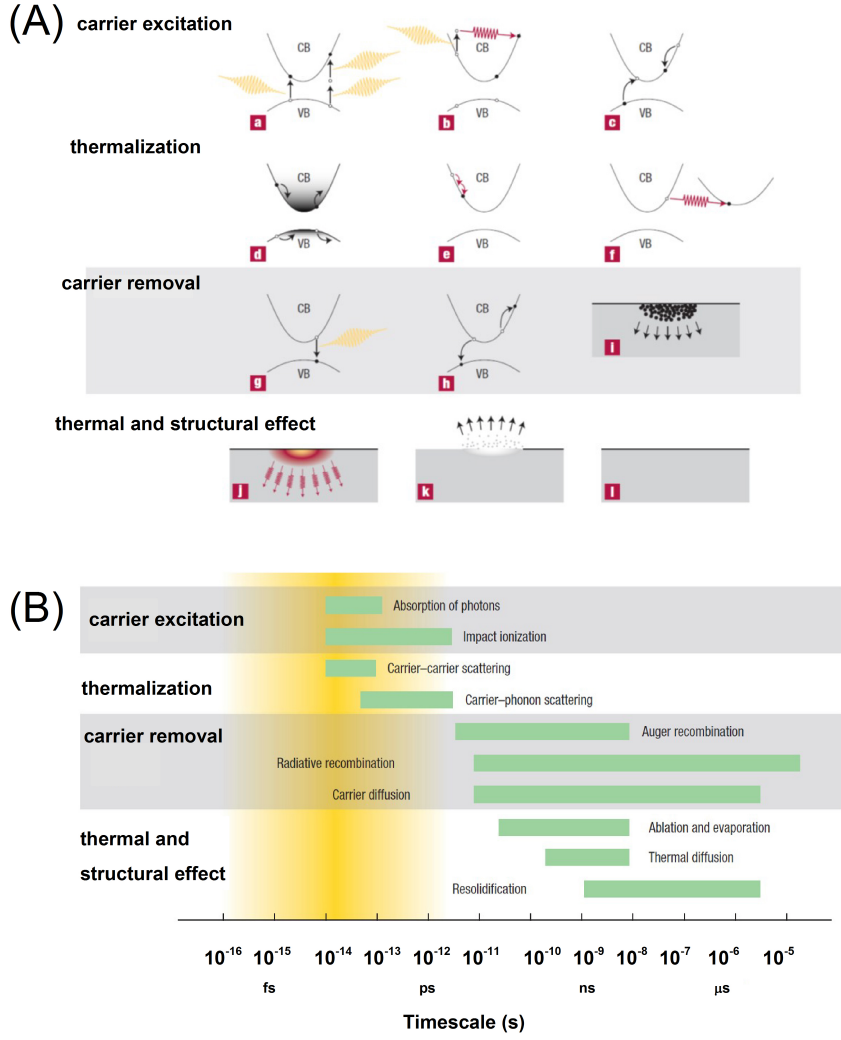

Figure 3.1 – (A) Electron and lattice excitation in a semiconductor excited with light: (a) multiphoton absorption, (b) free-carrier absorption, (c) impact ionization, (d) carrier distribution, (e) carrier-carrier scattering, (f) carrier-phonon scattering, (g) radiative recombination, (h) Auger recombination, (i) diffusion of excited carriers, (j) thermal diffusion, (k) ablation and (l) resolidification or condensation. (B) Timescales of the electron and lattice processes in laser excited solids. Reproduced from ref [63]

Regarding the field effect of the laser, even though the optical electric field is strong enough to lower the potential barrier for field evaporation, it has a very high oscillation frequency (10^{15} Hz). Such high frequencies translate into a time period of ∼1 femtosecond of the field oscillation at the surface. Considering that field evaporation occurs over a few picoseconds [64], this momentary oscillation in the potential barrier height is too short for field evaporation. Hence atoms being directly excited by the electric field of the laser can be excluded. An alternate method for atom excitation based on the optical rectification effect at metal surfaces was proposed by A. Vella et al. [65]. They proposed that since the electrons at the surface see an asymmetric potential, their oscillating motion inside the optical field is also not symmetric. Hence, the average position of the surface electrons moves slightly away from surface leading to a net electric field long enough to field evaporate an atom. To ascertain the dominant mechanism for field evaporation theoretical and experimental work was done to understand (1) the spatial distribution of absorbed light in the tip [66, 67, 68] and (2) the effect of laser properties (like power, wavelength, pulse duration) on the obtained mass resolution, surface diffusion, flux [24, 69] etc. The evidence gathered from these studies strongly support a thermally activated process under laser illumination. In detail,

- Surface migration of atoms was shown to occur at high laser powers [69]. Since surface migration is a thermally activated process, this observation supports a thermal effect of the laser.

- The observed charge state ratio during L-APT analysis is independent of the incident laser power (**Fig. 3.2**). Since the CSR ratio is only a function of field at the apex and is independent of the temperature (Chapter 2.2), this observation is strongly against a field effect of the laser.

- The mass resolving power decreased at higher laser power and/or in samples with a lower thermal diffusion coefficient of the sample [70, 69]. Considering that the tail of a mass peak predominantly effects the mass resolution in L-APT analysis, its dependence on the thermal properties of the material suggests a heating up of the specimen under laser illumination. Furthermore, the atom emission time after the interaction with the laser was observed to ∼2 μs for poor thermally conducting materials [69]. This is much longer than

the laser pulse length (∼femtoseconds). If the laser had a field effect, the emission times should be as short as the laser pulse.

- The dependence of the flux, at constant field, as a function of laser power at different base temperatures can only be explained by a thermally activated process. Indeed, as shown by F. Vurpillot et al. [24], physical parameters, such as evaporation time, obtained when explaining the above dependence for W using the field effect are erroneous. However, when explaining the dependence using the thermal effect of the laser, a good agreement with expected values is obtained for physical parameters like temperature, barrier height, vibration frequency etc.

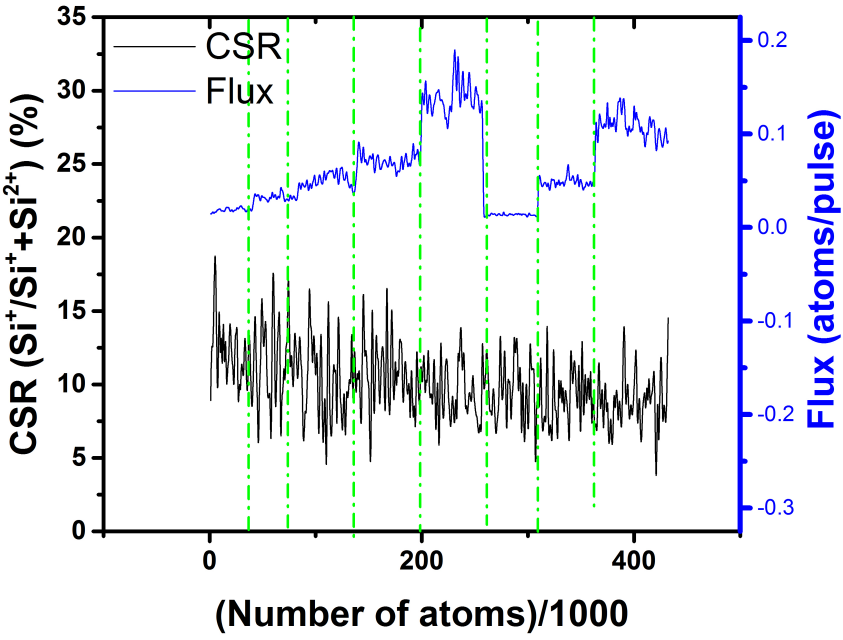

Figure 3.2 – No variation in CSR is observed when the incident laser power is changed (shown as a variation in flux on the secondary Y-axis) and the applied DC bias is maintained constant. The L-APT analysis was done on Si using a green laser.

One of the main experimental observations against a thermally activated process was the inconsistent short cooling times in materials with high thermal conductivity. For example, F. Vurpillot et al. observed a cooling time in W tips of $\sim 550 \pm 200$ ps [71] (using a pump-probe technique),

i.e. the heated area should be few 100 nm using the thermal diffusion coefficient of W. However, the small heated zone is inconsistent considering the large laser spot size (∼800 μm) and homogeneous heating of the tip (as suggested by Tsong et al. [72]). The small heated zone was later explained by Houard et al. [66]. They simulated absorption of light in a nanoscaled metallic tip using finite-difference time domain (FDTD) and demonstrated that the apex of a metallic tip behaves like a diffraction source and emits light in all direction. The interaction between incoming and diffracted light results in oscillating absorption zones on the tip surface. The period of these oscillations is equal to the wavelength of incident light (**Fig. 3.3(A)**) and the absorption density along the axis of the tip is maximum at the apex with rapid decay along the shank (**Fig. 3.3(B)**). This implies that the tip is heated in a small region close to the apex.

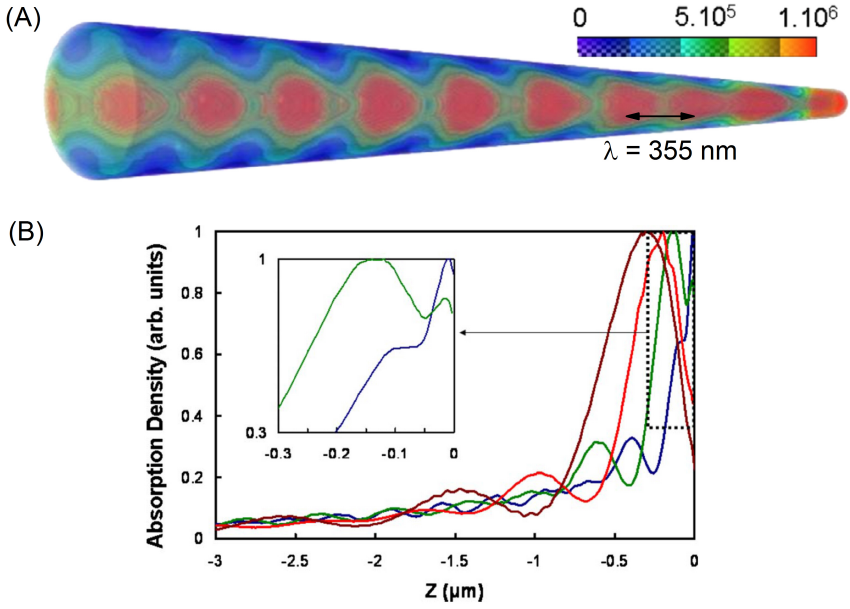

Figure 3.3 – (A) Absorption maps calculated by FDTD on Al tips (illuminated side) for incident laser of 355 nm. The color bar is in (W/m^3) and corresponds to the power absorption density for an incoming intensity of 1 W/m^2 (B) Normalized absorption density profile along tip axis for $\lambda = 360$ nm (blue), 515 nm (green), 800 nm (red) and 1200 nm (brown.) Inset: zoom of the absorption profile at the apex for $\lambda = 360$ nm (blue) and 515 nm (green). Reproduced from [66]

As outlined in chapter 1, the main issues with analyzing semiconducting/insulating materials using L-APT are the reduced spatial resolution and the high failure rate. The causes for the reduced spatial resolution are the transverse kinetic energy provided to the atom due to the temperature generation under laser illumination and the erroneous reconstruction due to the asymmetrical apex shapes obtained due to laser absorption. The observed high failure rate could be due to the inefficient laser absorption by high bandgap materials like SiO_2, Si_3N_4, HfO_2 etc., commonly used in nanoelectronic devices. To improve on these shortcomings a deeper understanding of the interaction between the laser and the semiconducting tip is required. To do this, we first developed a new algorithm to determine the temperature at the apex of a semiconducting specimen during L-APT analysis (Section 3.1). We then used the method to understand:

1. The thermal response of a semiconducting tip using Si under green (λ = 515 nm) illumination as an example (Section 3.1)
2. The effect of the laser on the apex shape of a moderately absorbing tip using Si under green (λ = 515 nm) illumination as an example (Section 3.2) and
3. The absorption mechanisms in tips analyzed by a sub-bandgap laser using GaN (bandgap E_g = 3.39 eV) analyzed via a green laser (2.4 eV) as a case study (Section 3.3).

In each section I will first discuss in detail the importance and the current state of the art of the subject. I will then summarize my contribution to the same. The results obtained during this doctoral project are thoroughly discussed in Articles I, II, and III attached at the end of the chapter.

3.1 Quantification of the temperature rise

In this section we will briefly discuss the method we developed to determine the temperature. The method is discussed in more detail in the Article I, attached at the end of the chapter.

The temperature rise in the specimen due to its interaction with a femtosecond laser is of great interest in the L-APT community. Accurate determination of the temperature reached during a L-APT measurement is vital for both (1) understanding the physical nature of the interaction between a nanoscaled tip and a femtosecond pulsed layer, and (2)

assessment of the effect the laser power has on the quality of the APT measurement. For instance, Gault et al. [73] showed that high laser powers lead to surface migration of atoms, thereby, degrading the lateral resolution. Furthermore, it has been demonstrated that the laser power has a direct impact on the accuracy of quantification of the technique [74, 75]. Also J. Bunton et al. [70] determined that the mass resolving power of the laser-assisted atom probe depends on the laser power, the laser spot size, the thermal diffusion coefficient of the sample etc. From the point of view of the physical understanding of the nature of this interaction, the temperature distribution over the apex would help in understanding the spatial distribution of the absorption. Moreover, the access to the dependence of the temperature on laser power would provide valuable insight into the absorption mechanisms (linear/non-linear) especially, in the case of high bandgap materials. However a direct correlation between the laser power and the temperature is not straightforward to predict. This is so because the tip represents a sub-wavelength object and concurrent processes of absorption, excited carrier generation, carrier migration, tip heating and cooling occur on extremely short time scales (picosecond - nanosecond).

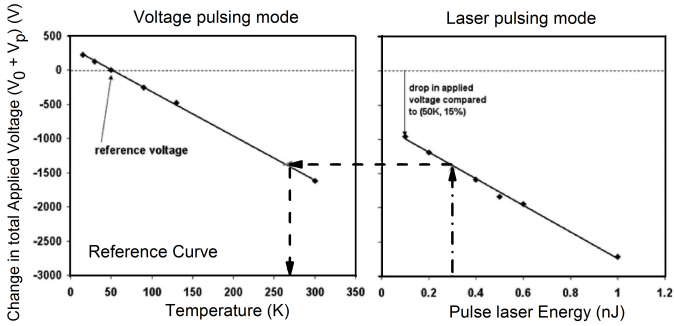

Figure 3.4 – Temperature determination using a combination of pulsed voltage APT and L-APT. Reproduced from [76]. Due to the erroneous analysis of semiconductors using voltage pulsed based APT for semiconductors, this method cannot be used for these materials.

Methods based on using a combination of pulsed voltage APT and L-APT have been proposed [77, 76] and are based on the assumption that the laser leads to a temperature increase. Hence, the temperature at the apex can be determined by comparing the voltage/field required to evaporate a specimen (at a given flux) at different laser powers to

a reference curve between voltage/field and base temperature. The reference curve is measured using pulsed voltage pulsed based APT at the same flux as the L-APT. However this method discussed cannot be employed for semiconductors as it relies on the propagation of high-voltage pulses through the tip, which is nearly impossible for semiconductors and insulators without excessive dispersion [25]. We developed a new method for temperature determination in semiconductors. The method is based on the physics of the field evaporation process, more specifically, the known exponential dependence (**Eq. 2.1**) of the evaporation flux ϕ on the apex temperature T.

3.1.1 The Method

As discussed in the previous chapter, the evaporation flux (ϕ) increases exponentially with any increase in field (F) or temperature (T) and is mathematically represented as an Arrhenius equation.

$$\phi = Aexp\left(\frac{-(Q_b)}{K_B T}\right) \tag{3.1}$$

where Q_b is the potential barrier height as a function of applied field, A is the pre-exponential constant and K_B is the Boltzmann constant. The natural log of **Equation 3.1** represents a straight line and states that at constant temperature, the $\ln(\phi)$ increases linearly with a decreasing potential barrier with a slope of $-\frac{1}{K_B T}$ (**Eq. 3.2**).

$$ln(\phi) = -\frac{Q_b}{K_B T} + ln(A) \implies T = -\frac{1}{K_B}\frac{d(Q_b)}{d(ln(\phi))} \tag{3.2}$$

Hence experimentally the temperature value can be determined via a L-APT measurement done at constant laser power (i.e. a constant temperature pulse) and varying the barrier height and measuring the corresponding change in flux. Since the barrier height is a function of applied electric field, it can be changed by the applied DC voltage. The barrier height was quantified using the scaling law (**Eq. 3.3**) proposed by Kreuzer and Nath (discussed in chapter 2).

$$Q_b = \left(\sqrt{1-\frac{F}{F_0}} + \frac{1}{2} \times \frac{F}{F_0} ln\left(\frac{1-\sqrt{1-\frac{F}{F_0}}}{1+\sqrt{1-\frac{F}{F_0}}}\right)\right) \times Q_0 \tag{3.3}$$

Taking a closer look at equation 3.3, the input parameters to calculate the barrier height are $\frac{F}{F_0}$, i.e. the field fraction, and Q_0.

Regarding field fraction, as discussed in chapter 2, it is equal to voltage fraction ($\frac{V}{V_0}$ **Eq. 2.11**). Hence, a way to calculate the temperature at the apex would be to first determine the V_0 value for every tip (method discussed in Chapter 2.3.2) and use the voltage fraction in equation 3.3 to calculate the barrier height. However, this method is tedious as V_0 is geometry dependent (ranging from 10 to 14 kV in the case of the tips of **Fig. 3.5(a)**) and needs to be measured for every tip. This is so because the applied voltage translates into an electric field at the apex, and while the field required to evaporate (at a given flux and temperature) is geometry independent, the voltage required to generate the desired field depends on the geometry of the tip (discussed in Appendix A). An elegant alternative would be to use the obtained CSR during the measurement to calibrate the V/V_0. As discussed in Chapter 2.3.2, the calibration curves link the CSR to the V/V_0 and are geometry independent (**Fig. 3.5(b)**).

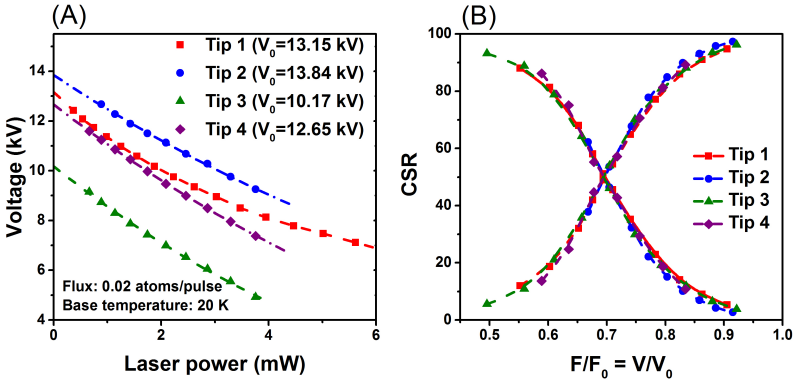

Figure 3.5 – (a) Geometry dependence of V_0. The different curves are calculated using a green laser (λ = 515 nm) on Si tips. The variation in V_0 for the different tips implies a different geometry of each. (b) Experimentally determined dependence of CSR on the V/V_0 for different tips. As can be seen they are independent of the geometry of the tip. These curves are referred to as calibration curves in this thesis.

Concerning Q_0, values ranging from 5.03 – 6.2 eV have been reported in literature calculated experimentally as well as theoretically [60, 78, 79]. The temperature values obtained in this thesis are calculated using Q_0 = 5.86 eV, observed from first principle molecular dynamic simulation performed in ref [60]. The error induced on the temperature value due to the uncertainty on Q_0 is discussed in detail in section 3.1.2.

In summary, the process flow for determining the temperature at the apex is (**Fig. 3.6**):

1. Run a L-APT analysis at constant laser power and measure the change in flux as a function of applied voltages (**Fig. 3.6(1)**).
2. The change of voltage at each data point corresponds to a change in field. The latter implies that each data point also has a unique CSR (**Fig. 3.6(2)**)
3. Convert the obtained CSR at each step to V/V_0 using experimentally determined calibration curve (**Fig. 3.6(3)**).
4. The V/V_0 values are in-turn used to calculate the barrier height using the scaling law proposed by Kreuzer and Nath and Q_0=5.86 eV (**Fig. 3.6(4)**).
5. Finally, the slope of the linear regression of $\ln(\phi)$ and barrier height is used to calculate temperature, since the slope is equal to $\frac{-1}{K_B T}$ (**Fig. 3.6(5)**).

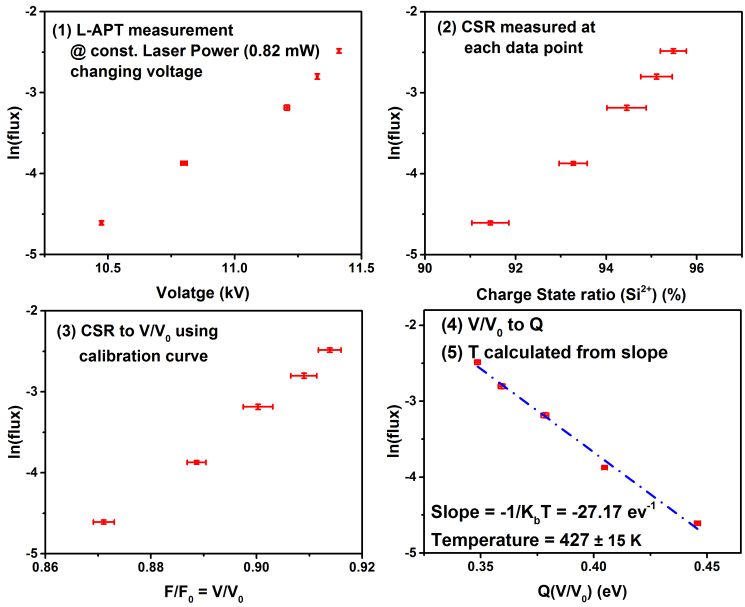

Figure 3.6 – Process flow for determining the temperature at the apex of the specimen. The shown example is for a Si tip illuminated by a green laser ($\lambda = 515$ nm) and an incident power of 0.82 mW

3.1.2 Error analysis

To evaluate the error of the derived temperature values, we rewrite Eq. 3.2 as:

$$T = -\frac{1}{K_B} \frac{\overbrace{\frac{d(Q_b)}{d\left(\frac{V}{V_0}\right)}}^{1}}{\underbrace{\frac{d(ln(\phi))}{d(CSR)}}_{2} \times \underbrace{\frac{d(CSR)}{d\left(\frac{V}{V_0}\right)}}_{3}} \tag{3.4}$$

Concerning the error of the determined temperatures, Eq. 3.4 already shows a major advantage of the proposed method, i.e. it only implies first derivatives. Hence, it is insensitive to the absolute values of unknown parameters like A. Going into more details, error on the derived temperature value could be due to:

- an error on the quantification of the three differentials in **Eq. 3.4** due to inaccurate determination of constants like Q_0, V_0 etc. and/or,
- an error originating from the statistical variation on the two experimental parameter ϕ and CSR.

In this thesis, we refer to the error induced due to an erroneous quantification of the differentials in **Eq. 3.4** of as systematic errors because they are independent of the measurement. The error originating due to the statistical variation is called as a random error.

3.1.2.1 Systematic error

The various sources of systematic errors are:

1. *Erroneous modeling of the barrier height* (1 in **Eq. 3.4**). The Kreuzer and Nath's scaling law accurately predicts the change in Q_b as a function of applied field, as shown in chapter 2.3.3. The only unknown parameter which has a direct impact on the temperature value is Q_0. To calculate the error on the derived temperature value originating due to Q_0, lets rewrite **Eq. 3.3** as

$$Q_b = f\left(\frac{V}{V_0}\right) Q_0 \tag{3.5}$$

Substituting **Eq. 3.5** in **Eq. 3.3** and using error propagation theory and to calculate the error on T due to Q_0, we get:

$$\Delta T = \frac{\partial(T)}{\partial(Q_0)} \times \Delta Q_0 \implies \frac{\Delta T}{T} = \frac{\Delta Q_0}{Q_0} \tag{3.6}$$

The relative error on Q_0 from the values reported in scientific literature is $\frac{\Delta Q_0}{Q_0}$ ~0.08 [60, 78, 79], i.e. the ΔT due to Q_0 is $\sim 0.08 \times T$. Hence, for a temperature of ~300 K, a systematic error of $\pm$24 K is present due to the uncertainty on Q_0. Please note that since Q_0 is a multiplication term in Q_b, the relative difference between two derived temperature values, i.e. $\frac{T_i - T_j}{T_i}$, is independent of Q_0.

2. *Inaccurate determination of the flux* (2 in **Eq. 3.4**). The evaporation probability as described by the Arrhenius equation (**Eq. 3.1**) explicitly assume that the evaporation probability of each atom is independent of the other atoms, i.e. removal of an atom has no effect on the evaporation probability of the other. The probability distribution (P) as a function of number of pluses (n_p) taken by each atom to evaporate can then me modeled using a Poisson process and is mathematically defined as:

$$P = K_D exp(-n_p \times K_D) \tag{3.7}$$

where K_D is the average flux in atoms/pulse. However, De Geuser et al. demonstrated that the evaporation probability of the surface atoms is also a function of the neighboring atoms [80]. They showed that the evaporation of a single atom may locally enhance the electric field and consequently lead to rapid evaporation of neighboring atoms. This implies that, experimentally a higher $P(n_p)$ is obtained for low n_p (**Fig. 3.7(a)**) and hence the experimental average flux (ϕ) is always higher than the flux (K_D) predicted by the Arrhenius equation. K_D can be calculated by fitting Eq. 3.7 to the tail of the experimental $P(n_p)$ since the tail represents uncorrelated evaporation events. A constant ratio between ϕ and K_D observed for the range of fluxes used to measure the temperature value (**Fig. 3.7(b)**) implies that the higher flux observed due to correlated evaporation has no effect on the determined temperature value. This is so because the proposed method to calculate temperature depends on $\ln(\phi)$ and is a differential technique.

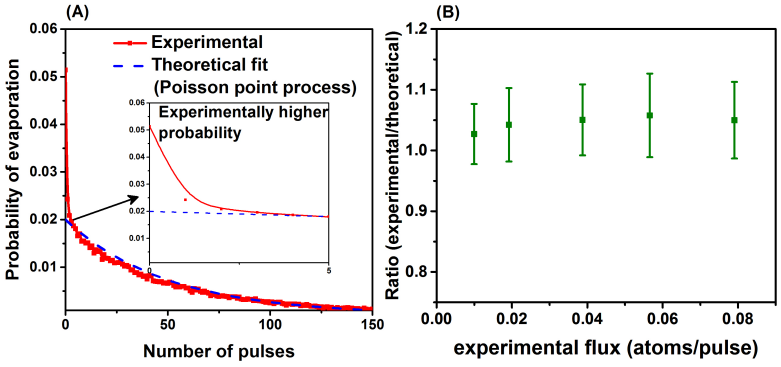

Figure 3.7 – (A) Experimental (red) and theoretical (blue) probability distribution of the number of pulses between evaporation events. The experimental distribution is measured using Si tip illuminated by a green laser. The theoretical curve is calculated from **Eq. 3.7**. The area under the experimental curve is higher than the theoretical curve, i.e. $\Phi > K_D$. (B) Ratio of the experimentally determined to the theoretically calculated flux. The theoretical flux was determined by fitting the tail of the experimental curve.

3. *Experimental determination of V_0* (3 in **Eq. 3.4**). As shown in chapter 2.3.2, V_0 is calculated as the extrapolation towards zero laser power of the laser power v/s voltage curve (measured at constant flux and assuming that at zero laser power the temperature at the apex is 0 K). However, at zero laser power the temperature at the apex is equal to the base temperature set during the measurement. Due to this the V_0 value is underestimated or in other words the V/V_0 is overestimated. This implies that the calculated barrier height (using the Kreuzer and Nath scaling law) is always underestimated. From **Eq. 3.4**, the estimated temperature value is a function of $\frac{\partial(Q_b)}{\partial\left(\frac{V}{V_0}\right)}$. Taking into account that in the range of V/V_0 used to derive T, Q_b can be approximated to vary linearly with V/V_0, $\frac{\partial(Q_b)}{\partial\left(\frac{V}{V_0}\right)}$ is equal to:

$$Q_b = Q'\left(1 - \frac{V}{V_0}\right) \implies \frac{\partial(Q_b)}{\partial\left(\frac{V}{V_0}\right)} = -Q' \tag{3.8}$$

where Q' is a proportionality factor resulting from the linearization. As can be seen Eq. 3.8, $\frac{\partial(Q_b)}{\partial\left(\frac{V}{V_0}\right)}$ is independent of V_0 hence,

the underestimation in the experimental V_0 has minor impact on the derived temperature values in the range where Q' remains constant. Indeed, on deliberately overestimating V_0 and calculating the resulting temperature values using the same set of experimental data (ϕ and CSR) **(Fig. 3.8)** a similar T is derived for a range of V_0 values ($V_0 = (V_0 + 4)$ kV).

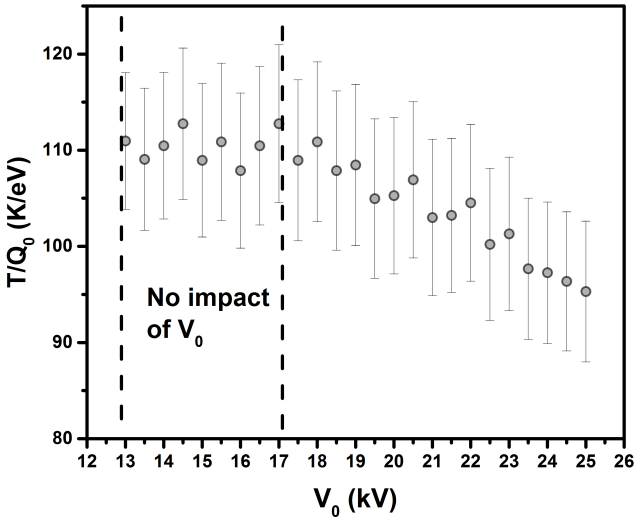

Figure 3.8 – Impact of underestimation of V_0 on the derived temperature values. The different T/Q_0 were calculated on the same set of experimental data of ϕ and CSR and iteratively overestimating the V_0. A similar temperature value is obtained in that range of V_0 values where the Q' (**Eq. 3.8**) remains the same. The error bar shown in the figure is the random error due to the statistical noise on ϕ and CSR (cf. section 3.1.2.2).

In summary, the only source of systematic error on the derived temperature values is the uncertainty on Q_0. However, since the described method is a differential technique, the relative difference between two temperature values is independent of Q_0. Hence, this method proves extremely useful to compare the temperature reached at the apex under different experimental conditions.

3.1.2.2 Random error

The random error originates from the statistical noise on the two experimental parameter ϕ and CSR. Obviously, increasing the number of

measured atoms reduces this random error. In more detail, the flux can be modeled as a Poisson process and hence, the random error on the flux can be obtained as the counting statistic error on a Poisson distribution, i.e. $\phi\sqrt{\frac{\phi}{N}}$, where N is the number of atoms. The statistical error on the CSR was calculated by dividing the collected data into smaller blocks of atoms. The error on CSR was then calculated as the standard deviation on the average CSR of individual blocks. A block size of ∼2 500 atoms minimized the error on the CSR. Furthermore, the precision on temperature will also depend on the range of CSR values considered, due to the non-linear relation between CSR and field fraction (**Fig. 3.5**). The temperature values were calculated by collecting 30 000 – 50 000 atoms. Using the counting statistic error on a Poisson distribution, the relative error on ln(ϕ), i.e. $\frac{\Delta ln(\phi)}{ln(\phi)}$, is between ~ $\pm 1 \text{x} 10^{-5}$ – $\pm 8 \text{x} 10^{-4}$. The relative error on CSR $\left(\frac{\Delta CSR}{CSR}\right)$ for a block size of 2500 – 5000 atoms was evaluated between ~ ±0.004 – ±0.01. Using error propagation theory (discussed in detail in article I), this results in a precision of $\frac{\Delta T}{T}$ ~ ±4 % – ±10 % i.e. a variation of ∼12-30 K for an estimated temperature of 300 K. *In this thesis, we always report the random error and neglect the systematic error due to Q_0.*

3.1.3 Thermal response of a Si tip under green laser

As a first case study, we applied the above described method to Si specimens to (1) sample the (potential) effects of dopant type and concentration as these, for instance, could lead to enhanced absorption due to free carrier absorption and (2) to gain insight into the heating of the specimen initially kept at two different base temperatures.

The (potential) effects of dopant type and concentration was studied by measuring temperature on four Si samples, of which two were n-type doped ($4 \text{x} 10^{14}$ atoms/cm^3 and $5 \text{x} 10^{19}$ atoms/cm^3) and the other two were p-type doped ($3 \text{x} 10^{15}$ atoms/cm^3 and 10^{19} atoms/cm^3) at different laser powers. All measurements were done using the Laser Assisted Wide Angle Tomographic Atom Probe (LAWATAP) from Cameca using laser pulsing (λ = 515 nm, 400 fs pulse duration). Assuming a spot size of 100 μm in diameter and all light is incident on the tip, the resulting laser influence (J/cm^2) for the used laser powers is summarized in Table. 3.1. However, since the spot size and cross-section of the tip over which the laser is incident is not known, laser power (mW) is reported throughout this thesis.

Laser power (mW)	Laser influence (J/cm^2)
1.22	1.56×10^{-3}
1.84	2.34×10^{-3}
2.82	3.60×10^{-3}
0.75	9.60×10^{-3}
1.38	1.75×10^{-3}
1.65	2.11×10^{-3}
1.96	2.50×10^{-3}
2.30	2.93×10^{-3}
2.75	3.50×10^{-3}
1.48	1.89×10^{-3}

Table 3.1 – Calculated laser influence (J/cm^2) for the range of laser powers (mW) used to calculate the temperature reached at the apex. The calculation is done assuming a spot size of 100 μm in diameter and all light is incident on the tip.

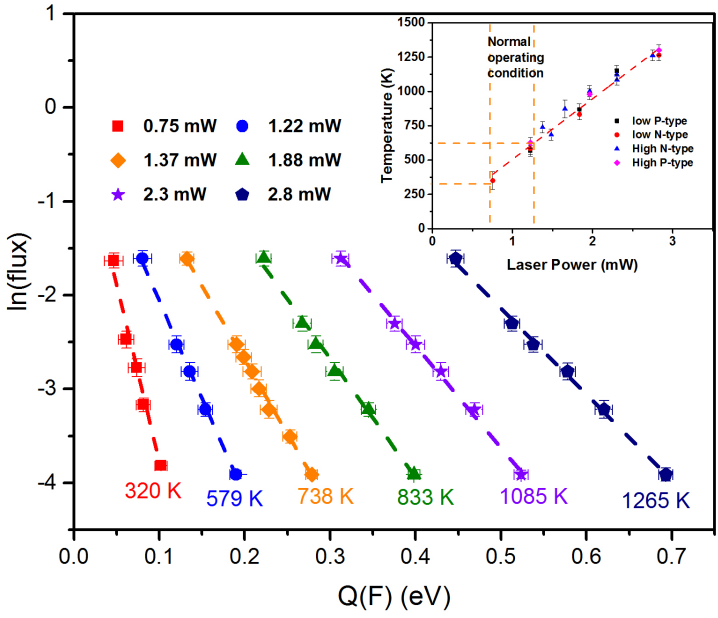

Figure 3.9 – ln(ϕ) v/s Q_b at different incident laser powers (λ = 515 nm) for Si. Please not the reported error on the temperature value (inset) is the random error and taking Q_0 = 5.86 eV

The temperature values obtained at different laser powers for Si

are shown in figure 3.9. In all cases the temperature varies linearly with laser power while ranging from ∼250 K to ∼1250 K for laser powers between 0.7 mW - 3 mW. The moderate temperatures (250 K-550 K) reached at low laser power) reached at low laser power under normal APT operating conditions (∼0.8-0.9 field fraction) and are in good agreement with those reported in literature [81, 82]. On the other hand at high laser powers very high temperatures close to the melting point of Si are reached. This result is consistent if one considers that nearly 60% of the energy for field evaporation is actually provided by the laser, meaning that the evaporation is essentially thermal. Indeed, at even higher laser powers melting of the tip is observed. Interestingly, from **Fig.** 3.9 we can already gain some insight into the absorption mechanism of Si and the pre-exponential constant A. The observed linear dependence of the temperature on laser power indicates negligible effect of non-linear absorption mechanism like free carrier absorption, multi photon absorption etc. Concerning the pre-exponential constant, the intersection point with the y-axis (i.e. A, **Eq. 3.2**) increases with increasing laser power. Since A is a function of the vibration frequency of atoms (ν) and the number of atoms available for field evaporation, the observed dependence may imply that ν increases with increasing temperature, opposed to the common assumption of it being independent of temperature.

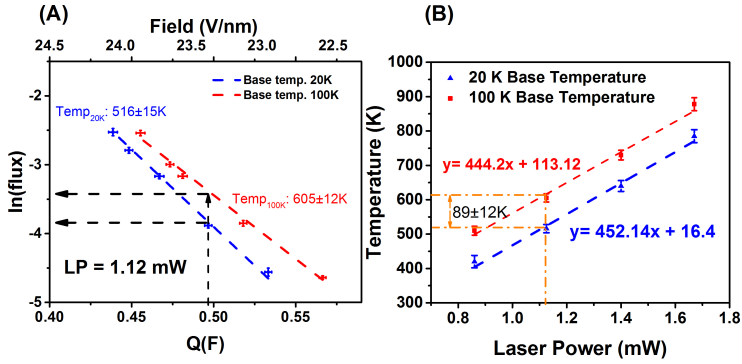

Figure 3.10 – (A) Flux as a function of barrier height (bottom X-axis) and field (top X-axis) at constant laser power (1.12 mW) for a Si tip analyzed using green laser and initially at 20 K (blue) and 100 K (red) temperature. A lower flux is observed for the same barrier height at 20 K. (B) Derived temperature values as a function of laser power at 20 K (blue) and 100 K (red). The difference between the two at the same laser power reflects the difference in base temperature. The temperature values were derived by collecting 5×10^4 atoms to minimize the random error

We used the method to gain insight into the thermal properties of semiconducting nanoscaled tips under laser illumination. Vurpillot et al. [24] and Silaeva et al. [83] observed a lower flux for specimen (W, Si, and Ge) initially kept at a lower base temperature (20 K) as compared to the specimen with a base temperature of 100 K at constant laser power and applied voltage (example for Si in **Fig. 3.10(A)**). This implies that the temperature at the apex (after laser pulsing) for the specimen initially at 20 K is lower as compared to the one at 100 K. On calculating the temperature at the apex, for Si tips under green ($\lambda = 515$ nm) illumination for a range of laser powers a difference of 89±12 K was obtained, mirroring the difference in the base temperature value (**Fig. 3.10(B)**). This result is unexpected and cannot be explained using the heat capacity (C_p) of bulk materials. In detail, the difference in energy required to heat a Si tip to ∼500 K from 20 K (i.e. $E_{20\text{-}500} = \int_{20}^{500} C_p dT$) or from 100 K ($E_{100\text{-}500} = \int_{100}^{500} C_p dT$) is

$$\Delta E_{20-100} = \int_{100}^{500} C_p dT - \int_{20}^{500} C_p dT = \int_{20}^{100} C_p dT \tag{3.9}$$

Since the C_p of semiconducting materials decreases with decreasing temperature (**Fig. 3.11**) and scales as $C_p \propto T^3$ at low temperatures [84] (**Fig. 3.11 (inset)**), ΔE_{20-100} is very small. This implies that the difference in the temperature reached after laser pulsing (assuming the same incident laser power) in sample initially kept at 20 K or 100 K should be much less than the difference in base temperatures.

The inconsistency between experiments (**Fig. 3.10(B)**) and theory may imply that the thermal properties of a biased nanoscaled semiconducting specimen may be different as compared to its bulk counterpart. In fact, C_p of nanowires (or in structures with high aspect ratio) is known to vary linearly with temperature at low temperatures [85]. Hence, the ΔE_{20-100} in nanowires is higher as compared to bulk Si. Furthermore, as will be discussed in Section 3.3, the amorphized shell present due to the Ga^+ ion beam damage during sample preparation modifies the optical and thermal properties of APT specimens as it has a higher absorption coefficient and a lower thermal diffusivity as compared to bulk materials. Moreover, amorphized shell show a less severe dependence of C_p on T [86]. Therefore, a more detailed study is required to understand the optical and thermal properties of APT samples to understand its thermal response under laser illumination.

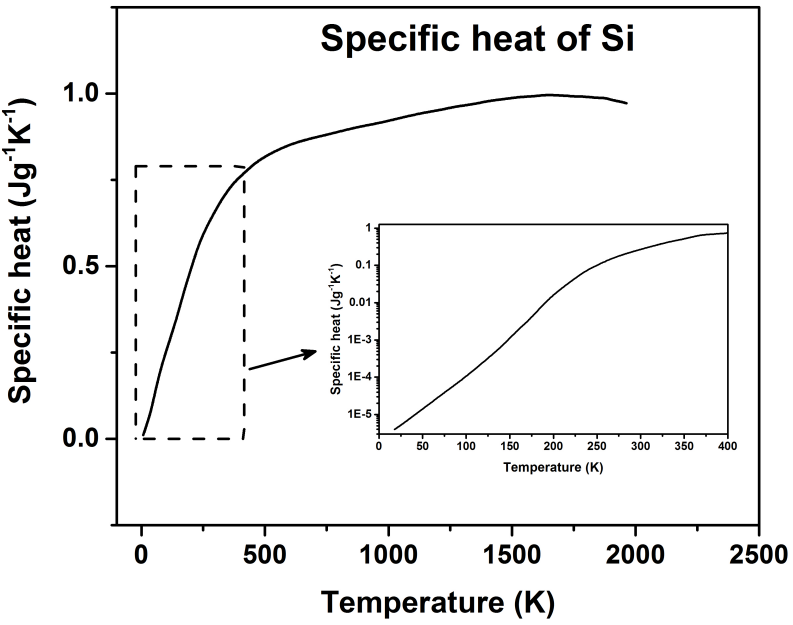

Figure 3.11 – Specific heat capacity of bulk Si as a function of temperature [1, 2].

To conclude, we developed a new method to determine the temperature at the apex of a nanoscaled semiconducting tip under laser illumination. The method is based on measuring the variation in evaporation flux as a function of applied voltage at fixed laser power. We used the method to gain insight into laser absorption process and the thermal response by a Si specimen illuminated by a green laser. The observed linear increase in temperature as a function of laser power implies the negligible impact of any nonlinear phenomenon in laser absorption by Si samples. Regarding the thermal response of a Si tip initially kept at 20 K and 100 K, we observed that the temperature difference between the two after laser pulsing is equal to the difference in base temperatures, i.e. ~80 K. This observation is remarkable and cannot be explained when considering the heat capacity of bulk Si. It may imply that the thermal properties of biased nanoscaled specimen is different from its bulk properties and a more in-depth study is required.

3.2 Tip Apex reshaping due to laser absorption

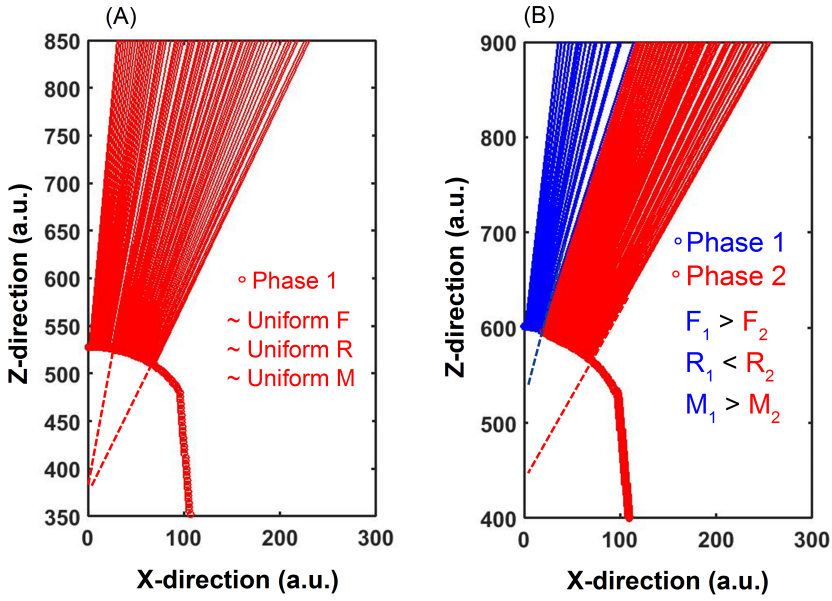

Figure 3.12 – (A) 2-D simulation in the XZ space of ion trajectories for field evaporation from hemispherical apex. The Z-direction is the direction of evaporation. Evaporated atoms have a common projection point (marked using a dashed line) and a uniform magnification over the whole apex. (B) Simulated ion trajectories of atoms evaporating from non-hemispherical apex. Atoms belonging to phase 1 (blue) have a higher threshold field of evaporation and hence a local sharper radius is formed at steady state. The projection point of phase 1 is closer to the apex as compared to phase 2. Hence a higher magnification is observed for phase 2. Please note that in the figure only half the tip is shown.

A major hurdle for exploiting the full potential of L-APT is degraded spatial resolution due to inaccurate reconstruction of analyzed specimens. The root cause to the potential inaccuracies in the reconstruction is the assumption of a perfectly hemispherical apex shape of the field evaporated specimen. In traditional reconstruction algorithms, the ion trajectories of the evaporated ions are modeled using a pseudo-stereographic projection law assuming a hemispherical apex shape [87, 26]. The reconstruction algorithm is described in more detail in Appendix B. In summary, the assumption of a hemispherical apex shape implies that all atoms

are projected from a common projection point and hence, have the same magnification (**Fig. 3.12(A)**). However, in the case of a non-hemispherical apex shape the ion-trajectory is a function of the direction and strength of the electric field in the immediate proximity to the evaporating atom. This field is in turn a function of the local curvature of the apex. Experimental evidence [31] and theoretical modeling [22] proves that the magnification is higher in the region of higher field, i.e. smaller local curvature (**Fig. 3.12(B)**) and trajectory overlaps can occur between ions evaporating from the interface of two local radii. This difference in magnification across the apex leads to artefactual low and high densities in the reconstructed data. De. Geuser et al. proposed an algorithm to correct these density variations due to magnification variations by homogenizing the density using an iterative algorithms [88]. However, it is still not possible to correct the artefact due to trajectory overlaps. Forward 3-D field evaporation simulations [89, 22] are able to assess the effect such distortion but of course a backward iteration, i.e. reconstruction, would require a continuous knowledge about the tip shape. Attempts to generate that information are under development by adding TEM imaging to an APT system in order to continuously extract the tip apex information [90].

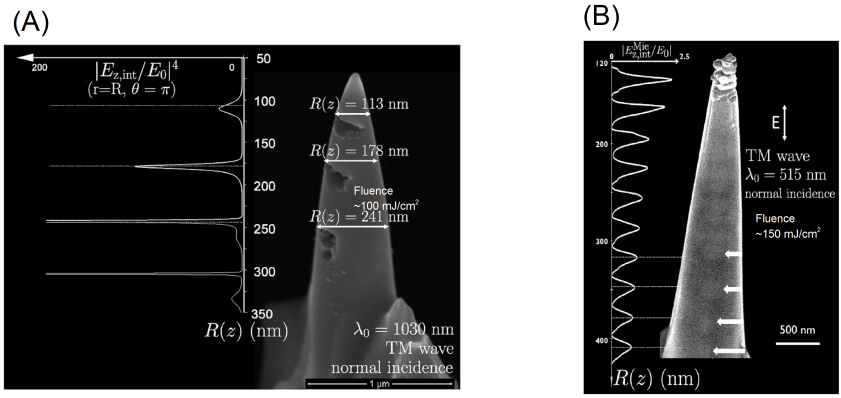

Figure 3.13 – Position of resonant radii for coupling of (a) IR (1030 nm) and (b) Green (515 nm) light in a Si tip. The SEM images of tips analyzed by respective wavelength at high-fluence show damage at the resonant radii. Reproduced from [91, 92].

In my opinion, to perfectly reconstruct the evaporated volume it is vital to be able to know the exact apex shape of the tip and the ion trajectories. Notwithstanding the benefit of a routine monitoring of the

tip apex, it is also important to understand the root physical cause for the non-hemispherical tip shape a this may lead to insight in its minimization. The origin for the local curvature can be 2-fold, (1) the difference in field evaporation characteristics of sub-phases and or layers in the tip and (2) interaction between the laser and the tip. For the case of a non-hemispherical tip shape appearing due to differences in field evaporation characteristics is well understood and can be predicted using electrostatic simulation (**Fig. 3.12**) [93, 89]. However, the effect of laser illumination on the apex shape of the tip is not so clear. S. Koelling et al. [28] and A. Kambham [30] reported non-hemispherical apex shapes for Si and Si-FinFET samples respectively analyzed under UV (343 nm) illumination. The formation of a non-hemispherical apex shape was attributed to the way light couples into a semiconducting tip. The coupling of light inside a semiconducting/insulating tip has been studied in detail by a number of authors [67, 68, 81]. In view of its reduced dimensionality the relevant conclusion is that, light couples inside a conical dielectric tip at optically resonant cross sections, i.e. at the positions at which the multiple internal reflections of light interfere constructively. These resonant radii (R_K) are approximately located at $\sim \frac{(2K+1)\lambda_0}{8n}$, where λ_0 is the wavelength of incident light, n is the real refractive index of the material and K = 1,2,3... is the order of the resonant radius (**Fig. 3.13**). Experimentally, the presence of these resonant radii has been observed as localized damaged areas on Si tips after analysis under IR (**Fig. 3.13(A)**) and green (**Fig. 3.13(B)**) light at high-fluence. However, in strongly absorbing cases (e.g. Si illuminated by a UV laser), almost all light is absorbed near the edge of the sample, i.e. no internal reflections of transmitted light occur and thus no interference patterns are observed [28] (**Fig. 3.14(A)**).

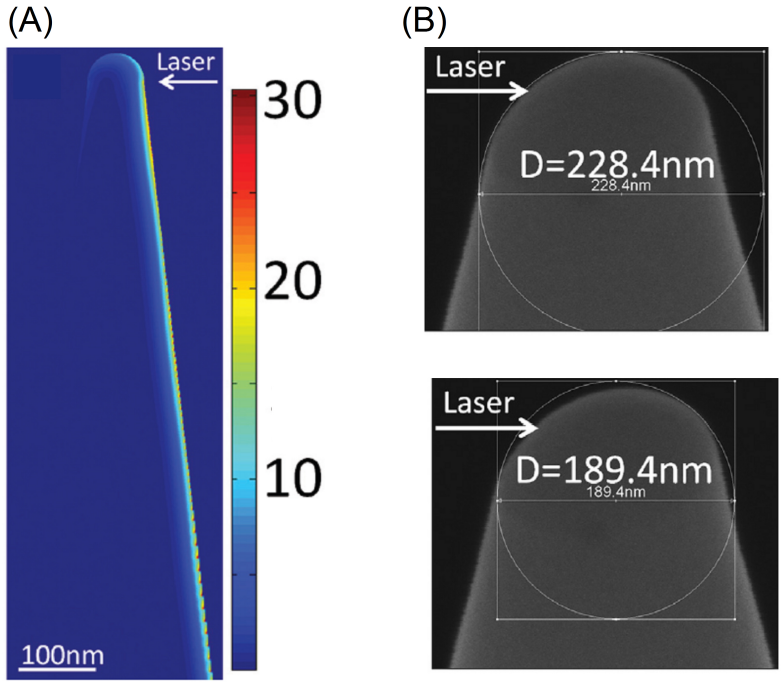

Figure 3.14 – (A) Spatial distribution of light in Si tips illuminated by a UV (λ = 343 nm) laser. (B) SEM images of apex shape of a Si tip after analysis under UV illumination. Reproduced from [28].

This strong one sided absorption leads to a temperature gradient across the apex surface. The temperature gradients in-turn leads to a non-uniform evaporation probability across the apex since, the latter increases with any increase in temperature (chapter 2, **Eq. 2.1**). To reach steady state, i.e. maintain a stationary tip shape with uniform evaporation probability across the whole surface, the apex reshapes (into a non-hemisphere) such that the resulting field counteracts the difference in evaporation probabilities (**Fig. 3.14(B)**). The significance of this effect depends on the absorption characteristics of the tip. For materials like Si which have a moderate absorption under green (λ = 515 nm) and IR (λ = 1030 nm), A. Vella et al. [81] and S. Koelling et al. [28] observed hemispherical apex shapes at moderate laser energies implying a uniform heating of the tip apex. However, during the course of this project we observed subtle non-hemispherical apex in Si samples analyzed

under green illumination, using TEM measurements. Most likely the discrepancy with previous work arises from the fact that in ref [81, 28] only SEM imaging was used whereas we exploit the higher resolution of TEM. In this section we will briefly discuss these non-hemispherical apex shapes and their relation to the spatial distribution of absorbed light. This is discussed in more detail in Article II attached at the end of the chapter.

The impact of the laser on the apex shape of a Si tip illuminated by a green (515 nm) and IR (1030 nm) laser was studied using a combination TEM and L-APT measurements. The L-APT measurements were used to measure the temperature and field distributions across the apex since, the final apex shape is a direct consequence of these distributions. The TEM measurements were used to analyze the apex shape after L-APT measurements.

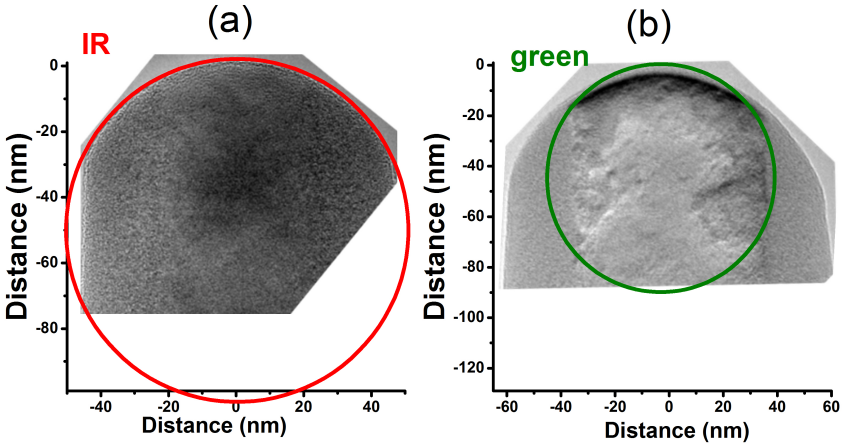

Figure 3.15 – TEM micrographs of Si tips after analysis under (a) IR ($\lambda = 1030$ nm) and (b) green ($\lambda = 515$ nm). The apex shape of the tip analyzed with an IR laser hemispherical while, for the tip analyzed using green laser has a smaller local curvature at the center.

The TEM micrographs showed a hemispherical apex shape for tips analyzed using IR laser while, a slightly asymmetric apex shape for the ones analyzed under green laser is observed (**Fig. 3.15**). Since TEM micrographs are 2-D projections of a 3-D object, the actual shape of the apex is hard to quantify [94]. However, the observed non-hemispherical (respectively hemispherical) apex shape is sufficiently clear to conclude a non-uniform (respectively uniform) effect of green (respectively IR) laser

on Si tips. The uniform effect by the IR laser is rather easy to explain based on its coupling in a Si tip (**Fig. 3.13(A)**). The first-order (K = 1) resonant cross section for IR light is very far away from the apex along the shank of the tip (R_1 ~110 nm). The laser-induced heat, must therefore diffuse towards the tip apex prior to stimulate evaporation and will thus become uniform across the tip cross-section before it reaches the apex. However, understanding the non-uniform effect of the green laser is not so straightforward.

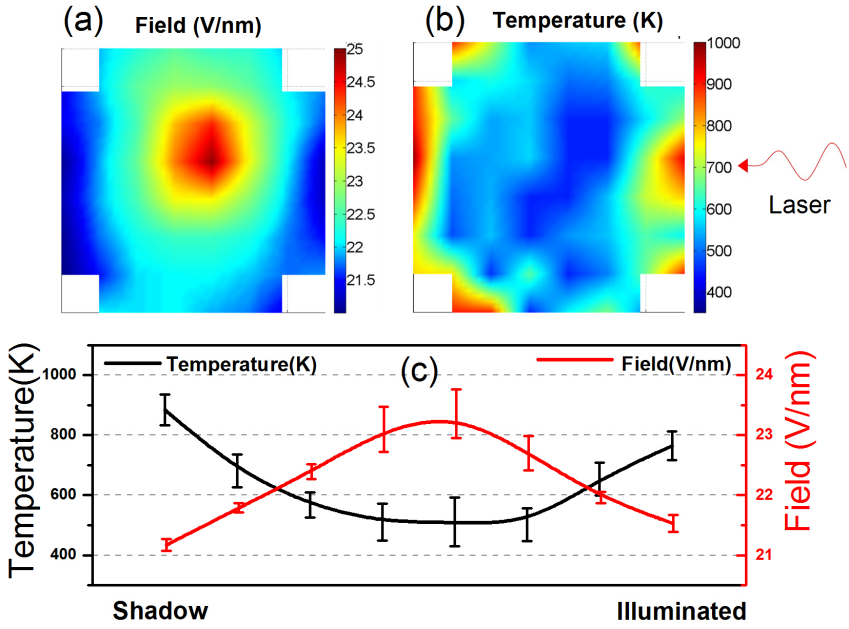

Figure 3.16 – Field (a) and temperature (b) distribution across the apex of a Si tip analyzed by a green laser. The high field in the center is due to the presence of a low index pole (<100>) (c) 1-D profile of the distributions along the direction of light propagation

To understand this, we first experimentally measured the field and temperature distributions over the apex at steady state. The experimental 2-D distributions (**Fig. 3.16 (A) & (B)**) were calculated by dividing the detector hit map into small blocks and using the method described in section 3.1 in each block. To maintain an acceptable error in the temperature or field calculated in each block (~2500 atoms/block), $\sim 1.5 \times 10^4$ atoms were collected/measurement and the 10 cm PSD

was divided into blocks measuring 1 cm × 1 cm. These experimental distributions were then compared with the theoretically modeled spatial distribution of absorbed light.

A 2-fold symmetry was observed in the experimental temperature/field distributions, with a higher temperature (lower field) on the sides illuminated by the laser and the one opposite (shadow side) and a lower temperature (higher field) in the middle (**Fig. 3.16**). Furthermore, the distributions were slightly asymmetric, with the temperature (respectively field) being the highest (respectively lowest) on the shadow side.

Absorbed power density in a 3-D object representing an APT tip was numerically simulated using discrete-dipole approximation (ADDA v.0.79 code) [95] with an assumed refractive index of $\widetilde{n} = 4.22 + i0.06$ [96]. The resulting squared relative internal electric field amplitude ($|E_{z,int}/E_0|^2$) of the coupled light from the simulation was converted to relative absorbed power using the divergence of the Poynting vector (**Eq. 3.10**) [97].

$$\frac{P_{abs}}{P_0} = \frac{\left(\frac{1}{2}\omega Im(\varepsilon)\right)}{c} \times \left|\frac{E_{z,int}}{E_0}\right|^2 \tag{3.10}$$

where P_{abs} is the absorbed power density in W/m^3, P_0 is the incident power density in W/m^2, $|P_{abs}/P_0|$ is relative absorbed power in m^{-1}, ε_0 is the free space permittivity, $Im(\varepsilon)$ is the imaginary part of the relative dielectric permittivity, c is the speed of light, $|E_{z,int}|$ is the magnitude of the total internal electric field and $|E_0|$ is the magnitude of the incident electric field. The simulated relative absorbed power in the XZ plane of a Si tip is shown in Figure 3.17(a), X being the direction of light propagation and Z the direction of the tip axis. In order to verify if the non-uniformity of the absorbed light is the reason for the non-uniform temperature distribution at the apex, three characteristics of the simulated absorbed light were compared to experimental observations. Namely, (1) the pattern of the absorbed light in the XY plane, (2) the relative magnitude of the absorbed light on the illuminated and the shadow side of the tip and (3) the change in magnitude of the absorbed light as a function of depth (Z-direction) for both the illuminated and the shadow side.

1. The experimental field and temperature distributions show a 2-fold symmetry across the tip apex (**Fig. 3.16**), similar to the first absorption maxima in the simulations, i.e. at a cone radius of ∼60 nm. The two are in good qualitative agreement considering that maximum *cone radius* of a Si tip that can be analyzed in the

L-APT at a flux of 0.01 atoms/pulse and a FR of ~10% - 14% is ~67 nm[1].

2. Regarding the distribution of absorbed light, more light is coupled on the shadow side of the tip at the first absorption maxima. This will translate to a higher temperature/lower field on the shadow side of the tip. The same behavior is observed in the experimental temperature/field distributions (**Fig. 3.16**).

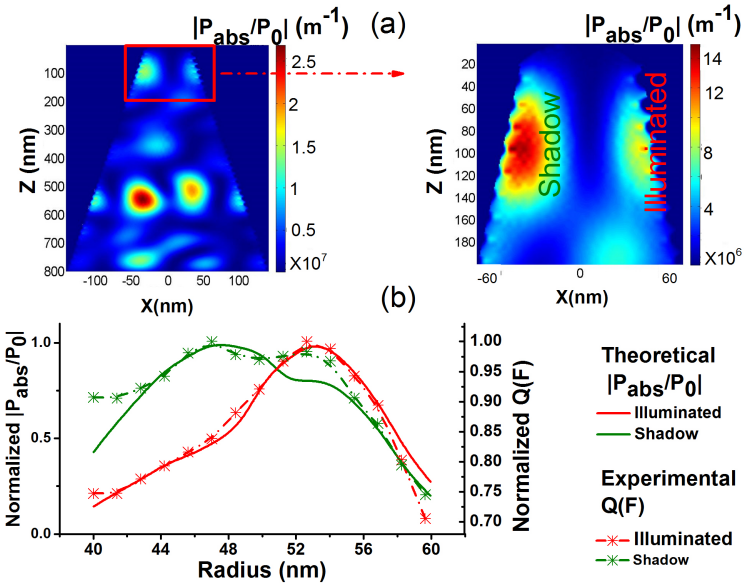

Figure 3.17 – (a) ADDA Simulation of a Si tip illuminated by green laser. (b) Correlation between the relative absorbed power in the XY plane (solid line) and the change in field required (dashed line) to evaporate at constant flux. The field and $|P_{abs}/P_0|$ have been normalized to the max value of field and $|P_{abs}/P_0|$ respectively.

3. As discussed previously any temperature variation will (temporarily) lead to a non-uniform evaporation causing the tip to reshape such that the resulting field non-uniformity compensates the temperature non-uniformity. Since the field translates into a barrier height, we compare in **Figure 3.17(b)** the calculated experimental

[1]The maximum *apex radius* that can be successfully analyzed under the above mentioned conditions is ~80 nm, which corresponds to a *cone radius* of ~67 nm due to truncation of the apex (**Fig. 3.15**).

change in barrier height (based on the experimental data of field, right y-axis) with the modeled relative absorbed laser power on the illuminated and the shadow side. To have maximum sensitivity of the electric field to any change in temperature at the apex due to a change in absorbed laser power, L-APT measurement (constant flux and laser power) was done at low flux (0.01 ± 0.002 atoms/pulse), high FR (10%-14%) and a low base temperature (20 K). The obtained data are represented as a function of increasing radius (i.e. Z-direction). An excellent qualitative agreement is obtained between the two i.e., any increase (resp. decrease) in the theoretically expected absorbed power indeed perfectly correlates with the experimental observation of an increase (resp. decrease) in barrier height and thus apex temperature.

The good agreement between the simulated absorbed light in the tip and the experimental data suggests that the non-uniform effect of the green laser is due to the non-uniform distribution of absorbed light inside the tip.

To conclude, in this section using a combination of TEM and L-APT, we have shown that the apex of a Si tip is non-hemispherical (resp. hemispherical) when analyzed with a green (515 nm) (resp. IR (1030 nm)) laser. The resulting tip shape is a direct consequence of the temperature distribution at the apex. The later in-turn depends on the location of the resonant absorption sections. For tips analyzed with the IR laser, the absorbed light is far away from the apex. Hence, the generated heat must diffuse towards the apex to stimulate evaporation and thus will become uniform across the tip cross-section before it reaches the apex resulting in a hemispherical apex. The situation in green is very different as the laser is absorbed non-uniformly close to the apex. The experimental observation of the fingerprint of this non-uniform absorption in the temperature distribution at the apex indicates; the tip apex is not at thermodynamic equilibrium before field evaporation is triggered. The non-uniform temperature distribution at the apex results in the experimentally observed asymmetrical apex shape. This observation point towards the presence of a non-hemispherical apex shape in most materials whenever light resonantly couples in close proximity to the apex. This in-turn signifies that the assumption of a hemispherical apex shape by most reconstruction algorithms is wrong, hence, leading to imperfect data analysis.

3.3 Absorption in high bandgap materials

The ability to analyze materials using a sub-bandgap laser has been demonstrated extensively in the scientific literature. For example, Agrawal et al. [98] performed analysis on GaN nanowires (bandgap 3.39 eV) using a green laser (2.28 eV), analysis on bulk MgO (bandgap 7.8 eV) using green (2.28 eV) and UV (3.61 eV) laser was demonstrated by B. Mazumder et al. [99]; D. Larson et al. showed L-APT results on bulk Al_2O_3 layers [100]. However, a physical interpretation of the effect which promotes laser assisted field evaporation has been a topic of discussion in the scientific community. Several phenomena have been proposed to explain this process. E.P. Silaeva et al. proposed that the free holes could be attracted to the surface due the electric field inside the material which in turn could absorb light the same was as free electrons absorb light in metals [83]. Another mechanism could be the increased absorption in semiconductors due to photon-assisted tunneling of electrons from the valence to the conduction band (Franz–Keldysh effect) [101]. Alternatively it has also been suggested (using DFT simulations) that the bandgap in semiconductors and insulators decreased when submitted to the very high fields needed for evaporation thereby, increasing the absorption efficiency [102]. Note however that, these calculations were done for small clusters. An important item overlooked so far in most considerations is the presence of an amorphized layer at the tip side walls resulting from the ion beam interaction during the sample preparation. This amorphized layer is full of crystal defects which in turn could lead to enhanced absorption. Evidence for this process is provided through L-APT analysis wurtzite GaN (bandgap E_g = 3.39 eV) under green (λ =515 nm) illumination. The article III attached at the end of the chapter outlines the results comprehensively and demonstrates that the presence of an amorphized shell surrounding the crystalline tip contributes significantly to the absorption of green, i.e. sub-band gap laser light.

Tips were prepared with varying thickness of the amorphous GaN (α-GaN) shell using different acceleration voltages (30 kV, 8 kV, 5 kV, 1 kV) of the ion beam for the final cleaning step during sample preparation in the FIB (more details on sample preparation in Appendix 1). Subsequently, TEM micrographs were used to quantify the thickness of the amorphous GaN (α-GaN) shell. A thickness of $\sim$ 1.2 nm was observed for a tip cleaned at 1 kV. This thickness increased to $\sim$ 2.2 nm for an 8 kV clean. The observed thickness is in good agreement with the 0.8 nm (resp. 2.3

nm) implantation range as calculated with SRIM for a 1 kV (resp. 8 kV) Ga^+ beam incident on GaN at an angle of 85 ° [103].

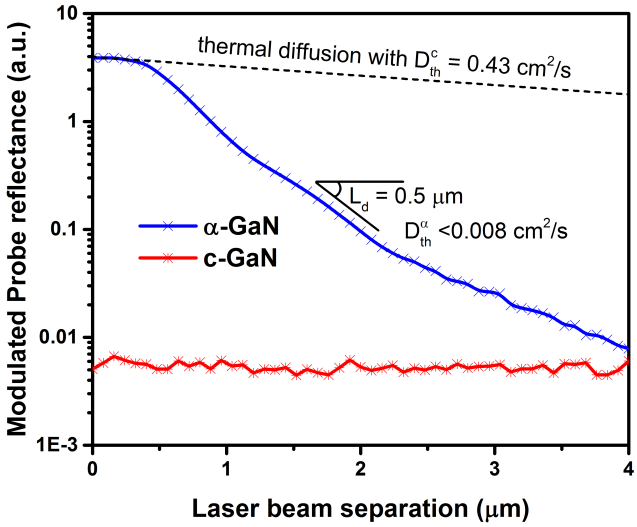

Figure 3.18 – Amplitude of the modulated probe reflectance signal measured on c-GaN (blue line) and α-GaN (red line) as a function of pump and probe beam separation. The lateral decay length L_d on α-GaN is much shorter than expected from thermal diffusion in c-GaN (black interrupted line), which evidences a degraded thermal diffusivity.

To probe the modified optical and thermal properties of the α-GaN layer, photo-modulated optical reflectance (PMOR) measurements were performed. PMOR is a pump-probe reflectance technique wherein a modulated-power near-infrared (NIR) pump laser, if absorbed, heats up the sample and hence modulates its refractive index [104]. The wavelength of the pump laser is 790 nm, i.e. its photon energy $E_{ph} = 1.57$ eV, and its modulation frequency is $\omega_{mod} = 1$ MHz. The pump-induced modulation of the refractive index is measured by means of the modulated reflectance of the probe laser ($\lambda = 670$ nm). Such photoreflectance techniques are widely used to study the damage caused by ion-implantation as the pump-induced heating and hence the modulated reflectance scale with sample damage [105, 106]. PMOR measurements were done using the TP630XP tool on a c-GaN blanket layer and an amorphized patch (20×20 μm^2). The amorphized patch was made on the same GaN wafer using a 30 kV Ga^+ FIB at 7.7 pA current for 100 s. As expected, the PMOR measurement on

the c-GaN sample shows a vanishing signal as a result of the transparency of c-GaN to the NIR pump laser ($E_{ph} < E_g$). Contrarily, measurement on the amorphized GaN showed a marked increase in absorption of the sub-bandgap NIR laser (**Fig. 3.18**). Additionally, the lateral decay length L_d of the modulated reflectance measured on the α-GaN area also demonstrates the poor diffusion of the heat generated inside the sample. If heat were able to diffuse as efficiently in α-GaN as in c-GaN, the signal decay would indeed be less abrupt. This is illustrated by the interrupted line of **Fig.** 3.18 which assumes a signal decay length $L_{th}^c = \sqrt{\frac{D_{th}^c}{\pi\omega_{mod}}}$ [107, 104] with the thermal diffusivity of c-GaN ($D_{th}^c = 0.43$ cm^2/s [108]). An estimate of the actual diffusivity of α-GaN can be derived from these PMOR measurements, keeping in mind that only a maximum value is determined as the decay length is convoluted with the pump and probe beam shapes (i.e. Gaussian beams with 0.5 μm radius each [104]). Using the decay length $L_d = 0.5\,\mu m$ of the PMOR signal measured on α-GaN, we deduce that the thermal diffusion length in α-GaN is $L_{th}^{\alpha} \leq 0.5\mu m$. This gives a maximal thermal diffusivity of α-GaN of $D_{th}^{\alpha} < 0.008$ cm^2/s [107], i.e. almost two orders of magnitude smaller than D_{th}^c. Such a dramatic degradation of the thermal diffusivity has also been observed in time-resolved photoreflectance measurements of FIB-amorphized Si [109].

The increased absorption and the decreased thermal diffusivity shown by PMOR measurements are at room temperature and on blanket films. To verify these at L-APT base temperatures (20 K - 80 K), and in nanoscaled samples, L-APT measurements were done using green laser (λ =515 nm, i.e. E_{ph} = 2.4 eV) on tips cleaned at different acceleration voltages. It was observed that a lower field was required to attain the same flux in tips with a thicker α-GaN, i.e. tips with a thicker α-GaN reached a higher temperature under laser illumination (**Fig. 3.19(A)**). The sub-bandgap absorption efficiency of each tip ($\varepsilon_{abs} = \delta T_{apex}/\delta P$) was extracted, from the measured variation in the apex temperature T as a function of the power P of the green laser (**Fig. 3.19(B)**). The latter was calculated using the method described in section 3.1. However, the Q_0 value for GaN is not known; hence, we only had access to the so-called normalized apex temperature, i.e. T_{apex}/Q_0 ratio. As shown in **Fig.** 3.19**(B)**, ε_{abs} scales with milling voltage. In particular, the tip cleaned at 8 kV absorbs the green laser light approximately 43% more efficiently than the tip cleaned at 1 kV voltage. This increase in ε_{abs} can be attributed to the increased thickness of the α-GaN shell at higher cleaning

voltages. Furthermore, when using high-voltage cleaning (30 kV), GaN tips show evidence of local melting after L-APT analysis at only 1.1 mW green laser power (**Fig. 3.19(B)**). In other words, a thick α-GaN shell leads to higher absorption efficiency such that the damaged tip can reach its melting point even at the lowest laser power.

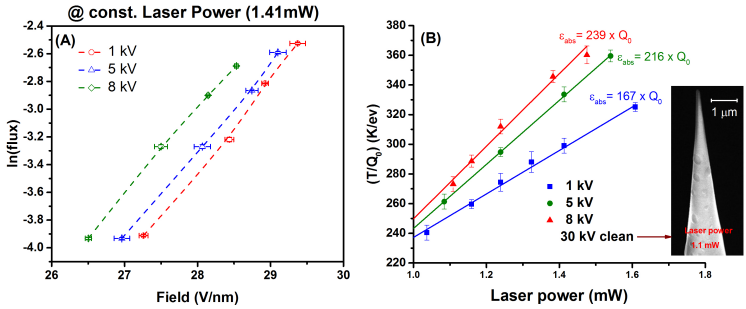

Figure 3.19 – (A) Impact of changing field on the observed flux at constant laser power (1.41 mW, λ = 515 nm) for tips cleaned at 1 kV, 5 kV and 8 kV. To reach the same flux a lower field is required for tips with thicker α-GaN (i.e. a higher clean energy) (B) Variation in normalized apex temperature T_{apex}/Q_0 as a function of the green laser power measured on GaN tips milled respectively at 1 kV (square), 5 kV (circles) and 8 kV (triangles) voltages. The absorption efficiency ε_{abs} (K/mW), which is obtained from the slope of the linear fits (colored lines), increases with milling voltage (B) Tip milled at 30 kV voltage which, after LAPT analysis at the lowest 1.1 mW laser power, shows evidence of melting.

Further evidence for the high absorption in the amorphized shell can be observed in the field distribution across the apex (**Fig. 3.20**). As explained in the previous section, in steady state, the field distribution has an inverse correlation with the temperature distribution at the apex. The linear variation in the field distribution observed in **Fig. 3.20** implies that the illuminated side is the hottest while the temperature on the shadow side is the lowest. This distribution in temperature is very similar to the one observed in Si when illuminated with a UV laser [28] and indicates one sided absorption in GaN. However, theoretically the coupling of green light in pure c-GaN tips occurs at resonant cross-sections (**Fig. 3.21**). Furthermore, only a fraction of this coupled light (if any) should be absorbed due to negligible absorption coefficient of c-GaN. Hence, theoretically we expect field distribution similar to the one observed in Si when illuminated by a green laser (**Fig. 3.16**). The reason

for this disparity could be the strong absorption in the α-GaN shell which is neglected in the simulation.

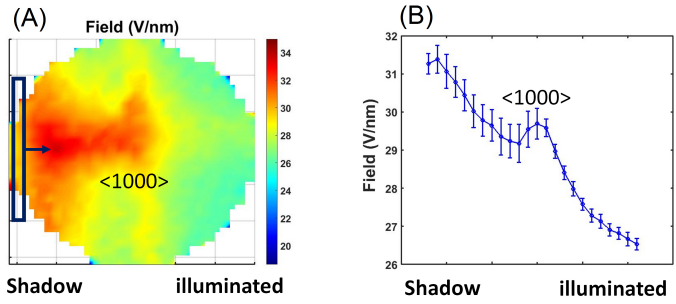

Figure 3.20 – (A) 2-D field distribution across the apex in GaN. (B) 1-D field profile across the surface. The value at each point is the mean value in a vertical selection of the detector (blue box in (A)). The error bar is the standard deviation in the vertical selection. The tip used for this measurement was cleaned with a FIB energy of 5 kV. Also note that the high field observed in the center is due to the presence of the <1000> pole.

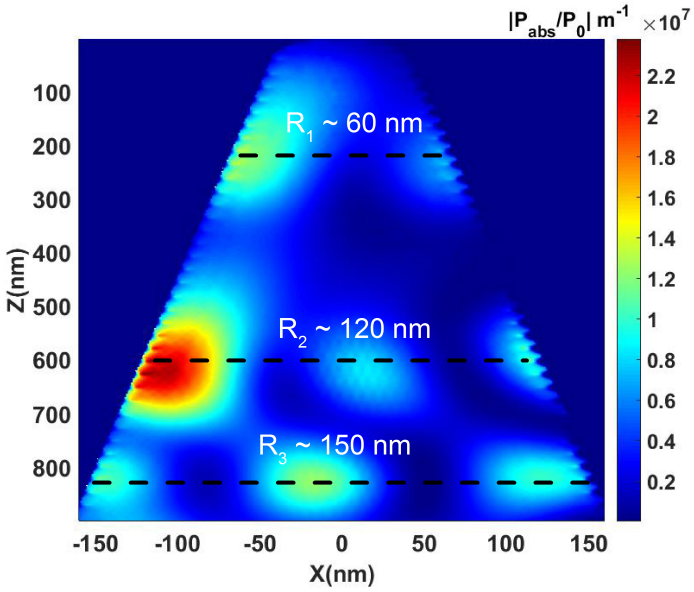

Figure 3.21 – Simulated absorption (using ADDA) in GaN illuminated by a green laser.

Increased absorption in amorphized semiconductors has been reported extensively in scientific literature [110]. For example, the absorption coefficient of α-Si at 515 nm is $\sim 3.4 \times 10^5$ cm^{-1}as compared to $\sim 1.4 \times 10^3$ cm^{-1}for c-Si. To the best of my knowledge no data exists for the absorption coefficient of α-GaN. Assuming that all the absorption occurs in the amorphized shell ($\sim$2 nm from SRIM) would yield an absorption coefficient of $\sim 5 \times 10^6$ cm^{-1}. However, considering that c-GaN is transparent at λ =515 nm, such high absorption coefficient of α-GaN is unexpected. Hence, more detailed studies are required to understand the optical properties of the amorphized layer and gain a better understanding of light absorption in such core-shell structures.

In summary, we have shown via experimental verification that the amorphized shell (created during tip preparation via FIB) has a much higher absorption and a lower thermal diffusivity as compared to the crystalline core. This, in turn, plays a dominant role in the unanticipated absorption of sub-bandgap light and hence in the possibility for L-APT analysis of a priori transparent semiconducting and insulating materials. This conclusion has both experimental as well as theoretical implications.

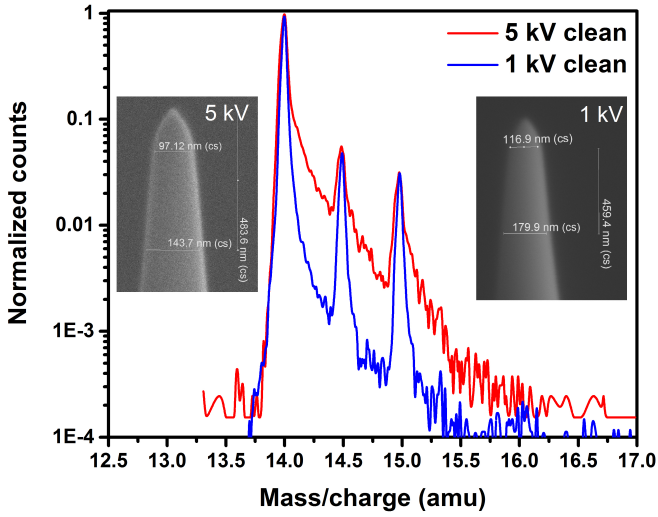

Figure 3.22 – Comparison of mass spectra obtained from Si tips cleaned at 5 kV(red) and 1 kV (blue), analyzed using the green laser and same laser power. Both the samples have similar shapes (SEM images) hence, the impact of geometry on the difference in mass spectra can be neglected.

Experimentally, the optimization of the amorphized layer could play a

vital role for successful L-APT analysis in certain materials. From a theoretical standpoint, while simulating laser assisted field evaporation, the impact of this layer shouldn't be neglected. As discussed the amorphized layer not only plays a role in light absorption but can also affect the spatial distribution of the absorbed light thereby affecting field evaporation. Furthermore, even for absorbing materials the amorphized shell acts as a second absorbing material with different light absorbing and heat conducting properties. This in-turn can have a major impact on the equilibrium apex shape and the thermodynamics of the tip. Evidence of the latter was observed in the mass resolution obtained in Si tips cleaned at different FIB energies and analyzed via the green laser. As can be seen in **Fig. 3.22** the mass resolution for the tip cleaned at 1 kV is much better than the one cleaned at 5 kV. However, a more detailed study in needed to fully understand the impact of the amorphized layer in absorbing materials.

3.4 Conclusions

In this chapter, we used experimental methods and numerical simulations to gain insight into the interaction of a pulsed laser with a nanoscaled needle-shaped field emitter. To do this we first developed an experimental procedure to quantify the temperature reached at the surface of the specimen during L-APT (Section 3.1). We then used the developed method to gain a deeper understanding of:

1. *Thermal response of the tip under laser illumination initially kept at two different base temperatures* (20 K and 100 K). A difference in flux (lower at lower temperature) is reported in scientific literature for L-APT analysis done at constant laser power and field [24, 83]. This implies that the temperature reached after laser pulsing is lower for the tip at lower base temperature. On calculating the temperature difference a variation of ~89K, i.e. mirroring the difference in base temperature, was observed for Si samples. This observation is remarkable and cannot be explained when considering the heat capacity of bulk Si and may imply that the thermal properties of biased nanoscaled specimen is different from its bulk properties. Hence, this calls for a more in-depth study of the thermal properties of APT specimens

2. *The spatial distribution of temperature at the apex of a Si sample and its effect on the equilibrium apex shape* (Section 3.2). It was already well known that strongly absorbing materials (e.g. Si under UV illumination) lead to a non-uniform temperature distribution at the apex and hence a non-hemispherical apex shape. For the first time, we showed, using a combination of TEM and L-APT, that even in moderately absorbing materials (in this study, Si under green illumination), laser pulsing leads to a non-uniform temperature distribution at the apex. On comparing the experimentally determined field/temperature distributions with the theoretically expected absorbed light, we concluded that the non-uniform temperature distribution under green laser is due to the non-uniform light absorption close to the apex. Also, the experimental observation of the fingerprint of non-uniform absorption in green proves that heat does not have time to diffuse across the tip cross-section before it triggers evaporation.

3. *The effect of amorphized shell (due to FIB) on absorption properties of the a-priori non-absorbing materials* (Section 3.3). Using GaN as an example, we experimentally verified that the α-GaN has a much higher absorption and lower thermal diffusivity as compared to c-GaN. We propose that in such materials the amorphized shells play a major role in light absorption, hence, facilitating laser assisted field evaporation. However, this layer also modifies the thermodynamics of the tip. For example, in GaN, the presence of this layer also leads to strong one-sided absorption. This leads to asymmetrical apex shapes and hence artefacts in the reconstructed data. Furthermore, our initial results on the Si samples with varying amorphized shell thickness suggest that thicker amorphized shell in absorbing materials lead to a lower mass resolution. We expect that this is due to the higher absorbance and the lower thermal diffusivity of these layers. However, a more detailed study is required to understand the impact of this layer on the thermal properties of absorbing samples. In summary, the optimization of the amorphous shell thickness is necessary to optimize the L-APT analysis.

Deriving the apex temperature of a nanoscaled semiconducting field emitter illuminated by a femtosecond pulsed laser

A Kumar[1,2], J Bogdanowicz[1], J Demeulemeester[1], J Bran[1,2], D Melkonyan[1,2], C Fleischmann[1] and W Vandervorst[1,2]

[1]Imec vzw, Kapeldreef 75, Heverlee – 3001, Belgium

[2] Instituut voor Kern- en Stralingsfysica, KU Leuven, Celestijnenlaan 200D, B-3001 Leuven, Belgium

Journal of applied physics, under review

Abstract

Evaluating the thermal processes occurring inside an illuminated nanoscale semiconducting tip is of the utmost importance for the physical understanding of laser assisted Atom Probe Tomography (L-APT). In this paper, we present a new methodology to evaluate the temperature at the apex of the tip using L-APT. The method is based on the known exponential dependence of the probability for field evaporation as a function of the temperature and the electric field at the apex. We use this method to gain insight into the thermal response of a Si specimen as a function of doping, laser power and initial temperature.

Introduction

The thermal effects induced by the light interaction with a nanometer scale tip are of interest for many metrology techniques such as photo-assisted scanning tunneling microscopy (STM), laser assisted Atom Probe Tomography (L-APT), Atomic Force microscope-assisted surface modification and nanofabrication, apertureless near-field optical microscopy (a-SNOM) etc. On the one hand techniques like STM, a-SNOM primarily use a pulsed laser on a tip to enhance the resolution, sensitivity or the scope of application (e.g. cancer cell photo-thermal therapy [1]) using optical phenomena like nanoscopic scattering, second harmonic generation, single- or two-photon fluorescence [2–4]. However the laser-tip interaction in these techniques also induces heating in the substrate and the tip, which might adversely affect the quality of the measurement. On the other hand, in techniques like L-APT, a pulsed laser is used to generate nanosecond thermal pulses in the tip [5]. This has helped to broaden the scope of materials that can be successfully analyzed, towards semiconductors and insulators [6]. In L-APT time-controlled atom-by-atom evaporation is achieved by a combined effect of a constant extraction voltage and a laser pulse. The field induced at the tip apex due to the applied voltage lowers the potential barrier for atom evaporation, while the laser pulse induces a nanosecond thermal pulse which provides the atom the necessary energy to cross the barrier. In combination with time-of-flight mass spectrometry, it provides three-dimensional atomic distributions, with elemental identification and near atomic resolution (0.5Å – 3Å) [7]. The relation between the laser characteristics (power, wavelength, pulse length etc.) and the resulting temperature at the apex of the tip is key for a quantitative description of the role of the laser pulse and its effect on spatial and mass resolution [8], quantification [9,10], surface migration [11] etc. However a direct correlation between the two is not straightforward to predict. This is due to the fact that the tip represents a sub-wavelength object and concurrent processes of absorption, excited carrier generation, carrier migration and tip cooling occur on extremely short time scales (picosecond-nanosecond). That said, L-APT is also uniquely suited for studying the thermal effects of the laser because the probability of emission of an atom in L-APT is a strong function of the thermal response of the illuminated tip [12]. This implies that the rate at which atoms emit can act as a probe for the thermal response of the tip. Methods to quantify temperatures at the apex of a

biased tip have been proposed using a combination of laser assisted and high voltage APT [13,14]. Unfortunately, they rely on the propagation of high-voltage pulses through the tip, which is nearly impossible for semiconductors and insulators without excessive dispersion [15], thereby, limiting the accuracy of these measurements on semiconductors and insulators.

In this paper, we present a direct method to determine the temperature at the apex of a semiconducting tip under laser illumination using L-APT. The method is based on the physics of the field evaporation process, more specifically, the known exponential dependence of the evaporation flux ϕ on the apex temperature T. We apply this method to Si samples with different doping levels and show that the temperature reached under green laser pulsing varies linearly with laser power. Furthermore the temperature reached is independent from the doping level or tip shape, pointing towards a negligible effect of non-linear absorption processes, background doping and tip shape. We also used the method to gain insight into the effect of the initial temperature on the thermal response of a Si tip under laser illumination.

2. Theoretical framework and experimental procedure

When submitted to a very high electric field F (~V/nm), an atom located at a surface has a finite probability to transition from its atomic to its ionic state and subsequently leave the surface. This phenomenon, called field evaporation, is explained by the lowering of the potential barrier Q for ionization as a result of the applied electric field. Quantitatively, the probability of this transition is typically modeled by a Maxwell-Boltzmann distribution of the velocity of the atoms at the surface and can be written in the form of an Arrhenius equation [12], i.e.

$$\phi = Aexp\left(\frac{-Q(F)}{K_B T}\right) \tag{3.11}$$

where ϕ is the observed flux in atoms/pulse, K_B is Boltzmann constant and A is the field-evaporation pre-exponential. Eq. (3.11) states that any reduction in barrier height or increase in temperature will lead to a corresponding exponential increase in evaporation flux. Looking more specifically at the impact on the flux of a changing barrier height, we

readily obtain by calculating the first derivative of (3.11) that

$$\frac{dln(\phi)}{dQ(F)} = \frac{-1}{K_B T} \tag{3.12}$$

Following eq. (3.12), it is clear that the temperature of an emitting surface can directly be accessed by varying the barrier height and measuring the corresponding change in flux. To apply this principle to L-APT, it must be reminded that, during an experiment, the barrier height is controlled by an applied DC voltage V. The relation between Q and V can be derived as follows. Kreuzer and Nath proposed a scaling law [16] between Q and F based on the charge exchange model of field evaporation [17] (Eq. 3.13).

$$Q(F) = \left[\sqrt{1 - \frac{F}{F_0}} + \frac{F}{2F_0} ln \left(\frac{1 - \sqrt{\left(1 - \frac{F}{F_0}\right)}}{1 + \sqrt{\left(1 - \frac{F}{F_0}\right)}} \right) \right] \times Q_0 \tag{3.13}$$

where Q_0 is the potential barrier at zero field, F_0 is the field required for evaporation at 0 K and F/F_0 is known as the field fraction (FF). Since the field at the apex is proportional to the applied voltage [18], F/F_0 is equal to V/V_0 (known as voltage fraction (VF)), where V_0 is the voltage required for field evaporation at 0 K. Eq. (3.13) can then be written as

$$Q(F) = \left[\sqrt{1 - VF} + \frac{1}{2}(VF) ln \left(\frac{1 - \sqrt{(1 - VF)}}{1 + \sqrt{(1 - VF)}} \right) \right] \times Q_0 \tag{3.14}$$

Eq. 3.14 can now be used to calculate the barrier height for a given voltage. The only unknowns are VF and Q_0.

To calculate the VF, determination of V_0 is required. The latter can be determined experimentally by calculating the ordinate of the curve between voltage as a function of laser power at constant flux (**Fig.** 3.23(A)) [19]. However V_0 is geometry dependent and is different for every tip (**Fig.** 3.23(A)), thereby making it necessary to pre-determine it for every sample. An elegant alternative would be to use the charge state ratios (CSR)[2] to determine the VF as the relation between the two is geometry independent. The geometry independence stems from the fact that the CSR is only a function of the field on the surface [20]. Indeed,

[2]CSR is defined as $(Si^{i+}/\Sigma Si)*100$, where Si^{i+} (i=1, 2) is the measured number of counts of Si^{i+} ions.

D.R. Kingham [20] theoreticized that the formation of singly/doubly charged ions relies on the tunneling probability of electrons from the evaporated ion back into the tip and scales with electric field. Considering that F_0 is constant for a given material, the dependence of CSR on FF (or VF) is also independent of geometry. Indeed, as shown in figure 3.23(b), the same CSR as a function of VF is obtained on different tips. The dependence of CSR on VF can be determined experimentally using the method in ref [19] and is illustrated in figure 3.23. In this paper, these curves will be referred as calibration curves. In summary, to calculate Q, it is required to determine the V_0 value and the corresponding calibration curve (for a particular material) only once. For all subsequent measurements, the observed CSR at each applied voltage can be used to calculate the VF and in turn the barrier height using eq. (3.14).

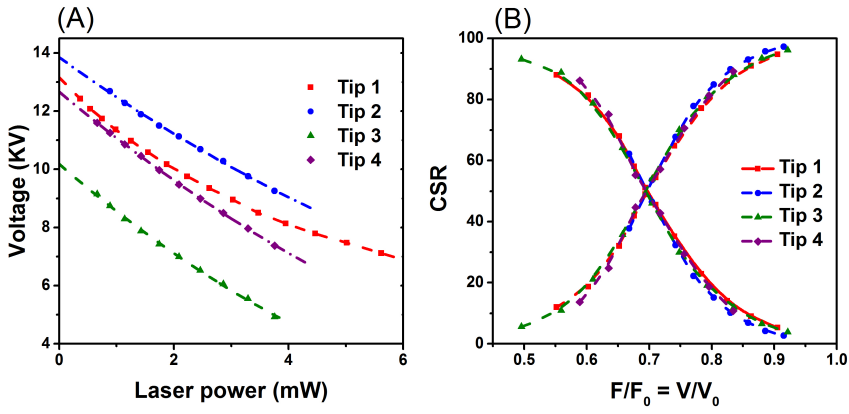

Figure 3.23 – (a) Experimental determination of V_0 for different tips. The dependence of CSR on VF can now be determined by plotting the CSR observed at each applied voltage as a function of V/V_0 (1(b)). As can be seen V_0 is geometry dependent but the CSR is independent of the geometry

Concerning Q_0, values from 5.03 – 6.2 eV calculated experimentally as well as theoretically have been reported in literature [21–23]. The temperatures mentioned in this paper were calculated using a value of 5.86 eV, observed from first principle molecular dynamic simulation performed in ref [23]. The propagated error due to Q_0 on the derived temperature value is discussed in Section 3.1.

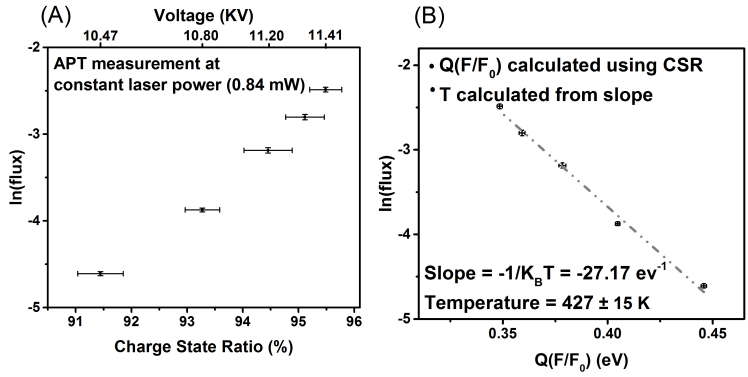

Figure 3.24 – Summary of the proposed temperature measurement technique. (A) L-APT analysis is performed at constant laser power and the change in flux is measured as a function of applied voltage (top x axis). The CSR measured at each voltage is then used to derive the variation in flux as a function of CSR (bottom x axis). (B) After translating CSR into V/V_0 using fig. 3.23(B) and then into Q using eq. 3.14, the flux is plotted as a function of Q. To access the temperature, linear regression is then used to calculate the slope between ln(flux) and Q.

To summarize, the mathematical basis of the technique developed in this paper is

$$T = \frac{-1}{K_B} \times \frac{\overbrace{\frac{d(Q)}{d(VF)}}^{Eq.\,3.14}}{\underbrace{\frac{d(ln(\phi))}{d(CSR)}}_{L-APT\,measurment} \times \underbrace{\frac{d(CSR)}{d(VF)}}_{Calibration\,curve}} \tag{3.15}$$

In practice, the temperature value at the apex can be derived by running an L-APT measurement at constant laser power and determining the variation in flux as a function of applied voltage (**Fig. 3.24(A) black**). Each applied voltage corresponds to a field at the apex and hence to a unique CSR (**Fig. 3.24(A) red**). The obtained CSR at each measurement point can then be used to calculate the VF using pre-determined calibration curves (**Fig. 3.23(b)**). Subsequently, the thus determined VF values are used to calculate the barrier height using Eq. 3.14 (**Fig. 3.24(B)**). Finally, on combining the Q(VF) values with the corresponding flux data (ln (ϕ)), the temperature at the apex can be derived from the slope of the linear regression [24] of the (ln (ϕ)) vs Q plot [eq. 3.12]. In the example shown in figure 3.24(B), a temperature value of

427±15 K was obtained for a laser power of 0.84 mW and a wavelength of 515 nm incident on a Si tip.

Please note, all L-APT measurements mentioned in this paper were done on a Laser Assisted Wide Angle Tomographic Atom Probe (LAWATAP) from CAMECA using a femtosecond pulsed laser (515 nm wavelength, 400 fs pulse length). The tips were prepared by the lift out method and sub-sequential annular Focused Ion Beam (FIB) milling [25], on a FEI NOVA-600 dual beam tool.

3. Results and discussion

In this section we will first discuss the error on the derived temperature values (Section 3.1). Thereafter, we will apply the method on Si specimens to (1) sample the (potential) effects of dopant type and concentration as these, for instance, could lead to enhanced absorption due to free carrier absorption (Section 3.2) and (2) to gain insight into the heating of the specimen initially kept at two different base temperatures (Section 3.3).

3.1. Accuracy of the derived temperature values

Concerning the error of the determined temperatures, Eq. 3.15 already shows a major advantage of the proposed method, i.e. it only implies first derivatives. In other words, it is independent from the absolute values of most unknown parameters such as the pre-exponential constant A and absolute values of $\ln(\phi)$, which therefore keeps the systematic error rather low. In more detail, the error on the temperature values (ΔT/T) depends on the error of the slope of $\ln(\phi)$ as a function of Q(VF) and is equal to Δs/s, where s is the slope. The error on the slope is in turn a function of the error on the Q(VF) and $\ln(\phi)$. The impact of the two was modeled using a Monte Carlo approach (**Fig. 3.25**). To quantify the ΔT/T, each value of $\ln(\phi)$ and Q was randomly changed within a defined maximum error, and the resulting temperature value was calculated. This process was repeated 10^4 times to generate a temperature probability distribution. ΔT/T was then calculated from the resulting probability distribution as $\frac{\Delta T}{T} = \frac{2\sigma}{\mu}$, where σ is the standard deviation and μ is the mean of the distribution. It was observed that the relative error on Q and $\ln(\phi)$ impacts ΔT/T almost linearly in the simulated range. However, the error on Q(VF) has a bigger impact on the ΔT/T as compared to the

error on ln(ϕ). The expected error range on both Q and ln(ϕ) is discussed in more detail below.

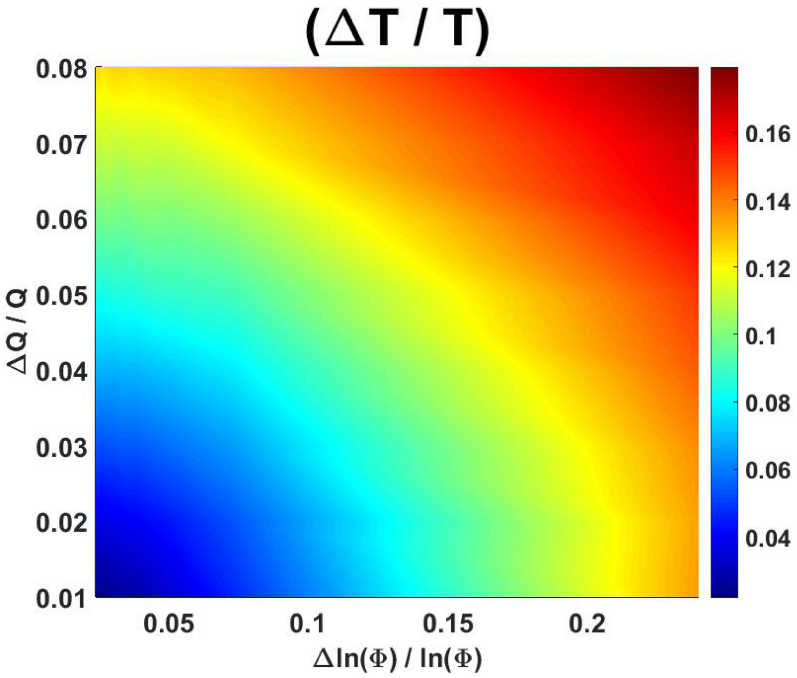

Figure 3.25 – Relative error on the derived temperature values as a function of relative error on ln(ϕ) and Q.

The sources of error (both random and systematic) on the barrier height and flux are:

$$\Delta ln(\phi) = \underbrace{\left|\frac{\partial(ln(\phi))}{\partial(\phi)}\right| \times \Delta\phi}_{systematic\,\&\,random\,error} \tag{3.16}$$

$$\Delta Q = \underbrace{\left|\frac{\partial(Q)}{\partial(VF)}\right| \times \Delta VF}_{systematic\,\&\,random\,error} + \underbrace{\left|\frac{\partial(Q)}{\partial(Q_0)}\right| \times \Delta Q_0}_{systematic\,error} \tag{3.17}$$

In this paper, VF is derived from the CSR hence, ΔVF is equal to

$$\Delta VF = \underbrace{\left|\frac{\partial(VF)}{\partial(CSR)}\right| \times \Delta CSR}_{random\,error} + \overbrace{\left|\frac{\partial(VF)}{\partial(V_0)}\right| \times \Delta V_0}^{systematic\,error} \tag{3.18}$$

Regarding the systematic errors, from equation 3.16, 3.17 and 3.18 the main sources are the experimentally determined flux, erroneous modeling of Q(VF), V_0 and Q_0. A detailed discussion on the effect of these systematic error on the derived temperature value is present in the main text (Section 3.1.2). In summary, it can be shown that the main source of systematic error on the derived temperature values is the Q_0. From Eq. 3.15, the inaccuracy on the temperature value due to Q_0 can be calculated as:

$$\Delta T = T' \times \frac{\partial}{\partial(Q_0)}\left(\frac{\partial(Q(VF))}{\partial(VF)}\right) \times \Delta Q_0 \implies \frac{\Delta T}{T} = \frac{\Delta Q_0}{Q_0} \tag{3.19}$$

where

$$T' = \frac{1}{K_B \times \frac{d(ln(\phi))}{d(CSR)} \times \frac{d(CSR)}{d(VF)}}$$

The reported values of Q_0 [21–23] in scientific literature vary by ~8 % hence, the inaccuracy on T due to Q_0 is $\Delta T = 0.08 \times T$.

Concerning the random error on the derived temperature value, it originates from the statistical noise on the two experimental parameters, Φ and CSR. Obviously, increasing the number of measured atoms reduces this random error. In more detail, the flux can be modeled as a Poisson process [26] and hence, the random error on the flux can be obtained as the counting statistic error on a Poisson distribution, i.e. $\phi\sqrt{\frac{\phi}{N}}$, where N is the number of atoms per data point. The statistical error on the CSR was calculated by dividing the collected atoms into smaller blocks of atoms. The error on CSR was then calculated as the standard deviation on the average CSR of individual blocks. In addition, the uncertainty will also depend on the range of CSR values used to determine the temperature, due to the non-linear relation between CSR and VF (**Fig. 3.23(B)**). When converting CSR to VF values, error propagation leads to higher uncertainties at the intervals where VF is less sensitive to changes in CSR, i.e. CSR (Si^{2+}) >95% and CSR(Si^{2+}) < 5%. The temperature values were calculated by collecting 30 000 – 50 000 atoms. Using the

counting statistic error on a Poisson distribution, the relative error on $\ln(\phi)$, i.e. $\frac{\Delta ln(\phi)}{ln(\phi)}$, is between ~ ±1x10^{-5} – ±8x10^{-4}. The relative error on CSR $\left(\frac{\Delta CSR}{CSR}\right)$ for a block size of 2500 – 5000 atoms was evaluated between ~ ±0.004 – ±0.01. Using error propagation theory, this leads to a $\frac{\Delta Q(VF)}{Q(VF)}$ of ~ ±0.025 - ±0.05. *From* **Fig.** *3.30, the above mentioned error ranges would result in a precision of ~ ±0.04 – ±0.1 i.e. a variation of ~12-30 K for an estimated temperature of 300 K.*

3.2. Effect of doping and tip shape

To sample the (potential) effects of dopant type and concentration, temperature measurements were done for four Si samples, of which two were n-type doped (4×10^{14} atoms/cm^3 and 5×10^{19} atoms/cm^3) and the other two were p-type doped (3×10^{15} atoms/cm^3 and 10^{19} atoms/cm^3).

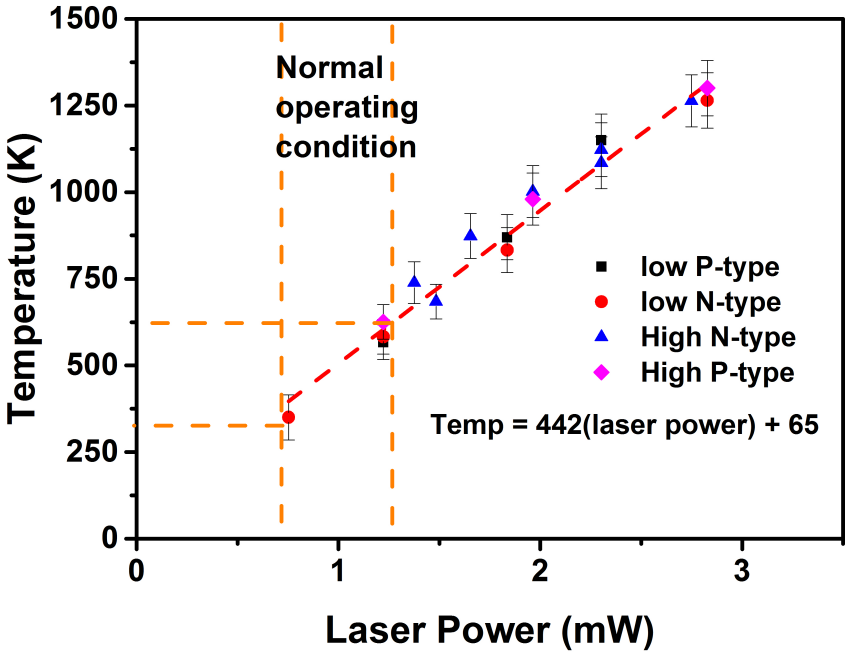

Figure 3.26 – Temperature as a function of laser power for tips with different n- and p-type doping levels. For normal operating conditions (10-20 % of the energy provided by laser for field evaporation) a temperature between 300 K and 550 K was calculated and temperatures ~1250 K were calculated for the highest laser power.

As shown in **Fig 3.26** , the obtained temperature values ranging from ~300 K to ~1250 K for laser powers between 0.7 mW – 3 mW, are completely independent of the doping level and type for the different tips implying that free carrier absorption is not an important parameter in our experiments. The statistics linked to the number of atoms (~30 000) collected for each measurement, lead to a $\frac{\Delta T}{T} \sim 0.06$ as presented in **Fig 3.26** . *Under normal APT conditions, i.e. at low laser powers (~10-20 % energy is provided by the laser for field evaporation), we obtain moderate temperatures (300 K-550 K) comparable to values reported in literature for metals [5,11]. At high laser power, temperatures close to the melting point of Si are reached (~1250 K).* Such high temperatures may be explained by the fact that at those powers the laser provides nearly 60 % of the energy for field evaporation i.e. thermal energy, implying that the evaporation is essentially thermal. Interestingly, the method as applied in **Fig 3.26** also helps deepen our insight into the physics of laser-assisted field evaporation. **Fig 3.26** indeed shows that the temperature varies linearly (T=$442 \times P + 65$) over the whole range of laser power (P) and is independent of the tip shape and doping. The obtained linear relationship points towards a negligible effect of non-linear processes like multiphoton absorption, free-carrier absorption or temperature-dependent heat diffusion. Furthermore, the limited impact of tip shape seems to imply a minor or non-existent impact of the a priori different absorption cross-section for the different tips due to their variable tip shape.

3.3 Thermal response of the specimen

In this section we will use the described method to gain insight into the thermal response of a Si tip, initially kept at two base temperatures of 20 K and 100 K respectively. Figure 3.27(A) shows that at the same laser power and barrier height (i.e. at same electric field), a lower flux is obtained for the specimen kept at a base temperature of 20 K. A similar impact of the base temperature, i.e. a lower flux at constant field and laser power, has been previously observed for a number of materials like W, Si, Ge [27,28]. This implies that the temperature at the apex (after laser pulsing) for the specimen initially at 20 K is lower as compared to the one at 100 K. On calculating the temperature at the apex, a difference of 89±12 K was obtained between the two tips mirroring the difference in the base temperature value (**Fig. 3.27(B)**). However, the observed difference in derived temperature values cannot be explained using heat capacity of bulk materials. In detail, the heat capacity (C_p) decreases with decreasing

temperature and varies as $C_p \propto T^3$ at low temperatures [29]. Hence, the energy required to heat Si from 20 K or 100 K to ~500 K is similar, i.e.

$$\left(E_{20-500} = \int_{20}^{500} C_P dT\right) \approx \left(E_{100-500} = \int_{100}^{500} C_P dT\right) \tag{3.20}$$

Eq. 3.20 implies that, the difference in the temperature reached after laser pulsing (assuming the same incident laser power) in sample initially kept at 20 K or 100 K should be much less than the difference in base temperatures.

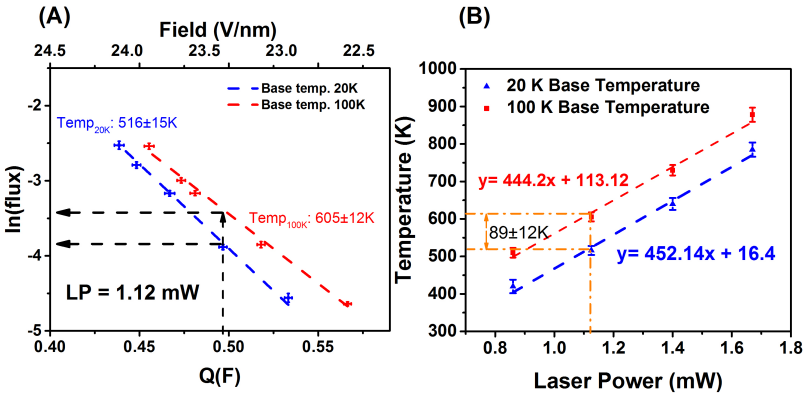

Figure 3.27 – (A) Flux as a function of barrier height (bottom X-axis) and field (top X-axis) at constant laser power (1.12 mW) at 20 K (blue) and 100 K (red) base temperature. A lower flux is observed for the same barrier height at 20 K. (B) Derived temperature values as a function of laser power at 20 K (blue) and 100 K (red). The difference between the two at the same laser power is equal to the difference in base temperature. The temperature values were derived by collecting 50 000 atoms to improve accuracy.

The inconsistency between theory and experiment may imply that the thermal properties of a biased nanoscaled tip are different from its bulk counterpart. Indeed, for nanowires (or in structures with high aspect ratios), $C_p \propto T$ [30], at low temperatures, i.e. the difference in temperature reached after laser pulsing in nanowires (initially at 20 K and 100 K) will be higher as compared to bulk materials. Moreover in our specimens, the outer shell (~ 5 nm) is amorphized due to Ga ion beam damage during sample preparations. Amorphized Si is known to have higher light absorption [31] and less severe dependence of C_p on T [32] therefore, further modifying the optical and thermal properties of

the APT sample as compared to bulk materials. Hence, a more detailed study is required to understand the optical and thermal properties of APT samples to understand its thermal response under laser illumination.

4. Conclusion

This work presents a method to determine the temperature of a nanoscale tip under femtosecond laser pulsing using L-APT. The method is based on measuring the variation in evaporation flux as a function of applied voltage at fixed laser power. We showed that temperatures at the apex of a Si tip illuminated with a green pulsed laser could vary between ~300 K and ~1250 K depending on the laser power. This method provides useful information into the absorption of light by biased nanoscaled specimens. For example, the observed linear increase in temperature as a function of laser power implies the negligible impact of any nonlinear phenomenon in laser absorption by Si samples. Moreover, the independence of the temperature at the apex from the tip shape suggests negligible impact of the a priori different absorption cross-section of the different tips. We also used the method to gain insight into the heating of the specimen kept at different initial base temperatures. We observed that the difference in the temperature reached after laser pulsing in the two cases was similar to the difference in the initial temperature. This observation is remarkable and cannot be explained when considering the heat capacity of bulk Si. This observation may imply that the thermal properties of biased nanoscaled specimen is different from its bulk properties and a more in-depth study is required.

The presented method is a new stepping stone in improving our understanding of the interaction of a femtosecond pulsed laser with a nanoscale object. For example in techniques like APT it gives insight into the absorption mechanisms ((non)linear), dependence on doping etc. and for techniques like a-SNOM, STM the derived temperature values can act as a benchmark for modeling the temperatures reached by a nanoscaled tip illuminated by a pulsed laser.

References

[1] Huang X, El-Sayed I H, Qian W and El-Sayed M A 2006 Cancer Cell Imaging and Photothermal Therapy in the Near-Infrared Region by Using Gold Nanorods J. Am. Chem. Soc. 128 2115–20

[2] Averbukh I S, Chernobrod B M, Sedletsky O A and Prior Y 2000 Coherent near field optical microscopy Opt. Commun. 174 33–41

[3] Zayats A V, Kalkbrenner T, Sandoghdar V and Mlynek J 2000 Second-harmonic generation from individual surface defects under local excitation Phys. Rev. B 61 4545–8

[4] Kawata Y, Xu C and Denk W 1999 Feasibility of molecular-resolution fluorescence near-field microscopy using multi-photon absorption and field enhancement near a sharp tip J. Appl. Phys. 85 1294–301

[5] Vella A 2013 On the interaction of an ultra-fast laser with a nanometric tip by laser assisted atom probe tomography: a review Ultramicroscopy 132 5–18

[6] Seidman D N 2007 Three-Dimensional Atom-Probe Tomography: Advances and Applications Annu. Rev. Mater. Res. 37 127–58

[7] Kelly T F and Miller M K 2007 Atom probe tomography Rev. Sci. Instrum. 78 031101

[8] Bunton J, Olson J, Lenz D and Kelly T 2008 Investigation of Performance-Influencing Factors in Pulsed Laser Atom Probe Microsc. Microanal. 14 1238–9

[9] Kumar A, Komalan M P, Lenka H, Kambham A K, Gilbert M, Gencarelli F, Vincent B and Vandervorst W 2013 Atomic insight into Ge1−xSnx using atom probe tomography Ultramicroscopy 132 171–8

[10] Riley J R, Bernal R A, Li Q, Espinosa H D, Wang G T and Lauhon L J 2012 Atom Probe Tomography of a-Axis GaN Nanowires: Analysis of Nonstoichiometric Evaporation Behavior ACS Nano 6 3898–906

[11] Cerezo A, Smith G D W and Clifton P H 2006 Measurement of temperature rises in the femtosecond laser pulsed three-dimensional atom probe Appl. Phys. Lett. 88 154103

[12] Tsong T T 2005 Atom-Probe Field Ion Microscopy: Field Ion Emission, and Surfaces and Interfaces at Atomic Resolution (Cambridge University Press)

[13] Kellogg G L 1981 Determining the field emitter temperature during laser irradiation in the pulsed laser atom probe J. Appl. Phys. 52 5320–8

[14] Marquis E A and Gault B 2008 Determination of the tip temperature in laser assisted atom-probe tomography using charge state distributions J. Appl. Phys. 104 084914
[15] Gault B, Vurpillot F, Vella A, Gilbert M, Menand A, Blavette D and Deconihout B 2006 Design of a femtosecond laser assisted tomographic atom probe Rev. Sci. Instrum. 77 043705
[16] Kreuzer H J and Nath K 1987 Field evaporation Surf. Sci. 183 591–608
[17] Gomer R and Swanson L W 1963 Theory of Field Desorption J. Chem. Phys. 38 1613–29
[18] Forbes R G, Edgcombe C J and Valdrè U 2003 Some comments on models for field enhancement Ultramicroscopy 95 57–65
[19] Mazumder B, Vella A, Gilbert M, Deconihout B and Schmitz G 2010 Reneutralization time of surface silicon ions on a field emitter New J. Phys. 12 113029
[20] Kingham D R 1982 The post-ionization of field evaporated ions: A theoretical explanation of multiple charge states Surf. Sci. 116 273–301
[21] Lyo I-W and Avouris P 1991 Field-Induced Nanometer- to Atomic-Scale Manipulation of Silicon Surfaces with the STM Science 253 173–6
[22] Miskovsky N M, Wei C M and Tsong T T 1992 Field evaporation of silicon in the field ion microscope and scanning tunneling microscope configurations Phys. Rev. Lett. 69 2427–30
[23] Ono T and Hirose K 2004 First-principles study on field evaporation for silicon atom on Si(001) surface J. Appl. Phys. 95 1568–71
[24] York D, Evensen N M, Martínez M L and Delgado J D B 2004 Unified equations for the slope, intercept, and standard errors of the best straight line Am. J. Phys. 72 367–75
[25] Miller M K, Russell K F, Thompson K, Alvis R and Larson D J 2007 Review of Atom Probe FIB-Based Specimen Preparation Methods Microsc. Microanal. 13 428–36
[26] De Geuser F, Gault B, Bostel A and Vurpillot F 2007 Correlated field evaporation as seen by atom probe tomography Surf. Sci. 601 536–43
[27] Silaeva E P, Vella A, Sevelin-Radiguet N, Martel G, Deconihout B and Itina T E 2012 Ultrafast laser-triggered field ion emission from semiconductor tips New J. Phys. 14 113026
[28] Vurpillot F, Houard J, Vella A and Deconihout B 2009 Thermal response of a field emitter subjected to ultra-fast laser illumination J. Phys. Appl. Phys. 42 125502
[29] Rohlf J W 1994 chapter 14 Modern Physics from a to Z (New York: Wiley)

[30] Kittel C 2004 Chapter 18 Introduction to Solid State Physics (Hoboken, NJ: Wiley)
[31] Townsend P D 1987 Optical effects of ion implantation Rep. Prog. Phys. 50 501
[32] Mertig M, Pompe G and Hegenbarth E 1984 Specific heat of amorphous silicon at low temperatures Solid State Commun. 49 369–72

Impact of non-uniform light absorption on the shape of semiconducting field emitters in laser-assisted Atom Probe Tomography

A. Kumar[1,2], J. Bogdanowic[2], M. Gilbert[3], F. Moyon[3], C. Fleischmann[2], D. Melkonyan[1,2], L. Arnoldi[1,2], J. Houard[3], A. Vella[3], W. Vandervorst[1,2]

[1]Instituut voor Kern- en Stralingsfysica, KU Leuven, Celestijnenlaan 200D, B-3001 Leuven, Belgium

[2] Imec vzw, Kapeldreef 75, Heverlee – 3001, Belgium

[3]GPM, UMR 6634 CNRS, Université et INSA de Rouen, 76801 Saint-Etienne du Rouvray Cedex, France

To be submitted

Abstract

The (recent) introduction of laser-assisted Atom Probe Tomography (LAPT) has extended the applicability of the Atom Probe technique to semiconducting and insulating materials thereby paving the way for metrology on nanoelectronic devices. However, a detailed understanding of the interaction of the involved laser and nanoscale semiconducting tip remains elusive and yet is vital for further improving data acquisition and treatment. In this paper, we use the steady-state shape of Si tip apexes to improve our insight into the laser-tip interaction. We show with transmission electron microscopy that the apex shape of a Si tip under green (resp. infrared) illumination is non-hemispherical (resp. hemispherical). Using LAPT measurements, we then prove that the apex shape is an image of the apex temperature distribution at the time of evaporation, as induced by the laser. Comparing these experimental results with simulations of the absorbed optical power in the tip, we demonstrate that evaporation assisted by a green laser occurs before any major heat diffusion because light is resonantly absorbed close to the apex. In infrared, conversely, as resonant absorption occurs far away from the apex, heat diffuses and is uniform across the tip cross section before it reaches the apex to trigger the evaporation.

Introduction

Laser-assisted atom probe tomography (LAPT) has emerged as a promising concept for 3D-compositional metrology of nanoelectronic devices [1]. This technique can indeed provide a three-dimensional atomic distribution with chemical identification and near atomic resolution (0.5 Å – 3 Å). In LAPT, the sample atoms are removed one at a time under the combined effects of a strong standing electric field and a pulsed laser. In practice, the sample is shaped in the form of a needle with small end radius ~40-100 nm such that the electric field at the apex reaches magnitudes close to those required for field evaporation (~10-40 V/nm). The laser is then used to generate thermal pulses inside the tip and release the apex atoms one by one [2]. One of the biggest hurdles for harnessing the full potential of LAPT is the accurate three dimensional reconstruction of the acquired data. Commonly used reconstruction algorithms assume a perfectly hemispherical apex shape and use a pseudo-stereographic projection law to calculate the original positions of the evaporated atoms [3]. The assumption of a perfect hemisphere explicitly implies uniform magnification from the whole apex. In cases when the apex is non-hemispherical, the assumption leads to artefactual density variations [4] hence, leading to inaccuracies in the quantification of the measured data. Non-hemispherical apex shapes have been reported e.g. in heterogeneous and embedded samples (FinFET) [5] and in cases of strong absorption for the laser light used (e.g. Si under UV illumination) [6]. As the absorptivity is a strong function of the laser wavelength, we study in this paper its role by analyzing the impact of laser wavelength on the tip shape of a Si tip. In the first part, we study the experimental impact of green (515 nm) and IR (1030 nm) pulsed lasers on Si tips. Using Transmission Electron Microscopy (TEM), we show that the steady-state apex shape remains hemispherical in the case of a Si tip analyzed with IR light but that a small asymmetry is generated when using a green laser. Based on LAPT measurements, we then demonstrate that the non-hemispherical tip shape in green (λ = 515 nm) is due to a non-uniform temperature distribution at the apex. In the second part, we compare the experimentally measured temperature distribution to the theoretically expected spatial distribution of the absorbed light in the dielectric tip. We conclude that the non-hemispherical tip shape in green is a direct consequence of the non-uniform light absorption at the tip apex and that heat hardly diffuses before it triggers evaporation. In IR, conversely, as

light is resonantly absorbed far away from the apex, heat diffuses and is uniform across the tip cross section before it reaches the apex to trigger the evaporation.

2. Materials and Methods

In order to study the impact of laser wavelength on the apex shape of a Si tip we used a combination of LAPT and TEM. We implemented LAPT measurements to gain insight into the temperature and field distributions at the time of field evaporation across the apex, since the apex shape is a direct consequence of these distributions. The distributions were quantified using the method described in Article I. Subsequent to LAPT measurements TEM was used to analyze the apex shape of field evaporated tips. The LAPT experiments were conducted on the Laser Assisted Wide Angle Tomographic Atom Probe (LAWATAP) from Cameca at 80 K sample temperature using IR (λ = 1030 nm) and green (λ = 515 nm) illumination. The tips were prepared by the lift-out method and sub-sequential annular Focused Ion Beam (FIB) milling [7], on a FEI Helios-450 dual beam tool. TEM was performed on a Cs-probe-corrected JEOL ARM 200F equipped with a Shottky field emitter and operating at 200 kV. The 2050 Fischion on-axis rotation tomography holder was used as it can mount rod shaped samples.

3. Results and discussion

It is commonly believed that LAPT analyses of Si tips under green (λ = 515 nm) and infrared laser (λ = 1030 nm) light lead to uniform heating and hence hemispherical apex shapes [6, 9]. However**, Fig. 3.28(a)** shows that this assumption holds true for tips measured with IR, the TEM micrograph of (**Fig. 3.28(b)**) shows that a green laser actually results in a slightly asymmetric apex. Most likely the discrepancy with previous work arises from the fact that in ref 5,8 only SEM imaging was used whereas we exploit the higher resolution of TEM in **Fig. 3.28**. Note that because of their projection through the apex, these TEM micrographs do not provide information about the actual shapes of the three-dimensional apexes [10] but they still suffice to conclude on a non-uniform (resp. uniform) field distribution at the apex in Si tips analyzed by green (resp. IR) laser [11,12].

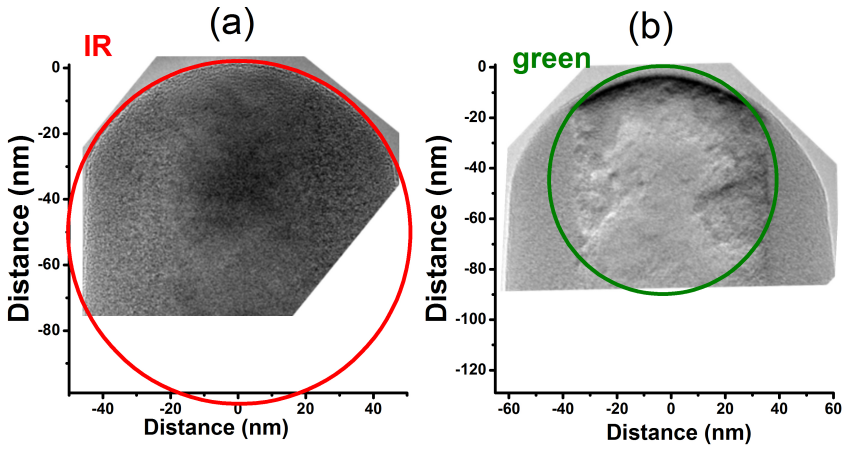

Figure 3.28 – Transmission Electron Micrograph of Si tips analyzed under (a) IR (λ = 1030 nm) and (b) green (λ = 515 nm) illumination. While analysis with an IR laser leads to a hemispherical apex, the green laser induces a non-hemispherical apex.

Inducing such a non-uniform tip shape (at steady state) can only be explained by assuming a non-uniform temperature distribution at the apex. Since the evaporation process depends on the interplay between temperature (induced by the laser pulse) and field (which is induced by the apex shape) [13], a non-uniform temperature distribution will induce a non-uniform evaporation across the tip apex leading to an asymmetrical apex shape. A steady state apex shape of the tip is achieved when the field distribution (resulting from the apex shape) counteracts the asymmetry in the temperature distribution such that the evaporation rate over the whole apex is constant. As such, the asymmetric apex of **Fig. 3.28(b)** demonstrates the non-uniform apex heating induced by the green laser. Conversely, the hemispherical apex shape under IR illumination (**Fig. 3.28(a)**) implies that the temperature distribution was uniform and that the electric field at the surface will be uniform. In other words, **Fig. 3.28(a)** implies univocally that IR light heats up the apex uniformly, i.e. the apex reaches an equilibrium state where the field is uniform.

The conclusions derived from these observations can be confirmed experimentally by measuring the field distribution across the apex of the tip. The field distribution can be measured using the Charge State Ratio (CSR). CSR is defined as $Si^{i+}/(\Sigma Si)$, where Si^{i+} (i=1, 2) is the measured

number of counts of Si^{i+} ions. Considering the now well-known Kingham curves for post ionization [14] which link the electric field F at the apex to the CSR, the field distribution across the apex of the tip is deduced (red line in **Fig. 3.29(A)**).

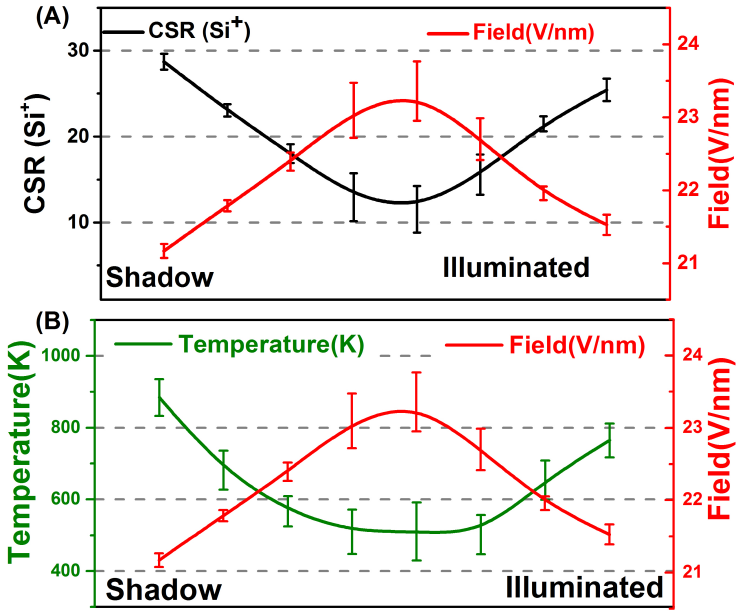

Figure 3.29 – (A) CSR (Si^{+}) distribution (black) and field distribution (red) across the apex of a tip analyzed in green ($\lambda = 515$ nm) in LAPT. (B) Temperature distribution (green) calculated using the method described in ref 7 and field distribution (red) across the apex of a tip analyzed in green in LAPT. The right region corresponds to the illuminated side while the left region is the shadow side of the apex. The value at each point is the mean value in a vertical selection of the detector. The error bar is the standard deviation in the vertical selection.

Indeed, the field distribution along the direction of propagation of the green laser is non-uniform, with lower field measured on the illuminated and shadow sides and a maximum in the center of the tip. To verify if this field distribution is a result of a non-uniform temperature distribution, the temperature distribution across the apex was quantified using the method described in Article I, i.e. from the slope $\frac{d(ln(\phi)}{dV}\Big|_P$ of the flux ϕ vs voltage V characteristic during an L-APT measurement at a fixed laser power. Indeed, as can be seen in **Fig. 3.29(B)**, the temperature and the field distribution have an inverse correlation. Note that even the slightly

lower field on the shadow side as compared to the illuminated side is also compensated by a slightly higher temperature. In summary, illumination of a Si tip with a green laser leads to a non-uniform temperature distribution. This non-uniformity in turn leads to a non-hemispherical steady-state apex such that the resulting field distribution compensates the effect of the non-uniform temperature distribution on the evaporation probability.

To understand the causal link between the electric field and temperature distributions of **Fig. 3.29** and the tip shape of **Fig. 3.28(b)**, we investigated how a tip transitions from a symmetric shape in IR to a non-hemispherical shape in green, looking at the temporal evolution of the emission pattern on the position-sensitive detector. More specifically, we recorded as a function of time the fraction of atoms reaching four different regions of equal detector surface area (**Fig. 3.30(b)**) when the laser of the LAWATAP is switched from IR to green. **Fig. 3.30(c)** shows that, upon changing the wavelength from IR to green, field evaporation started from the illuminated and the shadow sides of the tip apex, while hardly any atom evaporated from the central regions of the apex. With time, however, the relative number of atoms coming from the central regions increased and, after roughly 80 000 evaporated atoms, the number of atoms evaporating from each stripe equilibrated, i.e. a non-hemispherical steady-state apex shape was reached. This transition can be understood as follows. Given the initial hemispherical apex shape, the starting field is uniform across the apex [11, 12]. However, the green laser generates a non-uniform temperature distribution similar to that observed in **Fig. 3.29.** Subsequently, the hotter illuminated and shadow sides evaporate first, while the center of the apex remains untouched. This process erodes preferentially the heated regions and, as a consequence, reduces the local field in the illuminated and shadow regions. This transient stops when the electric field has the non-uniform distribution shown in **Fig. 3.29** allowing a uniform flux across the apex, i.e. when the (asymmetric) steady-state shape is reached. The same exercise was carried out in **Fig. 3.30(d)** for a tip transitioning from green to IR. As can be observed, during this transition, the evaporation initially started in the central regions of the apex and moved to the illuminated and shadow sides only after about 60 000 atoms. This can easily be explained by considering that because of the uniform heating induced by the IR laser, the emission pattern will reflect the field distribution and thus the tip shape. The asymmetrical evaporation probability (middle vs edges) is a clear indicator for the low field at the sides and thus the non-hemispherical tip shape under green.

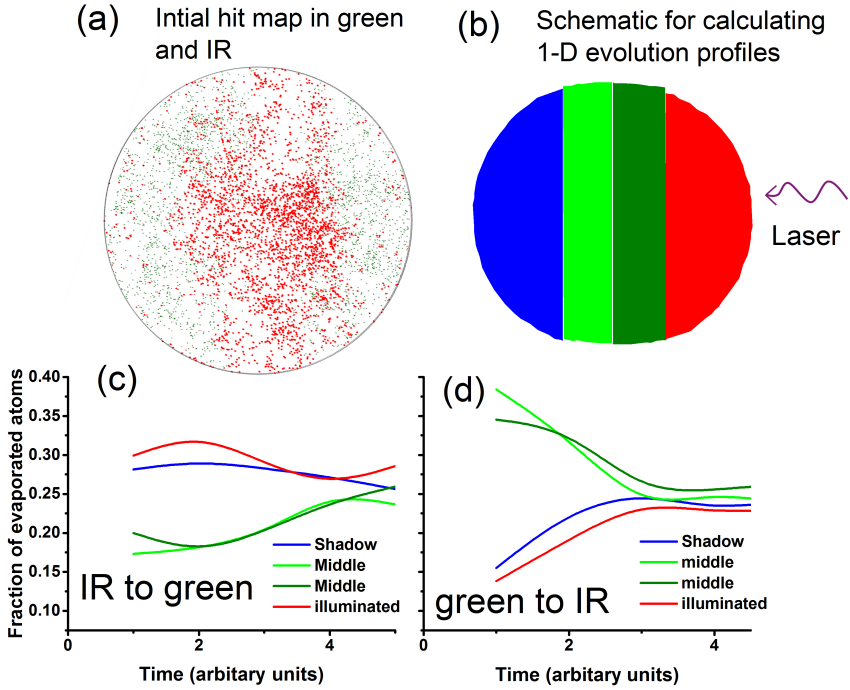

Figure 3.30 – (a) Hit positions on the detector at the start of the measurement. The red and green dots represent the hit positions in IR (1030 nm) and green laser (515 nm) respectively. (b) Schematic for calculating the 1-D temporal evolution emission pattern at different positions on the detector when the laser is switched from IR to green (shown in (c)) and from green to IR (shown in (d)). Evaporation starts on the sides (resp. the center) of the apex during a transition from IR to green (resp. green to IR). One unit along the x-axis corresponds to a block of sequentially evaporated 20000 atoms.

The above TEM and LAPT analyses provide unambiguous experimental evidence for the different heating distributions induced by the IR and green lasers. The reasons for these different laser-tip interactions go back to the fundamentals of the Si tip interaction with IR and green light, already studied in ref [9, 15, 16] and in particular to the locations along the tip where the light couples most efficiently. As shown in **Fig. 3.31(a)**, light couples inside a dielectric tip essentially at optically resonant cross-sections, i.e. where the multiple internal reflections of light interfere constructively. For light of wavelength λ_0 incident on a tip with real refractive index n, these resonant cross-sections are located at radii of approximate values $R_k \sim (2k+1)\lambda_0 / (8n)$ (k=1,2,..) [16]. Based on

just this insight, the uniform heating induced by the IR laser is rather easy to explain. The first-order (k=1) resonant cross section for IR light is indeed very far away from the apex along the shank of the tip (R_1~110 nm). The laser-induced heat needs therefore to diffuse to the apex in order to enable the evaporation process. During this diffusion the heat distribution can homogenize, leading to a uniform temperature across the tip cross-section and thus a uniform evaporation probability. When it comes to the heating induced by the green laser, the situation is quite different as a resonance is always present close to the apex (R_1~45 nm). Hence minimal heat diffusion is required to reach the tip apex and the distribution of absorbed light is reflected in the evaporation distribution. This non-uniformity can be understood by looking at the numerical simulations of the distributions of the resonantly absorbed power at the tip apex. **Fig. 3.31** shows $|P_{abs}/P_0|$, i.e. the numerically simulated absorbed power density normalized to the incident power P_0, in the XZ plane of a Si tip, X being the direction of light propagation and Z the direction of the tip axis. These calculations are done on a 3-D geometry using the discrete-dipole approximation method (ADDA v.0.79 code) [17] with an assumed refractive index 4.22+i0.06 [18]. The resulting squared relative internal electric field amplitude ($|E_{z,int}/E_0|^2$) of the coupled light from the simulation were converted to relative absorbed power using the divergence of the Poynting vector [19]. **Fig. 3.31(b)** shows a zoom on the region of the tip which can be analyzed with LAPT, i.e. the region where the conical tip has a radius < 70 nm [20]. Indeed the two-fold symmetry of the theoretical absorbed power, with a minimum at the center of the tip and maxima on the illuminated and shadow sides, clearly reflects (in opposition) the measured field distribution across the tip apex, shown in **Fig. 3.29**. Also finer details such as a slightly higher absorbed power on the shadow side than on the illuminated side, is in agreement with the asymmetric field distribution of **Fig. 3.29**. An even stronger correlation can be found by considering the evolution of the computed absorbed power and the measured temperature at the apex, as the tip erodes. For this purpose, on the experimental side, we measured the variations in the field, separately for the illuminated and shadow side, during the LAPT measurement of a Si tip analyzed at a constant flux and constant green laser power [21]. Subsequently, the recorded field values were converted to potential barrier height (Q(F)) using the scaling law proposed by Kreuzer and Nath [22] (solid lines of **Fig. 3.31(c)**). Noting that, in a constant-flux measurement, barrier height variations reflect temperature variations, the experimental curves actually indicate

the temperature variations as a function of depth (in units of increasing radius). On the theoretical side, we computed the absorbed power at the very apex for a tip [23] with a cone angle of 8° and with apex radii ranging between 40 and 60 nm to simulate the evolution of the tip shape subsequent to its erosion. The results are summarized in **Fig. 3.31(c)** and demonstrate that the variations of the theoretical absorbed power are in excellent qualitative agreement with the measured variations in barrier height and thus temperature. Any increase (resp. decrease) in the theoretically expected absorbed power indeed perfectly correlates with the experimental observation of an increase (resp. decrease) in barrier height and thus apex temperature.

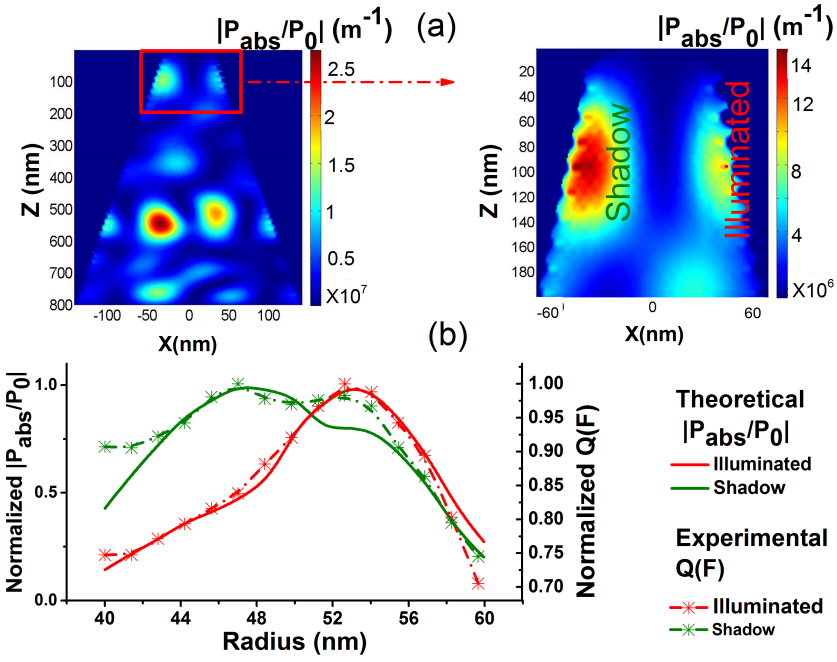

Figure 3.31 – (a) Simulated normalized absorbed power density inside an APT tip illuminated by a green laser incident normally to the tip axis with power P_0 (b) Zoom into the regions which can be analyzed in LAPT, i.e. the region with radius of the cone < 70 nm. (c) Correlation between the relative absorbed power in the XY plane (solid line) and the change in potential barrier height (Q(F)) (dashed line) during analysis to evaporate at constant flux and constant laser power. For easier comparison, the field and $|P_{abs}/P_0|$ have been normalized to their maximum values.

In summary, the non-uniform asymmetric shape under green

illumination is due to the non-uniform resonant green light absorption at the apex and the nearby location of the resonant cross-section. Due to this proximity, heat diffusion is minimal before the evaporation, which leads to minimal homogenization and thus evaporation patterns still bearing the fingerprint of the non-uniform absorption. Vice versa, in IR the distant location of the resonant absorption sites necessitates ample diffusion and thus broadening of the heat distribution leading to a hemispherical tip shape.

4. Conclusion

In this paper, using a combination of TEM and LAPT, we have shown that the apex shape of a Si tip is non-hemispherical (resp. hemispherical) when analyzed with a green (resp. IR) laser. We have demonstrated that the apex shape is a direct consequence of the temperature distribution at the apex and the location of the resonant absorption sections. Furthermore, the experimental observation of the fingerprint of non-uniform absorption in green indicates that the tip apex is not at thermodynamic equilibrium before field evaporation is triggered. The situation in IR is very different as light is absorbed far away from the apex. The IR laser-induced thermal pulse is therefore uniform across the cross-section before it reaches the emitting apex. *The conclusions in this paper point towards the presence of a non-hemispherical apex shape in most materials whenever light resonantly couples in close proximity to the apex. This in-turn signifies that the assumption of a hemispherical apex shape by most reconstruction algorithms is wrong, hence, leading to imperfect data analysis.*

References

1 M.K. Miller, A. Cerezo, M.G. Hetherington, and G.D.W.S. FRS, Atom Probe Field Ion Microscopy (Clarendon Press | Monographs on the Physics and Chemistry of Materials 52, 1996).
2 T.F. Kelly, A. Vella, J.H. Bunton, J. Houard, E.P. Silaeva, J. Bogdanowicz, and W. Vandervorst, Curr. Opin. Solid State Mater. Sci. 18, 81 (2014).
3 P. Bas, A. Bostel, B. Deconihout, and D. Blavette, Appl. Surf. Sci. 87–88, 298 (1995).
4 B. Gault, D. Haley, F. de Geuser, M.P. Moody, E.A. Marquis, D.J. Larson, and B.P. Geiser, Ultramicroscopy 111, 448 (2011).
5 J.H. Lee, Y.T. Kim, J.J. Kim, S.Y. Lee, and C.G. Park, Electron. Mater. Lett. 9, 747 (2013).
6 S. Koelling, N. Innocenti, A. Schulze, M. Gilbert, A.K. Kambham, and W. Vandervorst, J. Appl. Phys. 109, 104909 (2011).
7 A. Kumar, J. Bogdanowicz, J. Demeulemeester, julien Bran, D. Melkonyan, C. Fleischmann, and W. Vandervorst, Journal of Applied Physics, To be published, (n.d.).
8 M.K. Miller, K.F. Russell, K. Thompson, R. Alvis, and D.J. Larson, Microsc. Microanal. 13, 428 (2007).
9 A. Vella, Ultramicroscopy 132, 5 (2013).
10 L. Reimer, Transmission Electron Microscopy: Physics of Image Formation and Microanalysis (Springer, 2013).
11 D.J. Rose, J. Appl. Phys. 27, 215 (1956).
12 S. Bono and R.H. Good, Surf. Sci. 134, 272 (1983).
13 T.T. Tsong, Atom-Probe Field Ion Microscopy: Field Ion Emission, and Surfaces and Interfaces at Atomic Resolution (Cambridge University Press, 2005).
14 D.R. Kingham, Surf. Sci. 116, 273 (1982).
15 J. Bogdanowicz and W. Vandervorst, J. Quant. Spectrosc. Radiat. Transf. 146, 175 (2014).
16 J. Bogdanowicz, M. Gilbert, N. Innocenti, S. Koelling, B. Vanderheyden, and W. Vandervorst, Opt. Express 21, 3891 (2013).
17 M.A. Yurkin and A.G. Hoekstra, J. Quant. Spectrosc. Radiat. Transf. 112, 2234 (2011).
18 D.E. Aspnes and A.A. Studna, Phys. Rev. B 27, 985 (1983).
19 H. Kocer, S. Butun, E. Palacios, Z. Liu, S. Tongay, D. Fu, K. Wang, J. Wu, and K. Aydin, Sci. Rep. 5, 13384 (2015).

20 The maximum apex radius of a Si tip that can be analyzed in the LAPT at a flux of 0.01 atoms/pulse and a field reduction (FR) of ~10% - 14% is ~80nm. This apex radius translates to a cone radius ~67nm due to the truncation of the apex (figure 1(a))
21 In order to have maximum sensitivity of the electric field to any change in temperature at the apex, the LAPT measurement was done at low flux (0.01 atoms/pulse), high field reduction (FR) (10%-14%) and a low base temperature (20K). Where FR is defined as the reduction in the required electric field for evaporation, by the laser
22 H.J. Kreuzer and K. Nath, Surf. Sci. 183, 591 (1987).
23 The coupled laser power was simulated for an apex radius of ~ 35 nm, 42 nm, 50 nm, 58 nm. For every simulated apex radius, the peak power (on the illuminated and shadow side respectively) in the XY plane was chosen for every successive radius increase of 1.4 nm.

Impact of focused-ion-beam milling on sub-bandgap light absorption during laser-assisted atomprobe tomography

J Bogdanowicz[1], A Kumar[1,2], , M. Gilbert[3], J. Houard[3], A. Vella[3] and W Vandervorst[1,2]

[1]Instituut voor Kern- en Stralingsfysica, KU Leuven, Celestijnenlaan 200D, B-3001 Leuven, Belgium

[2] Imec vzw, Kapeldreef 75, Heverlee – 3001, Belgium

[3]GPM, UMR 6634 CNRS, Université et INSA de Rouen, 76801 Saint-Etienne du Rouvray Cedex, France

To be submitted

Abstract

This letter investigates the unexpected absorption of sub-bandgap light by semiconducting tips during laser-assisted atom probe tomography (LAPT) analysis. By means of a combination of transmission electron microscopy and photomodulated optical reflectance measurements, we show that the surface of a tip prepared with focused ion beam (FIB) is amorphized and subsequently absorbs electromagnetic waves with sub-bandgap photon energy. Using LAPT, we further confirm that the sub-bandgap absorptivity of a tip milled with FIB scales with the acceleration voltage used for the final tip cleaning, i.e. a thicker amorphized shell leads to more light absorption and hence more efficient heating of the tip apex. We conclude that the FIB-induced surface amorphization plays a crucial role in the laser-assisted field evaporation of materials which, if undamaged, are transparent to the used laser.

Laser-assisted atom probe tomography (LAPT) is a versatile technique with applications ranging from metals to semiconductors and insulators [1]. In LAPT, a sample in the shape of a sharp conical tip is evaporated atom by atom under the combined effects of a strong standing voltage and a pulsed laser [2]. LAPT is becoming popular e.g. in the semiconductor industry thanks to its unique capabilities for compositional analysis with virtually atomic resolution in three-dimensional nanoscale objects such as fin field-effect transistors (finFETs) [3, 4]. However, although the technique is becoming widespread, its underlying fundamental physics is still poorly understood. As a matter of fact, the actual mechanism leading the laser pulse to triggering the evaporation of atoms from the tip apex remains to be elucidated [5]. A topical example showing the limited physical insight into the laser-tip interaction is the intriguing observation that materials which are a priori transparent to the used laser can be evaporated. Indeed LAPT analysis of wide-bandgap semiconductors and insulators has been proven possible with sub-bandgap lasers [6-10]. Previous work suggests that this can be partly explained by a metallic transition which the tip undergoes when submitted to the very intense electric fields needed for evaporation [11, 12]. However, another phenomenon overlooked so far in this discussion is the role of the focused-ion-beam (FIB)-based tip preparation and, more specifically, the damage created through the interaction of the energetic Ga^+ beam with the tip material. In this paper, we investigate this effect and demonstrate that the damage induced by FIB contributes significantly to the absorption of sub-bandgap laser light. Using wurtzite GaN (bandgap E_g = 3.5 eV [13]) as a case study, we first demonstrate with transmission electron microscopy (TEM) that FIB milling results in an amorphous shell surrounding the complete tip. Photomodulated optical reflectance (PMOR) measurements then show that FIB-amorphized GaN (α-GaN) exhibits dramatically modified properties as compared to crystalline GaN (c-GaN), including a high absorptivity even at photon energies which c-GaN is transparent to. Finally, we demonstrate that the efficiency of a sub-bandgap laser to heat up the apex of an LAPT tip scales with the acceleration voltage used for the tip cleaning, i.e. with the thickness of the amorphized shell. We conclude that the FIB-amorphized shell plays a major role in the physics of laser-assisted field evaporation.

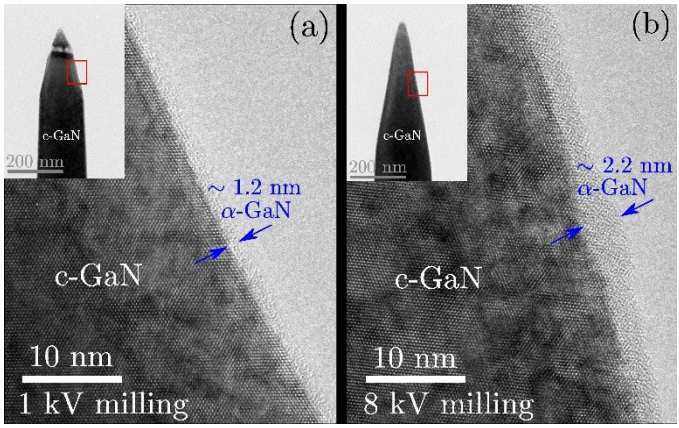

Figure 3.32 – Transmission electron micrographs of the sidewalls of GaN tips cleaned with a (a) 1 kV and (b) 8 kV Ga^+ beam in a Helios 450HP. An approximate 1.2 nm thick (resp. 2.2 nm) amorphized shell surrounds the c-GaN core of the tip cleaned at 1 kV (resp. 8 kV) voltage. Insets: low magnification micrographs of the tips. The red rectangles highlight the locations of the magnified regions. These micrographs were obtained before LAPT analysis, which explains the remaining Pt cap at the apex of the tip in inset of Fig. 1(a).

Most atom probe tips made of semiconducting or insulating materials are prepared using the micromachining capabilities of FIB [14]. To shape the sample into a conical tip as required for LAPT analysis (see e.g. insets of Fig. 3.29), an energetic (30 kV) focused Ga^+ beam is indeed used to sputter away the unwanted material. However, as a side effect, each incident Ga^+ ion also triggers a collision cascade inside the tip, which amorphizes the tip surface [15]. To minimize the thickness of the resulting amorphized shell, a lower-voltage cleaning is often used at the final stage of the tip preparation [14]. The thickness of the resulting amorphized shell indeed depends upon the acceleration voltage of the ion beam as well as on its incidence angle and on the stopping power of the sample [16, 17]. In the case of GaN considered in this paper, the TEM micrograph of **Fig. 3.32(a)** shows that a GaN tip cleaned with a low-voltage 1 kV FIB in a Helios 450HP exhibits an approximate 1.2 nm thick α-GaN shell surrounding its c-GaN core. The α-GaN shell thickness increases to 2.2 nm when the tip is cleaned at a medium-voltage (8 kV), as confirmed in **Fig. 3.32(b)**. The measured amorphized shell thicknesses are in correspondence with the range of Ga^+ ions implanted in GaN at an incidence angle of 85°, i.e. 0.8 nm and 2.3 nm respectively for 1 and 8 kV, as estimated with SRIM (Stopping and Range of Ions in Matter [17]).

To study the optical and thermal properties of the α-GaN layer, we performed PMOR measurements on blanket GaN layers. PMOR is a pump-probe technique wherein a modulated-power pump laser, if absorbed, heats up the sample and hence modifies its refractive index [18]. The pump-induced modulation of the refractive index is then measured by means of the modulated reflectance of the probe laser. Such photoreflectance techniques are commonly used in the semiconductor industry to study the damage caused by ion implantation as the pump-induced heating and hence the modulated reflectance scale with sample damage, i.e. the point defect density and thickness of the amorphized layer [19, 20]. Furthermore, whereas measurements with coincident pump-probe laser beams provide information on the local heating, collecting the PMOR signal as a function of the separation between the pump and probe laser beams also generates information on the heat diffusivity of the material [18, 21]. In this paper, the PMOR measurements were obtained at room temperature with the thermaprobe TP630XP tool, where the near-infrared (NIR) pump laser has a 790 nm wavelength (photon energy E_{ph} = 1.57 eV) and a modulation frequency ν_{mod} = 1 MHz, and the probe wavelength is 670 nm. In **Fig. 3.33**, we compare the modulated probe reflectance measured as a function of pump-probe beam distance respectively on c-GaN and α-GaN. The c-GaN sample is a blanket GaN layer grown on a sapphire substrate and the α-GaN sample refers to an area of the same sample which has been irradiated at normal incidence with a 30 kV Ga^+ FIB (0.7 pA current for 100 s, raster size 20×20 μm^2). As expected from the transparency of c-GaN to the NIR pump laser [22] ($E_{ph} < E_g$), only background noise (~0.006) is measured on the c-GaN sample, as can be confirmed e.g. from the independence of the signal from laser beam separation. Conversely, on the α-GaN area, a high modulated reflectance signal is measured, which implies that α-GaN efficiently absorbs the sub-bandgap NIR pump. Additionally, the lateral decay length L_d of the modulated reflectance measured on the α-GaN area also demonstrates the poor diffusion of the heat generated inside the sample. If heat were able to diffuse as efficiently in α-GaN as in c-GaN, the signal decay would indeed be less abrupt. This is illustrated by the interrupted line of **Fig. 3.33** which assumes a signal decay length $L_{th}^c = \sqrt{\frac{D_{th}^c}{\pi \omega_{mod}}}$ [18, 21] with the thermal diffusivity of c-GaN (D_{th}^c = 0.43 cm^2/s [23]). An estimate of the actual diffusivity of α-GaN can be derived from these PMOR measurements, keeping in mind that only a maximum value is determined as the decay length is convoluted with the

pump and probe beam shapes (i.e. gaussian beams with 0.5 μm radius each [18]). Using the decay length $L_d = 0.5\,\mu m$ of the PMOR signal measured on α-GaN, we deduce that the thermal diffusion length in α-GaN is $L^{\alpha}_{th} \leq 0.5\mu m$. This gives a maximal thermal diffusivity of α-GaN of $D^{\alpha}_{th} < 0.008$ cm^2/s [21], i.e. almost two orders of magnitude smaller than D^{c}_{th}. Such a dramatic degradation of the thermal diffusivity has also been observed in time-resolved photoreflectance measurements of FIB-amorphized Si [24].

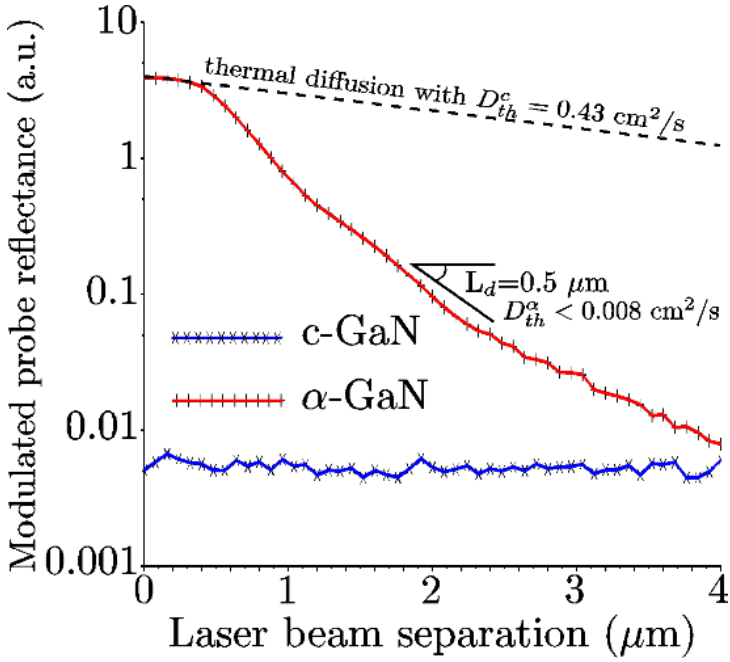

Figure 3.33 – Amplitude of the modulated probe reflectance signal measured on c-GaN (blue line) and α-GaN (red line) as a function of pump and probe beam separation. The measured signal on c-GaN, which is transparent to the NIR pump laser, is only due to background noise. α-GaN shows a high signal, indicative of efficient absorption and heating by the NIR pump laser. The lateral decay length L_d on α-GaN is much shorter than expected from thermal diffusion in c-GaN (black interrupted line), which evidences a degraded thermal diffusivity.

The PMOR measurements of **Fig. 3.33** indicate that the presence of the amorphized layer leads to the absorption of sub-bandgap laser light and thus local heating, an effect which is further sustained by the reduced thermal diffusivity of α-GaN. To demonstrate the impact of these

phenomena in case of the nanoscale conical geometry of LAPT tips, we studied the variations in temperature reached at the tip apex when tips with different α-GaN shell thicknesses are illuminated with sub-bandgap light. For this purpose, four GaN tips were milled at 30 kV. One tip was kept as milled while the others were cleaned at the respective acceleration voltages of 1 kV, 5 kV and 8 kV. According to SRIM calculations, this results in approximate amorphized shell thicknesses of respectively 0.8 nm (1 kV cleaning), 1.8 nm (5 kV cleaning), 2.3 nm (8 kV cleaning) and 5.4 nm (30 kV milling). The tips were then analyzed at 80 K with the green laser (λ=515 nm, i.e. E_{ph} = 2.4 eV) of the Laser-Assisted Wide-Angle Tomographic Atom Probe (LAWATAP) of Cameca. For the tips cleaned with 1-8 kV, we measured the apex temperature as a function of the laser power (**Fig. 3.33(a)**). The values were derived using the method described in Article I, ii.e. from the slope $\frac{d(ln(\phi)}{dV}\Big|_P$ of the flux ϕ vs voltage V characteristic during an L-APT measurement at a fixed laser power. Advantageously, the values obtained with this method are insensitive to the differences in the tip geometry induced e.g. by the different cleaning voltages [25]. However, it only gives access to the so-called normalized apex temperature, i.e. T_{apex}/Q_0 ratio, where Q_0 is the potential barrier to be overcome by a surface atom before it can evaporate without any applied electric field. For Si, Q_0=5.86 eV [26] but it is not known for GaN. As shown in **Fig. 3.34(a)**, T_{apex} as well as the heating efficiency $\varepsilon = \frac{\partial T_{apex}}{\partial P}$ both scale with the amorphized shell thickness. For instance, the tip cleaned at 8 kV heats up 43% more efficiently than the one cleaned at 1 kV, which shows the striking impact of the amorphized layer on the apex temperature. Note further that, assuming a value of Q_0 in the range of 3-5 eV, the tip apex temperature at low laser power (~ 1 mW) already is as high as 750-1250 K, which is significantly higher than the values reported for Si (~300 K [25]). In support of these high temperatures, we can mention that for the tip milled at 30 kV and illuminated at 1.1 mW, regions of localized melting can be observed (**Fig. 3.34(b)**). This tip can be understood to have reached very high temperatures as the melting point of GaN is expected to be >2500º C (this value assumes high pressure [27]).

These observations prove that the FIB-induced amorphization contributes dominantly to the absorption of green laser light by the GaN tips and hence to the final tip apex temperature. This has both experimental and theoretical consequences. First, from an experimental viewpoint, the optimization of the amorphous shell thickness can be

used advantageously to target a certain temperature and hence facilitate the evaporation. Second, from a theoretical point of view, any model attempting to describe the laser-assisted evaporation process in LAPT needs to include the critical effect of the FIB-induced amorphous layer. This is valid when the crystalline core is transparent to the laser light, as shown in this paper. This is also true in the case of an absorptive crystalline core, since the amorphized layer then provides a second independent absorption mechanism located at the tip surface, which is bound to impact the behavior of the laser-assisted evaporation significantly.

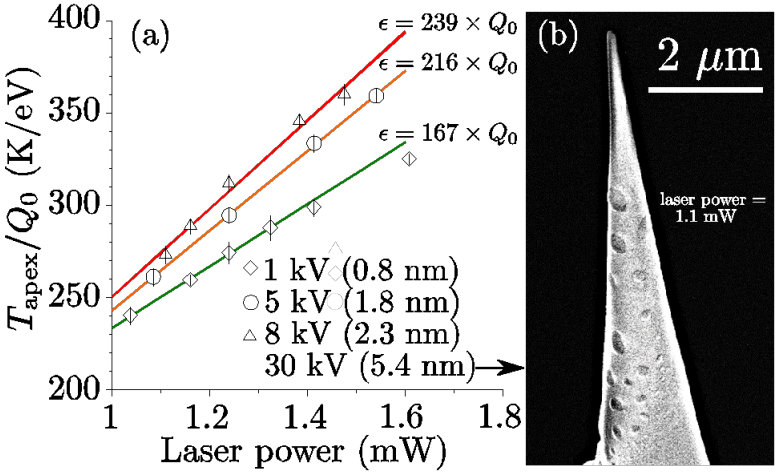

Figure 3.34 – (a) Variation in normalized apex temperature T_{apex}/Q_0 as a function of the green laser power measured on GaN tips cleaned respectively at 1 kV (diamonds), 5 kV (circles) and 8 kV (triangles) voltages. The thicknesses of the amorphized shells estimated with SRIM are indicated between brackets. The error on each normalized temperature value is given by the vertical bars. The temperature and the heating efficiency $\varepsilon = \frac{\partial T_{apex}}{\partial P}$ (K/mW) obtained from the slope of the linear fits (colored lines) both increase with the amorphized shell thickness (b) Scanning electron micrograph of a tip milled at 30 kV voltage showing evidence of melting after LAPT analysis at the low 1.1 mW green laser power.

To conclude, we have identified the impact of FIB preparation on the optical and thermal properties of GaN. We have shown that, as a result of the use of FIB to mill and clean the tip, an amorphized shell is present at the tip surface, which has a high absorptivity including at wavelengths which crystalline GaN is transparent to. This amorphized shell also shows poor thermal diffusivity. The combination of these effects

has a strong impact on the heating efficiency of LAPT tips under sub-bandgap illumination, which scales with the thickness of the amorphized shell. Estimates of the tip apex temperatures indicate very high values consistent with the observation that tips milled at a high voltage, i.e. with a thick amorphized shell, even show evidence of melting after low laser power illumination. We conclude that FIB-induced amorphization plays a dominant role in the unexpected absorption of sub-bandgap light and hence in the possibility for LAPT analysis of a priori transparent semiconducting and insulating materials. Its effect therefore should be included in any theoretical description of the evaporation process in LAPT.

Acknowledgments

The authors would like to thank Dr. Y. Saripalli and the GaN team of IMEC for the GaN sample as well as the Structural Analysis team of IMEC for the transmission electron micrographs.

References

[1] Y. Amouyal and G. Schmitz, MRS Bulletin 41, 13-18 (2016)

[2] B. Gault, F. Vurpillot, A. Vella, M. Gilbert, A. Menand, D. Blavette, and B. Deconihout, Review of Scientific Instruments, 77, 043705 (2006).

[3] M. Gilbert, W. Vandervorst, S. Koelling, A.K. Kambham, Ultramicroscopy 111, 530-534 (2011)

[4] D.J. Larson, T.J. Prosa, D.E. Perea, K. Inoue and D. Mangelinck, MRS Bulletin 41, 30-34 (2016)

[5] T. F. Kelly, A. Vella, J. H. Bunton, J. Houard, E. P. Silaeva, J. Bogdanowicz and W. Vandervorst, Current Opinion in Solid State and Materials Science 18, 81–89 (2014).

[6] L. Arnoldi, E. P. Silaeva, A. Gaillard, F. Vurpillot, I. Blum, L. Rigutti, B. Deconihout, and A. Vella, Journal of Applied Physics 115, 203705 (2014)

[7] R. Agrawal, R. A. Bernal, D. Isheim, and H. D. Espinosa, Journal of Physical Chemistry C, 115, 17688–17694 (2011)

[8] E. A. Marquis, N. A. Yahya, D. J. Larson, M. K. Miller, R. I. Todd, Materials Today, 13, 34-36 (2010)

[9] A. Vella, B. Mazumder, G. Da Costa, and B. Deconihout, Journal of Applied Physics, 110, 044321 (2011)

[10] D. Santhanagopalan, D. K. Schreiber, D. E. Perea, R. L. Martens, Y. Janssen, P. Khalifah, Y. S. Meng, Ultramicroscopy, 148, 57–66 (2015)

[11] E. P. Silaeva, M. Karahka, H.J. Kreuzer, Current Opinion in Solid State and Materials Science, 17, 211–216 (2013)

[12] E. P. Silaeva, L. Arnoldi, M. L. Karahka, B. Deconihout, A. Menand, H. J. Kreuzer, and A. Vella, Nano Lett., 14, 6066–6072 (2014)

[13] I. Vurgaftman, J. R. Meyer, and L. R. Ram-Mohan, Journal of Applied Physics 89, 5815 (2001)

[14] M. K. Miller, K. F. Russell, K. Thompson, R. Alvis, and D. J. Larson, Microsc. Microanal. 13, 428 (2007).

[15] B. Gault, M.P. Moody, J.M. Cairney, S.P. Ringer, Atom Probe Microscopy, Springer, New York Heidelberg (2012)

[16] J. Mayer, L. A. Giannuzzi, T. Kamino and J. Michael, MRS Bulletin, 32, 400-407 (2007)

[17] J. F. Ziegler and J.P. Biersack, The Stopping and Range of Ions in Matter, in D. A. Bromley, Treatise on Heavy-Ion Science 6, Springer Science+Business Media, New York (1985)

[18] J. Bogdanowicz, Photomodulated Optical Reflectance, Springer-Verlag, Berlin Heidelberg (2012)
[19] W. Vandervorst, T. Clarysse, B. Brijs, R. Loo, Y. Peytier, B. J. Pawlak, E. Budiarto, and P. Borden, AIP Conference Proceedings 683, 758 (2003)
[20] A. Salnick and J. Opsal, Journal of Applied Physics 91, 2874 (2002)
[21] L. Pottier, Appl. Phys. Lett. 64, 1618 (1994)
[22] J. F. Muth, J. H. Lee, I. K. Shmagin, R. M. Kolbas, H. C. Casey Jr., B. P. Keller, U. K. Mishra and S. P. DenBaars, Appl. Phys. Lett. 71, 2572 (1997)
[23] V. Bougrov, Gallium Nitride, in Properties of Advanced Semiconductor Materials, Eds. M.E. Levinshtein, S.L., Rumyantsev, M.S. Shur, John Wiley & Sons, Inc., New York, 2001.
[24] A. Othonos and C. Christofides, Phys. Rev. B 66, 085206 (2002)
[25] A. Kumar, J. Bogdanowicz, J. Demeulemeester, J. Bran, D. Melkonyan, C. Fleischmann, W. Vandervorst, under review at Laser Physics Letters.
[26] T. Ono and K. Hirose, J. Appl. Phys. 95, 1568 (2004)
[27] J. A. Van Vechten, Physical Review B, 7, 1476-1507 (1973)

Chapter 4

Atomic insight into $Ge_{(1-x)}Sn_{(x)}$ layers

In this chapter we discuss the use of L-APT to understand the contribution of Sn clusters and defect generation towards relaxation of strained metastable $Ge_{(1-x)}Sn_{(x)}$ layers. Since this was the first time the $Ge_{(1-x)}Sn_{(x)}$ system was studied using L-APT, we will first describe the field evaporation characteristics and the optimal conditions to analyze these layers (Section 4.1). Subsequently, we will present a new cluster analysis algorithm that was developed to extract ultra-fine clusters (few 10's of atoms) (Section 4.2) and apply it to gain insight into the role of Sn cluster formation in strain relaxation of these layers (Section 4.3). All our main results are discussed in more detail in the papers (Article IV and V) attached at the end of the chapter.

Scaling of Complementary-Metal-Oxide-Semiconductor (CMOS) devices for increased performance and functionality has led to an increased interest in metastable $Ge_{(1-x)}Sn_{(x)}$ layers due to their unique properties like larger lattice constant as compared to Ge and SiGe, ability to engineer band gap etc. Due to these appealing properties, $Ge_{(1-x)}Sn_{(x)}$ layers could potentially be used for:

- *Strained Ge based CMOS devices* - Thanks to the larger lattice constant of $Ge_{(1-x)}Sn_{(x)}$ layers as compared to Ge, they can be used to exert uniaxial compressive strain or biaxial tensile strain (depending upon the configuration they are integrated) into p-

CMOS device. For example Wang et al. [111] and Loo et al. [112] proposed embedding $Ge_{(1-x)}Sn_{(x)}$ in the source and drain region to induce uniaxial compressive stress in the Ge channel (**Fig. 4.1(a)**). Compressive strain in Ge leads to the splitting of the degenerate heavy and light hole valence bands; thus, increasing the hole mobility [113]. An alternate option could be to use ultrathin biaxial compressively strained $Ge_{(1-x)}Sn_{(x)}$ quantum well (QW) on Ge, as a channel material (**Fig. 4.1(b)**). This architecture makes use of the high mobility of charge carriers in $Ge_{(1-x)}Sn_{(x)}$ layer [114].

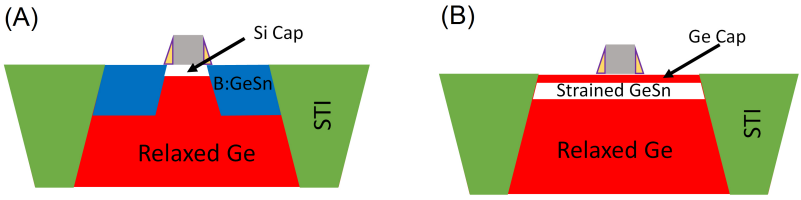

Figure 4.1 – Schematic representation of possible architectures of strained Ge p-MOSFET. (A) Uniaxial compressive Ge channel by embedded $Ge_{(1-x)}Sn_{(x)}$ S/D. (B) Biaxial compressive $Ge_{(1-x)}Sn_{(x)}$ QW on a Ge strain relaxed buffer. .

- *Complete group IV optoelectronic devices* - The band gap of $Ge_{(1-x)}Sn_{(x)}$ layers can be engineered by changing the Sn concentration in these layers. Shimura et al. [115] showed that the transition from an indirect to direct band gap occurs in these layers for a Sn concentration of ∼11 %. The cause of this transition is the faster lowering of the direct conduction band valley (Γ point) as compared to the indirect valley (L point), when Sn is added to the Ge lattice (**Fig. 4.2**). Furthermore, addition of Sn also leads to an increased absorption at the telecommunication wavelength (1550 nm - 1620 nm) [116]. These unique optical properties of $Ge_{(1-x)}Sn_{(x)}$ layers (and $Si_{(1-x-y)}Ge_{(y)}Sn_{(x)}$ layers) have proven it to be an exceptional candidate for all group-IV optoelectronic devices like IR lasers [117], photodetectors [118], electro-optical modulators [119] etc.

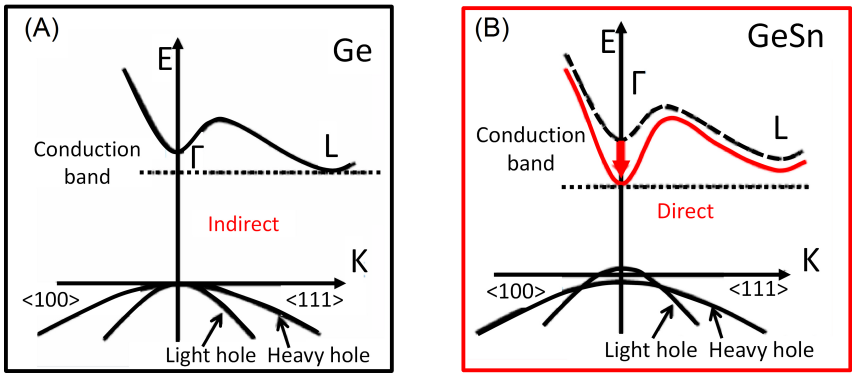

Figure 4.2 – (A) Band structure of Ge. (B) Band structure of $Ge_{(1-x)}Sn_{(x)}$. The introduction of Sn leads to transition from indirect bandgap to a direct bandgap. Reproduced from [6].

To adopt $Ge_{(1-x)}Sn_{(x)}$ layers for these applications, it is required that the Sn in the layer is substitutional and exists in its semiconducting α-Sn allotrope. Furthermore, for large scale industrial applications, these layers need to be grown with acceptable growth rates. This is challenging because:

- The diamond-cubic semiconducting α-Sn allotrope is unstable at high temperatures [120]. The α-Sn allotrope undergoes a spontaneous transition to its β-Sn metallic phase at 13.2 °C.
- There is a 14.7 % lattice mismatch between α-Sn ($a_0^{Sn} = 6.4892$ $\AA$) and Ge ($a_0^{Ge} = 5.6579$ $\AA$). The volume mismatch resulting from this lattice mismatch leads to an increased enthalpy of formation and hence, phase separation of the Ge and Sn [121]
- The surface free energy of Sn is lower as compared to Ge. Thereby, Sn has a strong tendency to segregate on the surface.
- The thermodynamic solid solubility of Sn in Ge is < 1 % at 231 °C [122]). This leads to phase separation and surface segregation of Sn at higher temperatures.

Therefore $Ge_{(1-x)}Sn_{(x)}$, with the desired Sn content and strain, can only be grown at non-equilibrium conditions. Indeed, the phase separation of Sn only occurs when the system has enough energy to overcome the

(1) potential barrier for nucleation of β-Sn and (2) the kinetic barrier for surface diffusion of Sn. Hence, if the layers are grown at low temperature and high growth rate, precipitation of Sn and or formation of Sn clusters can be avoided. Epitaxial growth of meta-stable $Ge_{(1-x)}Sn_{(x)}$ layers, i.e. grown at non-equilibrium conditions, has been successfully demonstrated using chemical vapor deposition (CVD) [123] and molecular beam epitaxy (MBE) [124]. However, these layers exhibit high defect density due to the lowered surface mobility of adsorbed adatoms [125]. Furthermore, any post-annealing of the grown layers to reduce the defect density potentially leads to Sn cluster formation and or Sn segregation and in-turn strain relaxation in the grown layers [126, 127], thereby making them unsuitable for the desired applications. Hence, in order to implement $Ge_{(1-x)}Sn_{(x)}$, the underlying physical relation between layer relaxation, Sn cluster formation and defect generation needs to be understood. Moreover, it is extremely important to identify the conditions for the onset Sn cluster formation. L-APT due to its atomic resolution and its inherent ability to characterize 3-D volumes is perfectly suited to gain insight into Sn cluster formation in these layers.

All $Ge_{(1-x)}Sn_{(x)}$ layers studied during this doctoral project were grown epitaxially using low temperature CVD. The layers were grown using Ge_2H_6 and $SnCl_4$as the Ge and Sn precursor respectively on strain relaxed, <100> oriented Ge buffer layers. The deposition temperature was 320 °C and atmospheric pressure was used. More details on the film growth can be found in ref [123]. Furthermore, a 100 nm Ge cap was deposited in-situ on top of all samples (unless otherwise mentioned), to protect the $Ge_{(1-x)}Sn_{(x)}$ layer from ion damage during sample preparation.

4.1 Quantitative L-APT analysis of $Ge_{(1-x)}Sn_{(x)}$ layers

Characterization of compound semiconductors and multilayer structures using L-APT should be done with care, as the difference in field evaporation characteristics of the constituent elements and/or layers could potentially lead to artefacts in the reconstructed volume. Furthermore, potential non uniform laser absorption could lead to non-hemispherical apex shapes and hence inaccurate reconstructions. In this section we will first (Section 4.1.1) discuss the commonly observed artefacts and verify the presence (or absence) of these in the analyzed $Ge/Ge_{(1-x)}Sn_{(x)}/Ge$

samples. Furthermore, we will also present the optimum experimental conditions (laser power, wavelength, base temperature and reconstruction parameters) to analyze these layers. In Section 4.1.2, we will discuss the impact of laser absorption on the apex shape and the reconstructed data. All the results are discussed in more detail in Article IV, attached at the end of this chapter.

4.1.1 Field induced artefacts

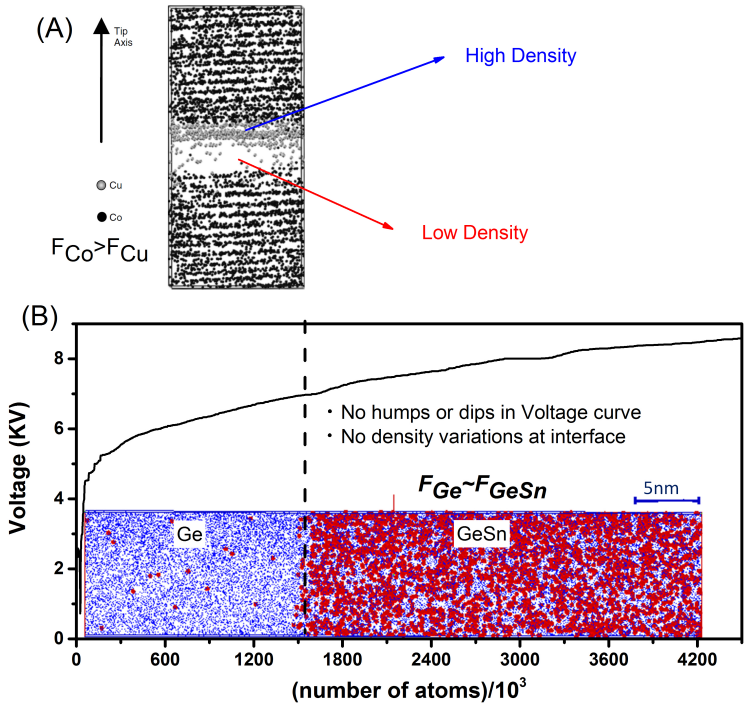

Figure 4.3 – Observed field induced artefacts in multilayer structures. (A) Three dimensional APT reconstruction of a Co/Cu multilayer stack. The field variation between Co and Cu causes density variations at the interface. Reproduced from ref [128]. (b) Voltage curve and APT reconstruction of a $Ge_{(1-x)}Sn_{(x)}$ layer. No humps or dips and no density variations at the interface are observed in the voltage curve and 3-D reconstruction respectively, implying the field required to evaporate Ge or $Ge_{(1-x)}Sn_{(x)}$ is similar. The L-APT analysis was done using green ($\lambda = 515$ nm)

One very common artefact when analyzing multilayer structures is the appearance of false low or high densities at the interfaces [128]. The cause of these density variations is the difference in the threshold field required to evaporate the different layers. For example, when transitioning from a layer requiring a high field to evaporate, to a layer requiring a low field, a high density region is observed (**Fig. 4.3(a)**). On the other hand, during the transition from a low field evaporating layer to a high field evaporating layer a low density is observed. These density variations are observed due to the incorrect assumption of a hemispherical apex during reconstruction of the acquired data. Indeed, two assumptions govern the calculation of the depth coordinate during reconstruction [26]. Firstly, the apex of the specimen is assumed to be a perfect hemisphere. Secondly, homogeneous evaporation is assumed from this hemispherical surface. The depth coordinate is then calculated simply by the order in which ions strike the position sensitive detector. In the algorithm, the increment in the z-coordinate of each collected atom is based on the average atomic volume and the assumed curved surface [26]. However, in cases with specimens containing multi-layer structures with different threshold evaporation fields, the apex re-shapes asymmetrically from one layer to another. 3-D simulations of field evaporation such specimens demonstrate that the artefactual depth calculated assuming a hemispherical apex is sufficient to produce the observed deformations of the reconstructed data [128]. During an experiment, the presence of layers with variable threshold evaporation field can also been observed in the voltage curve of a constant flux L-APT measurement as bumps (low field to high field) or dips (high field to low field). Regarding the $Ge/Ge_{(1-x)}Sn_{(x)}/Ge$ samples, no irregularities were observed in the voltage curve (**Fig. 4.3(b)**). Furthermore, homogeneous densities were observed across the interfaces in the reconstruction, implying that the field required to evaporate the two layers (i.e. Ge and GeSn) are similar (**Fig. 4.3(b)**).

Differences in threshold field evaporation values between the constituent elements of a compound semiconductor can potentially also lead to co-evaporation. Co-evaporation refers to simultaneous evaporation of two neighboring atoms (generally one low field evaporating and one high field evaporating) on the same laser pulse. Experimentally, co-evaporation is observed as an increase in the multi-hit count. Even though the detector available on our tool has multi-hit detection capability, if too many ions hit the detector simultaneously in close proximity, the signal generated by every hit may no longer be resolved and some of the ions are simply lost. This is called ion pile-up [49] and leads to erroneous quantification

of the stoichiometry of the analyzed layer. From experimental evidence it is known that a difference greater than 10 % between the threshold field evaporation values of the constituent elements can lead to co-evaporation [128]. The values available in the scientific literature for the threshold field evaporation (F_{ev}) for Ge and Sn are 29 V/nm and 23 V/nm respectively [49]. Hence, the above mentioned artefacts were of a great concern. The presence of co-evaporation was evaluated by comparing the distance distribution of the first nearest neighbor (1^{st}NN) atoms and the distance between the detected Ge-Sn multi-hits (**Fig. 4.4(A)**), as the distribution of multi-hits is characteristic of the distance between the atoms (involved in the multi-hit) on the surface of the tip. A broad distribution was observed for multihits with a mean ∼1.5 nm, while the mean for the 1^{st}NN distance distribution in the $Ge_{(1-x)}Sn_{(x)}$ layer was ∼2.4 $\AA$. The difference between the two distance distributions shows that the Ge and Sn atoms evaporating simultaneously are not neighboring atoms, therefore ruling out the presence of co-evaporation in $Ge_{(1-x)}Sn_{(x)}$ layers. This unexpected observation can be explained based on the fact that the reported values in scientific literature are for pure Ge and metallic β-Sn. The threshold field evaporation value is dependent on the local environment of the evaporating element, as well as its bonding. Since these are very different in the $Ge_{(1-x)}Sn_{(x)}$ alloy, the threshold field evaporation values could also be very different. Furthermore, the reported values have been calculated using the Mueller-Schottky model which, as discussed in chapter 2, is not extremely reliable.

Accurate quantification and spatial resolution in compound semiconductors is also a function of the fraction of the energy provided for field evaporation by the electric field (called field fraction (FF) = $\frac{F}{F_0}$) and the laser (called pulse fraction (PF) = $1 - FF$) [129]. A High pulse fraction, i.e. high laser energy, implies a high temperature at the apex which leads to migration of the surface atoms, hence a loss in spatial accuracy [73]. Furthermore, higher temperature also leads to the evaporation of molecular clusters [130]. Although the formation of clusters during field evaporation is not completely understood, it has been suggested that increased surface migration of atoms may be the cause of cluster formation [129]. Field evaporation of clusters would affect both spatial resolution and quantification. With regards to chemical accuracy, dissociation of clusters post field evaporation my lead to ion pile-up and/or potentially neutral formation [129]. Since the neutrals would not have enough energy to generate a signal on the detector, both ion pile-up and neutral formation result in reduced chemical accuracy. Also, the

spatial information of the atoms forming the cluster is lost hence causing a, loss in spatial resolution.

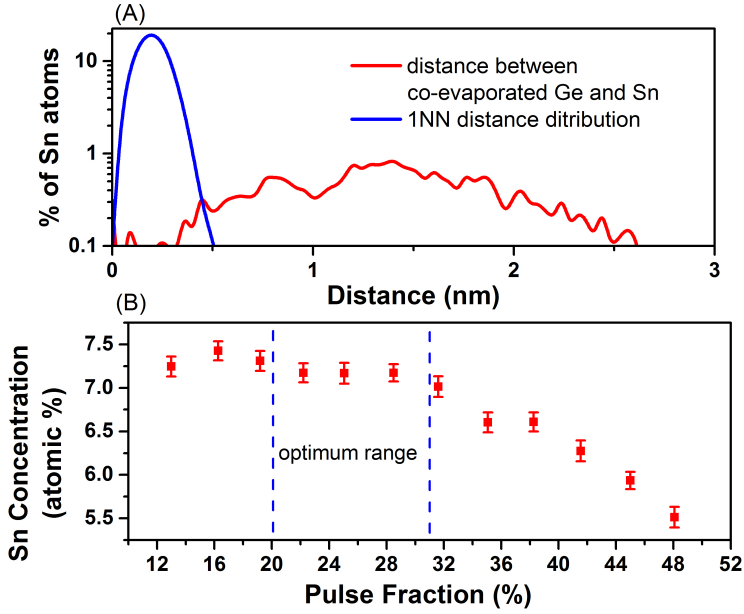

Figure 4.4 – (A) 1[st]NN distance distribution and distance distribution of co-evaporated Ge and Sn atoms. No correlation is observed between the two implying that the co-evaporated atoms were not neighbors. (B) Variation in measured Sn concentration as a function of pulse fraction. The error on the concentration value is based on counting statistics, $\sigma = \sqrt{(C_{Ge} \times C_{Sn})/N_{tot}}$, where C_i is the concentration of i (i = Ge and Sn) and N_{tot} is the total number of atoms [131]. The L-APT analysis was done using green (λ = 515 nm) laser.

High field, i.e. high field fraction, causes the evaporation of low field evaporating element in between successive laser pulses thereby causing it to be discarded as noise. This phenomenon is called DC evaporation [69] and leads to overestimation of the high field evaporating species. To evaluate the optimum balance between the electric field and laser energies for accurate quantification of the $Ge_{(1-x)}Sn_{(x)}$ layers, L-APT analysis was performed at constant flux and the change in voltage required at different laser powers to maintain the flux was measured. The field fraction and consequently the pulse fraction was calculated using the method described in section 2.3.2. The error on the concentration values obtained using L-APT is based on the counting statistics, $\sigma = \sqrt{(C_{Ge} \times C_{Sn})/N_{tot}}$,

where C_i is the concentration of i (i = Ge and Sn) and N_{tot} is the total number of atoms [131]. For these set of measurements ~5×10^4 atoms were collected per data point. The observed Sn concentration as a function of pulse fraction (**Fig. 4.4(B)**) shows a plateau in the Sn concentration (~7.1±0.12 atomic %) between ~20 % and 30 % pulse fraction. Furthermore, the Sn concentration in this region is consistent with RBS measurements (~6.8±0.7 atomic %). The Sn concentration decreases at higher pulse fraction and Ge are observed in this regime. This is consistent with thermal evaporation and a possible reason for the reduced Sn could be the inability to detect Sn clusters due to their high mass (maximum mass that can be detected in our tool is 300 amu). An increase in the Sn concentration was observed at pulse fraction < 20 %. This increase could be due to DC evaporation of Ge atoms. The presence of DC-evaporation is evident by looking at the counts rejected from the raw data but stored in the LAWATAP in a separate counter (called null counts) due to their detection/emission without correlation to the laser pulses. We observe that these counts increased from 400-500 to ~900-1200 for a 50 000 collected atoms under conditions of low pulse fractions i.e. high DC-fields. Hence, the optimum range for a quantitative measurement is at a pulse fraction of 20 % - 30 %. During an L-APT experiment, the optimum condition can be set by ensuring the CSR of Sn^{2+} between 50 % - 70 %. An interesting thing to note from the pulse fraction curve (**Fig. 4.4(B)**) is that at low pulse fraction we start preferentially loosing Ge atoms. This implies that Ge has a lower field evaporation threshold as compared to Sn. However, this difference has to be less than 10 % as we do not observe any co-evaporation.

In summary, no field related artefacts such as co-evaporation, density variations etc. were observed for these layers. Hence, an accurate reconstruction using conventional reconstruction algorithms is possible for the analyzed stack. One remarkable observation is that the field evaporation threshold of Ge was found to be lower than Sn in these layers. This is completely opposite to the theoretically predicted values for field evaporation of pure Ge and β-Sn. This discrepancy between experiment and theory may be explained considering that the field evaporation threshold is a function of the local environment of the evaporating element, as well as its bonding, which is very different in alloys as compared to pure materials. Furthermore, the theoretical values reported in literature were calculated using the Mueller Schottky model which as discussed in Chapter 2, is not accurate for semiconductors.

4.1.2 Laser induced tip apex reshaping

Regarding the laser induced artefacts, the TEM micrograph of an analyzed $Ge_{(1-x)}Sn_{(x)}$ tip shows an asymmetric shape (**Fig. 4.5(A)**). The cause of the asymmetry can be attributed to the high absorption coefficient of this material. To theoretically simulate the absorption in $Ge_{(1-x)}Sn_{(x)}$ the refractive index of Ge was used since the complex refractive index of the former is not known precisely. However, this assumption is not expected to induce major variations in the absorbed laser as the absorption coefficient of the two is of the same order of magnitude ($\sim 5 \times 10^5 cm^{-1}$) [116].

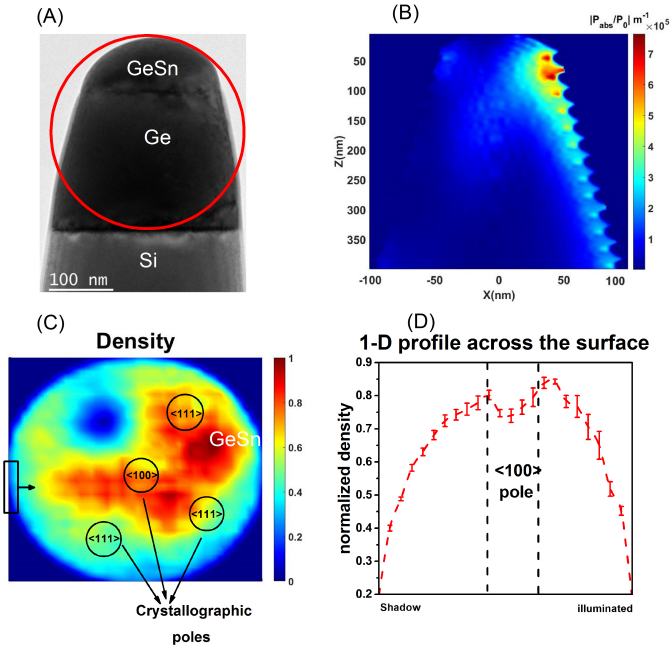

Figure 4.5 – (A) TEM micrograph of an analyzed $Ge_{(1-x)}Sn_{(x)}$ tip using green laser ($\lambda = 515$ nm). (B) Theoretically simulated absorbed laser power ($\lambda = 515$ nm) in a Ge tip using ADDA. (C) Density variations across the tip apex in $Ge_{(1-x)}Sn_{(x)}$. The density variations are artefacts caused due to different local magnification. The latter in turn is a result of different local radii. The low density at the poles is a common artefact in the L-APT data [3]. (D) 1-D profile of the density variation across the apex. The value at each point is the mean value in a vertical selection (shown as a rectangle in (A)) of the detector. The error bar is the standard deviation in the vertical selection.

The ADDA simulation of the absorbed laser power in Ge using

a refractive index of $\widetilde{n} = 4.5891 + i2.4495$ [132] shows a strong one sided absorption and an absence of resonance of the incident light (**Fig. 4.5(B)**). The one sided absorption has also been observed for Si illuminated by a UV laser [28] and leads to a non-uniform temperature distribution at the apex. This leads to a preferential evaporation of the hotter side and in-turn to an asymmetrical apex shape. However, on reconstructing the data using voltage based reconstruction algorithm [26], a minimal density variation (~ 3 %), was observed between the illuminated and the shadow side (**Fig. 4.5 (C) (D)**). Hence, no major laser induced artefacts are observed due to the non-uniform absorption. Furthermore, to negate the impact of small density variations, data mining (cluster analysis) was done on smaller volumes with similar densities and the artefact removal algorithm proposed by Stephenson et al. [34] was used.

4.2 Relaxation mechanisms of strained $Ge_{(1-x)}Sn_{(x)}$ layers

$Ge_{(1-x)}Sn_{(x)}$ layers relax when grown above a threshold thickness (Blakeslee limit [133]) or when annealed above a critical temperature (thermal stability). Potential mechanisms for strain relaxation include:

- *Crystal defects* such as misfit dislocations, threading dislocations etc. [134]. Indeed, the excess strain energy accumulated in the epitaxial layer can give rise to crystal defects which help relax the layer [135].

- *Sn cluster formation or precipitation* could also lead to strain relaxation because removal of a substitutional Sn atom would decrease the local strain the layer. This mechanism is further supported via theoretical simulation by Ventura et al. [136]. They predicted that certain configurations of Sn cluster were more favorable over substitutional Sn and could lead to layer relaxation. Sn clusters/precipitates have been observed in relaxed layers using TEM and Energy-dispersive X-ray spectroscopy (EDS) [127].

However, the impact of Sn cluster formation and/or defect formation on strain relaxation still remains unresolved. To determine the cause(s) of the strain relaxation, L-APT was used (Article V). The initial stages of Sn cluster formation (few 10's of atoms) during strain relaxation were studied via a new cluster analysis algorithm (Section 4.2.1).

4.2.1 Cluster analysis algorithm

In L-APT, clusters are usually defined as localized regions where the concentration of solute molecules is higher as compared to the rest of the matrix. Depending on the size of these volumes, cluster analysis in a L-APT dataset can be as simple as visual inspection (size > few nm in radius) or might need complicated statistical data mining approaches (few 10's of atoms < size < few 100's of atoms). A consequence of solute enrichment in these localized volumes is that the solute molecules are closely packed in contrast to the ones that are randomly distributed across the matrix. Most statistical data mining algorithms take advantage of the closely packed solute atoms to extract the clustered atoms. A general approach to select clustered atoms can be summarized as:

I. Define a characteristic property of the clustered volumes. This could be the maximum distance between clustered solute atoms (d_{max}), concentration/density of solute atoms in clusters etc.

II. Select the solute atoms which satisfy the defined property in Step I. These selected atoms are called core atoms.

III. The core atoms are grouped with neighboring atoms to form clusters. The condition to choose the neighboring atoms might be a derivative of the condition in Step I or can be a new set of conditions

A summary of the conditions used in Step I and III by commonly used algorithms to extract ultra-fine clusters is discussed below [34, 137, 138].

Density-Based Clustering algorithm (DBSCAN) [34]: In this algorithm, the condition to select the core and the neighboring atoms is based on the nearest neighbor (NN) distance distribution [139] of solute atoms. The NN distributions are used because an imprint (as a satellite peak) of the clustered atoms can be observed in these distributions since the solutes are more closely packed inside the cluster (**Fig. 4.6(A)**). Core atoms are selected as those solute atoms whose K^{th}NN solute atom lies at distance no more than specific value d_{max}. For example in **Fig. 4.6(B)** the atoms whose 5^{th}NN is$\leq$0.740 nm are selected as core atoms (blue). To calculate d_{max} the experimental K^{th}NN (5^{th}NN in **Fig. 4.6(A)**) of solute atoms is fitted with a multiphasic Poisson probability distribution with each phase having a different density ρ_i. The probability distribution as a function of the distance r is defined mathematically as

$$P_K(r,\rho,\alpha) = \sum_{i=1}^{M} \frac{3\alpha_i}{(k-1)!} \left(\frac{4\Pi}{3}\rho_i\right)^K r^{3K-1} e^{-\left(\frac{4\Pi}{3}\right)\rho_i r^3} \qquad (4.1)$$

where M is the number of phases and α_i is the relative weights of each phase. The number of phases can be estimated as M= (number of satellite peaks) + 1 and is mostly equal to 2. The fit parameters are then the relative weights α_i and density of each phase ρ_i. After performing the fit, d_{max} is defined as the maximum distance of the denser phase, i.e. the clustered phase. Subsequent to the selection of core atoms, the neighboring atoms are chosen as all atoms (solute or solvent) which are within d_{max} of the core atom (red spheres in **Fig. 4.6(B)**).

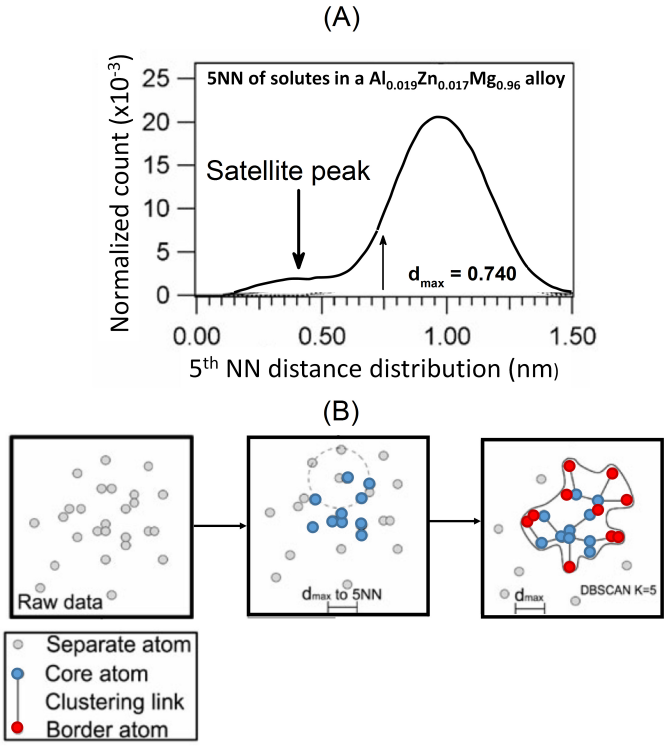

Figure 4.6 – (A) 5thNN distance distribution of solute atoms (Al and Zn) of an $Al_{0.019}Zn_{0.017}Mg_{0.96}$ alloy (reproduced from ref [34]). The presence of satellite peak in the distributions is characteristic of the presence of clusters in the analyzed volume. (B) Schematic representation of the DBSCAAN cluster analysis algorithm

Since the condition to choose neighbor atoms is linked to the order (K) used to define d_{max}, the size of the selected clusters will depend on K. Of course, using smaller values of K, helps in probing the local

environment around solute atoms hence, enabling the detection of ultra-fine clusters. However, at lower K (1-2) values, d_{max} is extremely sensitive to any artefactual changes in local atomic densities and/or local spatial resolution variations due to trajectory aberrations, local magnification effects etc. thereby, introducing a large error on small clusters. Using larger values of K, makes the method less prone to local variations but, because it probe large volumes it is insensitive to small clusters.

Core-Linkage algorithm: Stephenson et al. proposed improvements to DBSCAN to enable the extraction of small clusters [34]. In this algorithm, the two conditions, i.e. the condition to define core and neighboring atoms, are delinked by defining two separate characteristic distances, one for the core atoms (called d_{core}) and one for the neighbor atoms (called d_{link}). Thus, one uses a large K value for ultra-fine clusters to select the core atoms and a smaller K value is employed to select the border atoms. Furthermore, since the two steps are separate, alternative set of conditions can be used to select the core atoms, e.g. using a minimum atomic density in a local volume to choose the core atoms. Moreover, Stephenson et al. also proposed heuristical approaches to define/select the input parameters for the cluster search algorithms based on the complete spatial randomness model [140]. However, the core-linkage algorithm requires four input parameters, d_{core}, K of core atoms, d_{link}, K of border atoms, whose accurate determination is not trivial.

Delaunay Tessellation based algorithm: This algorithm is different from the above mentioned algorithms in terms of the method employed to define the characteristic distance d_{max} of the clusters and the condition used to select neighbor atoms [137]. In this cluster algorithm, d_{max} (called threshold radius (R_T) by the authors) is defined based on the radius distribution of the Delaunay tessellations [141] of the solute atoms (**Fig. 4.7(A)**). In the event where clusters are present in the L-APT volume, a satellite peak is present in the radius distribution of the Delaunay cells (**Fig. 4.7(B)**). This experimental distribution is then fitted with a theoretical distribution of a volume containing clusters [142]. The d_{max} can then be defined as either the maximum radius of the clustered distribution or mathematically calculated using the statistical analysis presented by Stephenson et al. [34]. Each Delaunay cell which has a radius less than d_{max} is called a clustered cell. The individual Delaunay cells are now grouped together to form a cluster using an erosion-expansion step as follows:

- cells of radius less than d_{max} are not considered as clustered cells if they have do not have more than one clustered cell as neighbor;
- cells of radius greater than d_{max} which are surrounded by at least three clustered cells are considered as clustered cells.

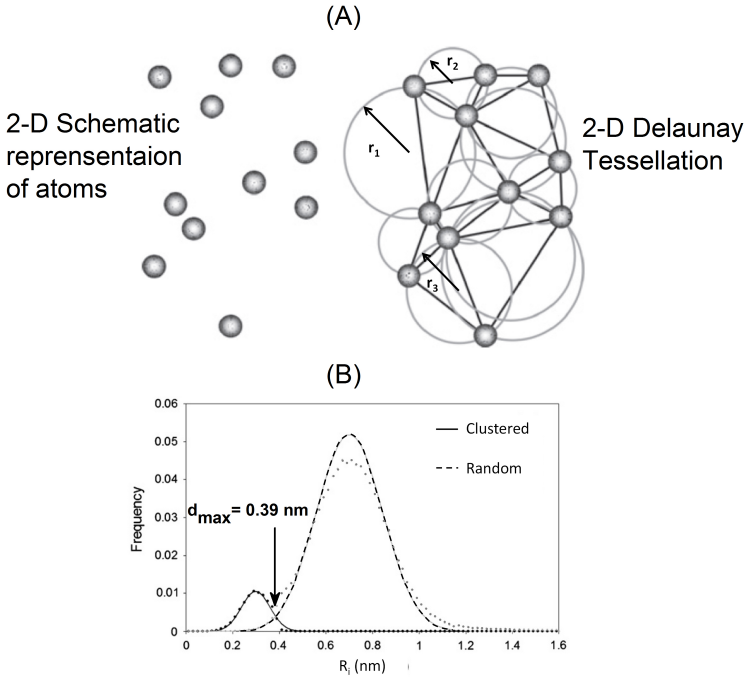

Figure 4.7 – (A) 2-D schematic representation of Delaunay tessellation/triangulation. (B) Distribution of radii of circumsphere of Delaunay cells. The satellite peak is characteristic of clusters. Reproduced from [137].

One of the biggest advantages of this method is that it requires only one input since no additional input is required to group clustered cell. Furthermore, since to create a Delaunay tessellation, it requires at least three neighbors, it is less sensitive to the artefactual fluctuations in densities. In retrospect, since this algorithm is only limited to the 3^{rd}NN, a satellite peak may not be visible in the Delaunay radius distribution depending on the contrast between the concentration/composition of cluster and matrix.

The above mentioned algorithms (core-linkage and Delaunay based) although suited for extracting ultra-fine clusters, cannot be used directly for the $Ge_{(1-x)}Sn_{(x)}$ system. The reason for this is that in the $Ge_{(1-x)}Sn_{(x)}$ system, the satellite peak of the Sn clusters in the KNN distance distributions is superimposed on the distance distribution of the randomly distributed atoms (**Fig. 4.8(A)**), i.e. the characteristic NN distance distribution of clustered atoms is also present in randomly distributed Sn atoms. Furthermore, the amplitude of the satellite peak is low making it hardly discernible in the global K^{th}NN distance distribution. This created the challenge to,

- first define the characteristic distance distribution of clustered atoms (d_{max}, d_{link}) and
- Second, even if a certain value for d_{max} was chosen, applying the above mentioned algorithms would select all atoms whose nearest neighbors are at distance less than d_{max}. Hence, selecting a portion of the randomly distributed Sn atoms as well.

To mitigate these challenges, a 4-step approach was developed to extract the Sn clusters and is summarized below. A detailed description is presented in Article V.

1. As a first step, the core-linkage algorithm was applied to remove the majority of the randomly distributed Sn atoms. This had two main consequences, (1) increase the ratio of clustered to randomly distributed Sn in the selected volume, (2) group and label the Sn atoms which might be clustered. The Sn atoms selected after this step are labeled Sn_{CL}. As can be seen in **Fig. 4.8(B)**, after the first step all atoms giving rise to the satellite peak, i.e. the clustered Sn atoms, have been selected. However, we have also selected some of the randomly distributed Sn atoms. Hence, each selected volume consists of either randomly distributed atoms (Sn_{ran}) or a mixture of random plus clustered Sn atoms (Sn_{c+r}). In Step 2 and 3 we will deconvolute the clustered and the randomly distributed Sn atoms.
2. In order to deconvolute the clustered and randomly distributed Sn atoms we will first precisely define the characteristic K^{th}NN distance distribution of clustered Sn atoms, for all possible orders of K. Subsequently in Step 3 the clustered atoms are selected based on these characteristic distances. Step 2 and 3 is a part of the new Distribution and Deconvolution refinement (DAD) developed during

this thesis project. The characteristic distance of the clustered Sn atoms were defined by taking advantage of the fact that++ the K^{th}NN distance distribution of the volumes containing only Sn_{ran} will be a Poisson distribution, since a subset of a random distribution remains a random distribution. However, this distance distribution would be attenuated as compared to the one before the core-linkage step, since the total number of randomly distributed Sn atoms is lower. In the case of volumes containing Sn_{c+r}, the K^{th}NN distribution remains the same as the original distribution. This is due to the fact that the local environment of the clustered Sn atoms does not change, since we purposely selected the neighboring randomly distributed Sn atoms by overestimating d_{link}. Hence in the aggregated K^{th}NN distance distribution of individual volumes, the satellite peak becomes clearer and well defined **Fig. 4.8(C)**, i.e. we now have information about the exact spatial distribution of Sn atoms in clusters. Also note that, the spatial distribution of Sn atoms for clusters of different sizes (in terms of number of Sn atoms present) might be different. Therefore, the K^{th}NN distance distribution of individual volumes containing equivalent number of Sn_{CL} atoms were calculated and aggregated, where K= 1 to (number of Sn atoms in the volume)-1 i.e. for example in volumes that contained 6 Sn_{CL} atoms, we calculated 1-5NN distance distribution individually for each volume and aggregated the resulting distance distribution. After this step, we were able to identify the satellite peaks, for all orders of the NN distributions and for all the different sizes (in terms of number of Sn atoms) of the selected volumes. Examples of such curves are shown **Fig. 4.8(C)**, where 4^{th}NN distribution is shown for volumes containing 5, 6 and 7 Sn_{CL} atoms.

3. In this step the clustered and the randomly distributed Sn atoms were deconvoluted based on the now known characteristic distance distribution of clusters. In volumes which contain only randomly distributed Sn atoms, only some or none of the atoms will be present at the characteristic distances, for all possible orders of K. Hence, only those volumes were selected as clusters which contained all Sn atoms at the characteristic distance of a cluster. However it should be noted that before the deconvolution, Sn atoms which are present outside the maximum characteristic distance from the core atoms need to be discarded. Since these are the randomly distributed Sn atoms which were selected due to the overestimated d_{link}. For e.g.,

in a volume containing 7 Sn atoms, suppose the max characteristic distance (6NN) was 7.1Å. So all atoms in a volume which contained 7 Sn atoms, which were present at distances larger than 7.1Å from the core Sn atom were removed.

4. As a last step, we merge the clusters having common Sn atoms in order to properly quantify them and to understand the nature of the clusters in terms of size, Sn distribution etc. Furthermore, all the solvent atoms (Ge in our case) present within the finally selected cluster volumes were chosen as a part of the cluster.

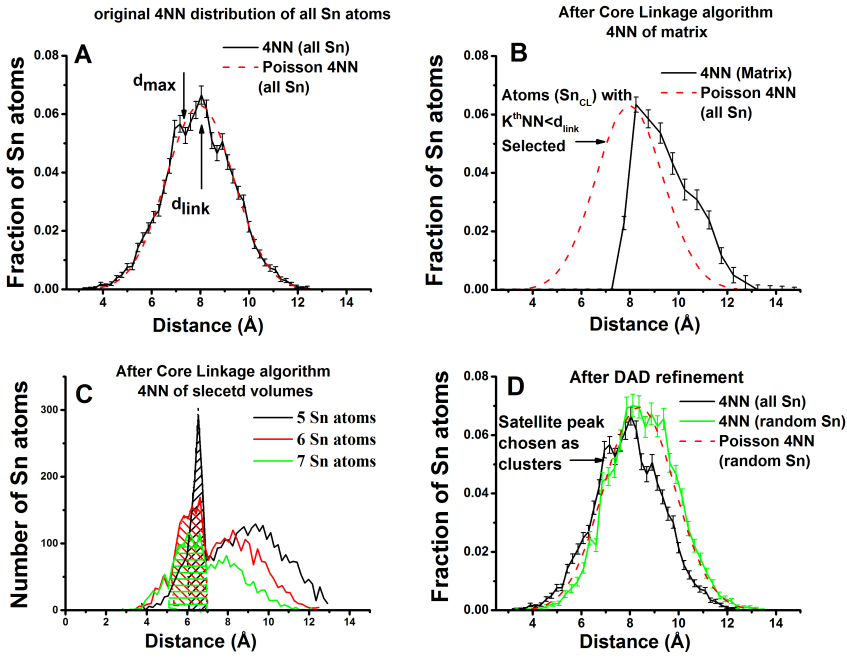

Figure 4.8 – Evolution of the $K^{th}NN$ distance distribution of Sn atoms during the cluster analysis algorithm. (A) Experimental and theoretically modeled $4^{th}NN$ distance distribution of Sn atoms before cluster analysis. The theoretical distribution is for a single phase completely random solid solution using **Eq. 4.1**. (B) $4^{th}NN$ distribution of the matrix (randomly distributed atoms) after the application of Core-linkage algorithm. (C) $4^{th}NN$ distribution of the selected volumes after the application of Core-linkage algorithm. The shaded region marks the characteristic distance for the $4^{th}NN$ in clusters. (D) $4^{th}NN$ distribution of the matrix (randomly distributed atoms) after the application of DAD refinement.

The 4^{th}NN distance distribution of the matrix after cluster analysis (containing the randomly distributed Sn atoms) is shown in **Fig 4.8(D)** (green curve). As can be seen the distribution now matches the theoretically predicted distribution for a random solid solution (dashed red line, calculated using the Sn atoms in the matrix) very well, meaning we have successfully selected and removed the clustered Sn atoms.

In summary, using the proposed algorithm it is possible to reliably extract ultra-fine clusters. The biggest advantage of the presented method is that we can deconvolute clustered atoms from randomly distributed atoms in cases when the characteristic distance distribution of clustered atoms is a subset of the distance distribution of random atoms. An added advantage of the proposed algorithm is that it can also distinguish between noise and real satellite peaks. This is so because, if the cluster analysis is done using a noise peak in the global K^{th}NN distance distribution, the aggregated K^{th}NN distribution of local volumes (Step 2) will only show a Poisson distribution since we will again by probing volumes containing only randomly distributed Sn atoms.

4.2.2 Role of Sn clusters in strain relaxation of $Ge_{(1-x)}Sn_{(x)}$ layers

In scientific literature it has been shown that $Ge_{(1-x)}Sn_{(x)}$ layers tend to relax (1) when grown above a certain threshold thickness [135], known Blakeslee limit [133] or (2) due to post growth thermal anneal [127]. The potential mechanism of strain relaxation in these layers are defect generation [124] and Sn cluster formation [127]. In this section, using the developed cluster analysis algorithm, we will gain insight into the complex interplay between strain relaxation, crystalline defect and Sn cluster formation. To do this, we studied two sets of samples, one in which relaxation occurred due to thickness (**Table 4.1 I.A-I.C**) and the second, in which relaxation occurred due to a post growth rapid thermal anneal (RTA) (**Table 4.1 II.D-I.J**). All the samples had a Sn concentration of $\sim$7 at% measured using XRD and RBS. The strain relaxation degree (SRD) of the samples was calculated as:

$$SRD = \frac{(a_{//GeSn} - a_{//Ge})}{(a_{0GeSn} - a_{//Ge})} \tag{4.2}$$

where a_{0GeSn} is the experimental relaxed GeSn lattice constant and $a_{//GeSn}$ and $a_{//Ge}$ are the experimental in-plane GeSn and Ge lattice

constants, respectively. These lattice constants value were determined by High-resolution X-ray diffraction reciprocal space mapping (HR-XRD RSM) of the asymmetric (224) GeSn and Ge Bragg reflections.

sample ID	Sample structure	Treatment	SRD (%)
I.A	Ge cap (100nm) / $Ge_{0.93}Sn_{0.07}$ (40 nm)	As grown	0
I.B	Ge cap (100nm) / $Ge_{0.93}Sn_{0.07}$ (145 nm)	As grown	26
I.C	Ge cap (100nm) / $Ge_{0.93}Sn_{0.07}$ (530 nm)	As grown	75
II.D	$Ge_{0.93}Sn_{0.07}$ (80nm)	RTA at 500°C	8
II.E	$Ge_{0.93}Sn_{0.07}$ (80nm)	RTA at 540°C	27
II.F	$Ge_{0.93}Sn_{0.07}$ (80nm)	RTA at 580°C	36
II.G	$Ge_{0.93}Sn_{0.07}$ (80nm)	RTA at 620°C	37
II.H	$Ge_{0.93}Sn_{0.07}$ (80nm)	RTA at 640°C	48
II.J	$Ge_{0.93}Sn_{0.07}$ (80nm)	RTA at 660°C	75

Table 4.1 – $Ge_{(1-x)}Sn_{(x)}$ sample ID, sample structure, post growth treatment and strain relaxation degree (SRD).

No cluster could be extracted in the samples relaxing due to the thickness (Sample I.A, I.B, I.C) (**Fig. 4.10(A)**). Hence, in these samples Sn-clusters (if any) are not present or are below the detection limit of clusters via L-APT analysis. As Sn clusters are non-existent (or only present in extremely low levels), it seems that Sn-cluster formation is not the driving force for layer relaxation. Since one does however observes an increase in defect density (misfit dislocations, threading dislocations etc.) with layer relaxation [134, 135], defect generation could potentially be the main source for strain relaxation in these layers.

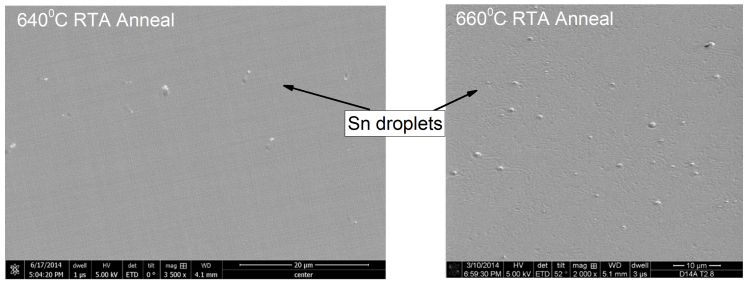

Figure 4.9 – Sn droplet formation in Sample II.H (annealed at 640 °C, left) and II.J (annealed at 660 °C, right), observed from SEM.

In the layers relaxing due to a thermal anneal, Sn clusters were observed. The following observations were made regarding Sn clusters/diffusion in these sample:

- Sn clusters were observed for anneal temperatures between 540 °C to 640 °C (Sample II.E - II.H) and the fraction of Sn atoms in clusters in the layer increased with anneal temperature.
- For the layers annealed at 640 °C and 660 °C (Samples II.H and II.J), Sn diffusion was observed in the Ge pseudo substrate and at the surface of the layer. The Sn concentration (as measured via L-APT) decreased to ~5 at% and ~1.5 at%, for anneal conditions of 640 °C and 660 °C respectively. Sn droplet formation on the surface was also detected for these samples (using scanning electron microscope (SEM) , **Fig 4.9**).
- No clusters were observed in the samples annealed at 520 °C and 660 °C. In the sample annealed at 660 °C, absence of cluster formation might be explained considering that the Sn concentration in the layers is at its thermodynamic equilibrium limit ($\sim$ 1.5 at%) and excess Sn has diffused to the surface and formed Sn droplets (**Fig 4.9(B)**).

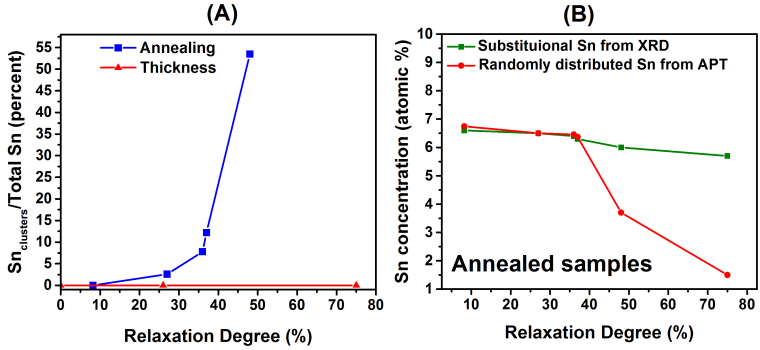

Figure 4.10 – (A) Percentage of Sn in clusters as a function of SRD for samples relaxing due to thickness (red) and RTA (blue) (B) Sn concentration from APT and XRD as a function of SRD for samples relaxing due to RTA.

Since we do observe a concurrent increase in layer relaxation and cluster density upon annealing, we will now discuss whether the formation of Sn clusters play a role in the layer relaxation. To clarify this we compared:

1. The SRD and amount of Sn in clusters as a function of anneal temperature (**Fig. 4.10(A)**) - No direct relation between the SRD and the amount of Sn in clusters was observed. In detail, for the layers annealed at temperatures ranging from 500 °C to 580 °C (Samples II.D – II.F), we observed a change in the relaxation degree from 8 % to 36 % respectively, whereas the amount of Sn in clusters only increased from 0 % - ~7 % of the total Sn atoms. In contrast, for annealing treatments between 580 °C to 640 °C, the layer relaxed only by an additional 14 %, but the Sn in clusters increased by ~ 47 % . These observations indicate that the Sn cluster formation has minimal impact on the layer relaxation.

2. Substitutional Sn as a function of Anneal - The Sn concentration measured using XRD (**Fig. 4.10(B) green line**) is derived from the measured lattice constant of $Ge_{(1-x)}Sn_{(x)}$ [135], assuming all Sn is substitutional. For the layers annealed at 640 °C and 660 °C, the Sn concentration as measured via XRD (~6 % and ~5.7 % respectively) is higher than the actual Sn present in the layer (measured using L-APT). This points towards the fact that in these samples the lattice spacing (i.e. relaxation) is no longer a function of the substitutional Sn content. A potential reason for this could be if defect formation in these layers precedes the Sn out diffusion. Indeed, defect formation would lead to an increase in the in-plane lattice constant hence, relaxing the layer. The subsequent Sn out diffusion due to the thermal anneal would not lead to a compression of the lattice.

The above observations indicate that Sn cluster formation, i.e. Sn redistribution, is a result of the layer trying to reach its thermodynamic equilibrium and has minimal influence on layer relaxation and defect formation is potentially the main cause of relaxation in the layers relaxing due to the thermal anneal. Indeed, an increase in defect density on annealing these layers has been reported extensively in literature [127, 143, 144]

4.3 Conclusions

In this chapter, we used L-APT to gain insight into the relaxation mechanisms in strained $Ge_{(1-x)}Sn_{(x)}$ layers. In order to do this we first:

- Verified the absence of field induced artefacts like preferential evaporation, co-evaporation, local magnification etc. in the studied

$Ge/Ge_{(1-x)}Sn_{(x)}/Ge$ sample structure. This leads to the conclusion that Ge and Sn inside the $Ge_{(1-x)}Sn_{(x)}$ layer have a similar evaporation field at variance with the different values for pure Ge and β-Sn in scientific literature. This discrepancy between experiment and theory may be explained considering that the field evaporation threshold is a function of the local environment of the evaporating element, as well as its bonding, which is very different in alloys as compared to pure materials. Furthermore, the theoretical values reported in literature were calculated using the Mueller Schottky model which as discussed in Chapter 2, is not accurate for semiconductors.

- Verified the presence asymmetrical laser absorption leading to density variations in the reconstructed data. A density difference of ~3 at% was observed from the illuminated to the shadow side. To negate the impact of these density variations, statistical analysis were done on sub-volumes having uniform densities.

- Studied the impact on laser and field on the quantification of $Ge_{(1-x)}Sn_{(x)}$. For quantitative analysis of these layers an optimum pulse fraction of 20 % - 30 %) was observed. Experimentally, this optimum range can be controlled by maintaining the Sn^{2+} CSR between 50 % - 70 %.

- Developed a new cluster analysis algorithm to extract Sn clusters within a random Sn distribution.

Mechanisms for strain relaxation were studied in layers relaxing due to their thickness or due to a post growth rapid thermal anneal treatment. Our findings suggest that the main relaxation mechanism in these layers is potentially defect formation irrespective of the cause of relaxation. No Sn clusters were observed in the layers relaxing due to increased layer thickness. For the layers relaxing during a thermal anneal, Sn clusters were observed for an anneal temperature between 580 °C-640 °C. At higher temperature, the layer reaches its thermodynamic equilibrium Sn concentration of 1.5 at%, through surface segregation and precipitation. Nonetheless, no correlation could be established between Sn-cluster formation and the strain relaxation degree of the layer, implying that Sn-cluster formation has little or no effect on layer relaxation.

Atomic insight into $Ge_{1-x}Sn_x$ using Atom Probe tomography

Arul Kumar[1,2], Manu P. Komalan[1], Haraprasanna Lenka[1,2], Ajay Kumar Kambham[1,2], Matthieu Gilbert[1], Federica Gencarelli[1,3], Benjamin Vincent[1], Wilfried Vandervorst[1,2]

[1]Imec vzw, Kapeldreef 75, Heverlee – 3001, Belgium

[2] Instituut voor Kern- en Stralingsfysica, KU Leuven, Celestijnenlaan 200D, B-3001 Leuven, Belgium

[3] Department of Metallurgy and Materials Engineering, KU Leuven, Kasteelpark Arenberg 44, Leuven, Belgium

Ultramicroscopy 132, 171 (2013); doi:10.1016/j.ultramic.2013.02.009

Abstract

$Ge_{(1-x)}Sn_{(x)}$ is receiving a growing interest in the scientific community, as it has important applications in opto-electronic devices, (as stressor) Source/Drain materials for Ge and SiGe MOSFETS. It is predicted that at 10% Sn concentration or even lower, unstrained $Ge_{(1-x)}Sn_{(x)}$ will exhibit a direct band gap. Moreover, in strained $Ge_{(1-x)}Sn_{(x)}$ the expected concentration of Sn for this cross-over is even lower.

As the theoretical Sn incorporation in $Ge_{(1-x)}Sn_{(x)}$ is less than 1%, and $Ge_{(1-x)}Sn_{(x)}$) is prone to relaxation, routes towards the growth of metastable strained films has been extensively explored. Although $Ge_{(1-x)}Sn_{(x)}$ films (with x up to 10%) have been grown using various methods like molecular beam epitaxy, CVD growth etc. there remain issues with tendency of these layers to relax. Detailed studies on the relaxation mechanisms and effects on the Sn-atoms require suitable characterization techniques. Various techniques have been used to study the surface of the film, crystallography or concentration of Sn in the film but none of them provides information at the atomic scale as they average over many layers and atoms. Atom probe tomography (APT) analysis, on the other hand, is one such method that can provide atomic scale resolutions (~0.3 nm) due to its ability to perform atom by atom analysis.

In this paper we explore the use of APT for characterizing $Ge_{(1-x)}Sn_{(x)}$ layers. We comment on the difference of field evaporation values of Ge and Sn in $Ge_{(1-x)}Sn_{(x)}$ layer by taking a closer look at the co-evaporation of the two elements and comment on the accuracy of depth reconstruction of APT for $Ge_{(1-x)}Sn_{(x)}$ layer. Comparing the Sn-distributions and their local surroundings we saw a tendency for the Sn to locally enrich forming Sn clusters. Higher order clusters were observed for the relaxed sample.

Introduction

$Ge_{(1-x)}Sn_{(x)}$ is receiving a growing interest in the scientific community, as it has important applications as opto-electronic devices, (stressor) Source/Drain materials for Ge and SiGe MOSFETS etc. It is predicted that at 10% Sn concentration or even lower, unstrained $Ge_{(1-x)}Sn_{(x)}$ will exhibit a direct band gap, since the point conduction band minimum decreases more rapidly than the L point valley with increasing Sn concentration [1, 2]. Moreover, in strained $Ge_{(1-x)}Sn_{(x)}$ the expected concentration of Sn for this cross-over is even lower [3, 4].

However the solubility of Sn in Ge according to thermodynamics is less than 1 at % [5]. Also there is large lattice mismatch (14.6%) between the elements and the diamond-cubic structure of α-Sn is unstable above 13°C [6]. Nevertheless, significant efforts have been made and $Ge_{(1-x)}Sn_{(x)}$ have been grown using various methods like molecular beam epitaxy, CVD growth etc. Still there are limits to thickness, concentration, annealing temperatures beyond which the layer starts to relax by segregation of Sn. Hence a characterization technique is required to study these limits and the transition regimes between fully strained and fully relaxed layers.

Various techniques like Raman spectroscopy, X-Ray Diffraction (XRD), X-Ray photoelectron spectroscopy (XPS), Reflection high-energy electron diffraction (RHEED), Rutherford Back Scattering (RBS), and Secondary ion Mass Spectroscopy (SIMS) etc. have been used to study the surface of the film, crystallography or concentration of Sn in the film. However, since these characterization techniques are inherently 1-D and average over many layers and atoms, it is virtually impossible to get an insight in the atomic scale migration (precipitation, clustering, kinetics etc.) during transition from a metastable phase to a relaxed configuration. Atom probe tomography on the other hand is inherently 3-D and also enables us to probe the atomic scale as it is essentially an atom by atom analysis characterization technique. Therefore we implemented the use of atom probe tomography to study the (re)-distribution of Sn atoms at the atomic scale in the Ge matrix during the transition from a fully strained to a partially relaxed layer.

In this paper we describe the use APT for characterizing $Ge_{(1-x)}Sn_{(x)}$ layers. We comment on the difference of field evaporation values of Ge and Sn in $Ge_{(1-x)}Sn_{(x)}$ layer by taking a closer look at the co-evaporation of the two elements and comment on the accuracy of depth reconstruction of APT for $Ge_{(1-x)}Sn_{(x)}$ layer. We also propose a correlation between

the formation of higher order Sn-Vacancy complexes (Sn_xV_y) and the relaxation of the layer.

2. Experimental details

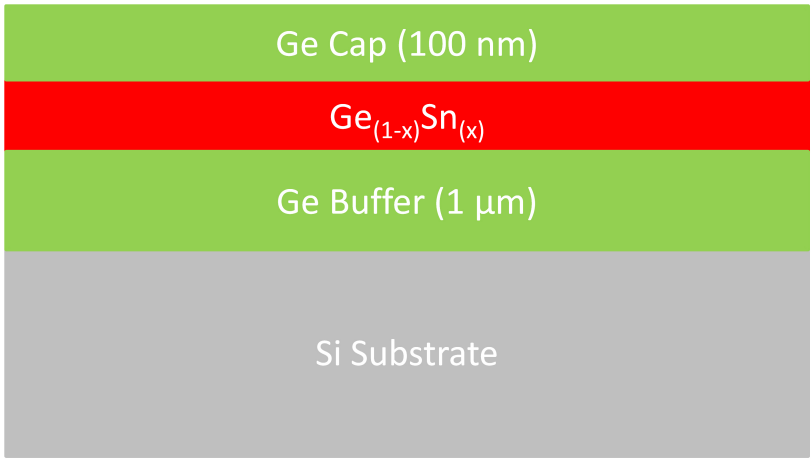

Figure 4.11 – Schematic of the sample for L-APT analysis

$Ge_{(1-x)}Sn_{(x)}$ samples were grown using the CVD technique; the details of the CVD growth is given in Reference [7] and [8]. The sample structure is shown in figure 4.11. $Ge_{(1-x)}Sn_{(x)}$ layers were grown on a <100> oriented, epitaxially grown Ge Buffer layer on a Si substrate. Two samples were measured using APT, a fully strained ∼40 nm thick $Ge_{(1-x)}Sn_{(x)}$ (sample A) and a partially relaxed, ∼142 nm thick $Ge_{(1-x)}Sn_{(x)}$ sample (sample B), with targeted Sn concentrations (x) of ∼5 %. To facilitate the focused ion beam preparation of the APT-tip, a 100 nm Ge layer was grown in-situ on top of the $Ge_{(1-x)}Sn_{(x)}$ layers. The XRD measurements of the sample are shown in figure 4.12 and we can clearly see that sample A is fully strained sample B is partially relaxed (26%). The strain relaxation degree R was calculated as:

$$R = \frac{(a_{//GeSn} - a_{//Ge})}{(a_{0GeSn} - a_{//Ge})} \tag{4.3}$$

where a_{0GeSn} is the experimental relaxed GeSn lattice constant and $a_{//GeSn}$ and $a_{//Ge}$ are the experimental in-plane GeSn and Ge lattice

constants, respectively. These lattice constants value were determined by High-resolution X-ray diffraction reciprocal space mapping (HR-XRD RSM) of the asymmetric (224) GeSn and Ge Bragg reflections using the Bede Metrix-L XRD tool, with a wavelength of the incident X-rays of λ=1.54 Å.

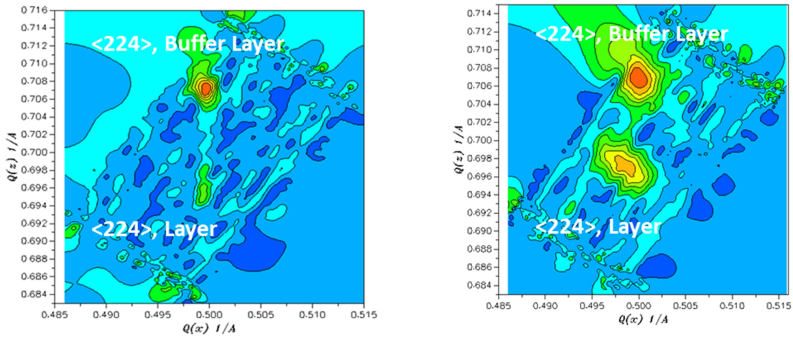

Figure 4.12 – HR-XRD RSM map of sample A (left) and Sample B (right). For sample A the diffraction peaks coming from the substrate and the layer lie on the same line with an in-plane lattice parameter of 0.5664 nm, while the diffraction peaks in sample B the diffraction peaks from the substrate and the layer do not lie on the same line with an in-plane distance of 0.56595 nm for the layer. The $Ge_{(1-x)}Sn_{(x)}$ layer for sample B is 26% relaxed.

To prepare the tip for APT analysis annular Focused ion Beam (FIB) milling was done using the lift out method [9]. The tips were made using a FEI NOVA-600 FIB. After the annular milling to form the desired tip shape the oxide layer between the Ge cap layer and the Pt deposited during lamella preparation needed to be removed as the oxide layer evaporated erratically leading to tip failure. Ge develops severe topography [10] under Ga-irradiation (Figure 4.13) hence the cleaning had to be done at extremely low ion beam currents (1.6 pA) and at low voltage (5 kV) as at high beam currents the tip deforms.

The L-APT analysis was done on Laser Assisted Wide Angle Tomographic Atom Probe (LAWATAP) from Cameca. This system is equipped with a laser generating 400 fs pulses at a wavelength of 1030 nm (IR) (~1-60 mW), 515 nm (green) (~0.6-10 mW), or 343 nm (UV) (~0.3-60 mW).

The experiment was carried out at 15 K and at a wavelength of 515 nm (green). The raw data was reconstructed using 3D data software from Cameca using the voltage curve reconstruction method. To determine

the pulse fraction curves (figure 4) 50 000 atoms were collected for each point.

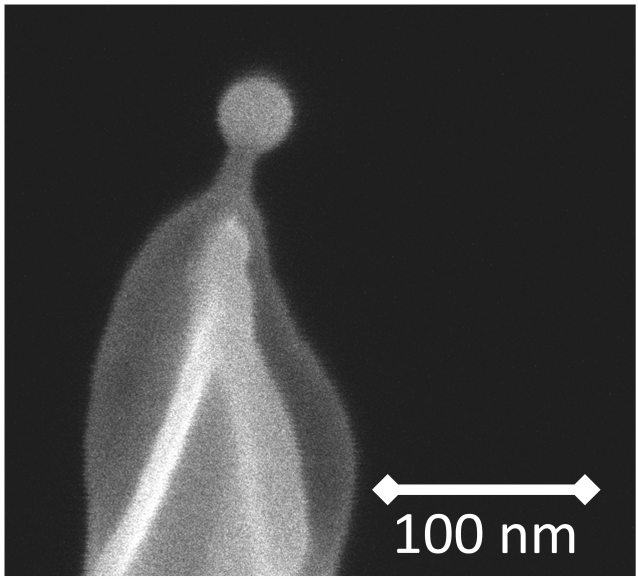

Figure 4.13 – SEM image of a deformed tip due to cleaning at high currents (9.7 pA) and voltage (30 kV)

Angular-dependent channeling Rutherford Backscattering Spectroscopy (RBS/C) Channeling experiments were performed along the <100> axial direction to quantify the fraction of Sn atoms on substitutional, interstitial, and random sites in the epitaxial $Ge_{(1-x)}Sn_{(x)}$ films. The RBS/C experiments were performed using 2.0 MeV He+ ions from the 6SDH tandem accelerator (NEC, USA) equipped with an Alphatross ion source. The experimental end-station was a 5-axis goniometer developed at the Forshungszentrum Jülich [11]. The solid angle of the PIPS detector was 0.42 msr, the scattering angle was 170°. A standard acquisition setup with detector energy resolution of about 16 keV was used. The beam spot was confined to 1x1 mm^2, the current was limited to 10 nA, and the accumulated charge was 40 μC. In-house developed analysis software was used to fit the spectra and to deduce the concentration. The fraction of Sn in substitutional sites (SnGe) of the $Ge_{(1-x)}Sn_{(x)}$ films was calculated from the measured minimum back scattered yields χ_{Ge} and χ_{Sn} using

the expression [12], Sn substitutionality in Ge = Sn_{Ge} = (1 - χ_{Sn}) / (1 - χ_{Ge}).

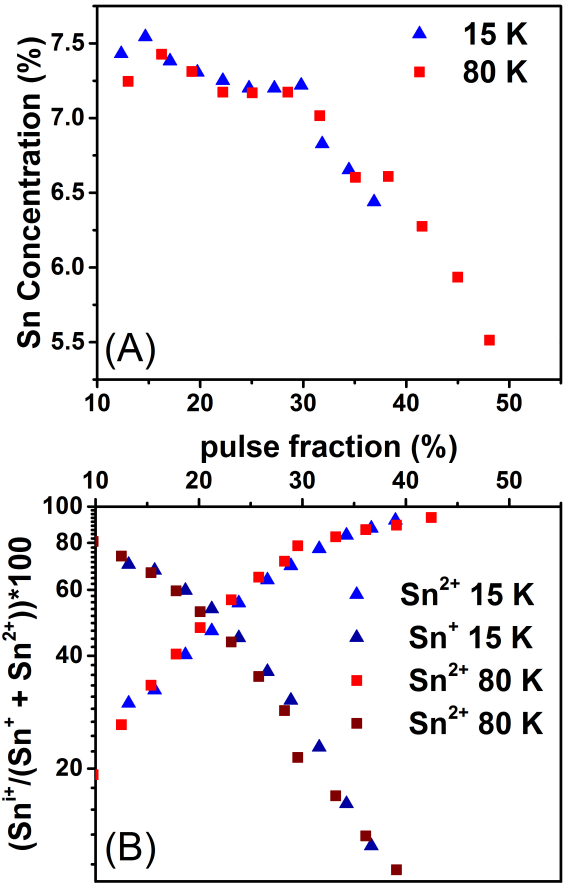

Figure 4.14 – (a) Effect of laser power and temperature on total Sn content. (b) Effect of laser power and temperature on (Sn^{2+}/(Sn^{+}+Sn^{2+}))*100 and (Sn^{+}/(Sn^{+}+Sn^{2+}))*100.

3. Results and Discussion

Since no atom probe results on the $Ge_{(1-x)}Sn_{(x)}$ layer existed yet, our initial work was to establish the correct experimental conditions (like laser power, sample temperature, reconstruction parameters etc.) in order to have reliable qualitative and quantitative results. To study the effect of laser power and temperature, pulse fraction curves at different temperatures were measured. Figure 4.14(a) shows the pulse fraction [13] v/s the Sn content measured. We observe that Sn-concentrations consistent with RBS data are obtained for pulse fractions between 20 %-30 % while for high pulse fractions (35 %-50 %) these appear underestimated. Also molecular clusters were seen in the mass spectra at higher pulse fractions. We suspect that evaporation in-between laser pulses might be occurring leading to the reduced detection of Sn atoms. On the other hand at low pulse fraction (~10 %-20 %), higher Sn concentrations were observed as compared to RBS and XRD values. Since we see an increase in the Sn concentration, it seems that we preferentially loose Ge atoms due to DC evaporation [14] whereby Ge would have a lower field evaporation versus Sn. The presence of DC-evaporation is evident by looking at the counts collected in the (long, 10msec) time window in between two laser pulses. Their detection/emission without correlation to the laser pulses is indicative of a (DC)-field induced emission whereby the absence of any timing signal prevents their mass identification. They are typically rejected from the raw data but stored in the LAWATAP in a separate counter. We observe that these counts increased from 400-500 to ~900-1200 for a 50 000 collected atoms under conditions of low pulse fractions i.e. high DC-fields. It is clear, as shown in Figure 4.14a, that the window for the pulse fraction leading to a correct quantification, is very narrow. At the same time it is observed that a correct choice of Sn^{2+} pulse fraction, i.e. 47 % - 70 %, leads to a Sn^{2+}/Sn^{+} ratio between 0.43 and 1.14 (Figure

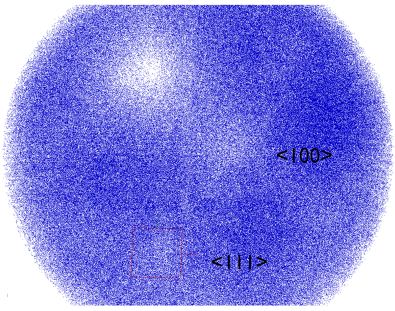

Figure 4.15 – Crystallographic poles seen at 15K.

4.14(b)). Hence we can use this ratio as a monitor for the pulse fraction and use it as control parameter for adjusting the laser power.

With respect to the sample temperature during the evaporation of the $Ge_{(1-x)}Sn_{(x)}$ layers, we note that at a sample temperature of 15 K poles become visible (figure 4.15) whereas these are absent at 80 K. Planes were clearly visible in the reconstructed images of the raw data obtained at 15 K. Thus we can assume that the thermal migration at 15 K was suppressed in the sample. The samples were reconstructed using the voltage curve reconstruction method in the reconstruction software.

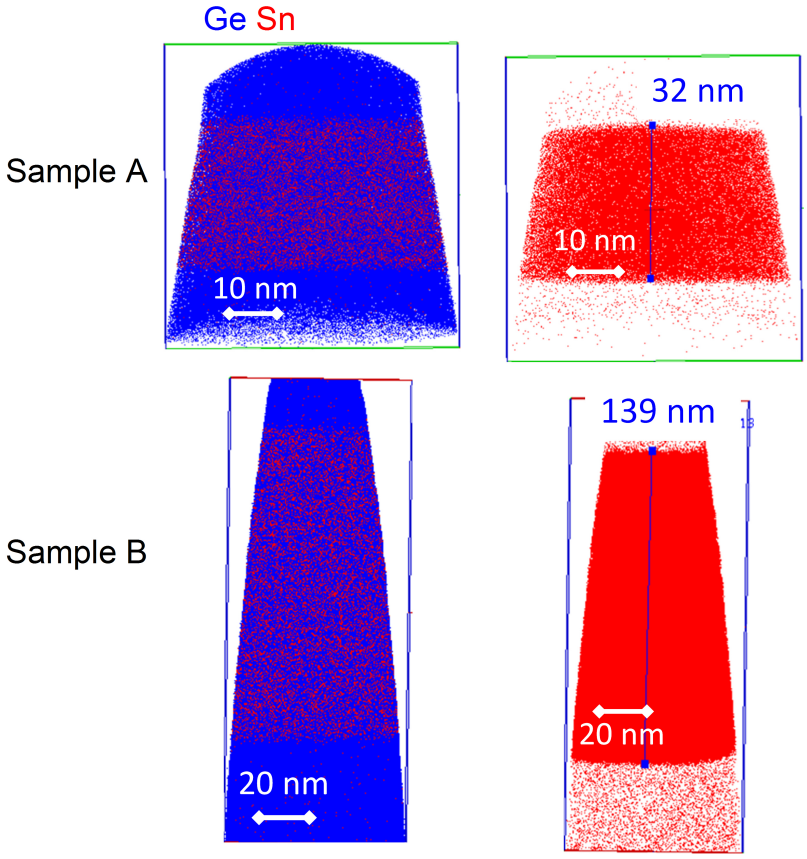

Figure 4.16 – Reconstructed APT data. The thickness of the Sample A obtained from the APT is 32 nm and of sample B is 139 nm.

The flux variations in the whole experiment were within acceptable limits and no irregular humps were seen in the voltage during the transition from the Ge layer to the $Ge_{(1-x)}Sn_{(x)}$ layer and vice versa. Thus we can safely assume that the field evaporation values of Ge and $Ge_{(1-x)}Sn_{(x)}$ layer are similar. Therefore reconstruction artifacts due to dissimilar field evaporation values are not expected. To find the optimum reconstruction parameters a number of considerations were included. These are : the expected thickness of the layer from RBS measurements, the (planarity of the) curvature of the interface between $Ge_{(1-x)}Sn_{(x)}$ layer and Ge, the distance between the atomic planes in the Ge buffer layer, the curvature of the atomic planes in the $Ge_{(1-x)}Sn_{(x)}$ and the Ge buffer layer. The reconstruction parameters were first roughly estimated to keep the interface between the Ge and the $Ge_{(1-x)}Sn_{(x)}$ layer straight and the thickness of the $Ge_{(1-x)}Sn_{(x)}$ layer close to the RBS-values. The reconstruction parameters were further fine-tuned to have the best agreement with the expected value of the distance between <111> planes in the Ge-buffer layer and to keep them straight and not following the tip curvature. It was found that the ratio between projection point (~2.2) and Eβ (~18) should be ~0.12 for the correct reconstruction. The reconstructed data is shown in figure 4.16.

A comparison of the data for the concentration and the thickness obtained from APT and RBS is shown in table 4.2. The values for the Sn concentration as obtained from APT and RBS are nearly the same. Also the thickness of the $Ge_{(1-x)}Sn_{(x)}$ layer of sample B was the same for APT and RBS. The larger difference in the thickness values for sample A (nominally 40 nm) is probably a shortcoming of the RBS measurements as for this case there is a large uncertainty due to the lack of depth resolution in the used configuration. TEM imaging of sample A confirmed a thickness of 31 nm of the $Ge_{(1-x)}Sn_{(x)}$ layer.

Sample	Thickness from RBS (nm)	Thickness from APT (nm)	Concentration from RBS (atomic %)	Concentration from APT (atomic %)
A	22±3	32	6.6±0.7	6.68±0.025
B	142±8	139	6.4±0.5	6.58±0.009

Table 4.2 – Comparison of thickness and concentration values obtained from RBS and APT

In order to assess the difference in the field evaporation values of Ge and Sn in $Ge_{(1-x)}Sn_{(x)}$ and the potential presence of reconstruction

artifacts (like displacement of atoms along the depth) originating from this difference we perform a detailed analysis of the multihits, which are counts from two of more atoms which evaporate at the same laser pulse. For single element materials (Ge, Si,..) under normal evaporation conditions the number of multihits is about 5 % of the total number collected atoms. For an alloy (composed of two or more elements), co-evaporation of the element with the lowest field evaporation value together with the element of the highest field evaporation value will occur thereby leading to an increase in multihits. Hence if the field evaporation values of Ge and Sn in $Ge_{(1-x)}Sn_{(x)}$ were very different, co-evaporation of the two elements would occur which would show up as increased multihits. Moreover if Sn were to co-evaporate with Ge, one would expect to see that the atoms contained in the multihits would reflect the average Sn concentration.

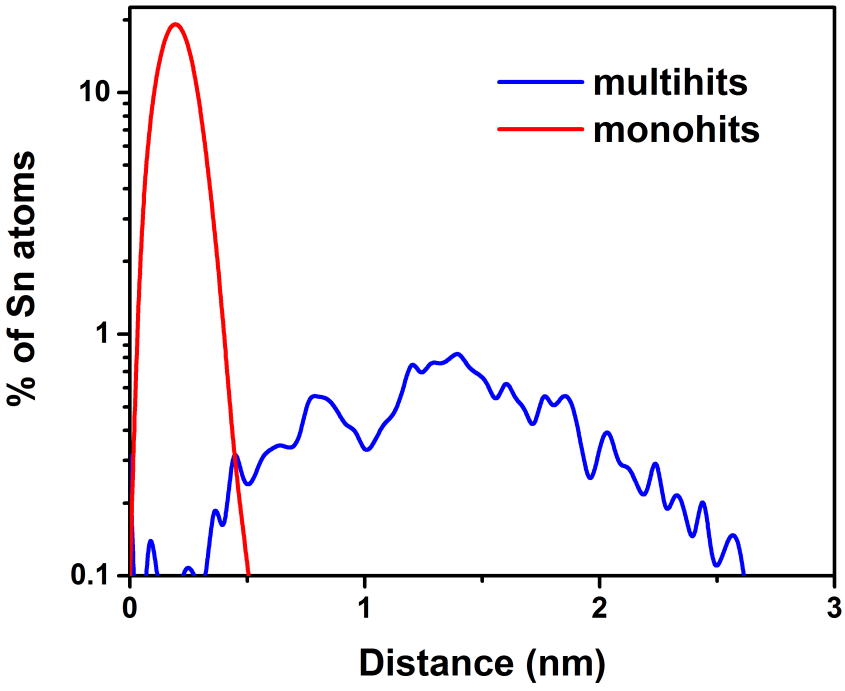

Figure 4.17 – In Red, 1st nearest neighbor distance distribution for Sn within the multihits if co-evaporation of Sn with Ge would occur. In Blue, observed distance distribution between Sn atoms and the corresponding co-evaporated atom, for all the multihits.

In practice we see that there is no increase in multihits, hence > 95% of all atoms evaporate as single atoms implying that the reconstructed distributions will not be affected by co-evaporation effects. Moreover the atomic concentration of Sn in the multihits was roughly < 3.5% instead of 7%, pointing towards a lower probability of Sn to co-evaporate with Ge. Further, a distance distribution graph, confined to the small fraction of atoms contained in the multihits, was plotted (using MATLAB) between the Sn atoms and the closest atom that evaporated concurrent with it (Figure 4.17). While the most probable distance for the first nearest atoms (Figure 4.17) was ~2-2.4 Å, a broad distribution, peaking around 15 Å is seen for the multihits. As this distance reflects the spacing between these two atoms on the tip surface (not a depth distribution) it indicates that in the majority of cases in a multihit, the atom which is co-evaporated with Sn, was NOT a neighboring atom, thereby ruling out that Sn preferentially co-evaporates with Ge. In fact the observations of preferentially loosing Ge atoms in the DC evaporation regime and Ge and Sn not co-evaporating in the $Ge_{(1-x)}Sn_{(x)}$ layer and the absence of any increase in multihits in the $Ge_{(1-x)}Sn_{(x)}$ alloy versus the Ge substrate, indicate that the field evaporation value of Sn in the $Ge_{(1-x)}Sn_{(x)}$ layer are very similar to Ge in the $Ge_{(1-x)}Sn_{(x)}$ layer. Hence it is fair to state that reconstruction artifacts induced by differences in field evaporation values are limited and that if atomic planes are visible in the reconstruction the location of the Ge and the Sn atoms within those planes reflects their true in-plane location and not a measurement artifact. As discussed already due to the different depth versus lateral resolution of APT it is possible to identify the location of atoms within/outside the lattice planes but not their interstitial versus substitutional position within the lattice plane.

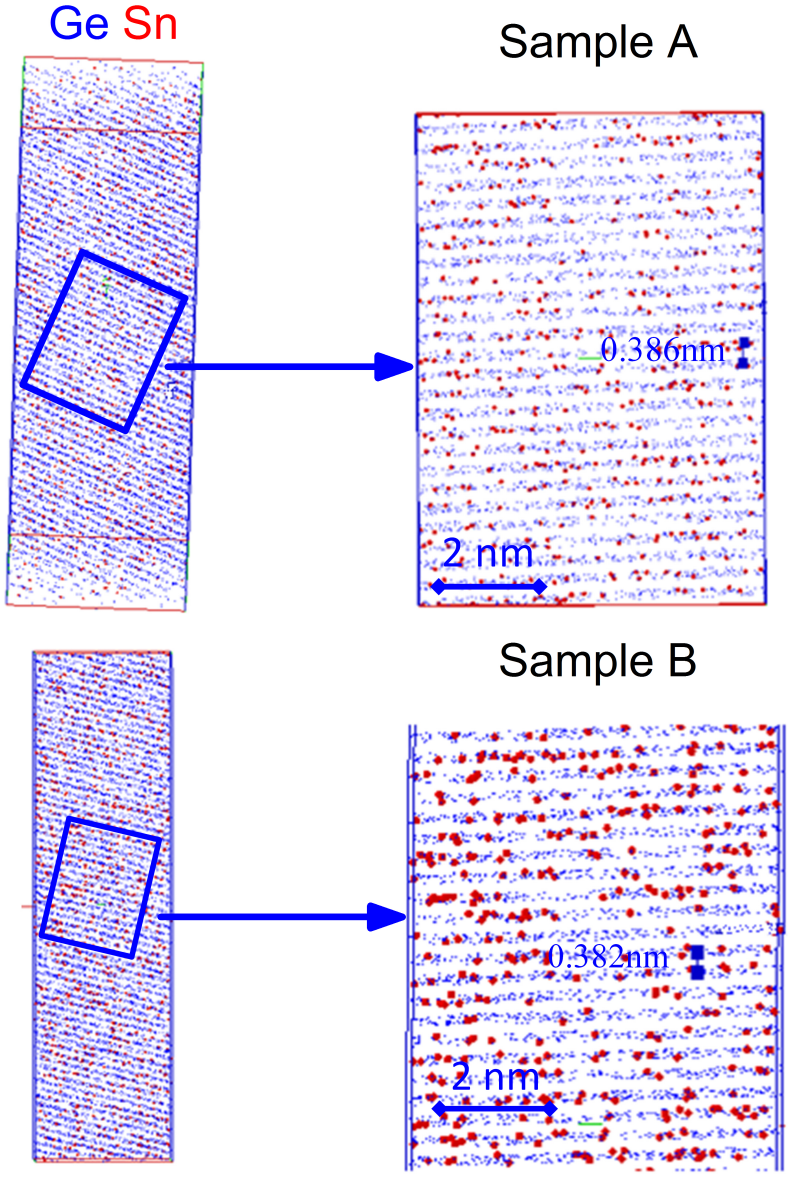

Figure 4.18 – Planes in the <111> direction in Sample A (top) and Sample B (below)

This superior depth resolution can be exploited or the characterization of $Ge_{(1-x)}Sn_{(x)}$ layers as we were able to visualize atomic planes in the <111> direction (Figure 4.18). To observe these planes clearly, a Fourier Transform Filter (FTF) [15] with a threshold filter of 30 % was used. By doing a comparison of the Sn concentration in the volume before and after the Fourier transform filtering (table 4.3), we observed that the concentration of Sn did not change for the fully strained samples (Sample A) while there was a slight decrease in the concentration of Sn (0.2% for sample B, i.e. 3% of the total amount of Sn atoms is now detected outside a lattice plane) for the relaxed sample. The small decrease in concentration of Sn in planes, was always observed (for 12 different measurements) in the relaxed sample while for the strained sample the in-plane Sn concentration was always close to 100%. This decrease in Sn concentration can be attributed to the amount of Sn atoms which have diffused out of the lattice planes, since the Fourier transform filtering removes the atoms not located on the lattice planes. Hence we can infer that ~100% of the Sn atoms were sitting in the planes for Sample A, whereas for Sample B a few percent (3 %-5 %) appear to be missing. However due to the lack of resolution in the XY direction due to trajectory aberration, arising due to various thermal and electrostatic effects, it is not possible to conclude anything on the position of atoms in the plane. Although one could argue that APT is not suitable as an absolute technique for these kinds of measurements, we believe that the differences between the two samples are systematic and repeatable and thus reflect a real change in sample structure. The latter is confirmed by supplementary measurements using XRD and RBS channeling [12] (which are both standard analysis techniques extensively used in the semiconductor industry for probing layer relaxation and element substitutionality.)

Sample	Concentration Sn before FTF (%)	Concentration Sn after FTF (%)	Fraction of Sn in Plane
B	7.0	6.67	0.95
B	7.008	6.8	0.97
B	7.4	7.2	0.97
A	7.1	7.12	1.28
A	7.4	7.38	0.99
A	7.1	7.14	1.05

Table 4.3 – Comparison of Sn concentration before and after Fourier Transform Filter. The decrease in Sn concentration after the Fourier Transform filter can be attributed to the Sn atoms diffused out of the crystallographic planes, since the Fourier Transform filter, filters out the atoms diffused out of the planes. Hence we can infer that ~100 % of the Sn atoms were sitting in the atomic planes for Sample A, whereas 97 % of the Sn atoms were sitting in atomic planes for Sample B

To further understand the relaxation process we performed a statistical analysis on the spatial distribution of the Sn-atoms looking specifically for Sn-cluster formation. In this context we define clusters as regions where the Sn-concentration supersedes the average Sn-concentration locally substantially. To probe this localized Sn concentration, we generate a histogram of the actual Sn concentration in a small volume. The input value for the cluster analysis is the radius of the small volume used to assess the "local" deviation from the average concentration. The input values are calculated based on the following reasoning. If one considers an average Sn-concentration of 7 %, the number of Ge atoms surrounding 1 Sn atom for a homogeneous distribution of Sn is 13. Vice versa one can define around each Sn-atom a volume of 13 atoms which will (on average) contain one Sn-atom and 13 Ge-atoms (i.e. the total volume contains 14 atoms). The parameters used for cluster identification are listed in table 4.4 whereby we apply the above reasoning using the Sn concentration in the volume of analysis.

Sample	Radius of analysis volume (Å)	Threshold concentration (Sn_2V)	Threshold concentration (Sn_4V_2)	% of Sn atoms in Sn_2V	% of Sn atoms in Sn_4V_2
A	5.64	15.1	32.6	39 %	5.40 %
B	5.59	14.7	31.75	31 %	20.50 %

Table 4.4 – Value of threshold concentration and the radius of analysis volume used for cluster analysis.

The results of the above analysis are shown in **Fig.** 4.19. We observed that for sample A ~39 % of the Sn atoms were located in a volume with a localized concentration of ~14 % whereas for sample B this is only 31 %. Moreover in Sample A we found that 5.4 % of the Sn atoms is contained in a volume with a localized concentration of ~30 % whereas in Sample B this amounts to 20.5 %. Finally it is noteworthy that substantial amounts of Sn are found in volumes with higher localized concentrations as compared to the average Sn concentration pointing towards the existence of Sn in a clustered form. It is worthwhile to note that A. Chroneos et al. predicted theoretically the formation of stable Sn2-vacancy (Sn2V) in $Ge_{(1-x)}Sn_{(x)}$ [17] and also predicted negative activation energies for the further clustering of such vacancy complexes. The discrete peaks in distribution of Sn at specific concentration values (multiples of the average concentration) are explained by the formation of Sn complexes. Although we cannot detect vacancies, their occurrence at values of (15, 23,...) is indicative of Sn vacancy complexes. Indeed within a volume with a Sn_2V complex, two Sn atoms are very close by and the Sn concentration in this local volume is nearly twice the average concentration as the number of Sn atoms in the 14-atom volume is now 2 and the number of Ge atoms is reduced to 11 because of the replacement of 2 Ge atoms by one vacancy and the additional Sn atom. A similar calculation can be made to explain the other localized concentrations assuming that they are based on the agglomeration of Sn-vacancy complexes (Sn_xV_y). The presence of an increased amount of more complex clusters (Sn_4V_2, Sn_3V) for the relaxed layer suggests that the formation of these complex clusters occurs concurrently with the relaxation of the $Ge_{(1-x)}Sn_{(x)}$ layers.

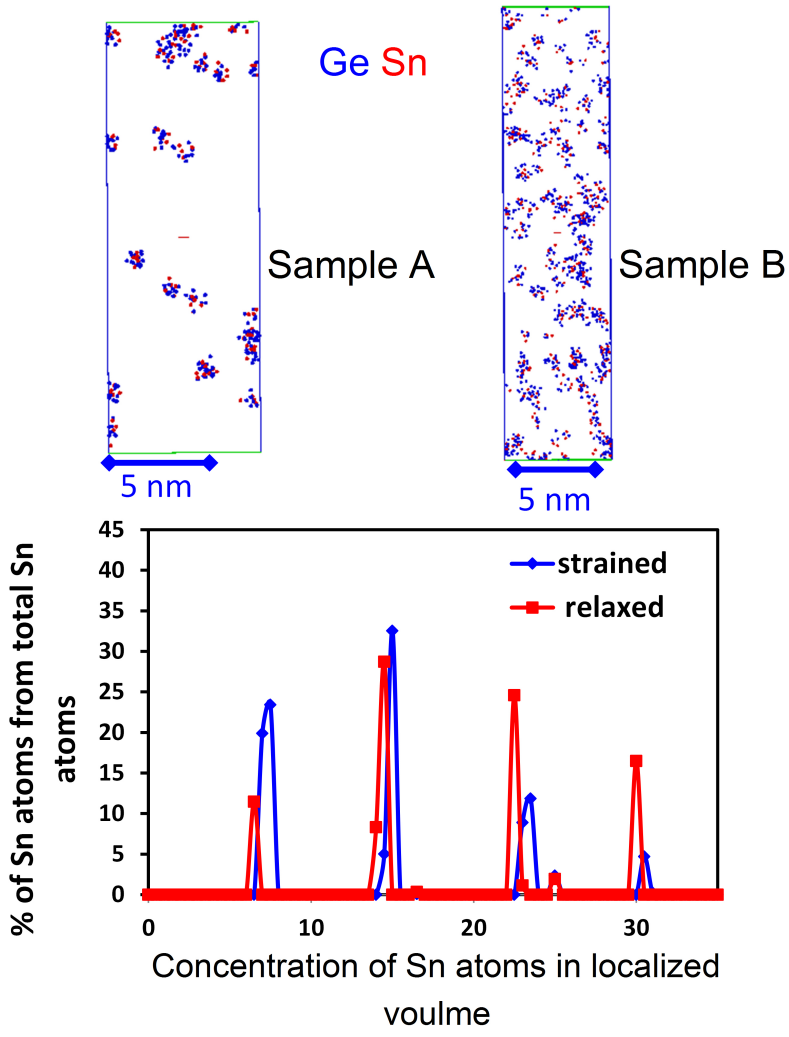

Figure 4.19 – (A) Cluster formation in $Ge_{1-x}Sn_x$ layer in sample A (left) sample B (middle) from cluster identification tool. (B) Localized Concentration Distribution of Sn using Fixed volume approach

4. Conclusion

In this paper we study $Ge_{(1-x)}Sn_{(x)}$ layers using atom probe tomography. We describe the optimum operating conditions to accurately measure the $Ge_{(1-x)}Sn_{(x)}$ layer and demonstrate that the optimum pulse fraction is between 20% and 30%. The latter can be diagnosed during the analysis by monitoring the Sn^{2+}/Sn^{+} ratio. Also at 15 K it was possible to see crystallographic poles and lattice planes after Fourier transform filtering.

In order to assess potential reconstruction and/or evaporation artifacts, we analyzed the multihits and concluded that no increase from a regular multihit frequency can be observed. Only Furthermore within those multihits only ~0.1 % of the co-evaporated atoms were neighboring atoms. These observations lead us to believe that the difference in the field evaporation values of Ge and Sn is minimal and does not lead to errors in the reconstructed distributions.

We observe that the Sn atoms are sitting in the lattice planes for fully strained with a 3 % reduction for a partially relaxed sample consistent with XRD and RBS channeling observations. When comparing a strained and a relaxed layer, we found that 39 % of the Sn atoms were sitting in Sn_2 vacancy complexes in the strained case as compared to 31% in the relaxed sample. Moreover while only 5.4% of the total Sn atoms were seen in the Sn_4V_2 complex configuration for the strained sample, this increases to 20.5% of the total Sn-content in the relaxed sample. This suggests a correlation between the formation of larger Sn-vacancy complexes and relaxation of the $Ge_{(1-x)}Sn_{(x)}$ layers.

Acknowledgments

The authors would like to thank CAMECA for the technical support. We would also like to thank Janusz Bogdanowicz for helpful discussions relating to laser matter interaction.

References

[1] G. He and H. A. Atwater, Phys. Rev. Lett. 79, 1937 (1997).
[2] V. R. D'Costa, C. S. Cook, A. G. Birdwell, C. L. Littler, M. Canonico, S. Zollner, J. Kouvetakis, and J. Menendez, Phys. Rev. B 73, 125207 (2006).
[3] P. Moontragoon, Z. Ikonic, and P. Harrison, Semicond. Sci. Technol. 22 742 (2007).
[4] J. Mathews, R. T. Beeler, J. Tolle, C. Xu, R. Roucka, J. Kouvetakis, and J. Menendez, Appl. Phys. Lett. 97, 221912 (2010).
[5] J.P. Fleurial, A. Borshchevsky, Si-Ge-Metal Ternary Phase Diagram Calculations, J. Electroch. Soc., 137 (9), 2928 (1990).
[6] O. Gurdal, R. Desjardins, J. R. A. Carlsson, N. Taylor, H. H. Radamson, J.-E. Sundgren, and J. E. Greene, J. Appl. Phys. 83, 162 (1998).
[7] F. Gencarelli, B. Vincent, L. Souriau, O. Richard, W. Vandervorst, R. Loo, M. Caymax, M. Heyns, Thin Solid Films 520 (2012) 3211–3215
[8] Vincent et al., Applied Physics Letters 99, 152103 (2011)
[9] Michael K. Miller, Kaye F. Russell, Keith Thompson, Roger Alvis and David J. Larson, Microscopy and Microanalysis, 13 , pp 428-436 (2007)
[10] R.J. Kaiser, S. Koffel, P. Pichler, A.J. Bauer, B. Amon, A. Claverie, G. Benassayag, P. Scheiblin, L. Frey, H. Ryssel, Thin Solid Films, 9, pp 2323–2325 (2010)
[11] B. Holländer, H. Heer, M. Wagener, H. Halling, and S. Mantl, Nucl. Instrum. Methods B 161-163, 227-230 (2000).
[12] L.C. Feldman, J.W. Mayer, S.T. Picraux, in: Materials Analysis by Ion Channeling, Academic Press, New York, 1982
[13] Joseph H. Bunton, Jesse D. Olson, Daniel R. Lenz, and Thomas F. Kelly, Microsc. Microanal. 13, 418–427, 2007
[14] A. Cerezo, P.H. Clifton, A. Gomberg, G.D.W. Smith, Ultramicroscopy 107 (2007) 720–725
[15] P.J. Warren, A. Cerezo, G.D.W. Smith, Ultramicroscopy 73 (1998) 261,266.
[16] A. Chroneos, C. Jiang, R. W. Grimes, U. Schwingenschlögl, and H. Bracht, App. Phys. Lett. 94, 252104 (2009)

On the interplay between relaxation, defect formation, and atomic Sn distribution in $Ge_{(1-x)}Sn_{(x)}$ unraveled with Atom Probe Tomography

A Kumar[a,b], J Demeulemeester[b], J Bogdanowicz[b], J Bran[a,b], D Melkonyan[a,b], C Fleischmann[b], F Gencarelli[b,c], Y Shimura[a,b,d], W Wang[b,c], R Loo[b], W Vandervorst[a,b]

[a] Instituut voor Kern- en Stralingsfysica, KU Leuven, Celestijnenlaan 200D, B-3001 Leuven, Belgium

[b] Imec vzw, Kapeldreef 75, Heverlee – 3001, Belgium

[c] Department of Metallurgy and Materials Engineering, KU Leuven, Kasteelpark Arenberg 44, Leuven, Belgium

[d] Flemish Research Foundation (FWO), Pegasus Marie Curie Fellow

J. Appl. Phys. 118, 025302 (2015); http://dx.doi.org/10.1063/1.4926473

Abstract

$Ge_{(1-x)}Sn_{(x)}$ has received a lot of interest for opto-electronic applications and for strain engineering in advanced Complementary-Metal-Oxide-Semiconductor (CMOS) technology, because it enables engineering of the band gap and inducing strain in the alloy. To target a reliable technology for mass application in microelectronic devices, the physical problem to be addressed is to unravel the complex relationship between strain relaxation (as induced by the growth of large layer thicknesses or a thermal anneal) and defect formation, and/or stable Sn-cluster formation. In this paper we study the onset of Sn-cluster formation, and its link to strain relaxation using Atom Probe Tomography (APT). To this end, we also propose a modification of the core-linkage cluster analysis method [1], to overcome the challenges of, limited detection efficiency and lateral resolution of APT, and the quantitative assessment for very small clusters (<40 atoms) embedded in a random distribution of Sn-atoms. We concluded that the main relaxation mechanism for these layers is defect generation (misfit dislocations, threading dislocations etc.), irrespective of the cause (thickness of layer or thermal anneal) of relaxation and is independent of the cluster formation. The low thermodynamic solubility limit of Sn in Ge seems to be the driving force for Sn-cluster formation. Finally, we also discuss the spatial distribution of Sn in clusters and relate them to the theoretically predicted stable Sn clusters [2].

Introduction

The continuous scaling of Complementary Metal Oxide Semiconductor (CMOS) devices to increase the performance and functionality of modern microelectronic based systems has stimulated research in alternative materials to silicon. Ge based alloys are among the most promising materials for a high mobility metal-oxide-semiconductor-field-effect-transistor (MOSFET) [3]. In particular, in recent years a lot of effort has been put into the understanding of the growth and the fundamental properties of $Ge_{(1-x)}Sn_{(x)}$ layers [4,5], since $Ge_{(1-x)}Sn_{(x)}$ has appealing properties as a stressor material for high mobility Ge-CMOS devices. For instance, it has been shown that with a Sn concentration of ~5 % in the $Ge_{(1-x)}Sn_{(x)}$ S/D regions, enough stress is created in the Ge channel to outperform the hole mobility in strained Si-MOSFET [6]. Furthermore $Ge_{(1-x)}Sn_{(x)}$ layers are also being considered for 'all group-IV' optoelectronic devices, as simulations indicate an indirect to direct band transition at a Sn concentration of 8 % [7].

However, introducing substitutional Sn in a Ge matrix has proven to be a difficult task owing to the low thermodynamic solubility of Sn in Ge (<1 % at 231 °C) [8]. Moreover, the lattice constant of $Ge_{(1-x)}Sn_{(x)}$ layers is a function of the Sn content of the layer, due to the large lattice mismatch (17 %) between α-Sn and Ge. This further complicates the growth of high quality epitaxial layers, with the desired strain (compressive, tensile or relaxed) and sufficiently high Sn content (5 %-10 %) on Si or Ge substrates. The relevant physical properties, such as strain, band gap, charge carrier mobility etc. and hence the device performance are critically linked to defects and the Sn distribution in the layer. Therefore, a fundamental understanding is needed of the underlying material physics of defect formation and Sn distribution/redistribution in these layers during relaxation. In general, strained layers tend to relax (1) when grown above a threshold layer thickness (Blakeslee limit [9]) or (2) when thermally annealed above a critical temperature (thermal stability). Upon layer relaxation the formation of crystal defects like misfit dislocations, threading dislocations has been reported [5]. Also Sn cluster formation has been suggested as a possible relaxation mechanism, theoretically [2] as well as experimentally in a combined Transmission Electron microscopy (TEM) and Energy-dispersive X-ray spectroscopy (EDS) study [10]. Nonetheless, the complex relation between strain relaxation, and the formation of defects and/or Sn clusters still remains

unresolved, both for thickness or annealing induced relaxation. Grasping the (additional) role of Sn cluster formation therein would require their detection at very early stages of nucleation, which is however virtually impossible via conventional techniques (like TEM) due to their limited sizes (a few tens of atoms), their dispersion in a random Sn-distribution and low density (Number of clusters/cm^3).

Atom Probe Tomography (APT) offers an excellent approach to gain insight in the relation between relaxation and Sn cluster formation as APT assesses the atomic 3D distribution with near atomic resolution (0.5 Å – 3 Å). Since APT provides chemical identification with equal detection probability for all elements, it is fully quantitative. In literature [11,12] it has been demonstrated that, by using optimized data mining techniques on APT data, one can get information about the presence of clustered atoms and their 3-D distribution (size, composition etc.) thus providing insight into their formation mechanism. We have already demonstrated the application of APT for accurate quantitative measurements of $Ge_{(1-x)}Sn_{(x)}$ thin films [13].

The primary objective of this paper is to study defect formation and Sn-cluster formation in $Ge_{(1-x)}Sn_{(x)}$ layer, relaxing due to increased layer thickness or due to a thermal treatment. For the analysis of ultrafine clusters (10-40 atoms) present within a random Sn-distribution, however, a more comprehensive cluster mining algorithm compared to the one described in reference 13 is needed. To this end we had to develop a new methodology for cluster analysis, extending the previously developed cluster analysis algorithms [1, 12, 14] towards a reliable identification of ultra-fine clusters (section 3). In particular when studying the early stages of cluster formation, one is faced with the challenge to detect very small clusters -defined as localized Sn-enriched regions - in a matrix of otherwise still randomly distributed Sn atoms. Moreover, APT data suffer from artificial density variations related to trajectory aberrations and limited detection efficiency (~50 %) etc. These density variations could lead to a false identification or missing of Sn-clusters. Using this algorithm, we concluded that defect formation (misfit dislocations, threading dislocations etc.) is the main reason for layer relaxation irrespective of the cause of relaxation (thickness or thermal anneal). While Sn-cluster formation had little or no effect on relaxation. The solid solubility limit of Sn in Ge was probably the only driving force for Sn-cluster formation. Finally, we also comment on the spatial distribution of Sn in clusters and relate them to the theoretically predicted stable Sn cluster configurations.

2. Materials and Methods

$Ge_{(1-x)}Sn_{(x)}$samples with a nominal Sn concentration of ~ 7 % were grown using low temperature chemical vapor deposition (CVD) on a <100> Ge pseudo substrate at 320 °C and atmospheric pressure, using Ge_2H_6 and $SnCl_4$ as the Ge and Sn precursor, respectively. A more detailed description on the film growth can be found on ref [4]. We neglect the influence of Cl as both SIMS and APT measurements detect no Cl incorporation in the $Ge_{(1-x)}Sn_{(x)}$ layers or at the GeSn/Ge interface. In order to study the impact of layer thickness and thermal anneal on layer relaxation and cluster formation, two sets of samples were prepared, one with varying layer thickness, i.e. 40, 145 and 530 nm (see series I.A – C in table 4.5) and the other one with a constant thickness (~ 80 nm) annealed (rapid thermal annealing 40 s in N_2) at various temperatures, i.e. 500, 540, 580, 620, 640 and 660 °C (series II D-I in table 4.5). The strain (and relaxation) was measured using 2 dimensional High Resolution X-Ray Diffraction Reciprocal Space Mapping (2D RSM HRXRD) [10].

sample	Structure	Treatment	SRD (%)
I.A	Ge cap (100nm) / $Ge_{0.93}Sn_{0.07}$ (40nm)	As grown	0
I.B	Ge cap (100nm) / $Ge_{0.93}Sn_{0.07}$ (145nm)	As grown	26
I.C	Ge cap (100nm) / $Ge_{0.93}Sn_{0.07}$ (530nm)	As grown	75
II.D	$Ge_{0.93}Sn_{0.07}$ (80nm)	RTA at 500°C	8
II.E	$Ge_{0.93}Sn_{0.07}$ (80nm)	RTA at 540°C	27
II.F	$Ge_{0.93}Sn_{0.07}$ (80nm)	RTA at 580°C	36
II.G	$Ge_{0.93}Sn_{0.07}$ (80nm)	RTA at 620°C	37
II.H	$Ge_{0.93}Sn_{0.07}$ (80nm)	RTA at 640°C	48
II.J	$Ge_{0.93}Sn_{0.07}$ (80nm)	RTA at 660°C	75

Table 4.5 – List of samples used

Tips suitable for APT analysis were prepared by the lift out method and sub-sequential annular Focused Ion Beam (FIB) milling [15], on a FEI NOVA-600 dual beam tool. To limit ion beam damage in the region of interest, a 100 nm Ge cap was grown in situ (at low temperature) on top of the non-annealed samples (I.A, I.B, I.C). The effect of the cap layer on relaxation was not a concern for samples relaxing due to their increased thickness (I.A – I.C), since the measured strain relaxation on layers with or without the cap was same. For the annealed samples (II.D – II.J, the growth of such a cap layer was omitted to avoid any influence of the cap

layer on the Sn re-distribution during the ex-situ annealing. Due to the absence of any cap layer, the top ~15nm of the annealed samples was damaged by the ion beam during APT tip preparation. This region was omitted when performing the cluster analysis (section 3).

The APT analysis was done with the Laser Assisted Wide Angle Tomographic Atom Probe (LAWATAP) from Cameca using laser pulsing (wavelength 515 nm, 400 fs pulse duration) at 15 K sample temperature. The raw data were reconstructed using TAP3D data software from Cameca using the 'Voltage curve' reconstruction method [16]. All measurements were done within the optimum parameter window for quantitative compositional analysis. In ref. [13] it was shown that this is achieved by tuning the laser power such that the Sn charge state ratio (Sn^{2+}/Sn^{+}) lies between ~0.43 – 1.14. We have previously shown that the value for field evaporation of Sn and Ge is similar in the $Ge_{(1-x)}Sn_{(x)}$ layers and uniform 2-D desorption maps are obtained from APT measurements [13]. Hence no field evaporation artefacts, such as local magnification effects [17], correlated field evaporation of Sn and Ge [18] occur in these layers which might adversely affect the cluster analysis. The APT measurements were used to determine Sn-cluster and 1-D concentration profiles.

3. Cluster Analysis Algorithm

APT measurements of $Ge_{(1-x)}Sn_{(x)}$ layers lead to a data volume containing the 3D-distribution of the Ge and Sn-atoms. The objective of the cluster analysis algorithm was to extract from that 3D distribution those Sn-atoms that form a Sn-cluster. In this context, clusters were defined as localized regions of enriched Sn concentrations (local concentration of Sn higher than the average composition), which formed as a result of an external physical stimulus (e.g. temperature, stress etc.). These clusters can be identified relying on the fact that Sn atoms will be more closely packed than their counterparts distributed randomly in the alloy, due to the higher local concentration of Sn in the clusters. Thus, the distance to the K^{th} nearest neighbor ($K^{th}NN$) of a clustered Sn atom is smaller as the distance to the non-clustered Sn atoms (for K smaller than or equal to the number of Sn atoms in the cluster). The presence of clusters is seen as a satellite peak in the global $K^{th}NN$ distance distribution of the Sn atoms. In the layers analyzed in this study, the density (clusters/cm^3) of Sn-clusters was small with a distance distribution of the clustered

Sn atoms (satellite peak) being superimposed on the distribution of the randomly distributed matrix Sn atoms. Hence the satellite peak was small and hardly discernible in the global K^{th}NN distance distributions (see **Fig. 4.20(A)**). This created the challenge to:

1. Clearly identify the satellite peaks as it defines a range of characteristic K^{th}NN distances, at which Sn atoms are present in a cluster.

2. Successfully differentiate between the Sn atoms in the clusters and the randomly distributed Sn atoms whereby the latter statistically also can have the same characteristic distances as the clustered atoms

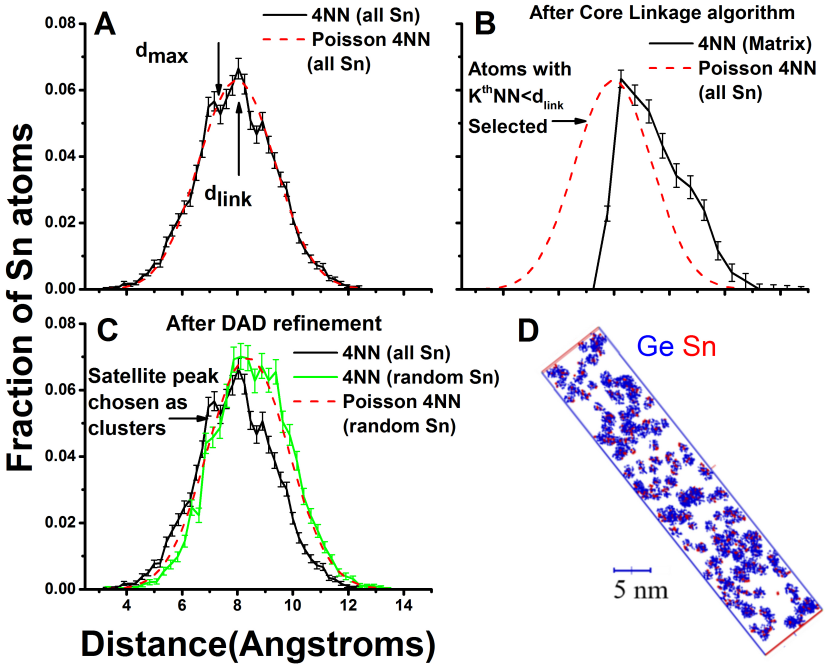

Figure 4.20 – (A) 4^{th}NN Distance distribution (black) of samples II.J. The Poisson distribution (red) is calculated using all the Sn atoms. The arrows mark the d_{max} (7.25 Å) and d_{link} (8 Å). (B) 4^{th}NN distribution of the matrix (black) after the application of the core-linkage algorithm. All the atoms with 4^{th}NN $\leq d_{link}$ are selected as clusters. (C) 4^{th}NN distribution of matrix Sn atoms (green), all the Sn atoms (black) and Poisson distribution of the matrix Sn atoms (red). The atoms giving rise to the satellite peak have been selected as clusters. (D) 3-D cluster distribution.

In order to overcome these challenges, a 3-step approach was used to identify and label the clustered-Sn atoms. As the first step, we applied the core-linkage algorithm [1] *to remove majority of the randomly distributed Sn atoms* (section 3.1). This step served 2 purposes, (1) increase the ratio of the clustered to the randomly distributed Sn atoms, locally in the volume selected after the application of core-linkage algorithm (2) group- and label the Sn atoms which might be clustered. In the second step, we defined the *characteristic distances of Sn atoms* in clusters based on the K^{th}NN distance distributions of the selected volumes individually (discussed below) and thereafter we de-convoluted the clustered and randomly distributed Sn atoms present in the selected volumes based on the characteristic distances of Sn atoms in clusters. Step 2 is a part of the new Distribution and De-convolution refinement (DAD, section 3.2) proposed in this paper. As a last step, we merge the clusters having common Sn atoms in order *to properly quantify them and to understand the nature of the clusters in terms of size, Sn distribution etc.*

3.1 Core-Linkage Algorithm

The core-linkage algorithm was developed by Leigh T. Stephenson et al. [1] and is a two-step process: (i) the core step, which defines the clustered atoms, and (ii) the linkage step, which links the neighboring atoms to the clustered atom. In the core step, Sn atoms which have their K^{th}NN neighbor less than or equal to a specific distance (defined as d_{max}) are selected to form the core atoms (Sn_{core}) of the cluster. These Sn_{core} atoms are then linked to their neighboring atoms ($Sn_{neighbour}$ and $Ge_{neighbour}$) within a specific distance (defined as d_{link}) from the core atom. In this study, d_{max} and d_{link} were chosen as follows: d_{max} was defined as that NN-distance where the satellite peak in the experimental K^{th}NN distribution coincides by the K^{th}NN distance distribution of a random solid solution as predicted by the Poisson statistics (Equ. (11) Ref 1). K is the highest order NN distance distribution for which a satellite peak was obtained (e.g. 6.75 Å in sample II.J for 4^{th}NN distance distribution figure 1.A). The d_{link} value should be chosen, such that, one is sure to encompass the neighboring clustered atoms as well as the randomly distributed atoms surrounding the cluster. Hence, we chose the d_{link} value as the mean of the K^{th}NN distance distribution (K being the order from which d_{max} was chosen), since by choosing the mean of the NN distribution, we have a high probability of also selecting the randomly distributed atoms around the cluster. It is essential that before applying the core-linkage algorithm,

'Artifact Removal' is done. 'Artifact Removal' takes into account the artefacts arising due to artificial density variations like blind spot on detector, zone lines, crystallographic poles in the APT data. In order to negate the effects of the artificial density variations on the K^{th}NN distance distributions and on the cluster analysis, a threshold density of atoms is chosen. All atoms in the regions where atomic densities $\leq$ threshold density are not taken into account for cluster analysis as core atoms. The minimum threshold density was calculated using equation 24 in ref [1]. After applying the Core-Linkage algorithm all the Sn atoms (Sn_{CL}) which have their K^{th}NN less than or equal to d_{link}, were selected as evident in the K^{th}NN distribution of the matrix (atoms which were not selected, figure 4.20(B))

3.2 Distribution and De-convolution Refinement

After the application of the core-linkage algorithm (step 1), we obtained a set of discrete volumes, where some contained only the randomly Sn atoms (Sn_{ran}), while some random plus clustered Sn atoms (Sn_{c+r}). The K^{th}NN distance distribution of individual volumes containing only randomly distributed Sn atoms (Sn_{ran}) will be a Poisson distribution, since a subset of a random distribution remains a random distribution. However, this distance distribution would be attenuated as compared to the one before the core-linkage step, since the total number of randomly distributed Sn atoms is lower. In the case of clustered Sn atoms, the K^{th}NN distribution remains the same. This is due to the fact that the local environment of the clustered Sn atoms does not change, since we purposely selected the randomly distributed Sn atoms around the clustered atoms by overestimating d_{link}. Hence, in the aggregated K^{th}NN distance distributions of individual volumes, the satellite peak becomes better defined. Note that for clusters containing different number of Sn atoms, the K^{th} nearest neighbor might not be at the same distance, i.e. the position of the satellite peaks for the same order of K might be different, for clusters containing different number of Sn atoms. Therefore as the second step in the cluster analysis algorithm, the K^{th}NN distance distribution curves of individual volumes were calculated and aggregated, for volumes containing equivalent number of Sn_{CL} atoms, where K= 1 to (number of Sn atoms in the volume)-1 i.e. for example in a volume that contained 6 Sn_{CL} atoms we calculated 1-5NN distance distribution. This was done for all the different sizes (in terms of number of Sn atoms present in the volume) of the selected volumes. After this step, we were

able to identify the satellite peaks, for all orders of the NN distributions and for all the different sizes (in terms of number of Sn atoms) of the selected volumes. Examples of such curves are shown figure 4.21, where 3^{rd}–6^{th}NN distribution (sample II.J) are shown for volumes identified after the core-linkage step, containing 5, 6 and 7 Sn_{CL} atoms.

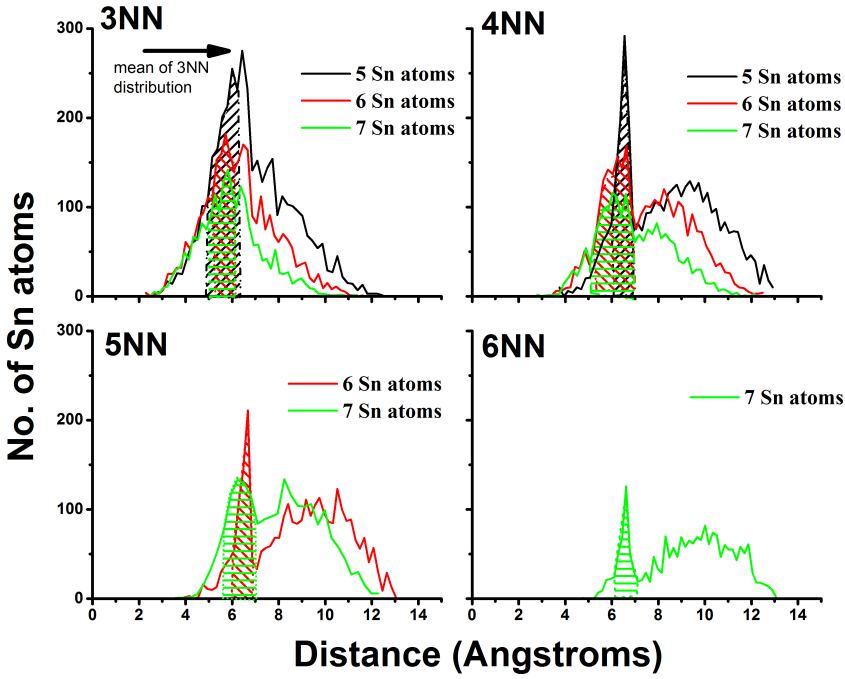

Figure 4.21 – Local K^{th}NN (3^{rd}NN-6^{th}NN) (sample II.J) distance distributions of clusters obtained after core linkage step containing 5 (black curve), 6 (Red Curve), 7 (green curve) Sn atoms. The scale of all the x and y-axis respectively is the same. The shaded regions in the different K^{th}NN distance distribution are the characteristic K^{th}NN distribution of clusters with various number of Sn atoms. Clusters of different sizes (in terms of number of Sn atoms) show/may show shift in the satellite peak. In the top left figure, the second peak in the 3^{rd}NN curve (black) is at the mean of the 3^{rd}NN distribution of the matrix, hence it comes from the randomly distributed Sn atoms.

Once we know the characteristic distance at which Sn atoms should be present in a Sn cluster, it is trivial to de-convolute the clustered and the randomly distributed Sn atoms in the selected volumes after the core-linkage algorithm. In the volume that contain randomly distributed Sn

atoms only some or none of the atoms will be present at the characteristic distances. Hence those volumes in which all the Sn atoms were sitting at the characteristic distances were chosen as clusters and the rest were put back into the matrix. However it should be noted that before the de-convolution we first had to remove those Sn atoms which were present outside the maximum characteristic distance, since these are the randomly distributed Sn atoms selected due to the overestimated d_{link}. For e.g., in a volume containing 7 Sn atoms, the max characteristic distance (6NN) was 7.1 Å in sample II.J. So all atoms in a volume which contained 7 Sn atoms, which were present at distances larger than 7.1 Å from the core Sn atom were removed.

The 4^{th}NN distance distribution of the matrix after cluster analysis (containing the randomly distributed Sn atoms) is shown in figure 4.20(C) (green curve). As can be seen the distribution now matches the theoretically predicted distribution for a random solid solution (dashed red line, calculated using the Sn atoms in the matrix) very well, meaning we have successfully selected and removed the clustered Sn atoms.

In the last step Ge atoms having a Sn_{core}-Ge distance greater than the max Sn_{core}-$Sn_{neighbor}$ were removed, and subsequently clusters containing more than 1 common Sn atom were linked. At the end of the cluster analysis we obtain information about the spatial distribution of the clustered atoms with their chemical identities (figure 4.20(D)). From this we can get information on the intrinsic cluster properties like size, density etc.

4. Strain relaxation in $Ge_{(1-x)}Sn_{(x)}$

Having established a methodology to identify Sn-cluster formation in APT data, we can use it to understand the role of Sn clustering during relation layer relaxation. Two case have been studied, (i) the relaxation resulting from an increase in thickness of the $Ge_{(1-x)}Sn_{(x)}$ layer and (ii) the other one relaxation during an anneal treatment (Table 4.5).

4.1 Relaxation due to thickness increase

The first study involves layer relaxation due to its thickness whereby the aim was to understand the role of Sn clusters in layer relaxation. In this study, layers with a Sn concentration of ~7 at% (based on APT measurements) were grown with different thicknesses (samples I.A –

I.C). The interface between the $Ge_{(1-x)}Sn_{(x)}$ layer and the Ge pseudo substrate was very sharp (~2nm/decade) with no Sn out-diffusion from the $Ge_{(1-x)}Sn_{(x)}$ layer. HRXRD-RSM measurements revealed that the relaxation degree of these layers increased from 0 %, 26 % to 75 % as the thickness of the $Ge_{(1-x)}Sn_{(x)}$ layer increased from 40 nm, 145 nm to 530 nm respectively (Table 4.5). Analyzing the APT data, we observe that the K^{th}NN distance distributions of these layers did not show any clear satellite peaks and only some noisy peaks. The latter are not representative for any cluster formation as evidenced by applying the cluster analysis algorithm using these as apparent satellite peaks. Indeed the resulting K^{th}NN distance distribution of the Sn_{CL} atoms gave broad distributions with no well-defined satellite peaks (figure 4.22 , for sample I.B). Hence the Sn-clusters (if any), are not present or below the detection limit of clusters via APT measurements. As they are non-existent (or only present in extremely low levels), it seems that Sn-cluster formation is not the driving force for the relaxation. Since one does however observes an increase in defect density (misfit dislocations, threading dislocations etc.) with layer relaxation [5], we believe that defect generation is the main source for strain relaxation in these layers.

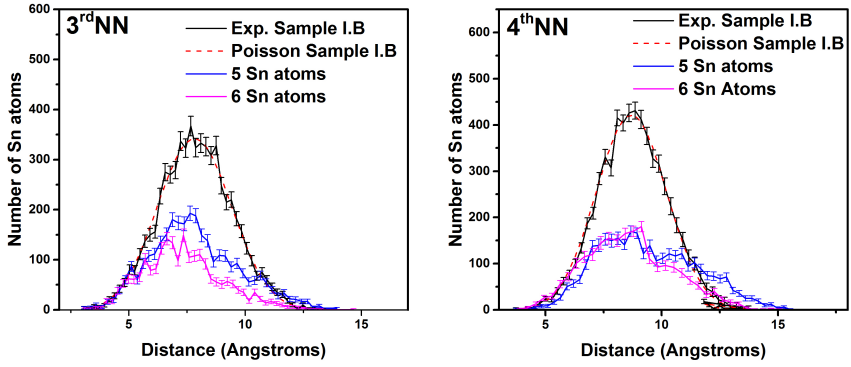

Figure 4.22 – 3^{rd}–4^{th} NN Distance distribution of Sample I.B. No distinct satellite peaks are observed in the K^{th}NN distribution of Sn_{CL} atoms, on application of DAD refinement (blue and pink curves). Hence the apparent satellite peaks observed in the original K^{th}NN distance distribution are just noise and not linked to cluster formation.

4.2 Relaxation due to Thermal Anneal

In the second case we explore the impact of an additional thermal treatment on the relaxation and cluster formation. In this case, layers with a thickness of 80nm and a 7at% Sn concentration were annealed between 500 °C to 660 °C (samples II.D – II.J). For the layers annealed at 640 °C and 660 °C (Samples II.H and II.J), Sn diffusion was observed into the Ge pseudo substrate and to the surface of the layer. The Sn concentration (as measured via APT) in these layers decreased to ~5 at% and ~1.5 at%, respectively. Sn droplet formation on the surface was also detected for these samples (using SEM).

Sn clusters were present in the $Ge_{(1-x)}Sn_{(x)}$ layers annealed between 540 °C to 640 °C. However, no clusters were observed (at least as detected by the cluster analysis algorithm) in Sample II.D (annealed at 500 °C) even though the layer relaxed a slightly (8%) from its original fully strained configuration. Also the layer annealed at 660 °C (Sample II.J) no Sn clusters could be identified. The absence of Sn clusters in the sample II.J could be due to the fact that Sn droplet formation and Sn diffusion removes all the excess Sn from the layer such that no driving force for Sn cluster formation remains.

4.2.1 Insight into spatial distribution and configuration of clusters

In this section we focus on the samples showing Sn cluster formation with the objective to gain insight into the cluster distribution, the spatial distribution of Sn atoms in the clusters and the cluster size distribution. For that purpose we studied the 3-D distribution of clusters (figure 4.23), the K^{th}NN distance distribution (figure 4.24) and the cluster number density [1] (figure 4.25) of the clustered Sn atoms, respectively. The cluster number density is defined as the number of clusters divided by the volume of analysis for a given number of Sn atoms in clusters. The K^{th}NN distance distribution provides useful insight into the distribution of Sn atoms within the clusters, while the cluster number density distribution provides information about cluster size distribution.

We observe an increase in the cluster density (clusters/cm3) when the anneal temperature is increased (figure 4.23). The clusters were uniformly distributed in the volume for all of the anneal conditions (figure 4.23), implying that clusters are not preferentially formed around defects like misfit dislocations or threading dislocations.

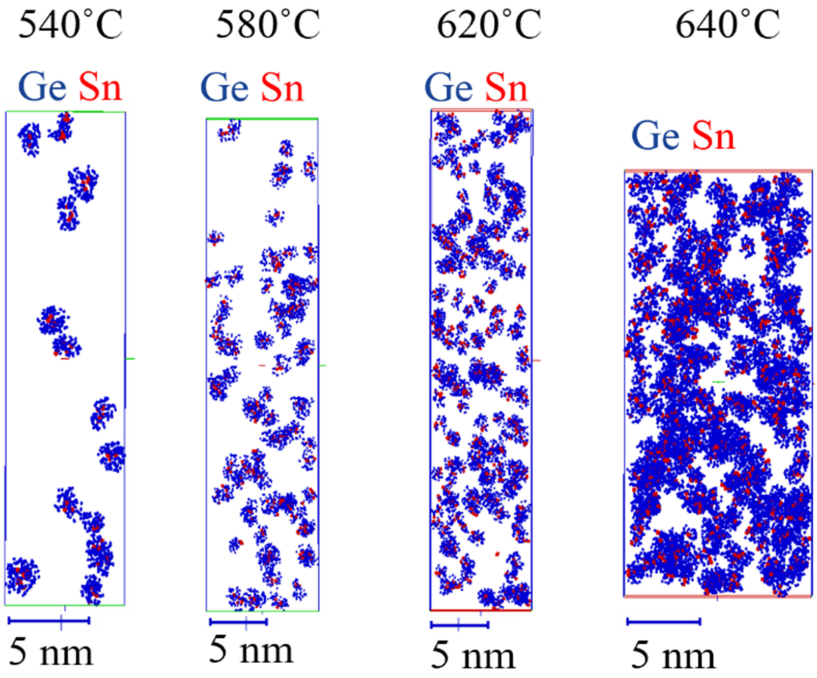

Figure 4.23 – 3-D spatial distribution of Sn-clusters for Sample II.E (540 °C), Sample II.F (580 °C), Sample II.G (620 °C) and Sample II.H (640 °C). The clusters are uniformly distributed in the volume. As the anneal temperature increases the density of clusters (clusters/cm^3) in the volume increases

The k^{th}NN distance distribution (1^{st}-4^{th}NN) of Sn in clusters is shown in figure 4.24. The mean of the K^{th}NN distance distributions is similar for all the layers. Also note that, due to the 50% detection efficiency in APT, the observed mean K^{th}NN distance distribution is ~1.25 times higher than the actual distance [12]. Furthermore, in APT the crystal information is lost due to the 50 % detection efficiency and limited spatial resolution (0.5 Å – 0.7 Å along the axis of the sample and 2 Å – 3 Å in the XY plane) and hence the reconstructed volume represents an amorphous random solid solution. As a result, the K^{th}NN distance distribution has a bell (Poisson) shape instead of sharp peaks corresponding to the atomic positions in the crystal lattice. Yet, from these distance distributions we can still obtain information about the position of the solute atoms in the

crystal lattice and based on this retrieve crystallographic information.

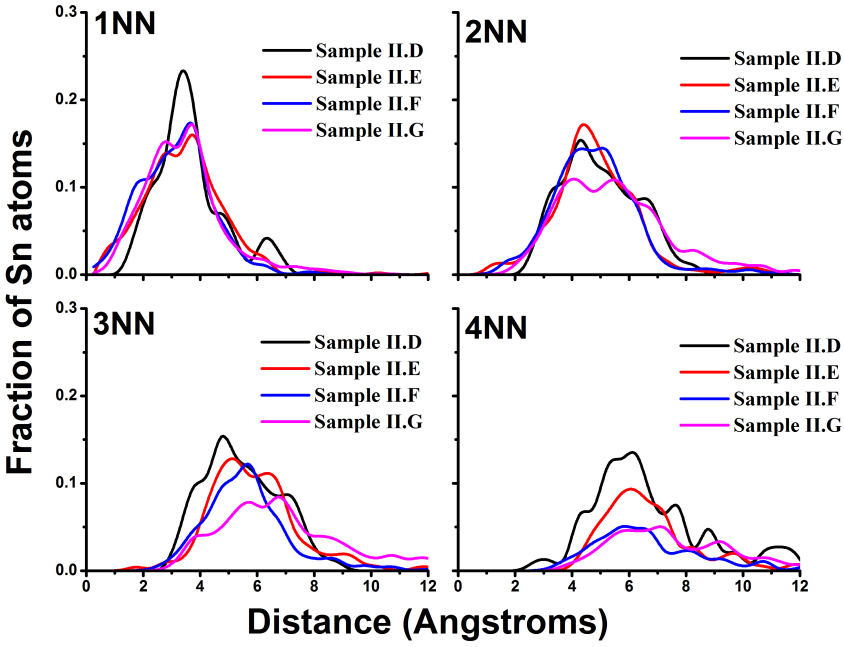

Figure 4.24 – 1st - 4thNN distance distribution of clustered Sn in sample II.E – II.H. The KthNN distance distribution of Sn in clusters is similar for all the annealed layers, meaning that the chemical nature of the clusters is the same in all the layers. The mean of the 1stNN distance of Sn in clusters is ~3.7 Å, which is equivalent to ~3.1 Å after accounting for the detection efficiency. This suggests that the Sn atoms situated in clusters is β-Sn in nature.

In detail, the distance distribution from APT measurements is modeled as a probability distribution of distances at which the KthNN solute atom should be present in an amorphous random solid solution. In a crystalline random solid solution the position of the majority of the solute atoms can be deduced as the closest lattice position to the mean of the KthNN distribution e.g. the actual 1NN distance of 3.8 Å for randomly distributed Sn atoms from APT measurements (plot not shown) corresponds to the 2NN distance (4 Å) in an α-Ge matrix, as confirmed via extended X-ray absorption fine structure (EXAFS) measurements by F. Gencarelli et al. [19]. The ability to distinguish between two different atomic positions in an amorphous or crystalline lattice structure is now dictated by the ability to distinguish between both resulting Poisson

distributions, which becomes a matter of signal statistics. In other words, if the counting statistics on the mean of the minority distribution (distribution of the cluster atoms) is larger than the error bar on the Poisson counting statistics of the majority distribution (distribution of the random atoms) at that distance, we can distinguish between the two distributions. In this study, clear satellite peaks in the K^{th}NN distance distributions are resolved, indicating that we have enough statistics to distinguish between the two Poisson distributions.

The actual K^{th}NN of the Sn atoms in clusters are 3 Å, 3.3 Å, 3.8 Å, 4.5 Å for the 1NN, 2NN, 3NN and 4NN distance respectively. These K^{th}NN distance compare well to the 1-4NN (3.02 Å, 3.2 Å, 3.7 Å, 4.4 Å respectively) to a β-Sn configuration as opposed to the 1-4NN in α-$Ge_{(1-x)}Sn_{(x)}$ matrix (2.4 Å, 4.0 Å, 4.7 Å, 5.6 Å respectively), indicating that the Sn atoms in clusters might be present in a β-Sn configuration. Furthermore, the similar K^{th}NN distribution of clusters for all layers implies that the clusters have the same spatial distribution irrespective of the anneal condition.

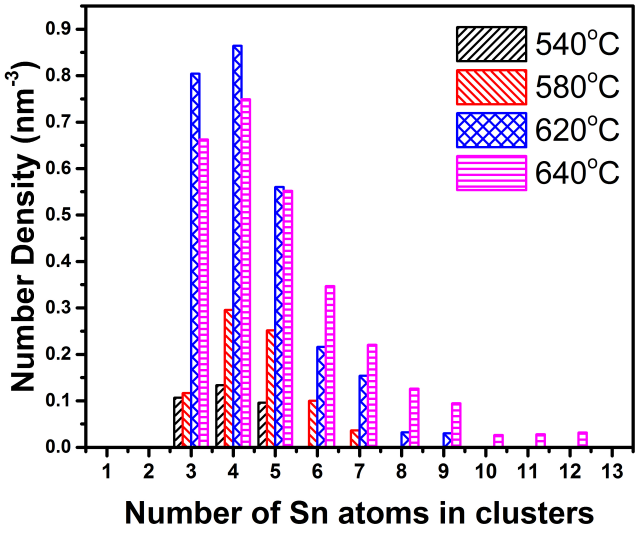

Figure 4.25 – Cluster number density as a function of Sn atoms present in clusters for the different anneal temperatures. A steady increase in the number density of clusters containing 3-4 Sn atoms is seen for the layers annealed at 540 °C till 620 °C. While for the layer annealed at 640 °C a decrease in the number density is seen for cluster containing 3-4 Sn atoms. A tail appears in the distribution at higher number of Sn atoms/cluster for an anneal temperature of 640 °C.

There is an increase in the cluster number density for the same number of Sn atoms/cluster for the layers annealed up till 620 °C, as evident from figure 4.25. However, for the layer annealed at 640 °C we observed a decrease in the number density for the same number of Sn atoms/cluster, and a tail appearing in the distribution for higher number of Sn atoms/cluster. The latter is due to the enhanced diffusion of Sn at this temperature. This enhanced diffusion is also evident from the fact that out diffusion of Sn is observed in the layer annealed at 640 °C. As seen from figure 4.25 the most probable number of Sn atoms per cluster for all the annealed layers is 3-4. Accounting for the 50 % detection efficiency, and the possible β-Sn configuration of the Sn clusters, it is likely that the clusters are present in a 6-Sn cluster-defect or a 7-Sn cluster-defect, as predicted by Ventura et al. [2]. Due to the limited detection efficiency and resolution we cannot observe vacancies in the APT data, thereby making it impossible to distinguish between the two cluster configurations predicted in reference [2].

4.2.2 Role of Sn clusters in layer relaxation

Sine we do observe a concurrent increase in layer relaxation and cluster density upon annealing, we will now discuss whether the formation of Sn clusters play a role in layer relaxation. To clarify this we compare the relaxation degree (as seen with XRD) as a function of temperature with the amount of Sn in clusters (figure 4.26).

The amount of the Sn atoms in clusters ($\left(\frac{Sn\ atoms\ in\ clusters}{Total\ Sn\ atoms}\right) \times 100$) as extracted from APT measurements increases non-linearly with the anneal temperature and relaxation degree (figure 4.26(A)). In detail, for the layers annealed at temperatures ranging from 500 °C to 580 °C (Samples II.D – II.F), we observed a change in the relaxation degree from 8 % to 36 % respectively, whereas the amount of Sn in clusters only increases marginally (0 %, ~2 %, ~7 % total Sn atoms). In contrast, for annealing treatments between 580 °C to 640 °C, the layer relaxed only by an additional 14 %, but there was a drastic increase in the amount of Sn in clusters (from ~7 % – ~18 %). For the layer annealed at 660 °C no Sn clusters were observed, as Sn had precipitated to the surface, and the bulk concentration of Sn in the layer has decreased to ~1.5 at% (thermodynamic solid solubility limit). The Sn concentration in the layer as a function of relaxation degree (figure 4.26(B)), showed no correlation between the lattice constants observed from XRD and the actual Sn (observed from APT measurements) in the layer. This points

towards the fact that on annealing the lattice spacing of the $Ge_{(1-x)}Sn_{(x)}$ layer is no longer a function of the substitutional Sn atoms. To rule out the impact of in-homogeneity of Sn distribution in the sample, APT analysis were done on multiple location on ~1 cm^2 piece of wafer used for XRD analysis.

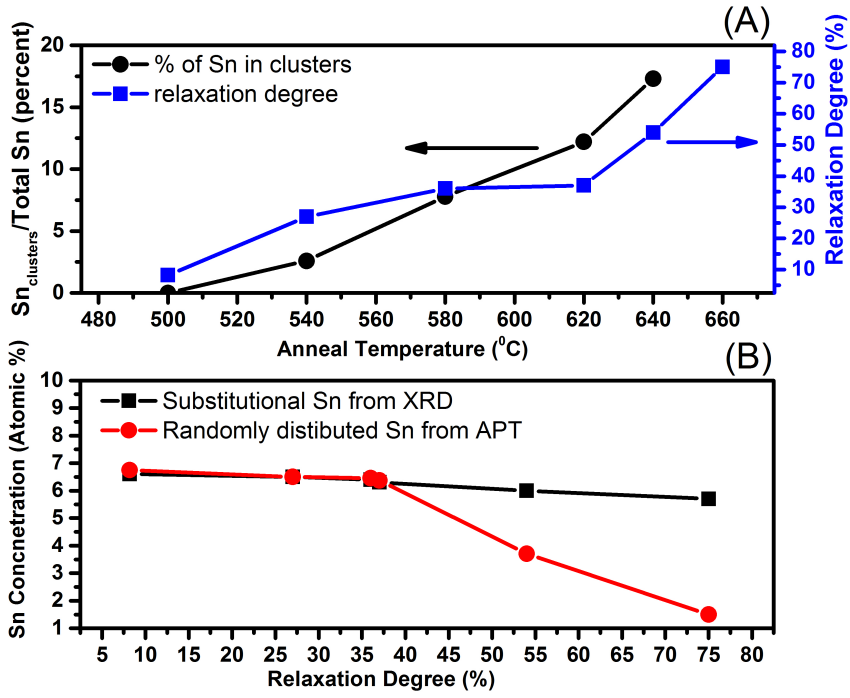

Figure 4.26 – (A) Relaxation degree versus Anneal temperature (blue). Percentage of Sn in clusters versus Anneal Temperature (black). Going from 500 °C to 580 °C, there is a huge change in relaxation degree (8 % to 36 %) but very little change in the Sn in clusters (0 to 7 %). Going for 580 °C to 640 °C the layer relaxes by only 15 % more, but a large amount of Sn (~18 %) is clustered. (B) Sn concentration from APT and XRD as a function of anneal temperature. At higher temperature anneals (>640 °C) there is no correlation between substitutional Sn and relaxation degree.

Furthermore the Scanning Electron Microscope (SEM) images of the different layers, we observed the appearance of a cross-hatch pattern at 540 °C which becomes denser as the layers were further annealed. This indicates that the density of misfit dislocations is also increasing as the

layer relaxes. This has also been reported in literature based on TEM observation [10].

In summary, our observations that (1) Sn-cluster formation is almost independent of the relaxation degree, and highly dependent on the anneal temperature, (2) no correlation between actual Sn present in the layer and the lattice constants exist and (3) no Sn cluster form when the layer relaxes due to thickness increases, imply that Sn-cluster formation in $Ge_{(1-x)}Sn_{(x)}$ is mainly driven by the thermodynamic solubility limit of Sn in Ge. The main relaxation mechanism of these layers, even when annealed, is defect generation, whereas Sn-cluster formation is not the main driving force.

Conclusion

In this work we have studied the driving forces for the relaxation of strained $Ge_{(1-x)}Sn_{(x)}$ layers. Previous research indicates that the layers might be relaxing through defect generation (misfit dislocations, threading dislocations etc.) and/or Sn-cluster formation. Using Atom Probe Tomography we have studied the 3D-Sn distribution and the formation of Sn-clusters using an extension to the Core-Linkage cluster analysis algorithm that enabled us to reliably quantify ultra-small clusters (20-100 atoms). The current findings suggest that the main relaxation mechanism in $Ge_{(1-x)}Sn_{(x)}$ layers is defect generation irrespective of the cause for the relaxation (i.e. increase in layer thickness or thermal anneal). No Sn clusters were present in the layers relaxing due to layer thickness. For the layers relaxing due to thermal anneal treatment, majority of the Sn-cluster (7 – 18 at% of total Sn present) were observed within a very narrow temperature window (580 °C - 640 °C) whereby at higher temperatures the layer re-establishes the thermodynamic equilibrium of Sn concentration in Ge (1.5 % Sn concentration) through surface segregation and precipitation. However no correlation between Sn-cluster formations during anneals at 580 °C - 620 °C and the relaxation degree of the layer could be established. Therefore we believe that Sn-cluster formation has little or no effect on layer relaxation.

Further analysis of the extracted clusters revealed that the spatial distribution of Sn atoms in clusters does not change irrespective of the anneal condition and that the Sn is likely sitting in β-Sn configurations in these clusters. The highest cluster number density was observed for clusters containing 6-8 Sn atoms per cluster (accounting for the ~50 % detection efficiency). The presence of 6-8 Sn atoms per cluster in a β-

Sn configuration suggests that the clusters are present as a 6-Sn cluster-defect or a 7-Sn cluster-defect, as predicted by Ventura et al. [2]. However due to the inability of the APT to detect vacancies, it is not possible to distinguish between the 2 configurations.

References

[1] L.T. Stephenson, M.P. Moody, P.V. Liddicoat, and S.P. Ringer, Microsc. Microanal. 13, 448 (2007).
[2] C.I. Ventura, J.D. Fuhr, and R.A. Barrio, Phys. Rev. B 79, 155202 (2009).
[3] G. Han, S. Su, C. Zhan, Q. Zhou, Y. Yang, L. Wang, P. Guo, W. Wei, C.P. Wong, Z.X. Shen, B. Cheng, and Y.-C. Yeo, in Electron Devices Meet. IEDM 2011 IEEE Int. (2011), pp. 16.7.1–16.7.3.
[4] F. Gencarelli, B. Vincent, L. Souriau, O. Richard, W. Vandervorst, R. Loo, M. Caymax, and M. Heyns, Thin Solid Films 520, 3211 (2012).
[5] S. Takeuchi, A. Sakai, K. Yamamoto, O. Nakatsuka, M. Ogawa, and S. Zaima, Semicond. Sci. Technol. 22, S231 (2007).
[6] B. Vincent, Y. Shimura, S. Takeuchi, T. Nishimura, G. Eneman, A. Firrincieli, J. Demeulemeester, A. Vantomme, T. Clarysse, O. Nakatsuka, S. Zaima, J. Dekoster, M. Caymax, and R. Loo, Microelectron. Eng. 88, 342 (2011).
[7] S. Gupta, B. Magyari-Köpe, Y. Nishi, and K.C. Saraswat, J. Appl. Phys. 113, 073707 (2013).
[8] R.W. Olesinski and G.J. Abbaschian, Bull. Alloy Phase Diagr. 5, 265 (1984).
[9] J.W. Matthews and A.E. Blakeslee, J. Cryst. Growth 27, 118 (1974).
[10] H. Li, Y.X. Cui, K.Y. Wu, W.K. Tseng, H.H. Cheng, and H. Chen, Appl. Phys. Lett. 102, 251907 (2013).
[11] D. Vaumousse, A. Cerezo, and P.J. Warren, Ultramicroscopy 95, 215 (2003).
[12] T. Philippe, F. De Geuser, S. Duguay, W. Lefebvre, O. Cojocaru-Mirédin, G. Da Costa, and D. Blavette, Ultramicroscopy 109, 1304 (2009).
[13] A. Kumar, M.P. Komalan, H. Lenka, A.K. Kambham, M. Gilbert, F. Gencarelli, B. Vincent, and W. Vandervorst, Ultramicroscopy 132, 171 (2013).
[14] C.K. Sudbrack 2004, Decomposition Behavior in Model Ni-Al-Cr-X Superalloys: Temporal Evolution and Compositional Pathways on a Nanoscale, Chicago: Northwestern University
[15] M.K. Miller, K.F. Russell, K. Thompson, R. Alvis, and D.J. Larson, Microsc. Microanal. 13, 428 (2007).
[16] B. Gault, D. Haley, F. de Geuser, M.P. Moody, E.A. Marquis, D.J. Larson, and B.P. Geiser, Ultramicroscopy 111, 448 (2011).
[17] M.K. Miller and M.G. Hetherington, Surf. Sci. 246, 442 (1991).

[18] F. De Geuser, B. Gault, A. Bostel, and F. Vurpillot, Surf. Sci. 601, 536 (2007).
[19] F. Gencarelli, D. Grandjean, Y. Shimura, B. Vincent, D. Banerjee, A. Vantomme, W. Vandervorst, R. Loo, M. Heyns, and K. Temst, J. Appl. Phys. 117, 095702 (2015).

Chapter 5

Conclusion and Outlook

The aim of this project was to evaluate and develop L-APT for metrology of compound semiconductors like GeSn, GaN, InP etc. The motivation to introduce L-APT for metrology of these advanced semiconductors stems from the current technology trends in the semiconductor industry. As evident from the ITRS road map of 2014 [9], future microelectronics devices are envisioned to employ these materials to improve performance and functionality. Furthermore, these devices will be of the order of few 10's of nanometer in the lateral dimension and will have a 3-dimensional architecture. Hence, to study the physical interactions in these devices, an analysis method is required that can characterize properties like layer thickness, composition, distribution of dopant, interfaces etc. at the sub-nanometer scale and in 3-D. L-APT is uniquely suited to this challenge due to its ability to provide atom distribution in the sample with elemental identification and near atomic resolution (0.5 Å - 3 Å) in 3-D.

In the introductory chapter, we defined two focus areas to understand and improve the decreased spatial resolution and the high failure rate when analyzing semiconducting materials and devices, (1) the interaction between the laser and the tip and (2) statistical analysis of the acquired data. This chapter is divided into three sections, one each for the focus areas and the last for perspective future developments for L-APT. In the first two sections I will first summarize the work done on the respective topic and subsequently outline some new ideas that need to be tested to further improve our understanding. In the final section I will discuss the future developments needed for alleviating some of the issues facing

routine application of L-APT for metrology of complex microelectronic devices.

5.1 Laser-Tip interaction

The degraded spatial resolution and the high failure rate in L-APT analysis of semiconducting materials and devices, among others, is caused due to erroneous reconstruction and inefficient laser absorption by high band gap materials like SiO_2, HfO_2 etc. commonly present in these devices. The inaccurate reconstruction is due to the presence on non-hemispherical apex shapes which lead to magnification variations and are not accounted for in conventional reconstruction algorithms. In this thesis we concentrated our efforts to understand the physical mechanism behind (1) the appearance of asymmetrical apex shapes due to laser absorption and (2) absorption of the laser by a-priori transparent materials. To do this we first developed a method to determine the temperature reached at the apex of a specimen during L-APT analysis Chapter 3.1. The method is based on the fact that the flux (ϕ) of field evaporation has an exponential dependence on the potential barrier (Q_b) for ionization and temperature (T), i.e.$\phi \propto exp^{-\frac{Q_b}{K_B T}}$. Hence the temperature during field evaporation at constant temperature (i.e. constant laser power P) is accessible via

$$T = -\frac{1}{K_B}\left(\frac{dln(\phi)}{dQ_b}\right)^{-1}\Bigg|_P \tag{5.1}$$

Using this method we succeeded in understanding:

1. **The impact of laser absorption on the apex shape of the specimen**: It has previously been shown that the steady state apex shape of highly absorbing materials is asymmetric [28]. The asymmetry is caused due to one sided absorption these materials leading to a temperature variation across the apex surface. In Chapter 3.2, we demonstrated that an asymmetry in the apex shape is also present in moderately absorbing materials. This conclusion is against the general notion of the scientific community as hemispherical apex shapes (using SEM micrographs) have been reported for moderately absorbing materials [28, 81]. From our analysis we found that the apex shape is a function of both the absorption depth and the spatial distribution of the resonantly

coupled light. In situations when the light couples in close proximity to the apex of the tip (e.g. Si under green illumination), minimal diffusion of the locally generated heat occurs before field evaporation. Hence, the temperature distribution at the apex still bears the fingerprint of the non-uniform absorption. To accommodate the effect of the non-uniform temperature distribution on the evaporation probability, the apex reshapes asymmetrically such that resulting field across the apex counteracts the effect of the temperature. Considering that in semiconductors and insulators, light couples non uniformly at resonant cross-sections and the position of this resonance depends on the wavelength (λ) and the real refractive index (n) as $\sim \frac{(2K+1)\lambda}{8n}$, commonly used laser ($\sim$515 nm and $\sim$343 nm) will couple close to the apex non-uniformly in most materials. Hence L-APT analysis would result in a non-hemispherical apex shape in most semiconductors and insulators.

2. **Absorption mechanisms in a-priori non absorbing tips**: APT analysis of high bandgap materials like GaN, MgO, Al_2O_3 has been demonstrated in scientific literature [98, 99, 100]. However, the physical mechanism behind the enhanced absorption in these structures has been a topic of discussion. In Chapter 3.3 we show that, the amorphized shell created as a result of FIB milling during sample preparation plays a vital role in light absorption. PMOR measurements of blanket amorphized GaN layers show an increased absorption and decreased thermal diffusivity of these layers. L-APT analysis of specimens with varying thickness of α-GaN shell demonstrated more efficient heating of the apex for thicker α-GaN shells. Hence, indicating that light absorption in the amorphized layer may be the dominant mechanism during L-APT analysis.

Our initial studies of the effect of the amorphized shells suggest that it not only increases absorption but also plays a role in the (1) spatial distribution of absorbed light and (2) the thermodynamics of the tip.

- Regarding the spatial distribution of absorbed light, the field distribution at the apex of GaN tips (cleaned at 5 kV) analyzed by a green laser (515 nm) suggest a strongly one sided absorption (**Fig. 3.20**). However, ADDA simulation of tips consisting of only c-GaN predict that light should couple at resonant cross-sections (**Fig. 3.21**). The reason for this disparity could be the strong absorption in the α-GaN shell. However, assuming

that all the absorption occurs in the amorphized shell (∼2 nm from SRIM) would yield an absorption coefficient of $\sim 5 \times 10^6$ cm^{-1}, which is doubtful considering that c-GaN is transparent at 515 nm. Hence, more detailed studies are needed to understand the optical properties of the amorphized layer and subsequently light absorption in such core-shell structures. For example, spectroscopic ellipsometry of these layers would give access to the complex refractive index as a function of wavelength. This information could in-turn be used to simulate the coupling of light in the APT tip.

- As shown in Chapter 3.3, the thickness of the amorphized layer also effects the mass resolution obtained for a Si sample analyzed by green laser. A higher mass resolution is obtained for tips with thinner amorphized layer (**Fig. 3.22**). Even more striking effect of the amorphized shell can be seen in the mass spectra of Si analyzed by an IR laser (1030 nm). The mass spectra for a Si tip analyzed with an IR laser shows a delayed secondary peak (called a hump) with an extremely bad mass resolution (red curve in **Fig. 5.1**). Dependence of this peak on parameters like laser power, applied DC bias, laser wavelength, tip cross section has been thoroughly discussed in scientific literature [145, 38, 146, 147]. In summary, the height of the hump with respect to the main peak increases with increasing laser power and applied DC Bias and the position of the hump has shown to be a function of laser wavelength. We observed that the height of the hump is also a function of the amorphized shell thickness. For the tips cleaned with FIB energies of 1 kV, no hump could be observed even for the highest laser energies that could be used before breaking the tip (**Fig. 5.1**). Furthermore, a higher Si^+ (∼5 atomic %) was observed for these tips as compared to the ∼0.5 atomic % for the tip cleaned at 5 kV, implying a more efficient heating of the apex in the former. Since the mass resolution of the spectra is a function of the heating and cooling down of the tip [72, 24], our initial studies are indicative of variation in the thermal properties of the specimen with different thicknesses of the α-Si shell. To further support our hypothesis, PMOR measurements of amorphized Si using a Ga beam of 30 kV on a Si wafer reveal that this layer is more absorptive and less thermally conductive as compared to crystalline Si. However, a more detailed study is required to understand the effect of this layer on light absorption and heat diffusion in the tip. One way would be to simulate the light

absorption (using ADDA) and thermal diffusion (using a simulation package like COMSOL) and experimentally verify the results using L-APT analysis.

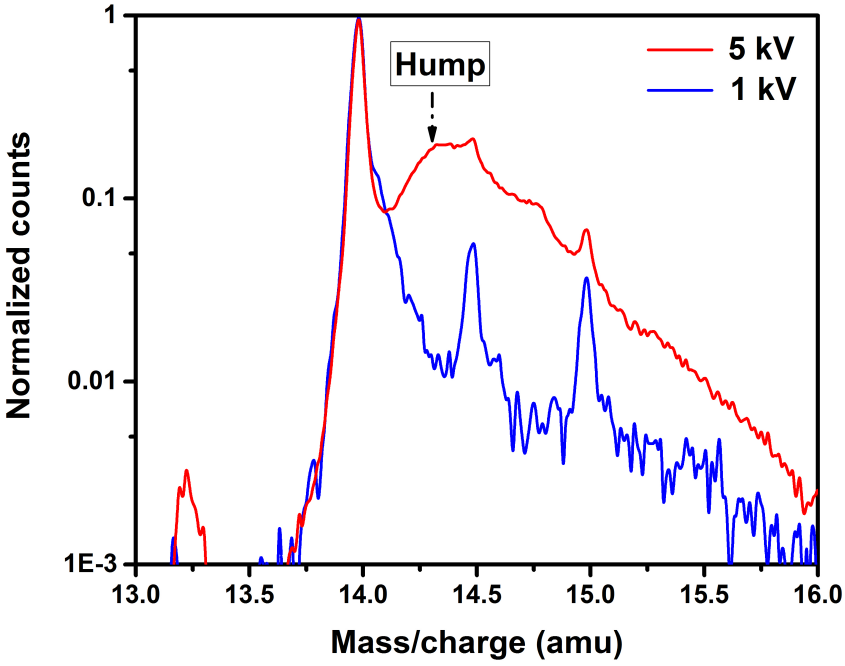

Figure 5.1 – Mass spectra obtained for a Si sample analyzed by an IR laser (1030 nm). The two curves represent tips cleaned using FIB energies of 5 kV and 1 kV corresponding to an amorphous shell thickness of 2.6 nm and 1.2 nm respectively from SRIM.

5.2 Statistical analysis of compound semiconductors

L-APT was applied to strained $Ge_{(1-x)}Sn_{(x)}$ layers grown on a pseudo Ge substrate to understand the role of Sn clusters in strain relaxation of these layers. As this was the first time these layers were analyzed using L-APT, we first studied the field evaporation characteristics of $Ge_{(1-x)}Sn_{(x)}$ to verify the presence (or absence) of commonly observed artifacts like co-evaporation, density variations at interfaces, effect of laser on tip shape etc. Subsequently, we developed a cluster analysis algorithm to extract ultra-fine clusters (few 10's of atoms) and used it to understand the role

of Sn clusters in strain relaxation of $Ge_{(1-x)}Sn_{(x)}$ layers relaxing due to (1) its thickness and (2) a post growth thermal anneal.

5.2.1 Field and Laser induced artifacts in $Ge_{(1-x)}Sn_{(x)}$ layers

The theoretically predicted threshold field evaporation values using the Mueller-Schottky model for Ge and β-Sn are 29 V/nm and 23V/nm respectively [49]. F. Vurpillot et al. showed that a difference greater than 10 % between the threshold field evaporation of constituent elements of compound could lead to field related artifacts. However, experimental evidence like:

- no correlation between the co-evaporated Ge and Sn atoms
- smooth voltage curve when transitioning from Ge to $Ge_{(1-x)}Sn_{(x)}$ layers and vice-a-versa
- uniform density across $Ge/Ge_{(1-x)}Sn_{(x)}$ interface
- correct stoichiometry for a wide range of applied fields

indicate no field induced artifacts were observed in analyzed $Ge_{(1-x)}Sn_{(x)}$ layers. In fact, the observed DC evaporation of Ge at high fields suggests Sn has a higher threshold field evaporation in $Ge_{(1-x)}Sn_{(x)}$ layers. This unexpected behavior can be explained considering the fact the reported threshold field evaporation is for pure Ge and β-Sn and since the field required for evaporation depends upon the local environment, the threshold field of constituent elements of an alloy may differ from their respective pure phases. Furthermore, the reported values were calculated theoretically using the Mueller-Schottky model and hence, are unreliable.

Concerning the artifacts due to laser absorption, TEM images of analyzed tips and ADDA simulations showed one sided absorption in the specimen illuminated by a green laser. However, on reconstructing the data, small density variations of $\sim$ 3 % were observed across the apex. The impact of the density variations on statistical analysis was negated by using sub volumes of the reconstructed data having uniform density.

5.2.2 Mechanism for strain relaxation in $Ge_{(1-x)}Sn_{(x)}$ layers

$Ge_{(1-x)}Sn_{(x)}$ layers tend to relax due to (1) their thickness [135] or (2) a thermal anneal [127]. The potential strain relaxation mechanisms are

defect formation like misfit and threading dislocations etc. [134] and Sn cluster formation [127]. During this doctoral project we concentrated our efforts in understanding the dominant mechanism for strain relaxation in these layers. To do this we first had to develop a cluster analysis algorithm to extract ultra-fine clusters (few 10's of atoms) as the available methods were not adequate. Subsequently, the dominant strain relaxation mechanism in these layers relaxing was identified by studying the evolution of the amount of Sn in clusters (if present) as function of the strain relaxation degree.

In the context of L-APT, clusters are defined as localized regions where the relative abundance of solutes is higher as compared to the matrix. This implies that in clusters, the solute atoms are more densely packed and hence the distance between solute atoms is smaller. Most conventional cluster analysis algorithms make use of this property to extract clusters [33, 34]. One of the primary input for these algorithms is the characteristic distance distribution of clustered atoms. However, in $Ge_{(1-x)}Sn_{(x)}$ layers the characteristic distance distribution of clusters is a subset of the distance distribution of randomly distributed atoms and hence cannot be defined. Furthermore, since both clustered and randomly distributed atoms can have nearest neighbors at similar distances, a deconvolution of the two is required. To tackle these issues we developed a refinement procedure, called Distribution and Deconvolution (DAD) refinement. Using this approach we could reliably extract ultra-fine Sn clusters present in $Ge_{(1-x)}Sn_{(x)}$ layers.

In order to understand the interplay between strain relaxation, defect generation and Sn clusters formation, L-APT analysis was done on two set of samples, (1) relaxing due to their thickness and (2) relaxing due to an RTA of 40 s. For the layers relaxing due to their thickness, no Sn clusters could be found. However, TEM micrographs showed an increase in the defect density of these layers. These observations indicate that the main relaxation mechanism in these layers is potentially defect generation. Alternatively, in the layers relaxing due to a RTA, Sn cluster formation was observed. However, on comparing the relaxation degree and the amount of Sn in clusters as a function of anneal temperature no correlation between the two was observed. Furthermore, appearance of a cross-hatch pattern was observed at a anneal temperature of 540^0C. The pattern became denser at higher anneal temperature thereby implying an increase in defect density as the layer relaxed. These observations indicate that Sn cluster formation is a result of the thermodynamic stability of the layer and play a negligible role in layer relaxation and defect formation is

potentially the main cause of relaxation. Furthermore, using the spatial distribution of Sn in clusters and the number of Sn atoms in clusters we gained useful insight into the configuration of the clusters. The spatial distribution of the Sn atoms suggested that the atoms were present in a β-Sn configuration, while the distribution of the number of Sn atoms suggests that most Sn clusters had 3-4 Sn atoms. Taking into account the 50 % detection efficiency, these observations suggest that the clusters are present as a 6-Sn cluster-defect or a 7-Sn cluster-defect, as predicted by C.I. Ventura et.al. [136] However, due to the inability to detect vacancies and the limited in-plane resolution of the L-APT we cannot distinguish between the two.

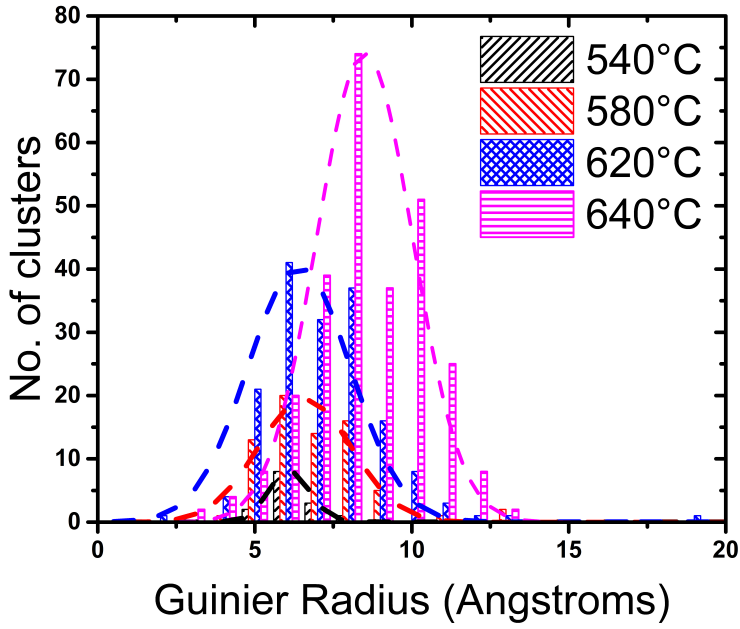

Figure 5.2 – Guinier Radius for Sn clusters in layers annealed at different temperatures. The Guinier radius is a measure of average size of the cluster [148]. Please note the dashed outline around the histogram is just a guide for the eye.

L-APT analysis can also be used to understand the thermodynamics of cluster growth in these layers. Our initial results on the cluster size as a function of anneal temperature showed that till an anneal temperature of 620 °C, the abundance of Sn clusters increased but the size distribution of the clusters did not change (**Fig. 5.2**). However, in the layer annealed at

640 °C, an increase in the abundance of clusters was observed along with a shift towards larger cluster size in the size distribution (**Fig. 5.2**). The shift in the distribution size maybe due to a change in the cluster growth regime, i.e. from a nucleation controlled growth to a diffusion controlled growth. However, to certify this hypothesis, L-APT measurements need to be done on layers annealed for different time at the same temperature.

5.3 Envisaged future development in L-APT

During this thesis we demonstrated the capability of L-APT to characterize multilayer stacks with sub-nm resolution and used it to gain insight into physical phenomenon like cluster formation, defect mediated diffusion etc., thereby allowing us to understand their impact on material properties. However, such high spatial resolution can only be achieved for samples which contain layers with (1) similar evaporation fields (2) moderately absorb the incident laser. The degradation in spatial resolution for alternate samples stems from the presence of a non-hemispherical apex shape. Indeed, the asymmetrical apex shape leads to magnification variations and trajectory overlap [22] which in-turn lead to density variations in the reconstructed data. The inability of conventional reconstruction algorithms [26] to correctly reconstruct data originating form asymmetrical apex shapes is the biggest hurdle for L-APT analysis. Few alternate algorithms based on correcting for the density variations in the observed detector hit map have been proposed in scientific literature [88]. However, these algorithms fail in cases when there is trajectory overlap or when detection efficiency for the constituent layers is different (for example the detection efficiency for oxides and nitrides is lower than Si [149]). In principle, a more accurate reconstruction should be possible by taking into account the shape of the apex and the exact trajectories of the emitted ions. Forward 3-D field evaporation simulations [89, 22] are able to calculate the ion trajectories originating from and asymmetrical apex, however a backward iteration i.e. reconstruction, would require a continuous knowledge about the tip shape. The apex shape can be obtained either by adding TEM imaging to the APT system or via simulating it by using the 3-D field evaporation simulators. L-APT systems with an inbuilt TEM are currently under development [90]. Calculating the apex shape using 3-D simulations would require in-depth knowledge of the threshold field evaporation for every constituent element. The difference in the threshold fields can

be calibrated using the 3-D evaporation simulations and refining the threshold field evaporation values iteratively till the steady state apex shape matches the experimentally determined apex shape (using 3-D TEM tomography). Reconstruction procedures based on using 3-D field evaporation simulators are currently being investigated [150].

Appendices

Appendix A

Sample Preparation & L-APT protocol

In this appendix I will first describe the procedure I followed to make specimens suitable for L-APT analysis during the project. Subsequently, I will layout the protocol for running a L-APT measurement.

A.1 Sample preparation

Specimen suitable for L-APT analysis is essentially in the shape of a needle with apex radius of $\sim 30\,nm - 50\,nm$. Semiconducting specimens are prepared using Focused Ion Beam (FIB) based procedures [151]. Conventional procedures like electropolishing are not suitable for these specimens as (1) no suitable enchants are known and (2) they can only be applied to wire-like structures, hence, are unsuitable for specimen preparation from wafers.

The process to prepare L-APT specimen consists of:

- Freeing a piece of wafer (called lamella) with the area of interest in it.
- Transporting the lamella and attaching it to a pre-sharpened W tip
- Sharpening the attached lamella into a needle shape suitable for analysis

Each step is shown in a figure and is discussed below.

In the first step the lamella is prepared on the wafer using FIB. To do this, two rectangular trenches are milled close to each other such that separation between the two inner edges of the trenches is equal to the desired width of the lamella (**Fig. A.1(A)**). Subsequently, the lamella is partially detached from the wafer by cutting two sides (left and bottom) of the lamella (**Fig. A.1(B)**). Please note that, since the lamella is prepared using a 5-30 KV Ga beam, a Pt cap is deposited to protect the top surface from damage by the ion beam. The Pt is deposited using the internal gas injection system.

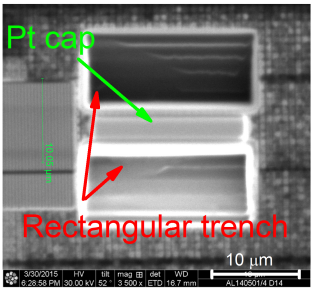

(a) The lamella on the wafer after the two rectangular trenches are milled. Pt cap is deposited to protect from Ga beam damage

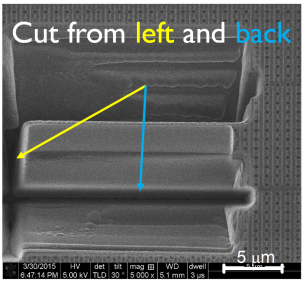

(b) Lamella partially freed from two sides by making cuts at the bottom and the left

Figure A.1 – Step I of sample preparation.

After lamella preparation, step II consists of first, attaching the lamella to a micromanipulator. The micromanipulator is welded to the lamella using Pt (**Fig. A.2(A)**). Subsequently, the last edge of the lamella is milled to free it completely from the wafer (**Fig. A.2(A)**). The freed lamella is then moved to the W tip and attached at the apex (again using Pt welds) (**Fig. A.2(B)**). A cut through the lamella is used to separate the lamella leaving a piece of it on the W wire and the rest on the micromanipulator. This way the leftover lamella can be used to make more tips (**Fig. A.2(B)**). The W wire used for mounting the sample are pre-sharpened with an apex radius of $\sim 1\,\mu m$ and attached to a Sn coated

copper rod. They can be ordered from GGB industries and it fits directly into the L-APT sample holder.

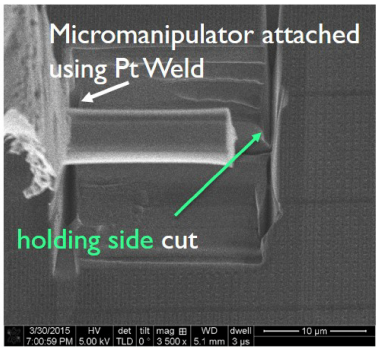

(A) Lift out of the lamella using the micromanipulator of the FIB tool the micromanipulator was attached via Pt deposited using the internal gas injection system before the lamella was freed

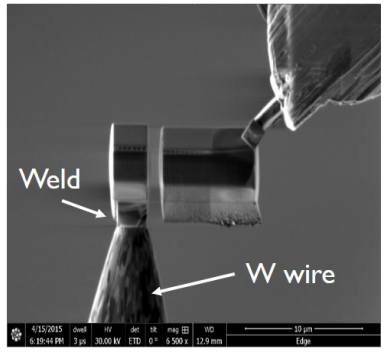

(B) The lamella is moved to a W tip with the micromanipulator. It is then attached to the W wire using Pt. FIB is then used to detach the remaining part of the lamella.

Figure A.2 – Step II of sample preparation.

Once a chunk of the lamella is attached to the W wire, Step III involves shaping the chunk into the shape of a needle with an apex radius of $\sim 30\,nm - 50\,nm$. This is achieved by annular milling using the FIB. The shape of the specimen after annular milling is shown in **Fig. A.3**. The sacrificial Pt cap deposited at the start of the specimen preparation procedure has much higher threshold for field evaporation as compared to Si, Ge, $Ge_{(1-x)}Sn_{(x)}$, GaN etc. Furthermore, the bonding strength of the Pt cap with that of the underlying layer is also extremely poor. This leads to high tip failure rate. Hence, for the samples prepared in this thesis, majority of the Pt cap was removed by scanning the tip apex using a low energy (5 KV) Ga^+ beam (**Fig. A.3(C)**).

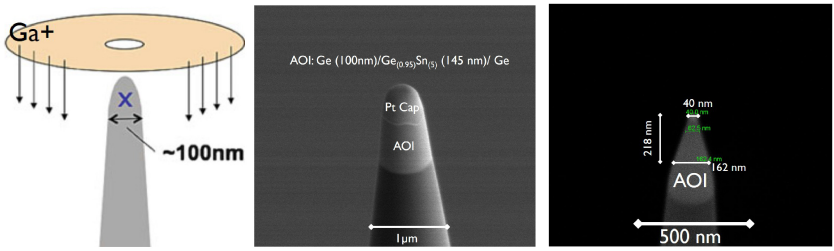

(A) Schematic of annular milling

(B) SEM image of a $Ge_{(0.95)}Sn_{(0.5)}$ tip before the final cleaning of the Pt cap

(C) SEM image of the final APT specimen. Please note, due to the high threshold field required to evaporate Pt, it is completely removed by scanning the tip surface, using a low energy (5KV) Ga^{+} beam

Figure A.3 – Step III of sample preparation.

A.2 Running a L-APT analysis

In this section I will briefly discuss the procedure to start a L-APT analysis. After the specimen preparation, the sample is introduced into the analysis chamber of the tool. The analysis chamber is under ultra-high vacuum (between 10^{-10} mbar - 10^{-11} mbar) and is equipped with a cold finger capable of cooling the tip down to 15 K. L-APT analysis are generally conducted with the specimen cooled to $\sim 80\,K - 20\,K$. A step-by-step procedure to conduct a L-APT analysis is given below.

- The first step is to roughly align the laser with the apex of the tip. In the tool present at IMEC, the laser can be moved in two directions, (1) parallel to the tip axis (X-direction) and (2) perpendicular to the tip axis (Y-direction). The laser creates a diffraction pattern when it interacts with the tip. Along the axis of the tip, the position of the apex can be roughly estimated when the diffraction spot disappears when the laser is moved in the x-direction away from the tip. The position of the apex in the direction perpendicular to the axis of the tip can be roughly estimated by the brightness of the diffraction spot (it is the brightest when aligned with the tip) (**Fig. A.4**).

- Once the laser is roughly aligned, the advanced delay line detector (ADLD) is switched on and a potential of $\sim 100\,V$ is applied between the tip and the detector. Subsequently, the potential bias between

the two is slowly increased till the point some counts are obtained at the expected masses. It is advisable that while increasing the applied voltage the laser position is also fine-tuned. This is done via the observed flux count, where the most optimal position of the laser is denoted by the position where maximum flux is obtained.

- Once the applied voltage is high enough, such that, (1) the evaporation of atoms occurs in a regular fashion, (2) species which are dominant at low field (e.g. peak at mass 19 amu, hydrides of constituent element) disappear from the mass spectra, the position of the laser is fine-tuned one final time. Afterwards, the voltage is increased to have the desired flux (at IMEC $\sim 0.005\,atoms/pulse - 0.05\,atoms/pulse$).

- The final step involves setting up the analysis condition to obtain quantitative results. As explained in Chapter 4, this done by setting the laser power and the applied voltage to have a desired CSR value of a constituent element at a particular flux value. Once the analysis conditions have been set up, the control of the measurement is given to the computer/software. The software automatically increases or decreases the voltage in pre-defined steps to maintain the measurement at a desired flux. This is known as a constant flux measurement. However, since the radius of the apex increases with depth due to the shank angle of the tip, the number of atoms present on the surface increases. This implies that the atoms testing the potential barrier for evaporation increases with depth. Writing the rate law (**Eq. 2.1**) in terms of atoms/second we get,

$$\phi = n_e \nu_{atom} exp\left(\frac{-Q(F)}{K_b T}\right) \tag{A.1}$$

where n_e is the number of atoms at the edge of an atomic terrace (i.e. atoms which experience the maximum field). Equation A.1 states that the flux (in atoms/sec) is also a function of number of atoms testing the potential barrier for field evaporation. Hence, keeping the flux constant in terms of atoms/pulse actually decreases the evaporation flux in terms of atoms per pulse per surface area.

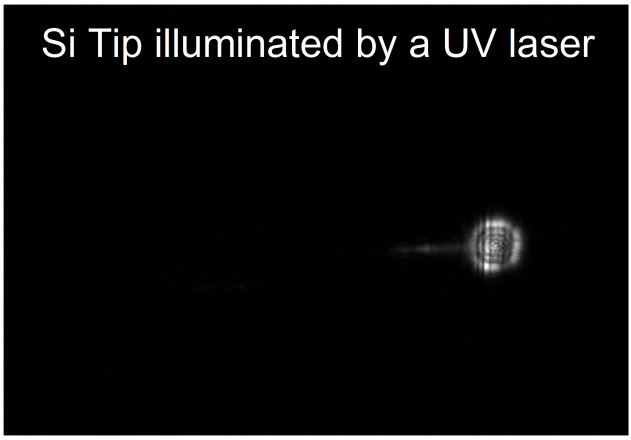

Figure A.4 – Diffraction spot at the tip apex

Appendix B

Reconstruction of APT data

In this appendix I will briefly discuss the method used for calculating the mass/charge ratio of the evaporated ions and reconstruction protocol to calculate the original XYZ coordinates of the evaporated ion. The below described reconstruction algorithm was introduced by Bas et al. [26]. This algorithm is used directly or in a slightly modified form by the majority of the APT community. In APT, a curved surface with a radius of $\sim 20\,nm - 50\,nm$ is projected onto a position sensitive detector of radius $\sim 5\,cm$. The raw data from an APT measurement are:

- the impact positions on the position sensitive detector
- the time between the laser/voltage pulse and an impact event on the detector, i.e. the time of flight of an ion
- the voltage required for field evaporation

From this data we have to calculate the mass/charge ratio of the evaporating element and the XYZ coordinates of the ion on the tip.

The mass/charge ratio of the evaporating ion can be calculated using conservation of energy as follows. Under the assumption that the ion takes a straight path to the detector and that it reaches its final velocity instantaneously, equating the initial kinetic energy E_{kin} of the ion to the potential energy $\mathrm{E}_{\mathrm{pot}}$ at the detector we get:

$$E_{kin} = \frac{1}{2}Mv^2 = \frac{1}{2}M\frac{d^2}{t^2} = nq_eV = E_{pot} \tag{B.1}$$

where M is the mass of the ion, nq_e is the charge, V is the applied potential and velocity $v = \frac{d}{t}$, d being the distance between the tip and the detector and t being the time of flight. Rearranging equation B.1 we can calculate the mass/charge ratio (**Eq. B.2**)

$$\frac{M}{n} = 2q_e V \frac{t^2}{d^2} \tag{B.2}$$

However, the flight path from the tip to the detector is not straight. Furthermore, the flight length for atoms evaporating from the center of the tip is less than for the atoms evaporating from the sides. To account for the error generated due to this, first an initial mass/charge spectra is generated using equation B.2. Subsequently, the mass/charge ratio is optimized by using 'voltage correction' and 'bowl correction' [152].

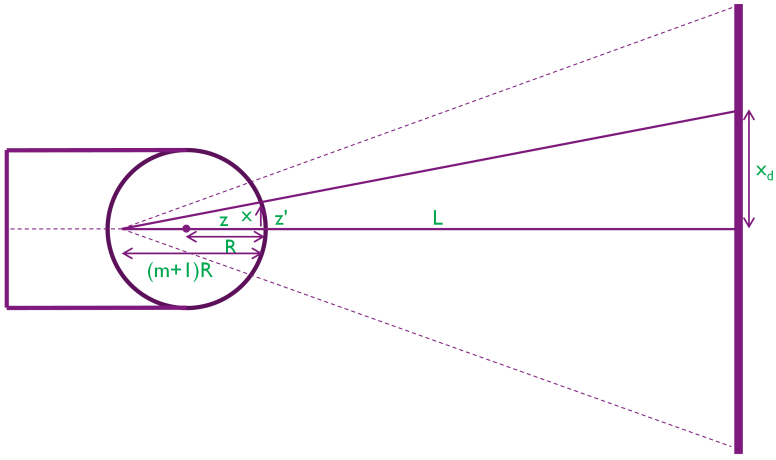

Figure B.1 – Schematic drawing of the point projection model proposed by Bas et al. [26] for reconstruction of APT data.

To reconstruct the raw data, i.e. to calculate the original XYZ coordinates of the evaporated ion the, Bas et al. took the following assumptions:

1. The surface of the specimen is a hemispherical cap
2. The trajectories of the ion can be modeled based on a point projection model (**Fig. B.1**).
3. Each atom has a constant average atomic volume (v_{at}). Although, each mass can have its own unique atomic volume.

4. The field F at an applied voltage V is given by $F = \frac{V}{\beta R}$, where R is the radius of the apex and β is a geometry parameter. Using electrostatics, one can derive that $\beta = 1$ for a sphere, $\beta = 2$ for a cylinder with hemispherical ends and ranges from2-8 for a typical APT specimen.

5. The tip axis is perpendicular to the detector

Using the above listed assumptions and simple geometrical considerations, one can easily deduce from **Fig. B.1** :

$$\frac{x}{x_d} = \frac{(m+1)R - z'}{(m+1)R + L} \implies x = x_d \frac{(m+1)R - z'}{(m+1)R + L} \tag{B.3}$$

where x_d is the x coordinate of the detected hit, x is the position of the atom on the tip, R is the radius of the tip, m is a projection parameter such that mR is the distance of the projection point from the surface of the tip, L is the distance from the tip surface to the detector and z' takes into account the curvature of the tip and is equal to:

$$z' = R - Z = R - \sqrt{R^2 - x^2} \tag{B.4}$$

where Z is the displacement of the point under consideration from the center of the semicircle in the Z-direction (**Fig. B.1**). Combining equation B.3 and B.4 and solving for x we get:

$$x = \frac{(Rmx_d)(L + (m+1)R) + \sqrt{R^2 x_d^2((L + (m+1)R)^2 - (m^2-1)x_d^2)}}{(L + (m+1)R)^2 + x_d^2} \tag{B.5}$$

However, no simple solution exist in two-dimensions for the position of the atom on the tip as, z' is a function of both x and y in three-dimensions. Hence, to avoid such complications equation B.5 can be approximated as:

$$\frac{x}{x_d} = \frac{(m+1)R}{L} \implies x = x_d \frac{(m+1)R}{L} \tag{B.6}$$

using the fact that $z' << mR << L$. Similarly:

$$\frac{y}{y_d} = \frac{(m+1)R}{L} \implies y = y_d \frac{(m+1)R}{L} \tag{B.7}$$

The magnification G achieved by projecting an atom at position x on the tip surface onto a position x_d on the detector is

$$G = \frac{x_d}{x} \tag{B.8}$$

combining equation B.6 and B.8 we get:

$$G = \frac{L}{(m+1)R} \tag{B.9}$$

The raw z-coordinate, i.e. the position of the atoms along the axis of the tip, can be calculated using the assumption of the constant volume of each atom. Ignoring the curved surface of the tip apex, the position of the N^{th} atom along the tip axis z_0, can be written as [153]:

$$z_0 = \sum_{i=1}^{N-1} \frac{L^2}{S_D Q} \frac{(F\beta)^2 v_{at}}{(m+1)^2} \times \frac{1}{(V_i)^2} \tag{B.10}$$

where $S_D$is the surface area of the detector, Q is the detection efficiency and $V_i$is the voltage required to evaporate the i^{th} atom. The z-coordinate (z) after accounting for the curvature of the tip apex, can be calculated as [26]:

$$z = z_0 - z' \implies z_0 - R\left(1 - \sqrt{1 - \frac{(m+1)^2 \times (x_d^2 + y_d^2)}{L^2}}\right) \tag{B.11}$$

Hence, the original xyz-coordinate of every atom prior to evaporation can be calculated using equations B.6, B.7 and B.11 respectively. Bas et al. also developed a reconstruction protocol if the tip axis was not perpendicular to the detector [26]. In this case the mathematical formulation to calculate the coordinates was also a function of the angle between the tip and the detector.

List of publications

Journal papers and Proceedings as first author

1. Kumar A, Gencarelli F, Kambham A K, Gilbert M, Vincent B and Vandervorst W, Study of Sn migration during relaxation of $Ge_{(1-x)}Sn_{(x)}$ layers using atom probe tomography, physica status solidi (c) 9 1924–30 (2012)

2. Kumar A, Komalan M P, Lenka H, Kambham A K, Gilbert M, Gencarelli F, Vincent B and Vandervorst W, Atomic insight into $Ge_{(1-x)}Sn_{(x)}$ using atom probe tomography, Ultramicroscopy 132 171–8(2013)

3. Kumar A, J. Demeulemeester, J. Bogdanowicz, J. Bran, D. Melkonyan, C. Fleischmann, Gencarelli F, W. Wang, R. Loo and Vandervorst W On the interplay between relaxation, defect formation, and atomic Sn distribution in $Ge_{(1-x)}Sn_{(x)}$ unraveled with Atom Probe Tomography, Journal of Applied Physics 118, 025302 (2015)

4. Kumar A, J. Demeulemeester, J. Bogdanowicz, J. Bran, D. Melkonyan, C. Fleischmann, and Vandervorst W, Deriving the apex temperature of a nanoscaled semiconducting field emitter illuminated by a femtosecond pulsed laser, Journal of Applied Physics, under review

5. Kumar A, J. Bogdanowicz, M. Gilbert, M. Floriyan, D. Melkonyan, C. Fleischmann, A. Vella and Vandervorst W, Impact of non-uniform light absorption on the shape of semiconducting field emitters in laser-assisted Atom Probe Tomography, Applied Physics Letters, to be submitted

6. J. Bogdanowicz*, Kumar A*, M. Gilbert, D. Melkonyan, C. Fleischmann, A. Vella and Vandervorst W, Impact of focused-ion-beam milling on sub-bandgap light absorption during laser-assisted atomprobe tomography, Ultramicroscopy to be submitted

Conference contribution as first author

1. Kumar A, Gencarelli F, Kambham A K, Gilbert M, Vincent B and Vandervorst W, Study of Sn migration during relaxation of $Ge_{(1-x)}Sn_{(x)}$ layers using atom probe tomography, E-MRS spring meeting, Strasbourg, France (2012)

2. Kumar A, Komalan M P, Lenka H, Kambham A K, Gilbert M, Gencarelli F, Vincent B and Vandervorst W, Atomic insight into $Ge_{(1-x)}Sn_{(x)}$ using atom probe tomography, 53rd International Field Emission Society (IFES) Conference, Alabama, USA (2012)

3. Kumar A, Gilbert M, Kambham A K, Gencarelli F, Loo R and Vandervorst W, Application of atom probe tomography to epitaxial layers 8th International Conference on Silicon Epitaxy and Heterostructures-ICSI, Nagoya, Japan (2013)

4. Kumar A, J. Demeulemeester, J. Bogdanowicz, J. Bran, D. Melkonyan, C. Fleischmann, Gencarelli F, W. Wang, R. Loo and Vandervorst W On the interplay between relaxation, defect formation, and atomic Sn distribution in $Ge_{(1-x)}Sn_{(x)}$ unraveled with Atom Probe Tomography, Atom Probe Tomography & Microscopy, Stuttgart, Germany (2014)

5. Kumar A, J. Demeulemeester, J. Bogdanowicz, J. Bran, D. Melkonyan, C. Fleischmann, and Vandervorst W, Thermal response of a nanoscaled field emitter under femtosecond laser pulse, Atom Probe Tomography & Microscopy, Stuttgart, Germany (2014)

Workshop contribution as first author

1. Kumar A, J. Bogdanowicz, M. Gilbert, M. Floriyan, D. Melkonyan, C. Fleischmann, A. Vella and Vandervorst W, Wavelength dependence of the apex shape of a semiconducting field emitter in laser-assisted Atom Probe Tomography, Atom probe workshop, Leoben, Austria (2015)

Journal papers and Proceedings as contributing author

1. Kambham A K, Zschaetzsch G, Sasaki Y, Togo M, Horiguchi N, Mody J, Florakis A, Gajula D, Kumar A and Gilbert M, Atom Probe Tomography for 3D-dopant analysis in FinFET devices, VLSI Technology (VLSIT), 2012 Symposium on (IEEE) pp 77–8 (2012)

2. Vincent B, Gencarelli F, Kumar A, Vantomme A, Merckling C, Lin D, Afanasiev V, Eneman G, Clarysse T and Firrincieli A, CVD Epitaxial growth of GeSn opens a new route for advanced Sn-based logic and photonics devices Silicon-Germanium, Technology and Device Meeting (ISTDM), 2012 International (IEEE) pp 1–2 (2012)

3. Gencarelli F, Vincent B, Demeulemeester J, Vantomme A, Moussa A, Franquet A, Kumar A, Bender H, Meersschaut J and Vandervorst W, Crystalline Properties and Strain Relaxation Mechanism of CVD Grown GeSn, ECS Journal of Solid State Science and Technology 2 P134–7 (2013)

4. Kambham A K, Kumar A, Florakis A and Vandervorst W, Three-dimensional doping and diffusion in nanoscaled devices as studied by atom probe tomography, Nanotechnology 24 275705 (2013)

5. Kambham A K, Kumar A, Gilbert M and Vandervorst W, 3D site specific sample preparation and analysis of 3D devices (FinFETs) by atom probe tomography Ultramicroscopy 132 65–9 (2013)

6. Loo R, Vincent B, Gencarelli F, Merckling C, Kumar A, Eneman G, Witters L, Vandervorst W, Caymax M and Heyns M, Ge1-xSnx Materials: Challenges and Applications ECS Journal of Solid State Science and Technology 2 N35–40 (2013)

7. Schrauwen A, Demeulemeester J, Kumar A, Vandervorst W, Comrie C, Detavernier C, Temst K and Vantomme A, On the nucleation of PdSi and NiSi2 during the ternary Ni (Pd)/Si (100) reaction Journal of Applied Physics 114 063518 (2013)

8. Gencarelli, F., Shimura, Y., Kumar, A., Vincent, B., Moussa, A., Vanhaeren, D., Richard, O., Bender, H., Vandervorst, W., Caymax, M. and Loo, R., Amorphous inclusions during Ge and GeSn epitaxial growth via chemical vapor deposition. Thin Solid Films, 590, pp.163-169 (2015)

Bibliography

[1] A. S. Okhotin, A. S. Pushkarskii, and V. V. Gorbachev. Thermophysical Properties of Semiconductors, Atom Publ. *House, Moscow*, 1972.

[2] P. Flubacher, A. J. Leadbetter, and J. A. Morrison. The heat capacity of pure silicon and germanium and properties of their vibrational frequency spectra. *Philosophical Magazine*, 4(39):273–294, March 1959.

[3] Baptiste Gault, Michael P. Moody, Julie M. Cairney, and Simon P. Ringer. Atom probe crystallography. *Materials Today*, 15(9):378–386, September 2012.

[4] Fabio D'Agostino and Daniele Quercia. Short-channel effects in MOSFETs. *Introduction to VLSI design (EECS 467)*, 2000.

[5] Juan C. Ranuárez, M.J. Deen, and Chih-Hung Chen. A review of gate tunneling current in MOS devices. *Microelectronics Reliability*, 46(12):1939–1956, December 2006.

[6] Federica Gencarelli. *Epitaxial growth of GeSn compounds for advanced CMOS and Photonics applications.* PhD thesis. KU Leuven, 2015.

[7] Mark Bohr. The evolution of scaling from the homogeneous era to the heterogeneous era. In *Electron Devices Meeting (IEDM), 2011 IEEE International*, pages 1–1. IEEE, 2011.

[8] D. Hisamoto, Wen-Chin Lee, J. Kedzierski, H. Takeuchi, K. Asano, C. Kuo, Erik Anderson, Tsu-Jae King, J. Bokor, and Chenming Hu. FinFET-a self-aligned double-gate MOSFET scalable to 20

nm. *IEEE Transactions on Electron Devices*, 47(12):2320–2325, December 2000.

[9] ITRS roadmap 2014.

[10] H Kawanami. Heteroepitaxial technologies of III–V on Si. *Solar Energy Materials and Solar Cells*, 66(1–4):479–486, February 2001.

[11] Cengiz S. Ozkan, William D. Nix, and Huajian Gao. Strain relaxation and defect formation in heteroepitaxial Si1-xGex films via surface roughening induced by controlled annealing experiments. *Applied Physics Letters*, 70(17):2247–2249, April 1997.

[12] T. U. Schülli, G. Vastola, M.-I. Richard, A. Malachias, G. Renaud, F. Uhlík, F. Montalenti, G. Chen, L. Miglio, F. Schäffler, and G. Bauer. Enhanced Relaxation and Intermixing in Ge Islands Grown on Pit-Patterned Si(001) Substrates. *Physical Review Letters*, 102(2):025502, January 2009.

[13] W. Vandervorst. Semiconductor profiling with sub-nm resolution: Challenges and solutions. *Applied Surface Science*, 255(4):805–812, December 2008.

[14] T. Wirtz, P. Philipp, J.-N. Audinot, D. Dowsett, and S. Eswara. High-resolution high-sensitivity elemental imaging by secondary ion mass spectrometry: from traditional 2d and 3d imaging to correlative microscopy. *Nanotechnology*, 26(43):434001, 2015.

[15] L C Feldman and and J. M. Poate. Rutherford Backscattering and Channeling Analysis of Interfaces and Epitaxial Structures. *Annual Review of Materials Science*, 12(1):149–176, 1982.

[16] D. Smeets, J. Demeulemeester, D. Deduytsche, C. Detavernier, C. M. Comrie, C. C. Theron, C. Lavoie, and A. Vantomme. Simultaneous real-time x-ray diffraction spectroscopy, Rutherford backscattering spectrometry, and sheet resistance measurements to study thin film growth kinetics by Kissinger plots. *Journal of Applied Physics*, 104(10):103538, November 2008.

[17] D.J. Larson, T.J. Prosa, D.E. Perea, K. Inoue, and D. Mangelinck. Atom probe tomography of nanoscale electronic materials. *MRS Bulletin*, 41(01):30–34, January 2016.

[18] K. Inoue, F. Yano, A. Nishida, H. Takamizawa, T. Tsunomura, Y. Nagai, and M. Hasegawa. Dopant distributions in n-MOSFET structure observed by atom probe tomography. *Ultramicroscopy*, 109(12):1479–1484, November 2009.

[19] Koji Inoue, Ajay Kumar Kambham, Dominique Mangelinck, Dan Lawrence, and David J. Larson. Atom-Probe-Tomographic Studies on Silicon-Based Semiconductor Devices. *Microscopy Today*, 20(05):38–44, September 2012.

[20] Oussama Moutanabbir, Dieter Isheim, Horst Blumtritt, Stephan Senz, Eckhard Pippel, and David N. Seidman. Colossal injection of catalyst atoms into silicon nanowires. *Nature*, 496(7443):78–82, April 2013.

[21] Tien T. Tsong. *Atom-Probe Field Ion Microscopy: Field Ion Emission, and Surfaces and Interfaces at Atomic Resolution.* Cambridge University Press, September 2005.

[22] F. Vurpillot, A. Bostel, and D. Blavette. Trajectory overlaps and local magnification in three-dimensional atom probe. *Applied Physics Letters*, 76(21):3127–3129, May 2000.

[23] Erwin W. Müller, John A. Panitz, and S. Brooks McLane. The Atom-Probe Field Ion Microscope. *Review of Scientific Instruments*, 39(1):83–86, January 1968.

[24] F. Vurpillot, J. Houard, A. Vella, and B. Deconihout. Thermal response of a field emitter subjected to ultra-fast laser illumination. *Journal of Physics D: Applied Physics*, 42(12):125502, 2009.

[25] B. Gault, F. Vurpillot, A. Vella, M. Gilbert, A. Menand, D. Blavette, and B. Deconihout. Design of a femtosecond laser assisted tomographic atom probe. *Review of Scientific Instruments*, 77(4):043705, April 2006.

[26] P. Bas, A. Bostel, B. Deconihout, and D. Blavette. A general protocol for the reconstruction of 3d atom probe data. *Applied Surface Science*, 87–88:298–304, March 1995.

[27] D. Blavette, E. Cadel, A. Fraczkiewicz, and A. Menand. Three-Dimensional Atomic-Scale Imaging of Impurity Segregation to Line Defects. *Science*, 286(5448):2317–2319, December 1999.

[28] S. Koelling, N. Innocenti, A. Schulze, M. Gilbert, A. K. Kambham, and W. Vandervorst. In-situ observation of non-hemispherical tip shape formation during laser-assisted atom probe tomography. *Journal of Applied Physics*, 109(10):104909, May 2011.

[29] J. H. Lee, Y. T. Kim, J. J. Kim, S. Y. Lee, and C. G. Park. 3d compositional characterization of Si/SiO2 vertical interface structure by atom probe tomography. *Electronic Materials Letters*, 9(6):747–750, November 2013.

[30] A. K. Kambham. *Atomic Scale Characterization of 3D structures (FinFETs) using Atom Probe Tomography.* Ph.D. Thesis. KU Leuven.

[31] M. K. Miller and M. G. Hetherington. Local magnification effects in the atom probe. *Surface Science*, 246(1):442–449, April 1991.

[32] A. Cerezo, T. J. Godfrey, and G. D. W. Smith. Application of a position-sensitive detector to atom probe microanalysis. *Review of Scientific Instruments*, 59(6):862–866, June 1988.

[33] Michael P. Moody, Leigh T. Stephenson, Anna V. Ceguerra, and Simon P. Ringer. Quantitative binomial distribution analyses of nanoscale like-solute atom clustering and segregation in atom probe tomography data. *Microscopy Research and Technique*, 71(7):542–550, July 2008.

[34] Leigh T. Stephenson, Michael P. Moody, Peter V. Liddicoat, and Simon P. Ringer. New Techniques for the Analysis of Fine-Scaled Clustering Phenomena within Atom Probe Tomography (APT) Data. *Microscopy and Microanalysis*, 13(06):448–463, December 2007.

[35] Olof C Hellman and David N Seidman. Measurement of the Gibbsian interfacial excess of solute at an interface of arbitrary geometry using three-dimensional atom probe microscopy. *Materials Science and Engineering: A*, 327(1):24–28, April 2002.

[36] D. Vaumousse, A. Cerezo, and P. J. Warren. A procedure for quantification of precipitate microstructures from three-dimensional atom probe data. *Ultramicroscopy*, 95:215–221, May 2003.

[37] S. Kölling and W. Vandervorst. Failure mechanisms of silicon-based atom-probe tips. *Ultramicroscopy*, 109(5):486–491, April 2009.

[38] Sebastian Koelling. *three dimensional compositional analysis of semiconductors with the Atom Probe*. Phd Thesis. KU Leuevn, 2011.

[39] Erwin W. Müller. Field Desorption. *Physical Review*, 102(3):618–624, May 1956.

[40] Robert Gomer and Lynn W. Swanson. Theory of Field Desorption. *The Journal of Chemical Physics*, 38(7):1613–1629, April 1963.

[41] W Schottky. Über den Einfluss von Strukturwirkungen, besonders der Thomsonschen Bildkraft, auf die Elektronenemission der Metalle. 15:872–878, 1914.

[42] R. K. Biswas and R. G. Forbes. Theoretical arguments against the Muller-Schottky mechanism of field evaporation. *Journal of Physics D: Applied Physics*, 15(7):1323, 1982.

[43] R. G. Forbes. An evaporation-field formula including the repulsive ion-surface interaction. *Journal of Physics D: Applied Physics*, 15(7):L75, 1982.

[44] Richard G. Forbes, R. K. Biswas, and K. Chibane. Field evaporation theory: A re-analysis of published field sensitivity data. *Surface Science*, 114(2):498–514, February 1982.

[45] Richard G. Forbes. A new formula for predicting low-temperature evaporation field. *Applied Physics Letters*, 40(3):277–279, February 1982.

[46] Richard G. Forbes. Field evaporation theory: a review of basic ideas. *Applied Surface Science*, 87–88:1–11, March 1995.

[47] T. T. Tsong and E. W. Müller. Field evaporation rates of tungsten. *physica status solidi (a)*, 1(3):513–533, March 1970.

[48] N. Ernst. Experimental investigation on field evaporation of singly and doubly charged rhodium. *Surface Science*, 87(2):469–482, August 1979.

[49] M. K. Miller, M. G. Hetherington, and G. D. W. Smith. *Atom Probe Field Ion Microscopy*. Clarendon Press, Oxford : New York, 1 edition edition, November 1996.

[50] R. G. Forbes and K. Chibane. Derivation of an activation energy formula in the context of charge draining. *Le Journal de Physique Colloques*, 47(C7):C7–65–C7–70, November 1986.

[51] Richard G. Forbes. Charge hopping and charge draining: Two mechanisms of field desorption. *Surface Science*, 102(1):255–263, January 1981.

[52] H. J. Kreuzer and K. Nath. Field evaporation. *Surface Science*, 183(3):591–608, May 1987.

[53] G. L. Kellogg. Measurement of activation energies for field evaporation of tungsten ions as a function of electric field. *Physical Review B*, 29(8):4304–4312, April 1984.

[54] David R. Kingham. The post-ionization of field evaporated ions: A theoretical explanation of multiple charge states. *Surface Science*, 116(2):273–301, April 1982.

[55] Roger Haydock and David R. Kingham. Post-Ionization of Field-Evaporated Ions. *Physical Review Letters*, 44(23):1520–1523, June 1980.

[56] G. L. Kellogg. Measurement of the charge state distribution of field evaporated ions: Evidence for post-ionization. *Surface Science*, 120(2):319–333, August 1982.

[57] S. C. Lam and R. J. Needs. Theory of field ionization. *Applied Surface Science*, 76–77:61–69, March 1994.

[58] B. Mazumder, A. Vella, M. Gilbert, B. Deconihout, and G. Schmitz. Reneutralization time of surface silicon ions on a field emitter. *New Journal of Physics*, 12(11):113029, November 2010.

[59] G. L. Kellogg. Temperature dependence of the silicon field evaporation voltage. *Surface Science Letters*, 124(2):L55–L59, January 1983.

[60] Tomoya Ono and Kikuji Hirose. First-principles study on field evaporation for silicon atom on Si(001) surface. *Journal of Applied Physics*, 95(3):1568–1571, February 2004.

[61] A. Cerezo, C. R. M. Grovenor, and G. D. W. Smith. Pulsed laser atom probe analysis of semiconductor materials. *Journal of Microscopy*, 141(2):155–170, February 1986.

[62] B. Gault, F. Vurpillot, A. Bostel, A. Menand, and B. Deconihout. Estimation of the tip field enhancement on a field emitter under laser illumination. *Applied Physics Letters*, 86(9):094101, February 2005.

[63] S. K. Sundaram and Eric Mazur. Inducing and probing non-thermal transitions in semiconductors using femtosecond laser pulses. *Nature materials*, 1(4):217–224, 2002.

[64] G. L. Kellogg. Measurement of activation energies for field evaporation of tungsten ions as a function of electric field. *Physical Review B*, 29(8):4304–4312, April 1984.

[65] A. Vella, B. Deconihout, L. Marrucci, and E. Santamato. Femtosecond Field Ion Emission by Surface Optical Rectification. *Physical Review Letters*, 99(4):046103, July 2007.

[66] J. Houard, A. Vella, F. Vurpillot, and B. Deconihout. Optical near-field absorption at a metal tip far from plasmonic resonance. *Physical Review B*, 81(12):125411, March 2010.

[67] J. Bogdanowicz and W. Vandervorst. On the understanding of local optical resonance in elongated dielectric particles. *Journal of Quantitative Spectroscopy and Radiative Transfer*, 146:175–180, October 2014.

[68] J. Bogdanowicz, M. Gilbert, N. Innocenti, S. Koelling, B. Vanderheyden, and W. Vandervorst. Light absorption in conical silicon particles. *Optics Express*, 21(3):3891, February 2013.

[69] A. Cerezo, P. H. Clifton, A. Gomberg, and G. D. W. Smith. Aspects of the performance of a femtosecond laser-pulsed 3-dimensional atom probe. *Ultramicroscopy*, 107(9):720–725, September 2007.

[70] Jh Bunton, Jd Olson, Dr Lenz, and Tf Kelly. Investigation of Performance-Influencing Factors in Pulsed Laser Atom Probe. *Microscopy and Microanalysis*, 14(Supplement S2):1238–1239, August 2008.

[71] F. Vurpillot, B. Gault, A. Vella, M. Bouet, and B. Deconihout. Estimation of the cooling times for a metallic tip under laser illumination. *Applied Physics Letters*, 88(9):094105, February 2006.

[72] H. F. Liu and T. T. Tsong. Numerical calculation of the temperature evolution and profile of the field ion emitter in the pulsed-laser time-of-flight atom probe. *Review of Scientific Instruments*, 55(11):1779–1784, November 1984.

[73] B. Gault, M. Müller, A. La Fontaine, M. P. Moody, A. Shariq, A. Cerezo, S. P. Ringer, and G. D. W. Smith. Influence of surface migration on the spatial resolution of pulsed laser atom probe tomography. *Journal of Applied Physics*, 108(4):044904, August 2010.

[74] James R. Riley, Rodrigo A. Bernal, Qiming Li, Horacio D. Espinosa, George T. Wang, and Lincoln J. Lauhon. Atom Probe Tomography of a-Axis GaN Nanowires: Analysis of Nonstoichiometric Evaporation Behavior. *ACS Nano*, 6(5):3898–3906, May 2012.

[75] Arul Kumar, Manu P. Komalan, Haraprasanna Lenka, Ajay Kumar Kambham, Matthieu Gilbert, Federica Gencarelli, Benjamin Vincent, and Wilfried Vandervorst. Atomic insight into Ge1-xSnx using atom probe tomography. *Ultramicroscopy*, 132:171–178, September 2013.

[76] Emmanuelle A. Marquis and Baptiste Gault. Determination of the tip temperature in laser assisted atom-probe tomography using charge state distributions. *Journal of Applied Physics*, 104(8):084914, October 2008.

[77] G. L. Kellogg. Determining the field emitter temperature during laser irradiation in the pulsed laser atom probe. *Journal of Applied Physics*, 52(8):5320–5328, August 1981.

[78] In-Whan Lyo and Phaedon Avouris. Field-Induced Nanometer-to Atomic-Scale Manipulation of Silicon Surfaces with the STM. *Science*, 253(5016):173–176, July 1991.

[79] N. M. Miskovsky, Ching Ming Wei, and Tien T. Tsong. Field evaporation of silicon in the field ion microscope and scanning

tunneling microscope configurations. *Physical Review Letters*, 69(16):2427–2430, October 1992.

[80] Frédéric De Geuser, Baptiste Gault, Alain Bostel, and François Vurpillot. Correlated field evaporation as seen by atom probe tomography. *Surface Science*, 601(2):536–543, January 2007.

[81] A. Vella. On the interaction of an ultra-fast laser with a nanometric tip by laser assisted atom probe tomography: A review. *Ultramicroscopy*, 132:5–18, September 2013.

[82] A. Cerezo, G. D. W. Smith, and P. H. Clifton. Measurement of temperature rises in the femtosecond laser pulsed three-dimensional atom probe. *Applied Physics Letters*, 88(15):154103, April 2006.

[83] E. P. Silaeva, A. Vella, N. Sevelin-Radiguet, G. Martel, B. Deconihout, and T. E. Itina. Ultrafast laser-triggered field ion emission from semiconductor tips. *New Journal of Physics*, 14(11):113026, 2012.

[84] James William Rohlf. chapter 14. In *Modern Physics from a to Z*. Wiley, New York, 1st edition edition, March 1994.

[85] Charles Kittel. Chapter 18. In *Introduction to Solid State Physics*. Wiley, Hoboken, NJ, 8 edition edition, November 2004.

[86] M. Mertig, G. Pompe, and E. Hegenbarth. Specific heat of amorphous silicon at low temperatures. *Solid State Communications*, 49(4):369–372, January 1984.

[87] D. Blavette, J.M. Sarrau, A. Bostel, and J. Gallot. Direction et distance d'analyse à la sonde atomique. *Revue de Physique Appliquée*, 17(7):435–440, 1982.

[88] F. De Geuser, W. Lefebvre, F. Danoix, F. Vurpillot, B. Forbord, and D. Blavette. An improved reconstruction procedure for the correction of local magnification effects in three-dimensional atom-probe. *Surface and Interface Analysis*, 39(2-3):268–272, February 2007.

[89] Christian Oberdorfer, Sebastian Manuel Eich, and Guido Schmitz. A full-scale simulation approach for atom probe tomography. *Ultramicroscopy*, 128:55–67, May 2013.

[90] M.K. Miller and T.F. Kelly. The Atom TOMography (ATOM) Concept. *Microscopy and Microanalysis*, 16(Supplement S2):1856–1857, July 2010.

[91] J. Bogdanowicz, M. Gilbert, N. Innocenti, S. Koelling, B. Vanderheyden, and W. Vandervorst. Light absorption in conical silicon particles. *Optics Express*, 21(3):3891, February 2013.

[92] J. Bogdanowicz, M. Gilbert, S. Koelling, and W. Vandervorst. Impact of the apex of an elongated dielectric tip upon its light absorption properties. *Applied Surface Science*, 302:223–225, May 2014.

[93] E. A. Marquis, B. P. Geiser, T. J. Prosa, and D. J. Larson. Evolution of tip shape during field evaporation of complex multilayer structures. *Journal of Microscopy*, 241(3):225–233, March 2011.

[94] Ludwig Reimer. *Transmission Electron Microscopy: Physics of Image Formation and Microanalysis*. Springer, November 2013.

[95] Maxim A. Yurkin and Alfons G. Hoekstra. The discrete-dipole-approximation code ADDA: Capabilities and known limitations. *Journal of Quantitative Spectroscopy and Radiative Transfer*, 112(13):2234–2247, September 2011.

[96] D. E. Aspnes and A. A. Studna. Dielectric functions and optical parameters of Si, Ge, GaP, GaAs, GaSb, InP, InAs, and InSb from 1.5 to 6.0 eV. *Physical Review B*, 27(2):985–1009, January 1983.

[97] Hasan Kocer, Serkan Butun, Edgar Palacios, Zizhuo Liu, Sefaattin Tongay, Deyi Fu, Kevin Wang, Junqiao Wu, and Koray Aydin. Intensity tunable infrared broadband absorbers based on VO2 phase transition using planar layered thin films. *Scientific Reports*, 5:13384, August 2015.

[98] Ravi Agrawal, Rodrigo A. Bernal, Dieter Isheim, and Horacio D. Espinosa. Characterizing Atomic Composition and Dopant Distribution in Wide Band Gap Semiconductor Nanowires Using Laser-Assisted Atom Probe Tomography. *The Journal of Physical Chemistry C*, 115(36):17688–17694, September 2011.

[99] B. Mazumder, A. Vella, B. Deconihout, and Tala'at Al-Kassab. Evaporation mechanisms of MgO in laser assisted atom probe tomography. *Ultramicroscopy*, 111(6):571–575, May 2011.

[100] DJ Larson, Rl Alvis, Df Lawrence, TJ Prosa, RM Ulfig, DA Reinhard, PH Clifton, SSA Gerstl, JH Bunton, DR Lenz, TF Kelly, and K Stiller. Analysis of Bulk Dielectrics with Atom Probe Tomography. *Microscopy and Microanalysis*, 14(Supplement S2):1254–1255, August 2008.

[101] L. V. Keldysh. Behavior of Non-metallic Crystals in Strong Electric Fields. *Soviet Journal of Experimental and Theoretical Physics*, 6:763, 1958.

[102] Elena P. Silaeva, Markus Karahka, and H. J. Kreuzer. Atom Probe Tomography and field evaporation of insulators and semiconductors: Theoretical issues. *Current Opinion in Solid State and Materials Science*, 17(5):211–216, October 2013.

[103] James F. Ziegler, M. D. Ziegler, and J. P. Biersack. SRIM – The stopping and range of ions in matter (2010). *Nuclear Instruments and Methods in Physics Research Section B: Beam Interactions with Materials and Atoms*, 268(11–12):1818–1823, June 2010.

[104] Janusz Bogdanowicz. *Photomodulated Optical Reflectance*. Springer Theses. Springer Berlin Heidelberg, Berlin, Heidelberg, 2012.

[105] W. Vandervorst, T. Clarysse, B. Brijs, R. Loo, Y. Peytier, B. J. Pawlak, E. Budiarto, and P. Borden. Carrier Illumination as a tool to probe implant dose and electrical activation. In *AIP Conference Proceedings*, volume 683, pages 758–763. AIP Publishing, September 2003.

[106] Alex Salnick and Jon Opsal. Quantitative photothermal characterization of ion-implanted layers in Si. *Journal of Applied Physics*, 91(5):2874–2882, March 2002.

[107] L. Pottier. Micrometer scale visualization of thermal waves by photoreflectance microscopy. *Applied Physics Letters*, 64(13):1618–1619, March 1994.

[108] Michael E. Levinshtein, Sergey L. Rumyantsev, and Michael S. Shur. *Properties of Advanced Semiconductor Materials: GaN, AIN, InN, BN, SiC, SiGe*. John Wiley & Sons, February 2001.

[109] Andreas Othonos and Constantinos Christofides. Ultrafast dynamics in phosphorus-implanted silicon wafers: The effects of annealing. *Physical Review B*, 66(8):085206, August 2002.

[110] M. Fried, T. Lohner, W. A. M. Aarnink, L. J. Hanekamp, and A. van Silfhout. Determination of complex dielectric functions of ion implanted and implanted-annealed amorphous silicon by spectroscopic ellipsometry. *Journal of Applied Physics*, 71(10):5260, 1992.

[111] Grace Huiqi Wang, Eng-Huat Toh, Xincai Wang, D.H.L. Seng, S. Tripathy, T. Osipowicz, Tau Kuei Chan, Keat Mun Hoe, S. Balakumar, Chih Hang Tung, Guo-Qiang Lo, G. Samudra, and Yee-Chia Yeo. Silicon-Germanium-Tin (SiGeSn) Source and Drain Stressors formed by Sn Implant and Laser Annealing for Strained Silicon-Germanium Channel P-MOSFETs. In *Electron Devices Meeting, 2007. IEDM 2007. IEEE International*, pages 131–134, December 2007.

[112] R. Loo, G. Wang, L. Souriau, J. C. Lin, S. Takeuchi, G. Brammertz, and M. Caymax. High Quality Ge Virtual Substrates on Si Wafers with Standard STI Patterning. *Journal of The Electrochemical Society*, 157(1):H13–H21, January 2010.

[113] M. V. Fischetti and S. E. Laux. Band structure, deformation potentials, and carrier mobility in strained Si, Ge, and SiGe alloys. *Journal of Applied Physics*, 80(4):2234–2252, August 1996.

[114] Jay Deep Sau and Marvin L. Cohen. Possibility of increased mobility in Ge-Sn alloy system. *Physical Review B*, 75(4):045208, January 2007.

[115] Yosuke Shimura, Wei Wang, Thomas Nieddu, Federica Gencarelli, Benjamin Vincent, Priya Laha, Herman Terryn, Stefan Stefanov, Stefano Chiussi, Joris Van Campenhout, Ngoc Duy Nguyen, Andre Vantomme, and Roger Loo. Bandgap Measurement by Spectroscopic Ellipsometry for Strained Ge1-xSnx. June 2013.

[116] Vijay R. D'Costa, Yanyan Fang, Jay Mathews, Radek Roucka, John Tolle, José Menéndez, and John Kouvetakis. Sn-alloying as a means of increasing the optical absorption of Ge at the C- and L-telecommunication bands. *Semiconductor Science Technology*, 24:115006, November 2009.

[117] G. Sun, R. A. Soref, and H. H. Cheng. Design of an electrically pumped SiGeSn/GeSn/SiGeSn double-heterostructure midinfrared laser. *Journal of Applied Physics*, 108(3):033107, August 2010.

[118] Jay Mathews, Radek Roucka, Junqi Xie, Shui-Qing Yu, José Menéndez, and John Kouvetakis. Extended performance GeSn/Si(100) p-i-n photodetectors for full spectral range telecommunication applications. *Applied Physics Letters*, 95(13):133506, September 2009.

[119] Richard A. Soref and Lionel Friedman. Direct-gap germanium-tin multiple-quantum-well electro-optical devices on silicon or germanium substrates, August 1996. U.S. Classification 257/18, 257/201, 257/616, 257/E29.078, 257/E31.035, 257/E31.061, 257/19, 257/103, 257/190, 257/E33.009; International Classification H01L31/105, H01L29/15, H01S5/34, H01L31/0352, H01S5/02, H01L33/06; Cooperative Classification H01L31/105, H01L29/155, H01L33/06, H01S5/3427, B82Y20/00, H01S5/34, H01S5/021, H01L31/035254; European Classification B82Y20/00, H01L29/15B2C, H01S5/34, H01L31/0352B3, H01L31/105, H01L33/06.

[120] Collaboration: Authors and editors of the volumes III/17A-22A-41A1a. Grey tin (alpha-Sn) phase transition pressure and volume change. In O. Madelung, U. Rössler, and M. Schulz, editors, *Group IV Elements, IV-IV and III-V Compounds. Part a - Lattice Properties*, volume a, pages 1–4. Springer-Verlag, Berlin/Heidelberg, 2001.

[121] P. K. Davies and A. Navrotsky. Quantitative correlations of deviations from ideality in binary and pseudobinary solid solutions. *Journal of Solid State Chemistry*, 46(1):1–22, January 1983.

[122] R. W. Olesinski and G. J. Abbaschian. The Ge-Sn (Germanium-Tin) system. *Bulletin of Alloy Phase Diagrams*, 5(3):265–271, June 1984.

[123] F. Gencarelli, B. Vincent, L. Souriau, O. Richard, W. Vandervorst, R. Loo, M. Caymax, and M. Heyns. Low-temperature Ge and GeSn Chemical Vapor Deposition using Ge2h6. *Thin Solid Films*, 520(8):3211–3215, February 2012.

[124] Shotaro Takeuchi, Akira Sakai, Koji Yamamoto, Osamu Nakatsuka, Masaki Ogawa, and Shigeaki Zaima. Growth and structure evaluation of strain-relaxed Ge 1- x Sn x buffer layers grown on

various types of substrates. *Semiconductor Science and Technology*, 22(1):S231, 2007.

[125] T. A. de Assis and F. D. A. Aarão Reis. Thin film deposition with time-varying temperature. *Journal of Statistical Mechanics: Theory and Experiment*, 2013(10):P10008, 2013.

[126] Shotaro Takeuchi, Akira Sakai, Osamu Nakatsuka, Masaki Ogawa, and Shigeaki Zaima. Tensile strained Ge layers on strain-relaxed Ge1 - xSnx/virtual Ge substrates. *Thin Solid Films*, 517(1):159–162, November 2008.

[127] H. Li, Y. X. Cui, K. Y. Wu, W. K. Tseng, H. H. Cheng, and H. Chen. Strain relaxation and Sn segregation in GeSn epilayers under thermal treatment. *Applied Physics Letters*, 102(25):251907, June 2013.

[128] Francois Vurpillot, David Larson, and Alfred Cerezo. Improvement of multilayer analyses with a three-dimensional atom probe. *Surface and Interface Analysis*, 36(5-6):552–558, May 2004.

[129] M. Müller, B. Gault, G. D. W. Smith, and C. R. M. Grovenor. Accuracy of pulsed laser atom probe tomography for compound semiconductor analysis. *Journal of Physics: Conference Series*, 326(1):012031, 2011.

[130] M. Müller, D. W. Saxey, G. D. W. Smith, and B. Gault. Some aspects of the field evaporation behaviour of GaSb. *Ultramicroscopy*, 111(6):487–492, May 2011.

[131] R. Prakash Kolli and David N. Seidman. Comparison of Compositional and Morphological Atom-Probe Tomography Analyses for a Multicomponent Fe-Cu Steel. *Microscopy and Microanalysis*, 13(04):272–284, August 2007.

[132] D. E. Aspnes and A. A. Studna. Dielectric functions and optical parameters of Si, Ge, GaP, GaAs, GaSb, InP, InAs, and InSb from 1.5 to 6.0 eV. *Physical Review B*, 27(2):985–1009, January 1983.

[133] J. W. Matthews and A. E. Blakeslee. Defects in epitaxial multilayers: I. Misfit dislocations. *Journal of Crystal Growth*, 27:118–125, December 1974.

[134] Shotaro Takeuchi, Akira Sakai, Koji Yamamoto, Osamu Nakatsuka, Masaki Ogawa, and Shigeaki Zaima. Growth and structure evaluation of strain-relaxed $Ge_{1-x}Sn_x$ buffer layers grown on various types of substrates. *Semiconductor Science and Technology*, 22(1):S231–S235, January 2007.

[135] F. Gencarelli, B. Vincent, J. Demeulemeester, A. Vantomme, A. Moussa, A. Franquet, A. Kumar, H. Bender, J. Meersschaut, W. Vandervorst, R. Loo, M. Caymax, K. Temst, and M. Heyns. Crystalline Properties and Strain Relaxation Mechanism of CVD Grown GeSn. *ECS Journal of Solid State Science and Technology*, 2(4):P134–P137, January 2013.

[136] C. I. Ventura, J. D. Fuhr, and R. A. Barrio. Nonsubstitutional single-atom defects in the Ge1-xSnx alloy. *Physical Review B*, 79(15):155202, April 2009.

[137] W. Lefebvre, T. Philippe, and F. Vurpillot. Application of Delaunay tessellation for the characterization of solute-rich clusters in atom probe tomography. *Ultramicroscopy*, 111(3):200–206, February 2011.

[138] Alexander Heinrich, Tala'at Al-Kassab, and Reiner Kirchheim. Investigation of the early stages of decomposition of Cu–0.7at.% Fe with the tomographic atom probe. *Materials Science and Engineering: A*, 353(1–2):92–98, July 2003.

[139] S. Torquato, B. Lu, and J. Rubinstein. Nearest-neighbour distribution function for systems on interacting particles. *Journal of Physics A: Mathematical and General*, 23(3):L103, 1990.

[140] Philip J. Clark and Francis C. Evans. Generalization of a Nearest Neighbor Measure of Dispersion for Use in K Dimensions. *Ecology*, 60(2):316–317, April 1979.

[141] Boris Delaunay. Sur la sphere vide. *Izv. Akad. Nauk SSSR, Otdelenie Matematicheskii i Estestvennyka Nauk*, 7(793-800):1–2, 1934.

[142] Lutz Muche. Distributional properties of the three-dimensional Poisson Delaunay cell. *Journal of Statistical Physics*, 84(1-2):147–167, July 1996.

[143] Benjamin R. Conley, Aboozar Mosleh, Seyed Amir Ghetmiri, Wei Du, Greg Sun, Richard Soref, Joe Margetis, John Tolle, Hameed A. Naseem, and Shui-Qing Yu. Stability of Pseudomorphic and Compressively Strained Ge1-XSnx Thin Films under Rapid Thermal Annealing. *ECS Transactions*, 64(6):881–893, August 2014.

[144] Wei Wang, Lingzi Li, Qian Zhou, Jisheng Pan, Zheng Zhang, Eng Soon Tok, and Yee-Chia Yeo. Tin surface segregation, desorption, and island formation during post-growth annealing of strained epitaxial Ge1-xSnx layer on Ge(0 0 1) substrate. *Applied Surface Science*, 321:240–244, December 2014.

[145] B. Mazumder, A. Vella, F. Vurpillot, G. Martel, and B. Deconihout. Surface carrier recombination of a silicon tip under high electric field. *Applied Physics Letters*, 97(7):073104, 2010.

[146] M. Gilbert, F. Vurpillot, A. Vella, H. Bernas, and B. Deconihout. Some aspects of the silicon behaviour under femtosecond pulsed laser field evaporation. *Ultramicroscopy*, 107(9):767–772, September 2007.

[147] Laurent Arnoldi. *Interaction Laser-Nanopointe sous champ electrique intense: Application a la sonde atomique*. University of Rouen.

[148] Chantal K. Sudbrack. *Decomposition behavior in model Ni-Al-Cr-X superalloys: Temporal evolution and compositional pathways on a nanoscale*. PhD thesis, Northwestern University, 2004.

[149] A. Devaraj, R. Colby, W. P. Hess, D. E. Perea, and S. Thevuthasan. Role of Photoexcitation and Field Ionization in the Measurement of Accurate Oxide Stoichiometry by Laser-Assisted Atom Probe Tomography. *The Journal of Physical Chemistry Letters*, 4(6):993–998, March 2013.

[150] Daniel Beinke, Christian Oberdorfer, and Guido Schmitz. Towards an accurate volume reconstruction in atom probe tomography. *Ultramicroscopy*, 165:34–41, June 2016.

[151] Michael K. Miller, Kaye F. Russell, Keith Thompson, Roger Alvis, and David J. Larson. Review of Atom Probe FIB-Based Specimen

Preparation Methods. *Microscopy and Microanalysis*, 13(06):428–436, December 2007.

[152] David J. Larson, Ty J. Prosa, Robert M. Ulfig, Brian P. Geiser, and Thomas F. Kelly. *Local Electrode Atom Probe Tomography*. Springer New York, New York, NY, 2013.

[153] D. Blavette, J.M. Sarrau, A. Bostel, and J. Gallot. Direction et distance d'analyse à la sonde atomique. *Revue de Physique Appliquée*, 17(7):435–440, 1982.